Structural and magnetic properties of Bi and Fe sites co-substituted bismuth ferrite

Thesis Submitted to AcSIR for the Award of the Degree of

Doctor of Philosophy

in **Chemical Sciences**

By

Manjunath B

AcSIR No: 10CC11J26072

Under the guidance of

Dr. P. A. Joy

CSIR-National Chemical Laboratory

Pune 411008, India

सीएसआईआर - राष्ट्रीय रासायनिक प्रयोगशाला
(वैज्ञानिक तथा औद्योगिक अनुसंधान परिषद)
डॉ. होमी भाभा मार्ग, पुणे - 411 008, भारत

CSIR - NATIONAL CHEMICAL LABORATORY
(Council of Scientific & Industrial Research)
Dr. Homi Bhabha Road, Pune - 411 008, India

CERTIFICATE

This is to certify that the work incorporated in this Ph.D. thesis entitled **"Structural and magnetic properties of Bi and Fe sites co-substituted bismuth ferrite"** submitted by **Mr. Manjunath B** to Academy of Scientific and Innovative Research (AcSIR) in fulfilment of the requirements for the award of the Degree of ***Doctor of Philosophy*** *in* ***Chemical Sciences***, embodies original research work under my supervision. We further certify that this work has not been submitted to any other University or Institution in part or full for the award of any degree or diploma. Research material obtained from other sources has been duly acknowledged in the thesis. Any text, illustration, table etc., used in the thesis from other sources, have been duly cited and acknowledged.

Manjunath B
Research Scholar

Dr. P. A. Joy
Supervisor

Date: 23 February 2018

Place: CSIR-NCL, Pune

Communication Channels

NCL Level DID : 2590
NCL Board No. : +91-20-25902000
EPABX : +91-20-25893300
: +91-20-25893400

FAX
Director's Office : +91-20-25902601
COA's Office : +91-20-25902660
SPO's Office : +91-20-25902664

WEBSITE
www.ncl-india.org

DECLARATION

I, hereby declare that all the experiments in the thesis entitled, "**Structural and magnetic properties of Bi and Fe sites co-substituted bismuth ferrite**" submitted for the degree of **Doctor of Philosophy in Chemical sciences** to Academy of Scientific and Innovative Research (AcSIR), has been carried out by me at the Physical and Materials Chemistry Division of CSIR-National Chemical Laboratory, Pune, India under the supervision of **Dr. P. A. Joy**. Research material obtained from other sources has been duly cited and acknowledged in the thesis. This work is original and has not been submitted in part of full by me for any degree or diploma to this or any other University.

Manju

(Manjunath B)

Date : 23.02.2018

CSIR-NCL

Pune, India.

Dedicated to

my achan, amma and namiyechi

Acknowledgements

It is a great pleasure to express my gratitude and sincere thanks to all those who helped me directly and indirectly to complete this work. This thesis would not have been possible without all these people and their constant encouragement.

First of all, I would like to express my immense and sincere gratitude to my research supervisor ***Dr. P.A. Joy*** *for his constant support, encouragement and guidance throughout my Ph. D. He taught me how to observe small things and how broad data analysis should be. I have learnt so many new things from him which I hope will be helping me in my future life*

I express my sincere thanks to the former directors Dr. S. Pal, and the present director, Dr. Ashwini Kumar Nangia, for allowing me to work in the prestigious Laboratory and making all the facilities available for my research work. I would like to acknowledge CSIR for the financial assistance in the form of a research fellowship. I wish to thank Dr. Anilkumar, former Head of the Physical Chemistry Division, for allowing me to use all the divisional facilities. My sincere thanks to all the DAC members Dr. Suresh Bhat ,Dr. K. Sreekumar and Dr.Nandini devi. They were kind enough to spend their valuable time for my evaluation presentations. The valuable suggestions given by them helped me to shape the thesis more perfectly.

I thank all my seniors, Lenin, Vijay, Sreeja, Khaja, Mangesh, Pankaj, Govind, Jaya, Bindhu and Anjali for their help and support in the initial stages of my work, and my lab mates, Ram, Mohan, Arun and Anupriya for providing the nice working environment in the lab. I take time to convey my gratitude to the project students who worked with me Subin, and Ushananshu for their help.I would like to thank all my friends who made my life at NCL more cheerful, Dev Raj, Suresh, Rajaperumal,Pandiraj, Suman, Anuj, Devaraj,Babasaheb,Prajitha and Leenechi, Rajesh, Jijil, Ashok and Prabhu.

I would like to thank all my teachers for their support given to me. My Msc professor Khader Sir was the one person who made attracted to 'magnetism'. My high school teachers Ravi mash, who made me interested in chemistry. Manjula Ma'am and pradeep maash, Ravi masah, Sureshan maash all made me reach here. My best friend, Famida has always been with me in my life. Vaishali and Shilpa have also been helping me in all the matters. I would like to express my gratitude to them.

Without a special mention to Mohan, Himadri Devaraj, and Chandan this acknoldegement will be incomplete. They were always with me in the NCL Days and without them the Pune life would have been really difficult. I would like to thank my friends Robbinson, Sjo, Aneesh, George, Prasad, Vinesh, Centhil for their constant support.

Manjunath. B

Contents

List of Tables

List of Figures

List of Abbreviations and symbols

AFM: Antiferromagnetism

DM: Dzyaloshinskii-Moriya

emu: Electromagnetic Unit

eV: Electron Volt

FC: Field Cooled

H: Magnetic field

Hc: Coercivity

M: Magnetization

M_{60}: Magnetization at 60 kOe

MD: Magnetodielectric

M_r: Remnant magnetization

ME: Magnetoelectric coupling

O: Orthorhombic

PCW: Powder cell for windows

R: Rhombohedral

RKKY: Ruderman-Kittel-Kasuya-Yosida

SEM: Scanning electron microscopy

SG: Spin Glass

SQUID: Superconducting Quantum Interference Device

T_C: Curie Temperature

T_N: Neel Temperature

VSM: Vibrating Sample Magnetometer

XPS: X-ray Photoelectron Spectroscopy

XRD: X-ray diffraction

ZFC: Zero Field Cooled

$\chi 2$: Goodness of the fit

Abstract

Magnetoelectrics, due to their coupled magnetic and electric order parameters, have potential applications in the areas of data storage, sensors and actuators, etc. The known magnetoelectrics show very low magnetoelectric coupling or show the coupling only at very low temperatures. This makes them impossible to use for the practical applications. There are very few room temperature magnetoelectrics and they have very low magnetoelectric coupling constant. Perovskite oxides (ABO_3) are the much investigated systems because of their various interesting properties such as ferromagnetism, ferroelectricity, ferroelasticity etc. Even though ferromagnetism and ferroelectricity are mutually exclusive, in perovskite oxides they can coexist, if magnetism can originate from one metal cation and ferroelectricity from the other. $BiFeO_3$ (BFO) belongs to this category, where ferroelectricity is from Bi and weak ferromagnetism from Fe, and is one the few single-phase room temperature multiferroics, which received tremendous attention. Though it can show high ferroelectric properties, it is antiferromagnetic, and due to the poor magnetic parameters, the magnetoelectric coupling is very low. To improve the magnetoelectric properties, magnetic properties of $BiFeO_3$ need to be improved. Many studies have been reported on attempts to enhance the multiferroic characteristics of BFO by different methods like reducing the size to nano dimensions below the spin periodicity, substitution at the Bi and Fe sites which destroys the spin cycloid structure, etc. Substitution by suitable metal ions of comparable size is a very effective method to alter the properties of $BiFeO_3$. Fe-site substitution by transition metal ions is widely studied to enhance the magnetic properties by the destruction of the spin cycloid structure due to the structural distortions as well as the magnetic contribution from the substituents. On the other hand, Bi- site substitution by rare earth ions and divalent ions can enhance the properties due to the structural distortions. Furthermore, in the case of divalent ion co-substituted compounds, in addition to the structural distortions, there will be charge compensation by the formation of Fe^{4+} and/or oxygen vacancies which may also improve the magnetic properties.

Co-substitution, $Bi_{1-x}A_xFe_{1-y}M_yO_3$ ($x = y$ or $x \neq y$), which is the simultaneous substitution at the Bi-site and the Fe-site in BFO, is attracting much attention, with possibilities of simultaneous tuning of the magnetic and electrical properties. The literature on the detailed magnetic properties of co-substituted $BiFeO_3$ is rare and therefore, the aim of this work is to study the detailed structural and magnetic properties of the divalent ion and

Mn co-substituted $BiFeO_3$. In this work, $BiFeO_3$ is co-substituted at the Bi and Fe sites with divalent metal ions (Ca, Sr and Ba) and Mn. Mn^{4+} formed for the charge compensation is expected to lead to ferromagnetic double exchange interaction, and thus enhancing the magnetic properties. The structural, magnetic and dielectric properties are studied using powder XRD, Raman spectroscopy, SEM, XPS, SQUID VSM, etc.

Chapter 1 deals with the general introduction to magnetic, ferroelectric and multiferroic properties of materials. Importance of $BiFeO_3$, being one of the few room temperature multiferroics, have been discussed. Literature review on the structural, magnetic and ferroelectric properties of $BiFeO_3$ is included. Various approaches to enhance the multiferroic properties of $BiFeO_3$ emphasizing on the substitution effects in $BiFeO_3$ are discussed in detail.

Chapter 2 describes the synthesis method and the experimental techniques used. Solid state synthesis method was used to prepare different materials. The details of various characterization methods like X-ray diffraction, Raman spectroscopy, SEM, XPS, magnetic and dielectric measurements are included. A brief discussion on the Rietveld refinement of the XRD patterns using the GSAS-EXPGUI program is also discussed.

Chapter 3 describes the structural, magnetic and dielectric properties of $Bi_{1-x}A_xFe_{1-x}Mn_xO_3$ (A= Ca, Sr and Ba). Effect of ionic radii of the substituent 'A' on the structural, magnetic and dielectric properties of $Bi_{1-x}A_xFe_{1-x}Mn_xO_3$ has been investigated. Ca^{2+} has almost similar ionic radii to Bi^{3+}, whereas Sr^{2+} and Ba^{2+} are larger ions. For Ca-Mn co-substitution, XRD studies shows rhombohedral structure (*R3c*) for $x \leq 0.1$ and orthorhombic structure (*Pbnm*) for $x \geq 0.2$ and for Sr-Mn co-substitution *R3c* to $R\bar{3}c$ structural change is observed around $x = 0.1$, whereas for Ba-Mn co-substitution, *R3c* to tetragonal (*P4mm*) structural change is observed around $x = 0.25$. Raman studies also supported this structural transition. Decrease in the unit cell parameters and the unit cell volume indicated the presence of smaller Mn^{4+} in all the compositions. Room temperature magnetization of the samples increased with increasing the degree of co-substitution, showing a maximum remanence and coercivity at $x = 0.15$ for all the three co-substituted systems. Low temperature magnetization data implied a spin-glass-like nature of the samples. Among Ca/Sr/Ba-Mn co-substituted samples, Ca-Mn co-substituted samples showed better magnetic and dielectric properties around the morphotropic phase boundary (MPB) region, $x = 0.15$.

The anomalous properties around x = 0.15 can be due to the MPB region around this composition or due to various exchange interactions among Fe^{3+}, Mn^{3+}, Mn^{4+} etc

Chapter 4 discusses the detailed structural, magnetic, dielectric, and magnetodielectric properties of $Bi_{1-x}Ca_xFe_{1-x}Mn_xO_3$. Large number compositions were synthesised near the MPB region. Rietveld refinement of the XRD patterns revealed rhombohedral structure (*R3c*) for $x \leq 0.11$ and orthorhombic structure (*Pbnm*) for $x \geq 0.2$. Compositions with $0.12 \leq x \leq 0.175$ showed *R3c+Pbnm* mixed phase. The magnetization of the samples increased with increasing co-substitution, showing a maximum remanence and coercivity at x = 0.175. Dielectric properties showed a maximum at x = 0.15 and magnetodielectric data showed a maximum at x = 0.1. Changes in the various structural parameters like Fe-O-Fe bond angle, rhombohedral angle, tilt angle, etc, along with the higher Mn^{3+} content around the MPB region could be leading to the enhanced properties in this region. The higher magnetic, dielectric and magnetodielectric parameters around the MPB region suggested possible magnetoelectric coupling.

Chapter 5 discusses the structural, magnetic and dielectric properties of $Bi_{1-x}Ca_xFe_{1-y}Mn_yO_3$ ($x \neq y$). Five different series of compositions were prepared with the general formula, $Bi_{1-x}Ca_xFe_{1-y}Mn_yO_3$ ($0.1 \leq y \leq 0.5$). The Mn content was fixed and the Ca content was varied to study the effect of Ca on the properties of the co-substituted samples. The objective was to identify whether other combinations of Ca and Mn can show better properties than that obtained for $Bi_{0.85}Ca_{0.15}Fe_{0.85}Mn_{0.15}O_3$. Rhombohedral (*R3c*) to orthorhombic (*Pbnm*) structural change was observed around x = 0.15 irrespective of the Mn content. Room temperature magnetization of the samples increased with increasing the calcium content with a maximum coercivity and remanence observed in the range x = 0.15 to 0.25 for different series. Magnetization of the samples increased with Mn content whereas the coercivity and remanence decreased. Dielectric constant showed a maximum value in the range of x = 0.1 to 0.25 for different series. Among the various compositions studied in the series $Bi_{1-x}Ca_xFe_{1-y}Mn_yO_3$, $Bi_{1-x}Ca_xFe_{0.9}Mn_{0.1}O_3$ showed better magnetic properties around x = 0.15.

Chapter 6 is a summary of the work discussed on different co-substituted compositions in the previous chapters. The possible reasons for the weak ferromagnetism shown by the co-substituted $BiFeO_3$ are discussed. Scope for future research based on the present results is also discussed.

Chapter 1

Introduction

1.1. Magnetoelectricity and multiferroism

In 1894, Pierre Curie was the first one to explain magnetoelectrics as the materials which can be magnetized by an electric field and polarized by a magnetic field or the materials where electric and magnetic orders are coupled [1]. P Debye, in 1926 coined the term 'magnetoelectric effect' (ME) [2]. This new property can be used for many interesting applications. Later, Landau had given a theoretical explanation for the magnetoelectric effect [3]. In 1959, Dzyaloshinskii proposed ME effect in antiferromagnetic Cr_2O_3 [4]. Experimental evidence for ME effect in Cr_2O_3 was given by Astrov in 1960 [5,6]. Cr_2O_3 being paraelectric and antiferromagnetic, ME coupling was not significant enough for device applications and hence not much interest was generated in this area of research in the coming decades. In 1994, a century after the discovery of ME effect, H. Schmid coined the term 'multiferroics' which are materials showing more than one ferroic orders like ferromagnetism, ferroelasticity or ferroelectricity [7]. In the current scenario, this definition of multiferroics has diluted including other types of magnetic, electric and elastic properties (para, ferri, antiferro, etc.,) and not just confined to 'ferro' orders. It should be noted that according to the actual definition, multiferroism and magnetoelectricity are different. In magnetoelectrics, the electric and magnetic orders are coupled whereas it is not a necessary condition for multiferroics which are materials showing two primary ferroic orders. The Venn diagram in figure 1.1 clearly describes multiferroics and magnetoelectrics. Figure 1.2 gives examples of materials belonging to each class. The triangular part at the intersection of ferromagnetic and ferroelectric subgroup and magnetoelectric subgroup represents 'magnetoelectric multiferroics' which are ferromagnetic ferroelectric magnetoelectrics. There are very few materials belonging to this class, hence it's called as 'holy grail'. Materials show high magnetoelectric coupling constant when they are multiferroic (both ferromagnetic and ferroelectric) [8-13].

Due to the coupling between magnetic and electric orders, multiferroics are potential candidates for high-density data storage with four-bit logic state and multiferroic random access memory (MFRAM). High accuracy magnetic sensors (10^{-12} T), actuators and magnetic refrigeration are also some of the main applications of multiferroic materials [14-17].

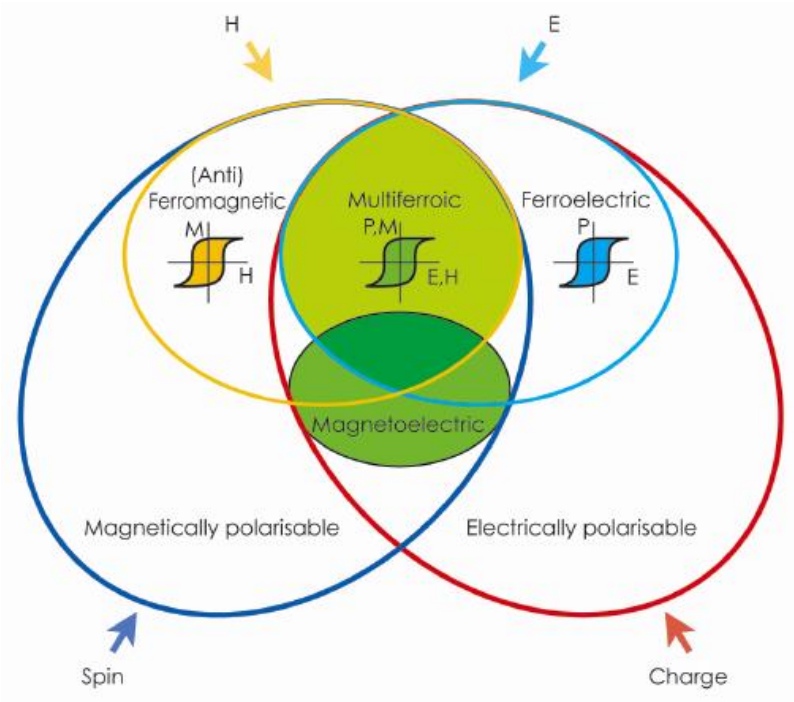

Figure 1.1. Venn diagram showing multiferroics and magnetoelectrics [18].

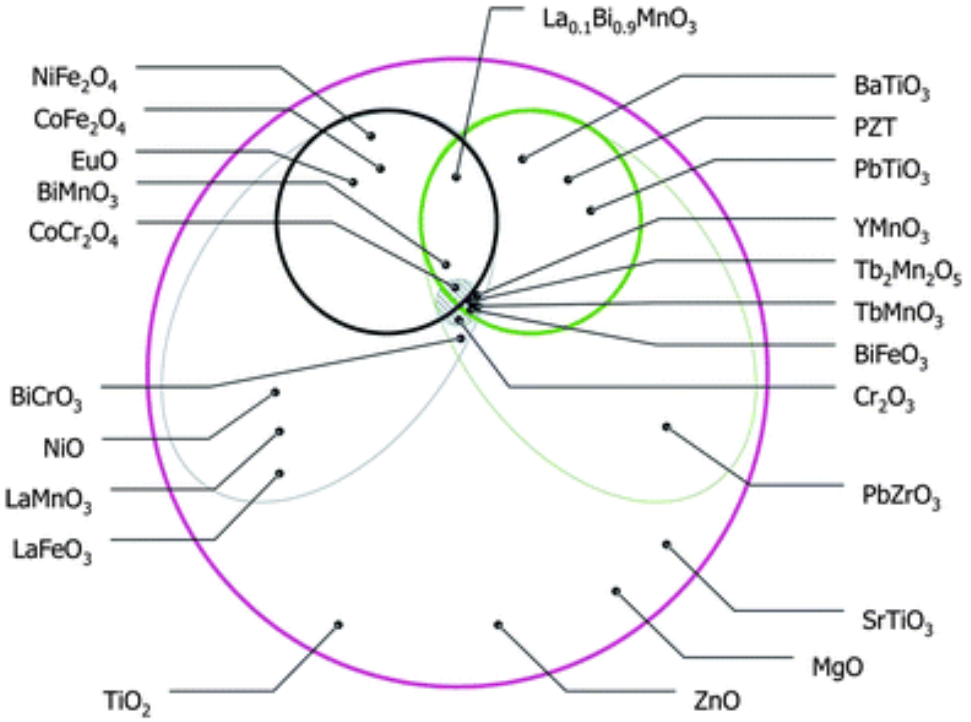

Figure 1.2. Venn diagram showing examples for different classes of magnetically and electrically polarizable materials [13].

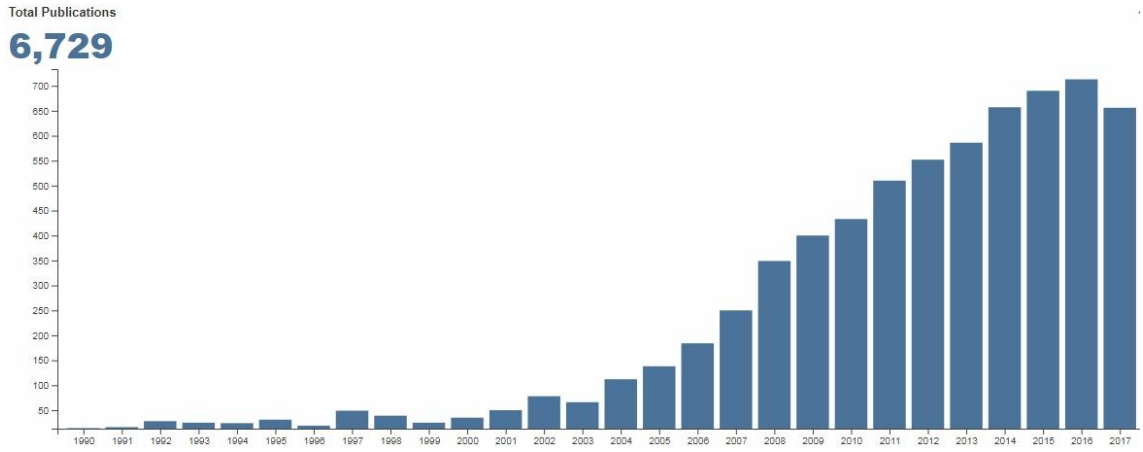

Figure 1.3. Year-wise publication in the field of *'magnetoelectric'*, generated from Web of Science [19].

Figure 1.3 gives the statistics of number of research articles on the topic 'magnetoelectric' by the web of science based search results. The total number of research articles is around 7000 from 1990 to 2017 which is a really huge number, and the number of publications picked up after 2000. This shows the immense interest in this research area. 'Renaissance of magnetoelectrics' actually started during the late 90's and early 2000's with the discovery of new materials showing magnetoelectricity and multiferroism as well as by the new theoretical approaches towards it.

1.2. Magnetism in materials

In atoms, magnetic moment arises from the spin and orbital motions of the electrons. In the case of spin magnetic moment, its direction is parallel to the spin axis and for orbital moment it is normal to the orbital plane. The orbital moment is given by,

$$\mu_{orbit} = eh/4\pi mc$$

Simialrly, the spin moment is given as

$$\mu_{spin} = eh/4\pi mc$$

where 'e' is the charge of the electron, 'h' is the Planck's constant, 'm' is the mass of the electron and 'c' is the velocity of light [20].

1.2.1. Types of Magnetism

Magnetism can be classified into five main classes namely diamagnetism, paramagnetism, ferromagnetism, antiferromagnetism and ferrimagnetism [20-23].

When an atom is having closed shells or completely filled shells, it shows diamagnetism. When placed in a magnetic field, diamagnetic materials show repulsion, or it shows negative magnetism. Diamagnetism is a universal property and shown by all materials but may be suppressed by other types of magnetism.

When materials possess unpaired electrons, it shows certain non-zero moment. Due to thermal energy, these moments will be randomly oriented and the net magnetic moment becomes zero. But when a magnetic field is applied, the moments try to orient towards the direction of the field and when the field is removed it goes back to the non-zero moment state. The classical theory of paramagnetism was given by Pierre Curie in 1895. Curie's law states that the magnetic susceptibility, given by $\chi = M/H$ where M is the magnetization per unit weight and H is the strength of the applied field, is inversely proportional to temperature for paramagnetic materials. $\chi_m = C/T$, where χ_m is the susceptibility per mole of the substance and C is the curie's constant, $C = N\mu^2_{eff}/3k$, where μ_{eff} is the effective paramagnetic moment in Bohr magnetons and k is the Boltzmann constant.

Some materials show spontaneous magnetization even in the absence of an applied magnetic field and are called as ferromagnets. Below a particular temperature, known as Curie temperature (T_C), they will be ferromagnetic and above T_C they are paramagnetic. In ferromagnets, there exists a long-range ordering because of which the moments align parallel to each other. Within the microscopic regions called domains, the moments will be aligned in the same direction, but in the absence of a field, the moments in different domains are aligned in different directions. When a magnetic field is applied, the moments in all the domains align in the direction of the field.

In antiferromagnetic materials, the moments are arranged anti-parallel to each other resulting in a zero net magnetic moment. Above the transition temperature, called Neel temperature (T_N), the material is paramagnetic [24]. The arrangements of the magnetic moments atoms/ions in different types of magnetic materials are shown in figure 1.4 [20]. There are four types antiferromagnetism, A-type, C-type, G-type and E-type as shown figure 1.5 [22,25]. In A-type antiferromagnetism, within a particular plane, the moments are

ferromagnetically coupled and among two neighbouring planes, the moments are antiferromagnetically coupled. In C-type, the moments are antiferromagnetically coupled within a plane and ferromagnetically coupled to the neighbouring plane. In G-type antiferromagnetism, moments are antiferromagnetically coupled to the nearest neighbours.

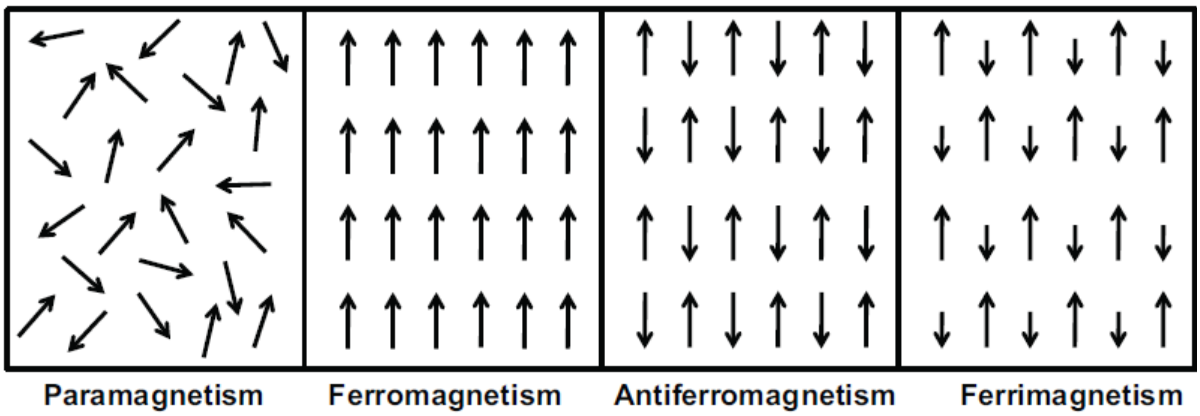

Figure 1.4. Arrangement of magnetic moments in different types of magnetic materials.

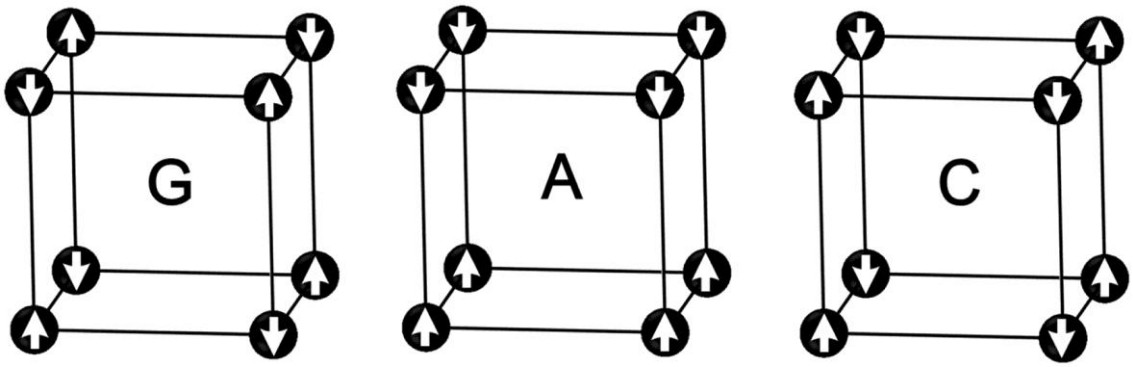

Figure 1.5. Different types of antiferromagnetism [25].

In ferrimagnetic materials, the adjacent moments are antiparallel, but there is only a partial cancellation of the moments due to the different magnitude of the adjacent moments. Like ferromagnets, ferrimagnets also shows a spontaneous magnetization below T_C and a paramagnetic behaviour above T_C. Most of the ferrites like cobalt ferrire, magnetite, etc., are ferrimagnetic.

For the ordered magnetic materials (ferro, antiferro and ferri), above their ordering temperature T_C or T_N, the susceptibility is inversely proportional to temperature given by,

$$\chi_m = C/(T- \Theta)$$

which is known as the Curie-Weiss law, where Θ is a constant known as the Weiss temperature, with the dimension of temperature.

Figure 1.16(a) shows the susceptibility vs. temperature plots for different magnetic materials [20]. Ferromagnetic materials show a large susceptibility whereas diamagnetic materials show no variation with temperature. Figure 1.6(b) shows the corresponding inverse susceptibility plots [20]. For paramagnetic materials, it passes through origin whereas ferro(ferri)magnetic materials show a positive Θ value (intercept) and antiferromagnetic materials show a negative Θ value.

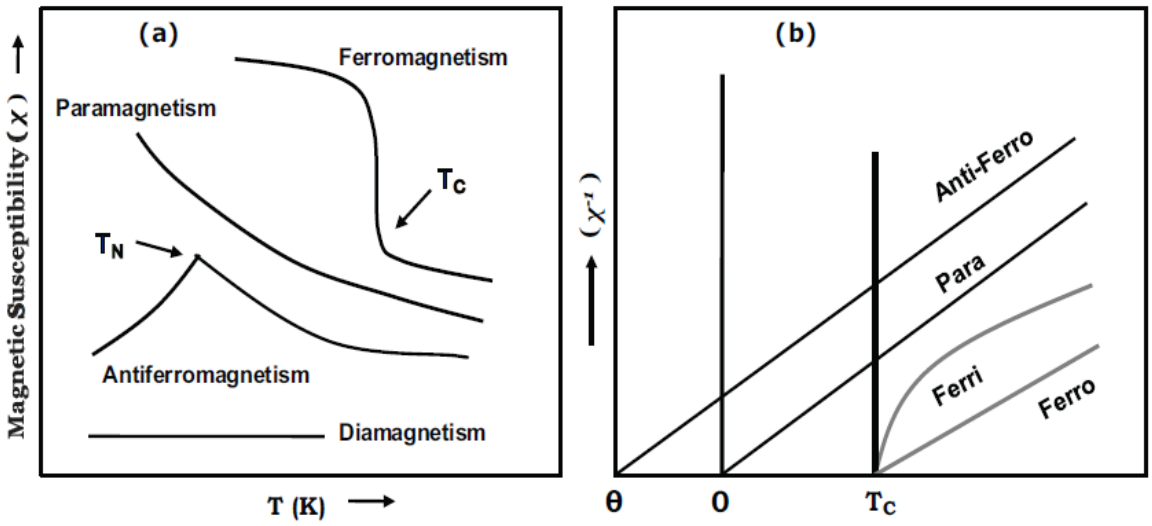

Figure 1.6. Temperature dependence of (a) the magnetic susceptibility and (b) inverse magnetic susceptibility of different types of magnetic materials.

1.2.2. Magnetic Hysteresis

The typical nature of the field dependence of magnetization for the dia, para/antiferro and ferro/ferrimagnetic materials is shown figure 1.7 [20]. Paramagnetic materials show a linear increase in magnetization with increasing field and when the field is reduced to zero, magnetization becomes zero. Diamagnetic materials show a linear decrease in magnetization

with increasing field. Ferro- and ferrimagnetic materials show a nonlinear increase in the magnetization with increasing field and in most of the cases, magnetization saturates (M_s) at higher fields. When the field is reduced to zero, there exists a remnant magnetization (M_r) for the ferro/ferrimagnetic materials. The field required to make remanence to zero is known as coercive field or coercivity (H_c). A magnetic hysteresis loop is observed for ferro- and ferrimagnetic materials when the field is cycled. Antiferromagnetic materials show M-H behaviour similar to paramagnetic materials.

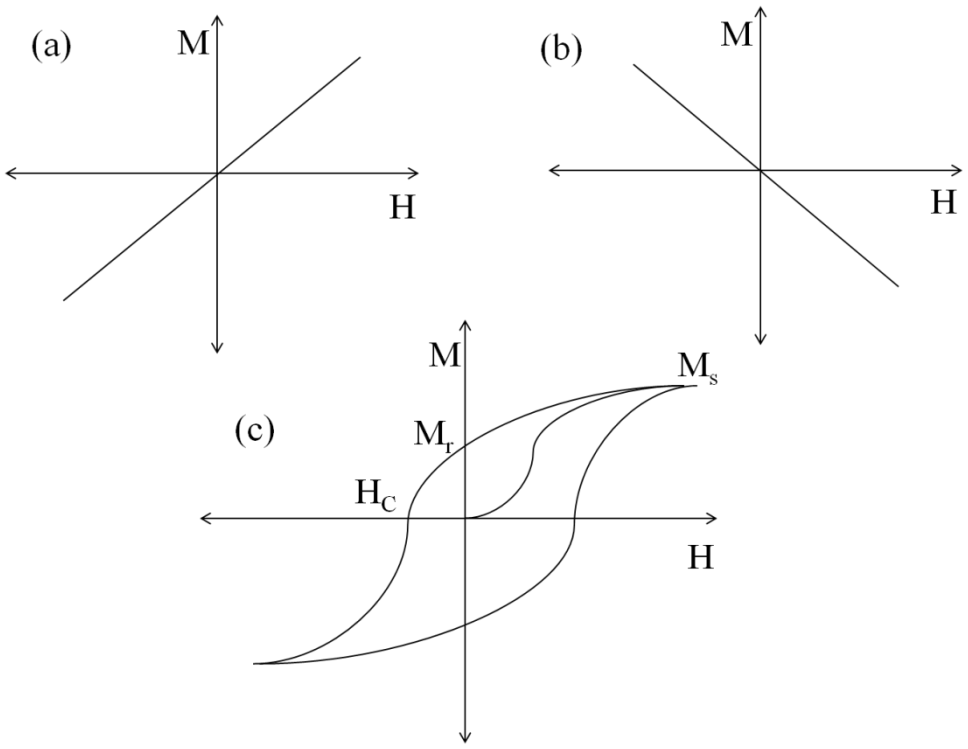

Figure 1.7. Magnetization as a function of field for (a) para/antiferromagnetic, (b) diamagnetic, and (c) ferro/ferrimagnetic materials.

1.2.3. Magnetic exchange interactions

Magnetic exchange interaction is the quantum mechanical exchange interaction between two magnetic atoms/ions. According to Heisenberg, magnetic exchange interaction between two atoms with spins S_i and S_j is given as

$$E_{ex} = -2J_{ex} (S_i \,.\, S_j) = -2J_{ex} S_i S_j \cos \theta$$

where J_{ex} is the exchange constant or exchange integral. If J_{ex} is positive, E_{ex} is minimum when $\theta = 0$ ($\cos\theta = 1$) or the moments are parallel. If J_{ex} is negative, E_{ex} is minimum when $\theta = 180$ ($\cos\theta = -1$), corresponding to antiparallel arrangement of moments. i.e., if J_{ex} is positive it corresponds to ferromagnetic exchange and if J_{ex} is negative, it is antiferromagnetic exchange interaction [20].

The magnetic interaction between two magnetic ions through a nonmagnetic ion, like oxygen, is known as indirect or superexchange interactions. Goodenough and Kanamori proposed some empirical rules about these types of interactions, by which nature of the exchange interaction between two magnetic ions can be predicted [26,27]. Double exchange (in perovskite manganites) is the hopping of electrons from one species to another through oxygen where the oxidation states of ions are interchanged. Double exchange always leads to ferromagnetism whereas superexchange in most cases are antiferromagnetic [28-30].

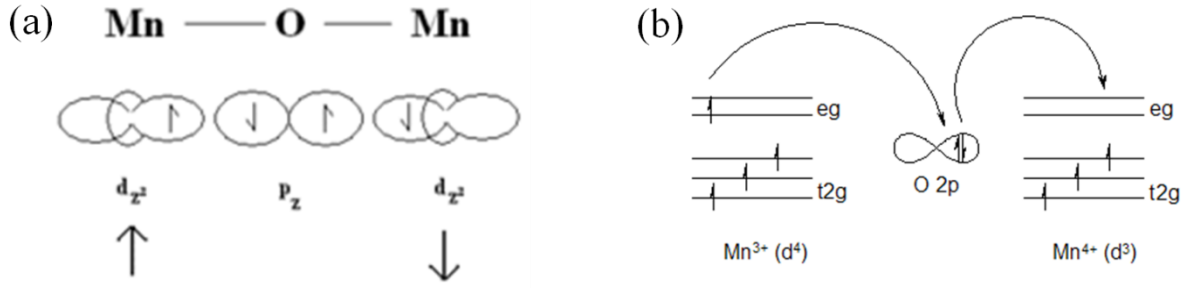

Figure 1.8. (a) Superexchange in MnO where indirect exchange of Mn d_z^2 electrons occurs through oxygen p_z orbitals [20], and (b) double exchange interactions in manganites, where hopping of e_g electrons between Mn^{3+} and Mn^{4+} occurs [23].

1.2.4. Weak ferromagnetism and Dzyaloshinskii–Moriya interaction

Dzyaloshinskii proposed a new theory of exchange interaction to explain the weak ferromagnetism shown by some antiferromagnetic materials like α- Fe_2O_3, Cr_2O_3, $MnCO_3$ $CoCO_3$, etc., [31]. Later Moriya [32] gave an explanation based on Anderson's superexchange theory [33]. This type of magnetic exchange interaction is known as the Dzyaloshinskii–Moriya (DM) interaction. It is the relativistic correction to the superexchange interaction. This antisymmetric, anisotropic exchange interaction is a combination of superexchange interactions and spin-orbit coupling. DM interactions will be absent in a system with inversion center.

DM interaction is given by the Hamiltonian,

$$H = D \,.\, (\overrightarrow{S1} \times \overrightarrow{S2})$$

where 'D' is a constant which depends on (proportional to) the spin-orbit coupling. DM interaction usually causes a canting of the moments and thus leads to weak ferromagnetism as shown in figure 1.9. Direction of the canting is determined by the sign of 'D'. In many cases, a noncollinear spin structure or spiral spin structure is formed due to the DM interactions. This noncollinear spin structure can also break the symmetry and can create ferroelectricity in certain materials.

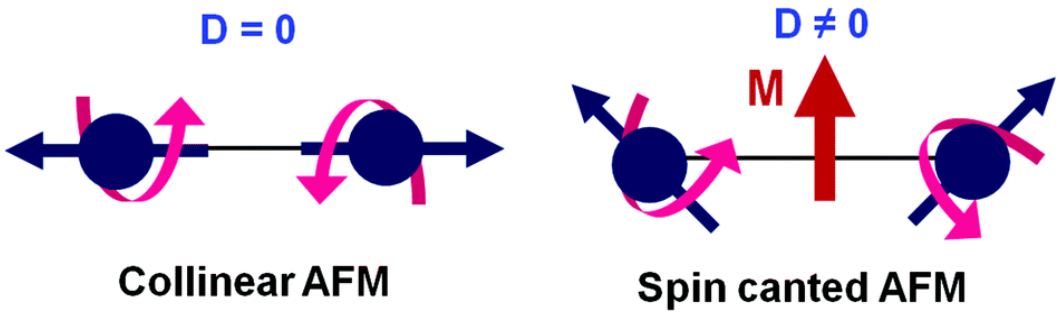

Figure 1.9. Illustration of Dzyaloshinskii–Moriya interaction [34].

As the microscopic origin of DM interaction is the relativistic spin-orbit coupling, its strength is proportional to Z^4, where Z is the atomic number. Usually, in 3d transition metals, spin-orbit coupling is very small but materials in which magnetism arises from 4d or 5d orbitals, DM interaction will be strong [35]. In perovskites such as $RMnO_3$ (R = Dy, Tb, Gd), DM interaction is linearly dependent on the displacement of the oxygen ions [36]. DM interactions play an important role in domain wall motions and in the formation of skyrmions (as in MnSi and $Fe_{1-x}Co_xSi$) [37,38]. DM interaction is a common phenomenon in incommensurate magnets, where the ferroelectricity is stabilised by DM interaction and this leads to a strong magnetoelectric coupling. For example, inverse DM interaction, which is the lattice response to the DM interaction, causes ferroelectricity in $DyMnO_3$ [39].

1.2.5. Jahn-Teller distortion

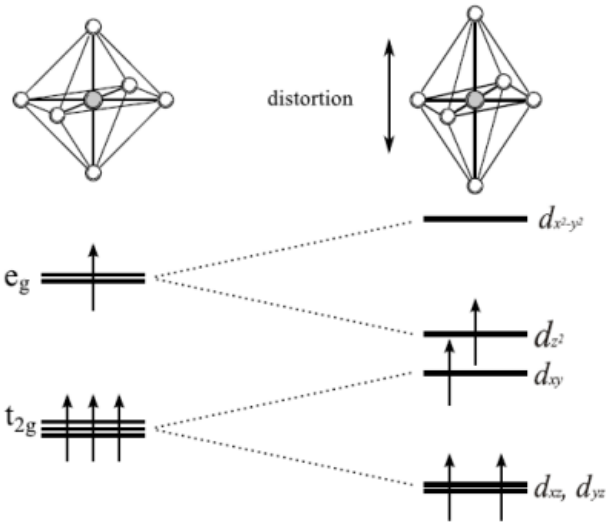

Figure 1.10. Jahn-Teller distortion of Mn^{3+} ion [46].

Jahn-Teller (JT) theorem states that in nonlinear molecules with degenerate orbitals, a distortion occurs in order to remove the degeneracy of the energy levels thus to lower the energy [40]. In an octahedral crystal field, d orbital of ions split into t_{2g} and e_g levels. When these energy levels are asymmetrically filled, degeneracy of the orbitals is developed and this degeneracy should be removed in order to lower the energy and to stabilize the system. The energy levels are split as shown in the figure 1.10. Usually, ions with asymmetrically filled e_g level show strong Jahn-Teller distortion. Cu^{2+} (***d^9 :*** t_{2g}^6, e_g^3***)*** and Mn^{3+} (***d^4:*** t_{2g}^3, e_g^1***)*** compounds are typical examples showing strong JT effect. Jahn-Teller distortion can cause structural distortions in a material. Interactions between the Jahn-Teller ions leads to lowering of the symmetry of crystal itself and is known as cooperative Jahn-Teller effect.

Compounds with ions having orbital degeneracy, Jahn-Teller active ions, shows many interesting properties like distorted crystal structure, structural phase transitions and complicated magnetic structure etc., than their analogous compounds without the orbital degeneracy [40-45]. Large anisotropy and high magnetostriction also result from Jahn-Teller effect [42]. Perovskite manganites, such as $LaMnO_3$, having Mn^{3+} (t_{2g}^3, e_g^1) ions are well known for showing Jahn-Teller distortions, whereas the Mn^{4+} (t_{2g}^3, e_g^0) is Jahn-Teller inactive [41,44]. In manganites, below a certain temperature, $T_{JT,}$ oxygen octahedra are distorted, leading to a structural transition. Usually an O_I ($c/a < 2^{½}$) orthorhombic structure is

observed for manganites with only Mn^{3+} ions [45]. In $LaMnO_3$, Jahn-Teller effect leads to the formation of short and long Mn-O bonds and thus the Mn-O-Mn exchange interaction becomes anisotropic. This also leads to orbital ordering phenomena [45].

1.2.6. Spin glasses

Spin glass state is the third most magnetic state found in the materials after ferromagnetism and antiferromagnetism [47]. Spin glasses are disordered or frustrated magnetic systems. Spin glass phase was first observed in magnetic alloys like $Cu_{1-x}Mn_x$, $Au_{1-x}Mn_x$ etc. The term spin glass was first introduced by B R Coles in 1970 [47]. For understanding, spin glasses can be illustrated by a triangular magnetic lattice as shown in figure 1.11(a) where the first and second spins are antiferromagnetically ordered; the third spin can choose two different spin states. This competing interactions lead to the frustrated magnetic system. In spin glasses, no long-range orders exist like ferromagnetism or antiferromagnetism, but they exhibit a spin glass transition temperature (T_g) or freezing temperature (T_f) below which the spins are disordered or frustrated [47] and show hysteresis and remanence. At high temperatures, they follow a Curie-Weiss behaviour.

Classical examples for the spin glasses are noble metals like Cu, Au, At, Pt, etc. weakly diluted with transition metal ions like Fe or Mn. In these magnetically diluted systems, as the distance between the magnetic spins (magnetic impurities) are random; some moments will have parallel, ferromagnetic exchange and others will have antiferromagnetic exchange leading to frustration. These impurity spins polarize the conduction electrons and interact with each other through the 'RKKY coupling' (Ruderman-Kittel-Kasuya-Yosida). The RKKY coupling has an oscillating nature with distance and disappears at large distances (figure 1.11(b)). Hence the coupling between the spins can be ferromagnetic or antiferromagnetic with respect to the distance also. The random distribution of the magnetic spins leads to a random distribution of the magnetic interactions. All these factors lead to spin glass behaviour. When the concentration of the magnetic impurities is high, impurities become the first or second neighbour to another impurity and magnetic clusters can form and usually show very large magnetic moments. The magnetic moments within these clusters will have the same direction, but in different clusters they will be randomly oriented and lead to frustration. This is known as 'mictomagnetism' or 'cluster glass as illustrated in figure 1.12 [47-51].

To be exact, in order to exhibit a spin glass phase, there should be randomness in position of the spins or in the exchange interactions (ferromagnetic or antiferromagnetic); site randomness where magnetic ions are random or bond disorder where exchange interaction with neighbouring spins are ferromagnetic and antiferromagnetic as illustrated in figure 1.12. Combination of randomness, frustration and competing interactions lead to spin glass phase.

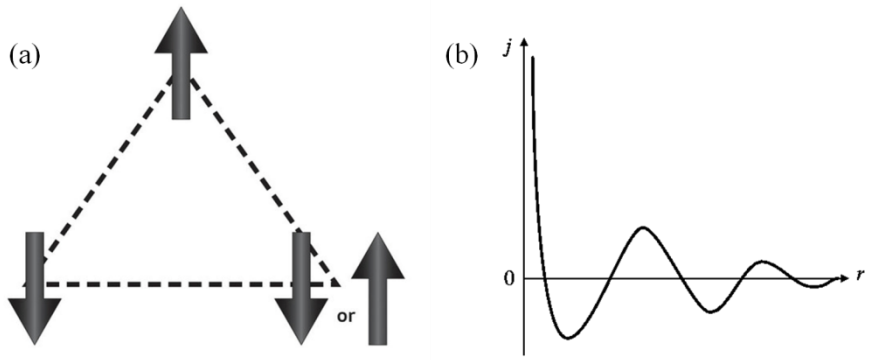

Figure 1.11. (a) Triangular magnetic lattice showing frustrated magnetism [52] and (b) the oscillatory RKKY coupling [50].

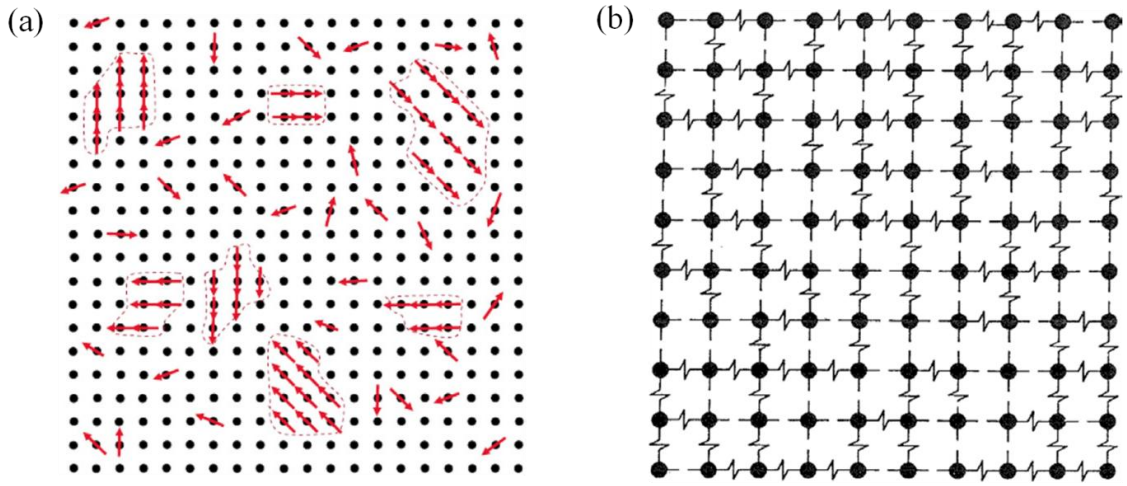

Figure 1.12. a) Site disorder and cluster formation. b) bond disorder; dashed lines show ferromagnetic exchange and zigzag lines show antiferromagnetic exchange [48].

1.3. Dielectrics and ferroelectricty

Dielectric materials are insulating or nonconducting materials which can store electrical energy. These materials can be polarized with the application of an electric field. Most of the ceramic materials are dielectric. Dielectric constant is the term which gives the measure of dielectric properties or the degree of the polarizability [53,54]. Dielectric permittivity (dielectric constant) is defined as,

$$\varepsilon_r = C/C_0$$

where C is capacitance with the material and C_0 is the capacitance with vacuum in-between the plates of a parallel plate condenser.

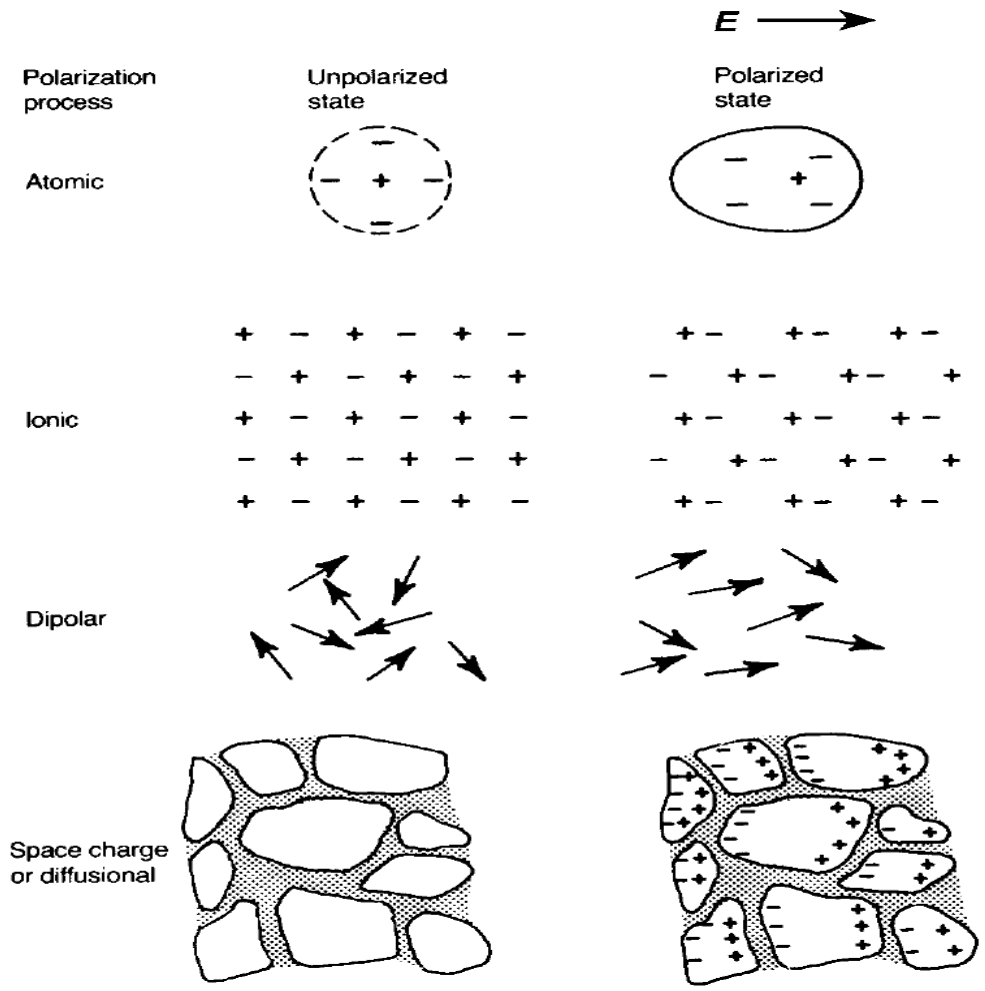

Figure 1.13. Different polarization mechanisms [53].

There are four different types of polarization mechanisms [53,54] such as electronic, ionic, dipolar and interface polarization as illustrated in figure 1.13. *Electronic polarization (atomic polarization)* occurs when the electron clouds are displaced away from the nucleus and the dipole is created due to the application of an electric field. *Ionic polarization* occurs in materials having ionic character, like in NaCl, where dipoles are already present. But due to symmetric structure, the net moment gets cancelled out. In the presence of an electric field, small displacement to these ions from the equilibrium position can lead to net dipolar moment. *Dipolar or orientation polarization* exists in materials having molecular dipoles which are randomly oriented due to thermal energy. Upon the application of an electric field, these dipoles get aligned and the materials get polarized. *Interface polarization* occurs when grain boundaries and the electrode-material interfaces have charge accumulation, which on application of electric field gets aligned and causes polarization in materials.

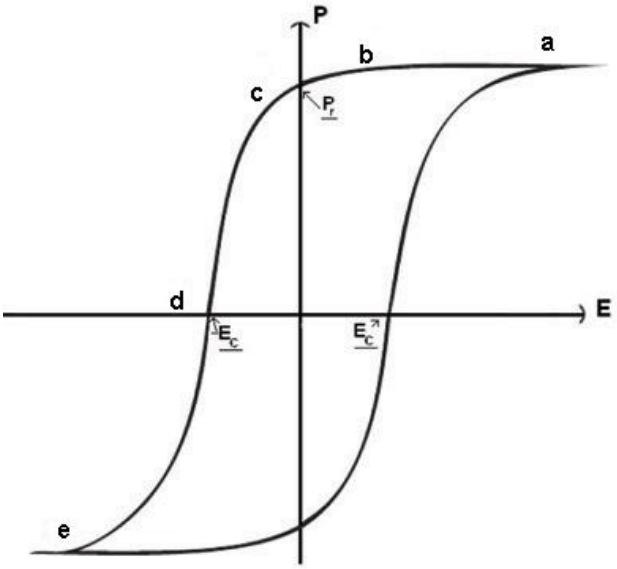

Figure 1.14. Polarization vs. electric field curve, known as P-E loop [59].

The phenomenon of ferroelectricity was first found in Rochelle salt (potassium sodium tartrate) by Anderson and later studied in detail by Valasek [55,56]. Materials showing spontaneous polarization (similar to a ferromagnetic material showing spontaneous magnetization in the absence of a magnetic field) even in the absence of an electric field are known as ferroelectric materials. The direction of the polarisation can be switched by applying an external electric field. To be ferroelectric, a material should be

non-centrosymmetric. Above certain temperature known as Curie temperature, T_C, ferroelectric materials become nonpolar paraelectric which is usually a centrosymmetric structure. Ferroelectric materials show a very high dielectric constant. $BaTiO_3$ is a typical example of ferroelectric materials where the ferroelectricity originates due to the displacement of the Ti atom in the crystal structure [57,58]. A typical polarization vs. electric field hysteresis (P-E loop) is shown in figure 1.14.

1.4. Magnetoelectric coupling

According to the Landau theory, free energy for the magnetoelectric system in terms of electric and magnetic fields can be expressed as [8]

$$F(E, H) = F_0 - P_i^S E_i - M_i^S H_i - 1/2\ \varepsilon_0\ \varepsilon_{ij}\ E_i E_j - 1/2\ \ \mu_0 \mu_{ij}\ H_i H_j - \alpha_{ij}\ E_i H_j - 1/2\ \beta_{ijk}\ E_i H_j H_k - 1/2\ \gamma_{ijk} H_i E_j E_k - \ldots..$$

where F_0 is the ground state energy.

From the above equation, polarization can be expressed as,

$$P_i (E, H) = - \partial F / \partial E_i = P_i^S - \varepsilon_0\ \varepsilon_{ij}\ E_j - \alpha_{ij}\ H_j - 1/2\ \beta_{ijk}\ H_j H_k - \ \gamma_{ijk} H_i E_j E_k - \ldots..$$

And magnetization can be expresses as,

$$M_i (E, H) = - \partial F / \partial H_i = M_i^S - 1/2\ \ \mu_0 \mu_{ij}\ H_j - \alpha_{ij}\ E_i - \beta_{ijk}\ E_i\ H_j - \ 1/2\ \gamma_{ijk} E_j E_k - \ldots..$$

Here P^S and M^S are spontaneous polarisation and magnetization, respectively, ε is the electric susceptibility, μ is the magnetic susceptibility, and α is the linear magnetoelectric coupling coefficient. β and γ are the second order and the third order coupling coefficients, respectively, which are negligibly small. For application purposes, the linear or the first order magnetoelectric coupling coefficient, α, should be large enough.

To be magnetoelectric, the symmetry consideration also should be satisfied. For ferromagnets, magnetic moment, 'm' is independent of spatial inversion whereas the time reversal switches the magnetic moment. For ferroelectrics, time reversal produces no change, but the spatial inversion switches the polarisation. Multiferroics which are both ferromagnetic and ferroelectric does not have these two symmetries (figure 1.15).

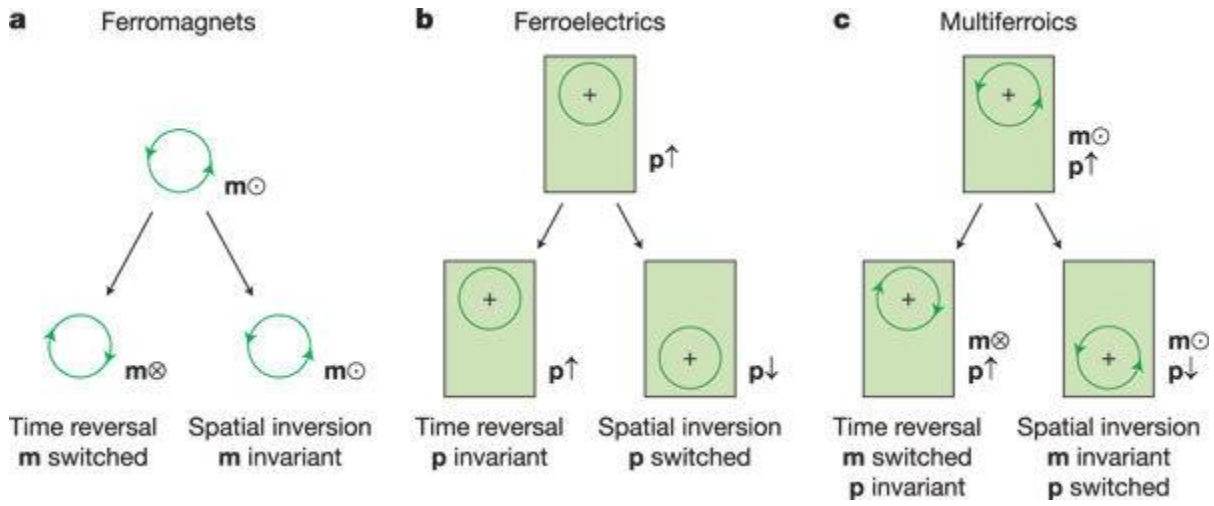

Figure 1.15. Time-reversal and spatial-inversion symmetries in multiferroics [11].

1.5. Type-I and type-II multiferroics

Multiferroics can be divided into two classes, type-I multiferroics and type-II multiferroics based on the mechanism of the origin of the magnetoelectric coupling [18]. Type-I multiferroics are multiferroics where magnetism and ferroelectricity have different origins. Type-I multiferroics have high ferroelectric properties and higher T_C. But usually, very low magnetoelectric coupling is observed in type-I multiferroics.

There are very few multiferroics since '***ferroelectric metals'*** cannot exist. To be ferroelectric, a material should be having high resistivity (no free electrons or unpaired electron) so that electric field could polarize it. And to show magnetism, it should have unpaired electrons. Again these unpaired electrons in ferromagnets cause conduction of electricity, and usually all ferromagnets are metals and ferroelectrics are insulators. To be magnetic, an atom should have unpaired electrons and to be ferroelectric, it should possess a closed shell. This "d^0 vs. d^n issue" leads to the scarcity of multiferroics [60].

Ferroelectricity in materials can also arise from other mechanisms as discussed below

1.5.1. Lone pair ferroelectrics

Here ferroelectricity in the material originates from the lone pair of electrons which are stereochemically active. Especially in the bismuth and lead-based compounds, the ns^2 lone pairs cause this type of ferroelectricity. Here mixing of ns^2 ground state with low lying ns^1

and np^1 excited levels occurs. The lone pair does not make a chemical bond with the oxygen but an electron density is formed around it as shown in figure 1.16. $BiFeO_3$, $BiMnO_3$, $PbVO_3$, etc., are some typical examples of this class of materials [18,61,62]. Though in $PbTiO_3$ the main contribution to ferroelectricity is from the displacement of the Ti ions, s^2 lone pair effect also should be taken into account [18, 63].

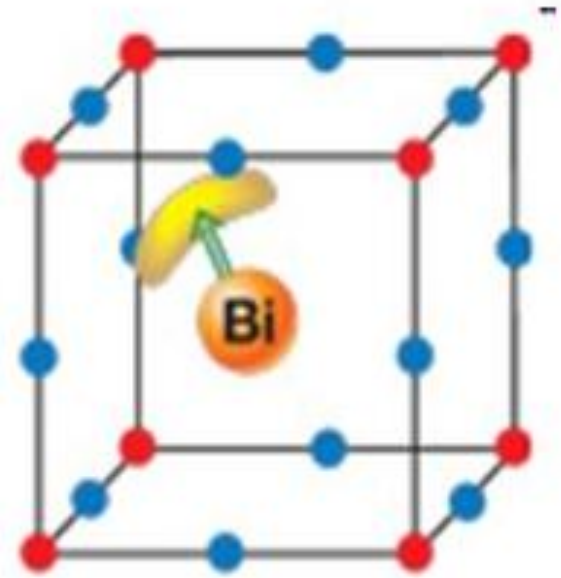

Figure 1.16. Stereochemical activity of Bi $6s^2$ lone pair in $BiFeO_3$ [18].

1.5.2. Geometrically frustrated ferroelectrics

In $YMnO_3$ hexagonal manganites, MnO_5 bypyramids tilt inorder to form a rigid close-packed structure (figure 1.17). This tilting of the bypyramids breaks the inversion symmetry and leads to ferroelectricity [18,64]. $CuFeO_2$ also exhibit geometrically induced ferroelectricity [65]. These types of compounds usually show a very high ferroelectric transition temperature than for the magnetic transition [18, 64-65].

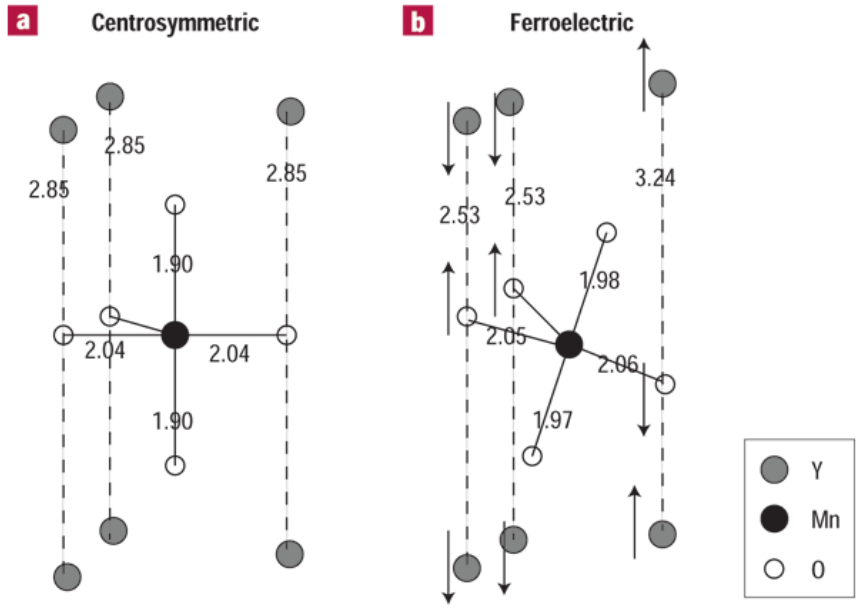

Figure 1.17. Tilting of the polyhedron in $YMnO_3$ [64].

1.5.3. Charge ordering

In compounds having mixed valent metals, charge ordering can be possible which leads to ferroelectricity [66-70]. Many of the hole-doped manganites are known to show charge ordering and ferroelectricity by this mechanism. $Pr_{1-x}Ca_xMnO_3$ is a typical example of charge ordered multiferroics [67-69]. $LuFe_2O_4$ and Fe_3O_4 also belong to this class [66,70]. Different types of charge ordering are possible as shown in figure 1.18. In site-centered charge ordering (figure 1.18(a)), the Mn^{3+} and Mn^{4+} ions are arranged at the alternative sites in a checkerboard arrangement where the metal sites become inequivalent but a centre of symmetry exists. Figure 1.18(b) shows the case where the charge is localized not on the sites but on the bonds, where the metal sites are equivalent and there exist a centre of symmetry. But the combination of these two (figure 1.18(c)) leads to non-centrosymmatric pattern and thus can exhibit ferroelectricity.

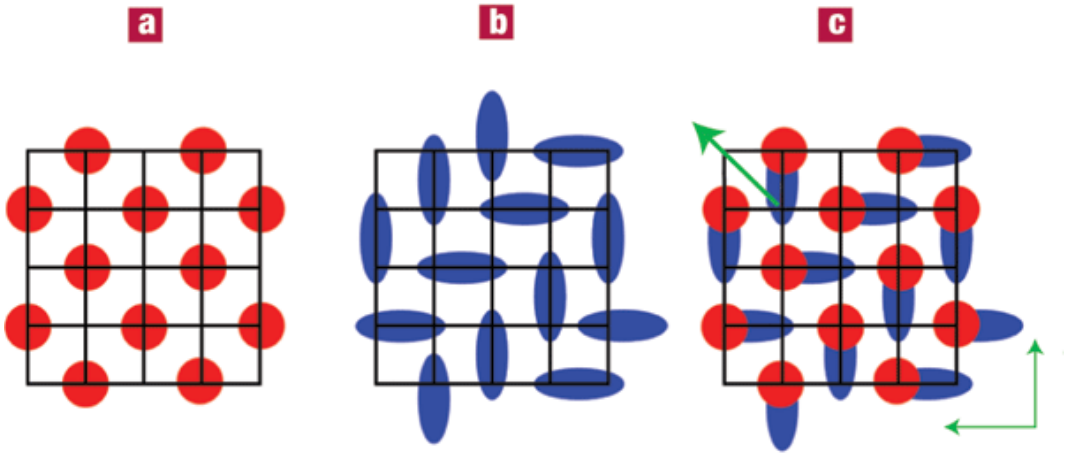

Figure 1.18. a) Site-centered charge ordering, b) bond centered charge ordering, and c) a ferroelectric intermediate state. The charge-ordered structure in which c lacks inversion symmetry, where the green arrow shows the direction of polarization [67].

In type-II multiferroics, ferroelectricity originates due to magnetic ordering, and in these materials the coupling is strong [71-79]. Here the inversion symmetry is broken due to the magnetic ordering. The recently discovered materials like $TbMnO_3$ [71,72,76], $TbMn_2O_5$ [73,74,77,78], $Ni_3V_2O_8$ [76], $MnWO_4$ [76], and $DyFeO_3$ [79] are examples for type-II multiferroics. Due to the low magnetic ordering temperature and very low polarization ($\approx 10^{-2}$ $\mu C/cm^2$), these materials cannot be used for room temperature applications [75,76].

As explained above, single phase multiferroic materials which show multiferroism/magnetoelectricity are very few. However, the property of multiferroism can be achieved by the 'product rule', where two materials having different properties can be combined and a new property can be achieved [80-83]. Composites of magnetostrictive materials ($CoFe_2O_4$) with piezoelectric materials ($BaTiO_3$) exhibit magnetoelectric coupling. When a magnetic field is applied to the composite, there occur a change in the dimension of the magnetostrictive material and this change in dimension acts a stress and is passed to the piezoelectric component of the composite. Due to this stress in the piezoelectric material, a polarization is produced. Thus, by applying a magnetic field, electrical polarization develops in the composites. The magnetoelectric effect in composites are relatively much less than that in the single phase materials and hence it is important to have single phase materials which show higher ME properties.

Table 1.1. Examples for single phase multiferroic compounds with their structure along with the magnetic and ferroelectric transition temperatures.

Compound	***Crystal structure, space group***	T_{FE} ***(K)***	T_M ***(K)***	***Reference***
Cr_2O_3	Rhombohedral, $R\bar{3}c$	Paraelectric	307	6
$BiMnO_3$	Monoclinic, C2/c	760	105	84,85
$BiFeO_3$	Rhombohedral, R3c	1103	673	12
$BiCrO_3$	Monoclinic, C2/c	420	114	85,86
$YMnO_3$	Hexagonal, $P6_3cm$	914	80	87
$DyFeO_3$	Orthorhombic, Pnma	3.5	645	88
$TbMnO_3$	orthorhombic, Pbnm	28	41	76
$TbMn_2O_5$	Orthorhombic, Pbam	38	43	78
$LuFe_2O_4$	Rhombohedral, R3m	330	330	66
$CoCr_2O_4$	Cubic, $Fd\bar{3}m$	25	93	89
$HoMnO_3$	Hexagonal, $P6_3cm$	900	70	90
$YbMnO_3$	Hexagonal, $P6_3cm$	900	80	91
$Ni_3B_7O_{13}I$	Cubic, $F\bar{4}3c$	64	64	92
$Ni_3V_2O_8$	Orthorhombic, Cmca	6	9	93

1.6. Perovskite oxides as multiferroics

Perovskites have the general formula ABX_3, where 'X' can be halogens or oxygen. The 'A' cations are bigger than the 'B' cations and are coordinated by 12 anions. B cations occupy at the octahedral position formed by the anions. Ideal perovskites have a cubic structure [94, 95]. A perovskite unit cell is shown in figure 1.19

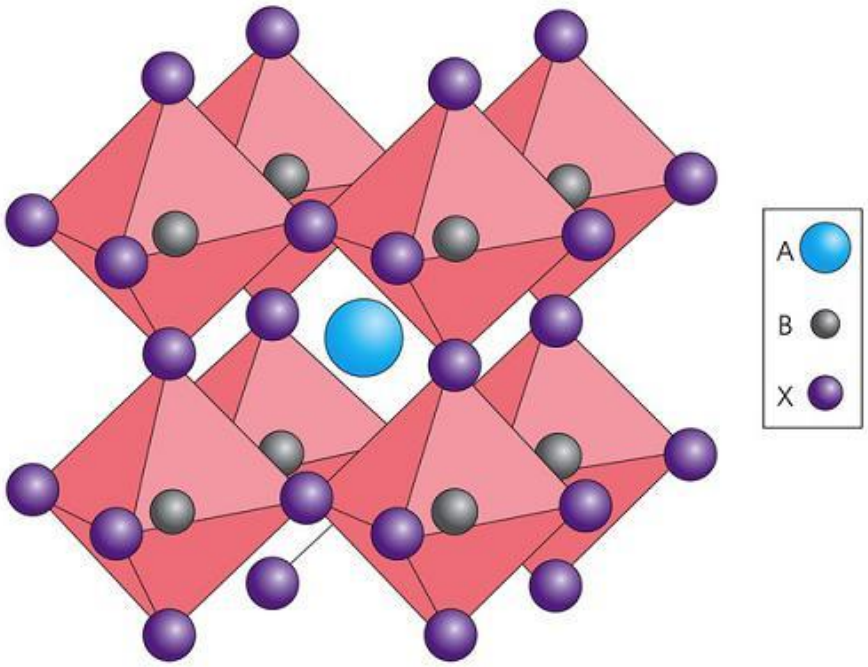

Figure 1.19. The Perovskite structure [96].

Perovskites are known to show various interesting properties like ferromagnetism ($BiMnO_3$, $YMnO_3$, $TbMnO_3$), ferroelectricity ($PbTiO_3$, $BaTiO_3$), ferroelasticity ($CaTiO_3$, $LaCoO_3$), pyroelectricity, piezoelectricity, superconductivity, multiferroism, magnetoelectricity, etc. Even though ferromagnetism and ferroelectricity are mutually exclusive, in perovskite oxides (ABO_3), they can coexist, since magnetism can originate from one metal cation and ferroelectricity from the other [60]. Easy synthesis methods, stability and easy tuning of the properties make perovskites an important class of compounds.

1.7. Bismuth ferrite as a 'super candidate' for multiferroism

Among the bismuth based perovskite oxides, $BiMnO_3$ and $BiFeO_3$ are the most studied ones. However, the low ferromagnetic transition temperature (105 K) and the requirement of high pressure synthesis methods make it difficult to use $BiMnO_3$ for applications [84]. Also, the ferroelectricity in $BiMnO_3$ is a controversial topic in the literature as in many cases it crystallises in C2/c phase (rather than C2) which is centrosymmetric and thus

non-ferroelectric [97]. Whereas the relatively simple synthesis methods and high magnetic/ferroelectric transition temperatures make $BiFeO_3$ the favourite one.

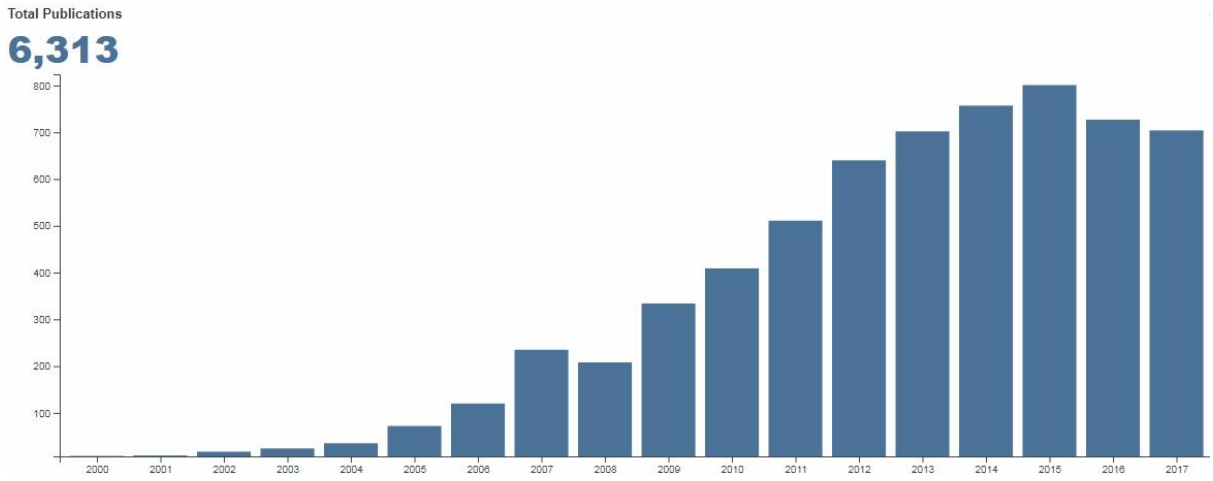

Figure 1.20. Year-wise publication in the field of *'$BiFeO_3$'*, generated from Web of Science [98].

Figure 1.20 gives the statistics of the number of papers published on the topic '$BiFeO_3$' from web of science based search for the period of 2000 to 2017. Around 6400 research articles are published which is relatively a huge number. The interest in $BiFeO_3$ started after Wang's paper published in the journal 'Science' in 2003 with enhanced magnetic and ferroelectric properties in the thin films [61]. Though the authors claimed to obtained enhanced magnetism from the epitaxial stress, later it was shown by Eerenstein *et al.* [99] that magnetism was coming from Fe^{2+} species in the samples. This article caused a tremendous impact on the worldwide researchers to work on bismuth ferrite based multiferroics. After 2003, an exponential rise in the number of publications can be seen in figure 1.21.

1.7.1. Crystal structure of $BiFeO_3$

$BiFeO_3$ has a distorted rhombohedral structure with R3c space group, with the unit cell parameters a = 5.58 Å and c = 13.9 Å [100,101]. The unit cell of $BiFeO_3$ is shown figure 1.22. Ferroelectricity in $BiFeO_3$ is from the $6s^2$ lone pair electrons of bismuth. The stereochemical lone pair of electrons make a covalent bond with oxygen 2p orbitals which

makes the Bi atom to shift towards [111] direction breaking the centre of symmetry and polarizing the molecule.

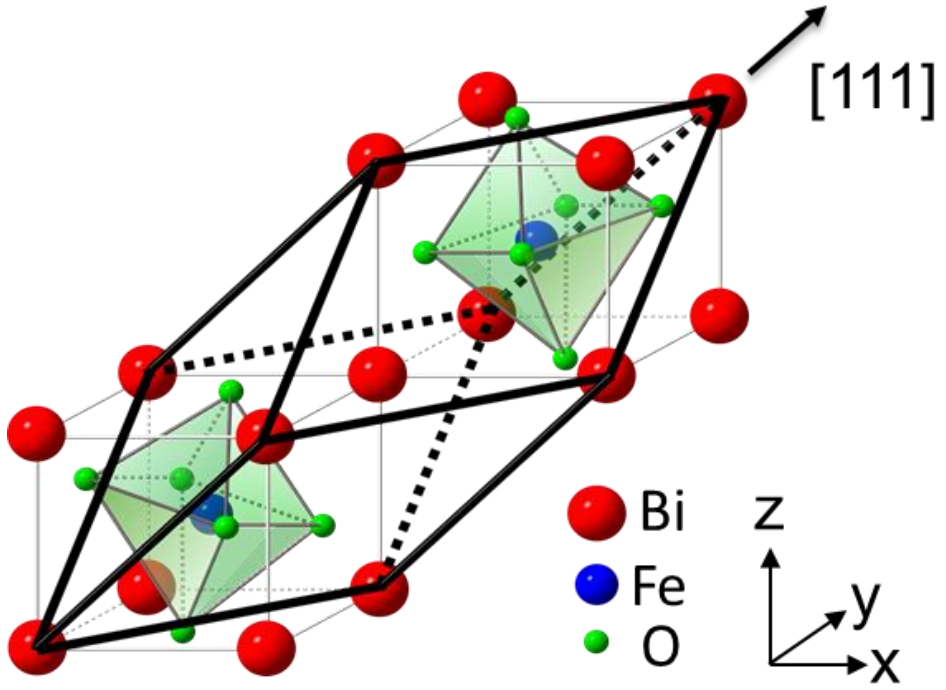

Figure 1.21. The unit cell of $BiFeO_3$ [102].

1.7.2. Phase diagram of Bi_2O_3-Fe_2O_3 system

It is very difficult to synthesise single phase $BiFeO_3$ by solid state synthesis method according to the phase diagram of Bi_2O_3-Fe_2O_3 system, shown in figure 1.22. $BiFeO_3$ is a thermodynamically metastable system. Phase pure $BiFeO_3$ is formed only in a very narrow composition range of the Bi_2O_3-Fe_2O_3 system in a very narrow temperature range. At higher temperatures, it dissociates into Bi_2O_3 and Fe_2O_3. Usually the bismuth-rich impurity phase $Bi_{25}FeO_{40}$ and the iron-rich $Bi_2Fe_4O_9$ are formed as impurities [103, 104].

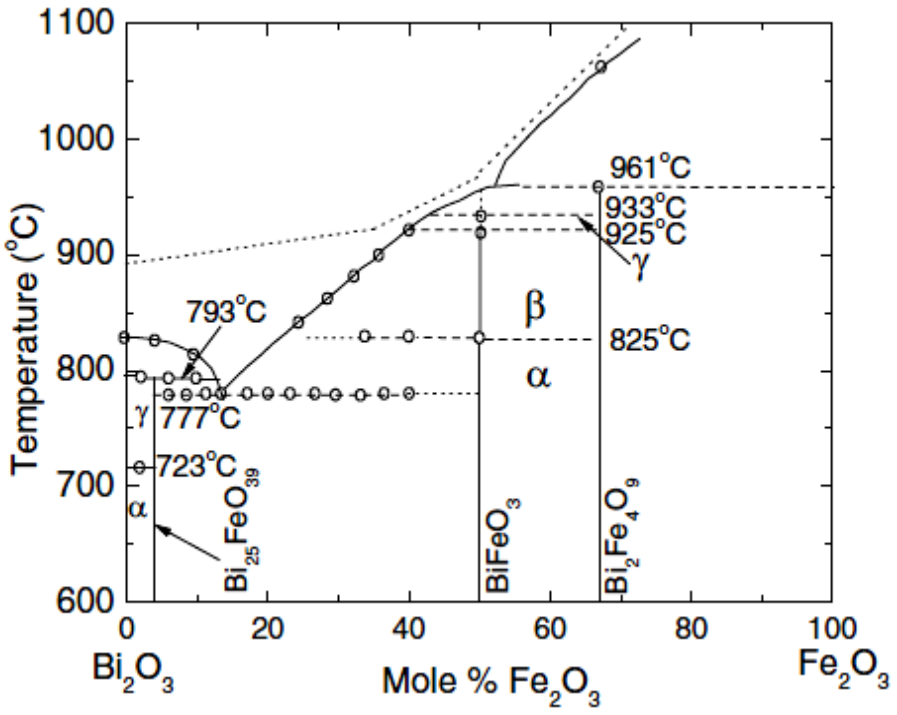

Figure 1.22. Bi_2O_3-Fe_2O_3 phase diagram [103].

1.7.3. Magnetic properties of $BiFeO_3$

$BiFeO_3$ (BFO) has a G-type antiferromagnetic structure with a Neel temperature of 643 K [105,106]. In G-type antiferromagnetism, the Fe atoms are antiferromagnetically coupled to the neighbouring atoms. It is actually canted antiferromagnetism with a canting angle of 153° which can allow a net magnetic moment. But Sosnowska *et al*. [107] have investigated the structure of $BiFeO_3$ by neutron diffraction and shown that $BiFeO_3$ has a spin cycloidal structure with a wavelength of 64 nm (figure 1.23). Within this 64 nm, the moments get cancelled and lead to zero net magnetic moment. Because of the low magnetic moment, BFO has a very low magnetoelectric (ME) coupling coefficient. This makes it difficult to use for application purposes. If the spin cycloidal structure is destroyed, BFO can show higher magnetic parameters and hence higher magnetoelectricity [107-111].

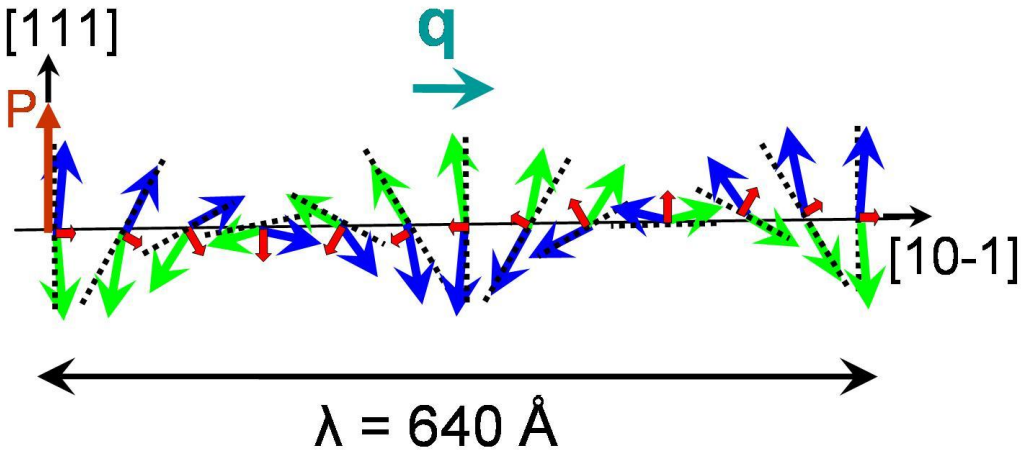

Figure 1.23. Spiral spin cycloidal structure of $BiFeO_3$ [112]. Green and blue arrows show the Fe moments. The red arrow is the resultant moment which has cycloidal form with a wavelength of 64 nm and a propagation vector (q) towards [10-1] direction. The resultant polarisation (shown by the red thick arrow) is towards the [111] direction.

1.7.4. Ferroelectric properties of $BiFeO_3$

$BiFeO_3$ is ferroelectric with Curie temperature of 1103 K [113,114]. $BiFeO_3$ can show high saturation polarization value upto 150 μC/cm^2. In $BiFeO_3$, ferroelectricity arises from the stereochemical activity of 6s^2 lone pair of electrons of Bi^{3+}. Though theoretically it is a better ferroelectric, the low resistance and leakage currents in the samples deteriorate the ferroelectric properties. Modified synthetic methods can improve the resistance and the dielectric properties [115-118].

1.8. Methods to improve multiferroicity of $BiFeO_3$

$BiFeO_3$ is already a better ferroelectric which can show a very high saturation polarisation. However, the poor magnetic properties make it a weak magnetoelectric. Improving the magnetic properties can enhance its multiferroic properties. There are different approaches used by researchers in order to achieve better magnetic properties and thus better multiferroism.

1.8.1. Nanoparticles and thin films

The weak magnetic nature of $BiFeO_3$ is due to the spiral spin cycloidal structure which has wavelength around 64 nm. Therefore, in bulk samples, the net magnetic moment which arises from the canted spin structure gets cancelled. If the size of the particles is below this spin periodicity (64 nm) range, $BiFeO_3$ can show a higher net magnetic moment. Park *et al.* studied the size dependent magnetic properties of $BiFeO_3$ for the first time and shown that with lowering the size, the magnetic properties of $BiFeO_3$ particles are enhanced [119] . Even in thin films, this size dependent magnetization exists. However, in thin films, the epitaxial stress of the films can cause distortion of the crystal structure and helps to enhance the magnetic properties.

1.8.2. Substitution effects

Proper substitution at the A (Bi) site or B (Fe) site in the ABO_3 structure can lead to enhancement of magnetic and ferroelectric properties of $BiFeO_3$.

1.8.2.1. Bi-site substituted $BiFeO_3$

i. Rare earth substitution

Ionic radii of trivalent rare ions are comparable to that of bismuth. Therefore, almost all rare earths can be substituted at the Bi site [120-125] in $BiFeO_3$. Thakuria and Joy [121] have studied different rare earth ions substituted $BiFeO_3$ and shown that Ho substituted $BiFeO_3$ shows the highest magnetic parameters as shown in figure 1.24. La-substitution for Bi has been studied widely in the literature, as La^{3+} eight coordination ionic radii is 1.16 Å which is very much closer to that Bi^{3+} (1.17 Å). But the lone pair effects from the Bi's $6s^2$ lone pairs will be suppressed upon La-substitution. A structural transition from rhombohedral *R3c* to orthorhombic *Pbnm* is observed in bulk and nanoparticles of La-substituted $BiFeO_3$ [122,123].

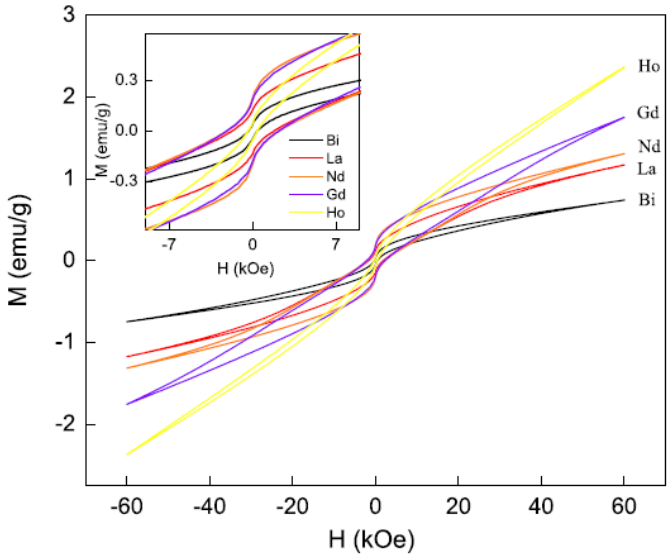

Figure 1.24. Magnetization vs. field curves for rare earth ions substituted $BiFeO_3$ [121].

ii. Divalent ion substitution

Bi-site can be substituted with divalent metal ions like Ca, Sr, Ba and Pb. Except for Ca, these ions have larger ionic radii than that of Bi [126-128]. Khomchenko *et al.* [126] have intensively studied divalent ion substitution in $BiFeO_3$. The authors have shown that with increasing ionic size, magnetization increases and Ba^{2+} having the larger ionic radius shows higher magnetic parameters (figure 1.25). Furthermore, with the increase in the degree of substitution, magnetic properties are improved as shown figure 1.26 [129]

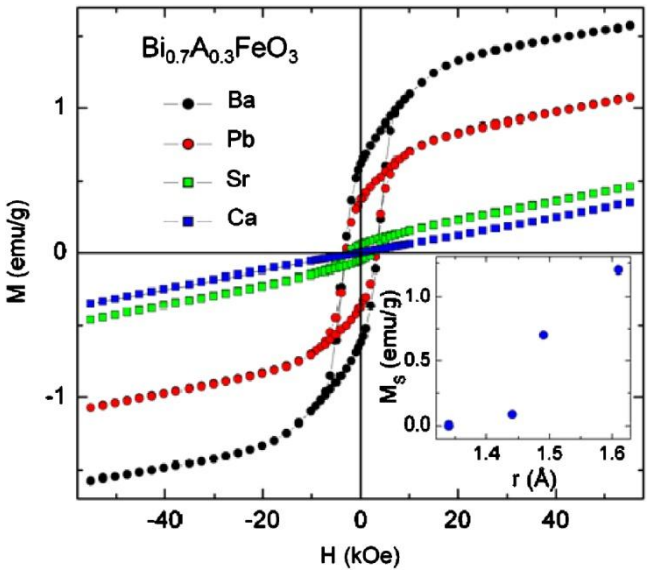

Figure 1.25. Magnetization vs. field curves for divalent ion substituted $BiFeO_3$ [126].

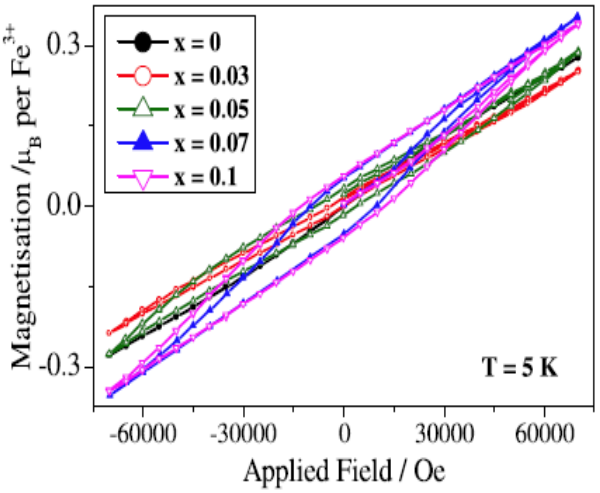

Figure 1.26. Magnetization vs. field curves for Ca substituted $BiFeO_3$ [129].

1.8.2.2. Fe-site substituted $BiFeO_3$

The Fe-site in $BiFeO_3$ can be substituted by transition metal ions having similar size to that of Fe^{3+} [130-135]. In addition to the structural changes by the substitution effect, magnetic contribution from the substituent atom also comes into the picture. Out of all the transition metals, Mn substitution has been studied extensively, as trivalent Mn and Fe have almost similar size, and therefore, the structural distortion due to size mismatch can be minimized. But Mn^{3+} being a Jahn-Teller active ion, structural distortion can occur. Also Mn has various stable oxidation states, which can also lead to better magnetic properties. Neutron diffraction studies by Sosnowska *et al* have shown that spiral spin structures get destructed in the case of Mn substituted $BiFeO_3$ [130]. Enhancements in the magnetic and ferroelectric properties in the Mn substituted samples are reported as shown figure 1.27 (a) and 1.27 (b), respectively. Similarly, substitution with Cr (figure 1.28) also show enhanced magnetic properties.

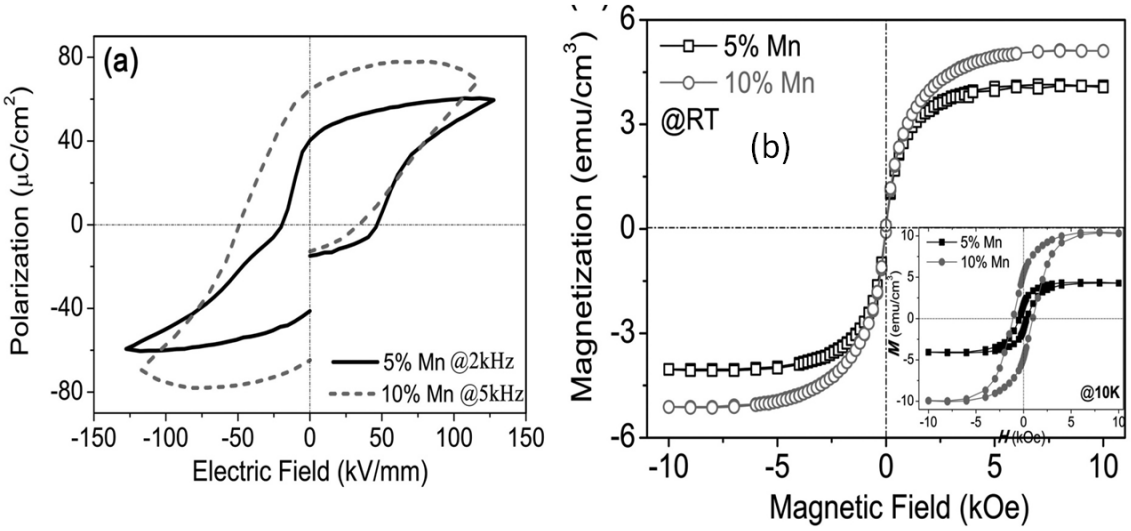

Figure 1.27. (a) P-E loops for Mn-substituted $BiFeO_3$ thin films and (b) magnetization vs. field curves for Mn-substituted $BiFeO_3$ thin films [133].

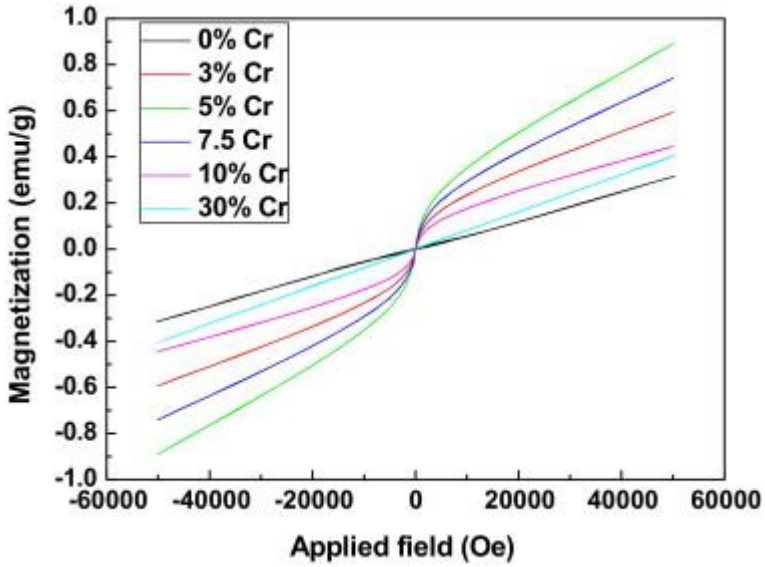

Figure 1.28. Magnetization curves for Cr-substituted $BiFeO_3$ nano particles [136].

1.8.3. Application of high magnetic field

When a very high magnetic field is applied, the spin cycloidal structure of $BiFeO_3$ is destroyed, and subsequently weak ferromagnetism is observed [138,139]. Popov *et al* have shown a linear magnetoelectric response in $BiFeO_3$ system in the presence of a very high magnetic field (280 kOe) [138].

1.9. Morphotropic phase boundary (MPB)

Morphotropic phase boundary (MPB) region is the phase composition region where the structural change from one phase to another occurs. In the case of dielectric and ferroelectric materials, it was observed that dielectric and ferroelectric properties show an anomaly in this structural phase transition region [140] as illustrated in figure 1.29. Even for magnetic properties, such an anomaly is observed in the MPB region [122,123]. Thakuria *et al.* [122] have shown that enhanced magnetic properties are observed in the MPB region for La substituted $BiFeO_3$ where a rhombohedral to orthorhombic structural transition occurs (figure 1.30). Magnetic parameters like Tc, Mr, Hc and Ms showed higher values at the MPB region, $x = 0.15$ as shown in figure 1.31.

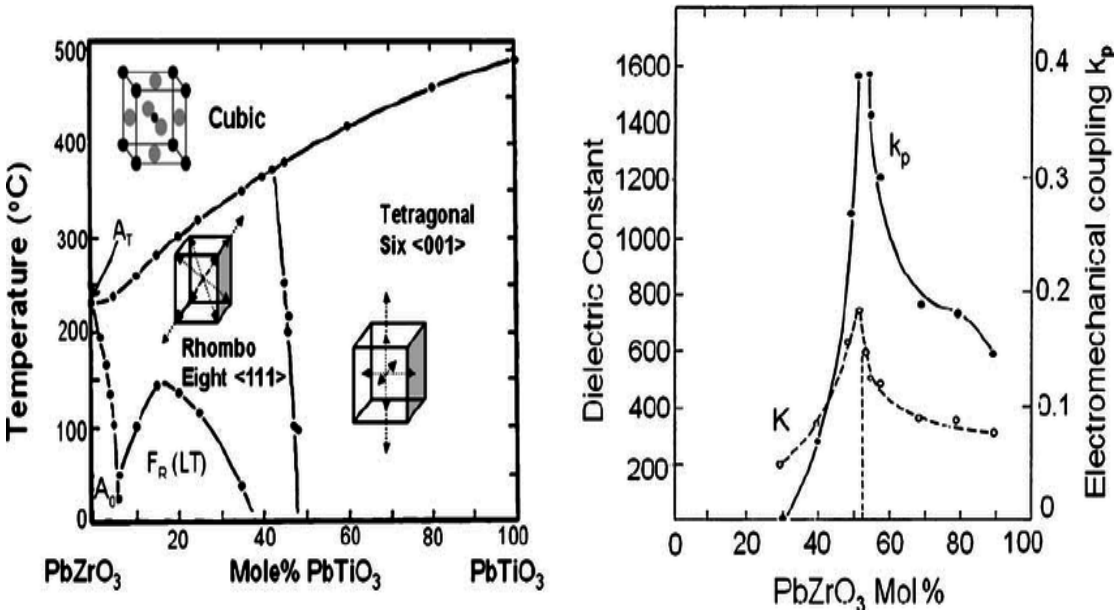

Figure 1.29. Structural transitions (left) and the enhanced parameters (right) around the MPB region of the piezoelectric compositions in the lead zirconate titanate system, $PbZr_{1-x}Ti_xO_3$ (PZT) [140].

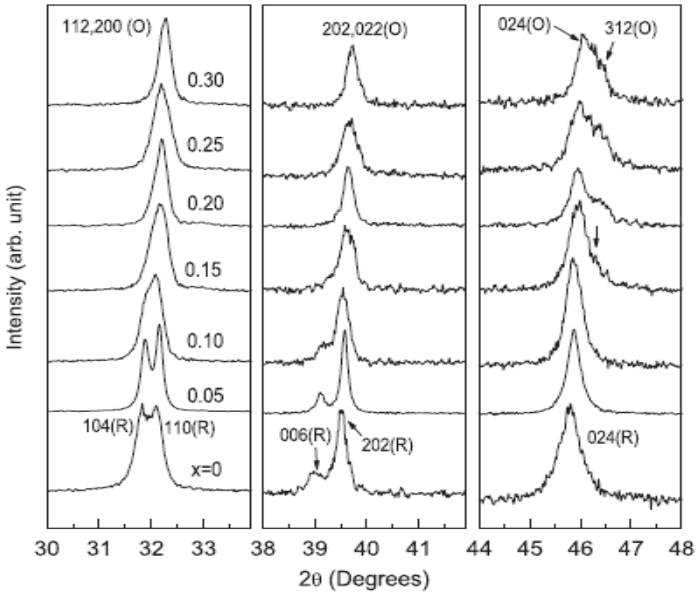

Figure 1.30. Powder XRD patterns indicating structural transition from rhombohedral (R) to orthorhombic (O) in nanoparticles of $Bi_{1-x}La_xFeO_3$ [123].

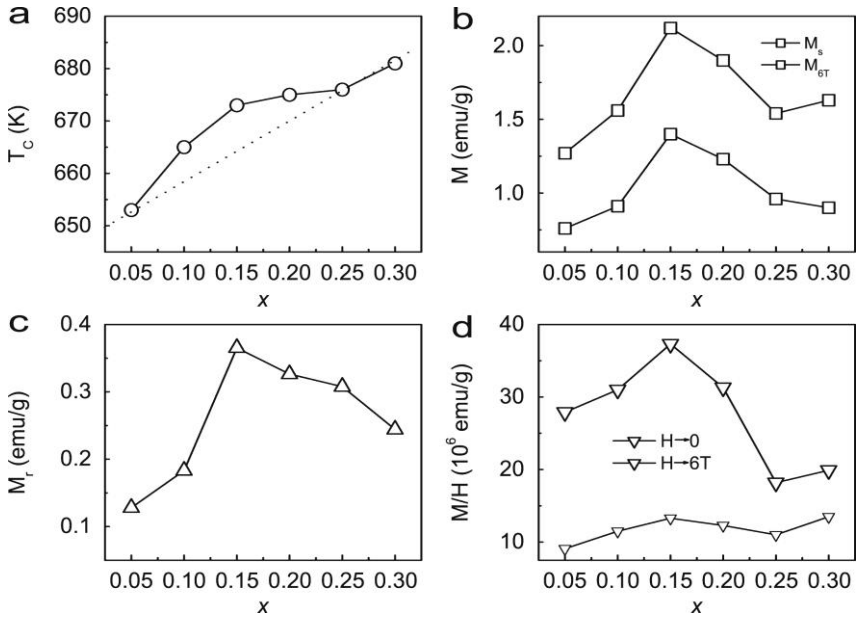

Figure 1.31. Higher magnetic parameters in the MPB region for nanoparticles of $Bi_{1-x}La_xFeO_3$ [123].

1.10. Simultaneous A-site and B-site substitution (co-substitution) in $BiFeO_3$

Co-substitution is the simultaneous substitution at more than one sites, for example in the A and B sites of the ABO_3 perovskite structure. Interest in co-substitution of BFO began when higher resistivity and electric properties were observed in the co-substituted BFO

samples [141, 142]. Later on, higher magnetic, ferroelectric and multiferroic properties were reported in many of the co-substituted BFO systems [143-145].

In $Bi_{1-x}A_xFe_{1-y}M_yO_3$ ($x = y$ or $x \neq y$), both the Bi- and Fe- sites are substituted simultaneously, where A is trivalent rare earth ion or divalent ions and M is a transition metal ion. The Bi-site can be substituted by trivalent rare earth ions or divalent ions like Ca, Sr, Ba or Pb of comparable size and the Fe-site can be substituted by first-row transition metal ions. In the case of trivalent rare earth ion substitution, magnetism may be improved from the structural changes associated with the difference in sizes of Bi the substituted ions as well as the contributions from the transition metal ion due to the suppression of the spiral spin order. However, in the case of divalent co-substituted compounds, there will be charge compensation by the formation of Fe^{4+} and/or M^{4+} and this may improve magnetism. Figure 1.32 shows the M-H curves of La and Mn/Co co-substituted BFO, where the co-substituted compositions show enhanced magnetic parameters (coercivity and magnetization) than the single site substituted BFO [143]. Gd and Ti co-substitution [144] also show similar trend as shown in figure 1.33.

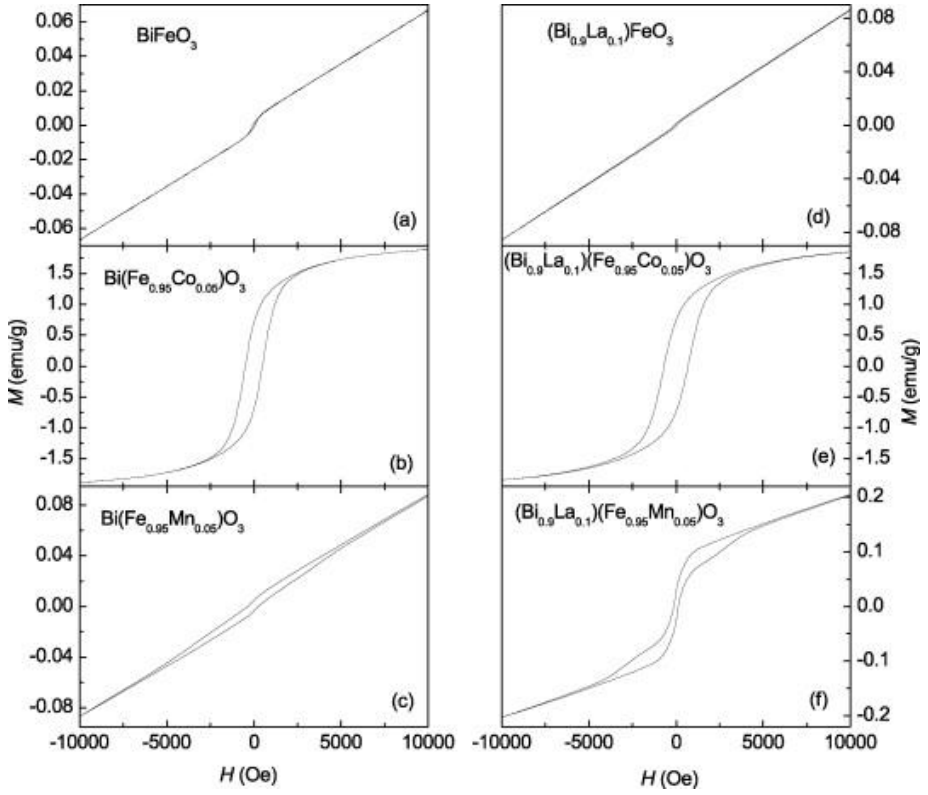

Figure 1.32. Comparison of the M vs. H curves of Bi-site, Fe-site and co-substituted $BiFeO_3$ [143].

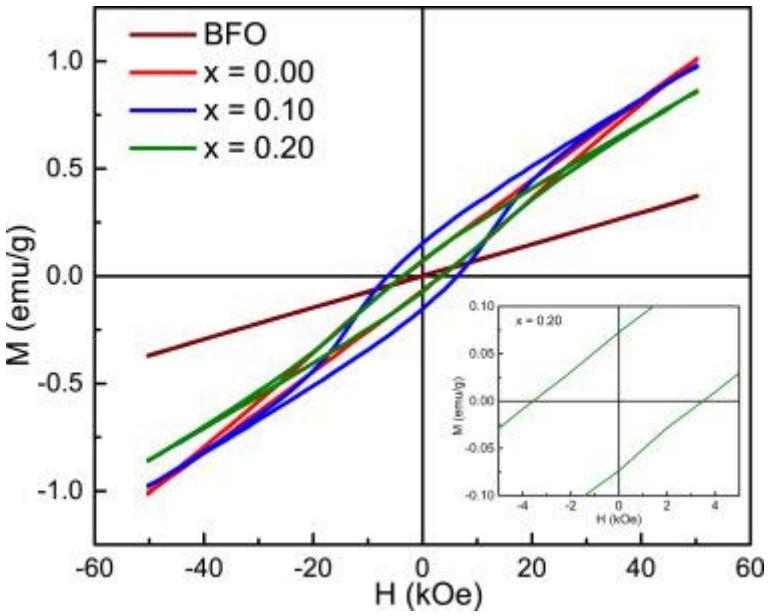

Figure 1.33. M vs. H curves for $Bi_{0.9}Gd_{0.1}Fe_{1-x}Ti_xO_3$ [144]

1.11. Scope of the present work

Magnetoelectric multiferroics are one of the most studied research areas in the recent times because of their application in the fields of information storage, sensors, actuators, etc. However, their practical application in real life is still far because of various issues. One of the main issues is that sufficient magnetoelectricity at room temperature is not yet achieved. Most of the known magnetoelectrics show maximum magnetoelectric coupling constant only at very low temperatures. This makes them impossible to use for practical applications and the known room temperature magnetoelectric multiferroics have very low magnetoelectric coupling constant. A material with the magnetic transition (T_C or T_N) and ferroelectric transition much above the room temperature is required for the application purposes. If it is possible to get a multiferroic material with a high magnetoelectric coefficient at room temperature it will be a great boom in the area of spintronics, data storage and sensors.

Many perovskite oxides like $BiMnO_3$, $BiFeO_3$, $YMnO_3$, etc., show multiferroic properties. Out of all the multiferroic materials, $BiFeO_3$ is the only known room temperature magnetoelectric multiferroic. However, because of its antiferromagnetic character and spiral spin structure, the magnetoelectric coupling value achieved is very low. To improve the magnetoelectric properties, magnetic properties of $BiFeO_3$ should be improved. By the destruction of the spin cycloidal structure of BFO, it may be possible to achieve ferromagnetism. A suitable substitution at the Bi- and/or Fe-site can break the spin

periodicity due to structural distortions and therefore can give rise to enhanced magnetic properties and thus possibly very high magnetoelectric coupling. Co-substitution is an effective method than the single site substitution to fine-tune the magnetic and electric properties concurrently. Co-substitution is very effective in reducing leakage current and hence enhancing the ferroelectricity. However, there are very few reports in the literature on the effect of co-substitution on the magnetic properties of $BiFeO_3$.

The objective of this work is to enhance the magnetic properties of $BiFeO_3$ through co-substitution. Current literature does not provide much information on the magnetic characteristics of the co-substituted systems. In this context, this study on the co-substitution of the BFO system has great significance. A detailed study on the structural and magnetic properties can throw light on the effect of co-substitution on improving the magnetic characteristics suitable for applications. The changes in the bond angle and bond length on co-substitution can affect the strength of the magnetic exchange interactions apart from the suppression of spin periodicity, which determine and improve the magnetic properties because of the effective overlapping of the orbitals. Therefore, it is essential to investigate the structure-property relations of the co-substituted materials.

Among the Bi-site substituted compositions, divalent ion substitution in $BiFeO_3$ is well studied due to the enhanced magnetic, ferroelectric and magnetoelectric properties. On the other hand, Mn substitution is well studied among the Fe-site substituted compositions which also enhance the magnetic and magnetoelectric properties of BFO. As already discussed, in the former case, in addition to the structural distortions caused by the substituent, oxygen vacancies formed also may enhance the properties. In the latter case, structural distortions along with the contribution from exchange interactions involving Mn may enhance the magnetic properties. In this context, we have carried out co-substitution at the Bi- and Fe-site with divalent ions and Mn, respectively, with general formula $Bi_{1-x}A_xFe_{1-x}Mn_xO_3$ (A = Ca, Sr, Ba) where Mn will exist in Mn^{4+} state in order to attain charge neutrality. The mixed valency of Mn can enhance the magnetic properties through ferromagnetic double exchange.

The end members of the $Bi_{1-x}A_xFe_{1-x}Mn_xO_3$ have different structures compared to that of $BiFeO_3$ and thus the co-substituted compositions may show different crystal structures than that of BFO. Thus, an MPB region may exist in $Bi_{1-x}A_xFe_{1-x}Mn_xO_3$, where the properties may be enhanced. Furthermore, not much literature is available on the low-temperature magnetic

properties of substituted and co-substituted BFO. In this regard, we have tried to analyse the low-temperature magnetic properties of divalent ion and Mn-substituted $BiFeO_3$. We have used X-ray diffraction (XRD) and Raman spectroscopy for the structural studies. Detailed, structural analyses in each case have been carried by Rietveld refinement of the XRD patterns. XPS studies have been carried out to check the oxidation states of Mn. Detailed, magnetic studies have been carried out using a SQUID magnetometer. Additionally, dielectric measurements have also been carried out for all the compositions.

References

[1] Curie P 1894 *J. Physique* **3** 393

[2] Debye P J 1929 *Polar molecules* (Chemical Catalog Company, New York)

[3] Landau L D and Lifshits E M 1969 *Course of Theoretical Physics: Electrodynamcis of Continuous Media* (Pergamon Press, London)

[4] Dzyaloshinskii I E 1960 *Sov. Phys. JETP* **10** 628

[5] Astrov D N 1960 *Sov. Phys. JETP* **11** 708

[6] Astrov D N 1961 *Sov. Phys. JETP* **13** 729

[7] Schmid H. 1994 *Ferroelectrics* **162** 317

[8] Fiebig M 2005 *J. Phys. D: Appl. Phys*. **38** R123

[9] Hur N, Park S, Sharma P. A, Ahn J S, Guha S, Cheong S W 2004 *Nature* **429**, 392

[10] Ramesh R 2003 *Science* **299** 1719.

[11] Eerenstein W, Mathur N D, Scott J F 2006 *Nature* **442** 7104

[12] Catalan G and Scott J F 2009 *Adv. Mater*. **21** 2463

[13] Scott J F 2012 *J. Mater. Chem.* **22** 4567

[14] Vopson M M 2015 *Crit. Rev. Solid State Mater. Sci.* **40** 223

[15] Scott J F 200*7 Nat. material**s*** **6** 256

[16] Yang F, Zhou Y C, Tang M H, Liu F, Ma Y, Zheng X J, Zhao W F, Xu H Y and Sun Z H. 2009 *J. Phys. D: Appl. Phys*. **42** 072004

[17] Hu J M, Nan T, Sun N X and Chen L Q 2015 *MRS Bull.* **40** 728

[18] Khomskii D 2009 *Physics* **2** 20

[19] The total number of publications in the field of magnetoelectrics from year 1990-2017 by searching the word *'magnetielectric'* in Web of scienc***e***

[20] Cullity B D, Graham C D 2009 *Introduction to magnetic materials* (John Wiley & Sons Inc, New York)

[21] West A R 2003 *Solid State Chemistry and its Applications* (John Wiley & Sons, Singapore)

[22] Viswanathan B, and Murthy V R K 1990 *Ferrite Materials: Science and technology* (Narosa Publishing House, New Delhi,)

[23] Goodenough J B 1963 *Magnetism and Chemical Bond* (John Wiley & Sons, New York)

[24] Neel L 1932 *Annales de physique* **18** 5

[25] Hu A Y and Wang H Y 2014 *J. Appl. Phys.* **116** 193903

[26] Kanamori J 1959 *J. Phys. Chem. Solids* **10** 87

[27] Anderson P W 1950 *Phys. Rev.* **79** 350

[28] Zener C 1951 *Phys. Rev.* **82** 403

[29] Anderson P W and Hasegawa H 1955 *Phys. Rev.* **100** 675

[30] De Gennes P G 1960 *Phys. Rev.* **118** 141

[31] Dzyaloshinsky I 1958 *J. Phys. Chem. Solids* **4** 241

[32] Moriya T 1960 *Phys. Rev.* **120** 91

[33] Anderson P W *Phys. Rev.* 1959 **115**2 2

[34] Sakar M, Balakumar S, Saravanan P and Bharathkumar S 2015 *Nanoscale* **7** 10667

[35] Park J G, Le M D, Jeong J and Lee S J 2014 *J. Phys. Condens. Matter* **26** 433202**.**

[36] Sergienko I A, Dagotto E 200*6 Phys. Rev.* B **73** 09444

[37] Mühlbauer S, Binz B, Jonietz F, Pfleiderer C, Rosch A, Neubauer A, Georgii R and Böni P 2009 *Science* **323** 915

[38] Yu X Z, Onose Y, Kanazawa N, Park J H, Han J H, Matsui Y, Nagaosa N and Tokura Y 2010 Nature **465** 901

[39] Zhang N, Dong S and Liu J M 2012 *Front. Phys.* **7** 408

[40] Kugel K I, Khomskii D I 1982 *Phys. Usp.* **25** 231

[41] Sawada H, Morikawa Y, Terakura K and Hamada N 1997 *Phys. Rev.* B **56** 12154

[42] Tokura Y and Tomioka Y 1999 *J. Magn. Magn. Mater*. **200** 1

[43] Blundell S 2001 *Magnetism in Condensed Matter* (Oxford University Press, London***)***

[44] Cussen E J, Rosseinsky M J, Battle P D, Burley J C, Spring L E, Vente J F, Blundell S J, Coldea A I, and Singleton J 2001 *J. Am. Chem.Soc.* **123** 1111

[45] Tokura Y (Ed.) 2000 *Colossal Magnetoresistive Oxides* (Gordon and Breach Science Publishers, Singapore)

[46] https://thiscondensedlife.wordpress.com/2017/05/15/jahn-teller-distortion-and-symmetry-breaking

[47] Mydosh J A 1993 Spin glasses: an experimental introduction (Taylor & Francis, London)

[48] Mydosh J A. 2015 *Rep Prog Phys.* **78** 052501

[49] Binder K and Young A 1986 *Rev. Mod. Phys.* **58** 801

[50] Ford P J 1982 *Contemp. Phys.* **23** 141

[51] Hurd C M 1982 *Contemp. Phys.* **23** 469

[52] http://www.riken.jp/en/research/rikenresearch/highlights/5366

[53] Moulson A J and Herbert J M 2003 *Electroceramics: Materials, Properties and Applications* (John Wiley and Sons Ltd ,2nd Edition, Chichester)

[54] Kao K C 2004 *Dielectric phenomena in solids* (Academic press, New York)

[55] Sawyer C B and C. H. Tower C H 1930 *Phys. Rev.* **35** 269

[56] Valasek, J 1921 *Phys. Rev.* **17** 475

[57] Kwei G H, Lawson A C, Billinge S J and Cheong S W 1993 *J. Phys. Chem.* **97** 2368

[58] Cohen R E 1992 *Nature* **358** 136

[59] Ok K M, Chi E O and Halasyamani P S 2006 *Chem. Soc. Rev*. **35** 710

[60] Hill N A 2000 *J. Phys. Chem.* B **104** 6694

[61] Wang J, Neaton J B, Zheng H, Nagarajan V, Ogale S B, Liu B, Viehland D, Vaithyanathan V, Schlom D G, Waghmare U V, Spaldin N A, Rabe K M, Wuttig M and Ramesh R 2003 *Science* **299** 1719

[62] Seshadri R and Hill N A 2001 *Chem. Mater.* **13** 2892

[63] King-Smith R D and Vanderbilt D 1994 *Phys. Rev*. B **49** 5828

[64] Van Aken B B, Palstra T T, Filippetti A and Spaldin N A 2004 *Nat. Mater*. **3** 164

[65] Ye F, Ren Y, Huang Q, Fernandez-Baca J A, Dai P, Lynn J W and Kimura T 2006 *Phys. Rev.* B **73** 220404

[66] Ikeda N, Ohsumi H, Ohwada K, Ishii K, Inami T, Kakurai K, Murakami Y, Yoshii K, Mori S, Horibe Y and Kito H 2005 *Nature* **436** 1136

[67] Efremov D V, van den Brink J, Khomskii D. I. 2004 *Nat. Mater.* **3**, 853

[68] Efremov D V, van den Brink J and Khomskii D 2005 *Physica* B **359** 1433

[69] van den Brink J, Khomskii D I 2008 *J. Phys. Condens. Matter.* **20** 434217

[70] Li C H, Wang F, Liu Y, Zhang X Q, Cheng Z H and Sun Y 2009 *Phys. Rev.* B **79** 172412

[71] Aliouane N, Argyriou D N, Strempfer J, Zegkinoglou I, Landsgesell S and Zimmermann M V 200*6 Phys. Rev.* B **73** 020102

[72] Kenzelmann M, Harris A B, Jonas S, Broholm C, Schefer J, Kim S B, Zhang C L, Cheong S W, Vajk O P, Lynn J W 2005 *Phys. Rev. Lett.* **95** 087206

[73] Saito K and Kohn K 1995 *J. Phys. Condens. Matter* **7** 2855

[74] Johnson R D, Mazzoli C, Bland S R, Du C H and Hatton P D 2011 *Phys. Rev.* B **83** 054438

[75] Kimura T, Goto T, Shintani H, Ishizaka K, Arima T H and Tokura Y 2003 *Nature* **426** 55

[76] Kimura T 2007 *Annu. Rev. Mater. Res* **37** 387

[77] Senff D, Link P, Hradil K, Hiess A, Regnault L P, Sidis Y, Aliouane N, Argyriou D N and Braden M 2007 *Phys. Rev. Lett.* **98** 137206

[78] Chapon L C, Blake GR, Gutmann MJ, Park S, Hur N, Radaelli P G and Cheong S W 2004 *Phys. Rev. Lett.* **93** 177402

[79] Tokunaga Y, Iguchi S, Arima T and Tokura Y 2008 *Phys. Rev. Lett.* **101** 097205

[80] Nan C W, Bichurin M I, Dong S X, Viehland D and Srinivasan G 2008 *J. Appl. Phys.* **103** 031101

[81] Hanumaiah A, Bhimashankaram T, Suryanarayana S V and Kumar G S 1994 *Bull. Mater. Sci*. **17** 405

[82] Suryanarayana S V 1994 *Bull. Mater. Sci.* **17** 303

[83] Srinivasan G 2010 *Annu. Rev. Mater. Res.* **40** 78

[84] Dos Santos A M, Parashar S, Raju A R, Zhao Y S, Cheetham A K and Rao C N R 2002 *Solid State Commun.* **122** 49

[85] Kimura T, Kawamoto S, Yamada I, Azuma M, Takano M and Tokura Y 2003 *Phys. Rev.* B **67** 180401

[86] Niitaka S, Azuma M, Takano M, Nishibori E, Takata M and Sakata M 2004 *Solid State Ion.* **172** 557

[87] Huang Z J, Cao Y, Sun Y Y, Xue Y Y and Chu C W 1997 *Phys. Rev.* B **56** 2623

[88] Rajeswaran B, Sanyal D, Chakrabarti M, Sundarayya Y, Sundaresan A and Rao C N R 2013 *EPL* **101** 17001

[89] Yamasaki Y, Miyasaka S, Kaneko Y, He J P, Arima T and Tokura Y 2006 *Phys. Rev. Lett.* **96** 207204

[90] Hur N, Jeong I K, Hundley M F, Kim S B and Cheong S W 2009 *Phys. Rev.* B **79** 134120

[91] Fabreges X, Mirebeau I, Bonville P, Petit S, Lebras-Jasmin G, Forget A, Andre G and Pailhes S 2008 *Phys. Rev.* B **78** 214422

[92] Ascher E, Rieder H, Schmid H and Stossel H 1966 *J. Appl. Phys.* **37** 1404

[93] Rogado N, Lawes G, Huse D A, Ramirez A P and Cava R J 2002 *Solid State Commun.* **124** 229

[94] Borowski M 2010 *Perovskites: structure, properties, and uses* (*Nova Science Publishers*, New York)

[95] Mitchel R H 2002 *Perovskites: Modern and Ancient* (Almaz Press, Thunder Bay)

[96] Green M A, Ho-Baillie A and Snaith H J. 2014 *Nat. Photon.* **8** 506

[97] Montanari E, Calestani G, Righi L, Gilioli E, Bolzoni F, Knight K S and Radaelli P G 2007 *Phys. Rev.* B **75** 220101

[98] The total number of publications in the field of bismuth ferrite from year 2000-2017 by searching the word *'$BiFeO_3$'* in Web of scienc*e*

[99] Eerenstein W, Morrison F D, Dho J, Blamire M G, Scott J F and Mathur N D. 2005 *Science* **307** 1203

[100] Michel C, Moreau J M, Achenbac Gd, Gerson R and James W 1969 *J. Solid State Commun.* **7** 701

[101] Kubel F and Schmid H 1990 *Acta Cryst*. B **46** 698

[102] https://www.intechopen.com/books/ferroelectrics-physical-effects/multifunctional-characteristics-of-b-site-substituted-bifeo3-films

[103] Palai R, Katiyar R S, Schmid H, Tissot P, Clark S J, Robertson J, Redfern S A T, Catalan G and Scott J F 200*8 Phys. Rev.* B **77** 01411***0***

[104] Selbach S M, Einarsrud M-A and Grande T 2009 *Chem.Mater***. 21** 169

[105] Fischer P, PoIomska M, Sosnowska I and Szymanski 1980 *J. Phys. C Solid State Phys.***13** 1931

[106] Smolenskii G A and Yudin V M 1965 *Sov. Phys. Solid State* **6**, 293

[107] Sosnowska I, Peterlin-Neumaier T and Steichele E 1982 *J. Phys.* C **15** 4835

[108] Ederer C, Fennie C J 2008 *J. Phys. Condens. Matter***. 20** 434219

[109] Ravindran P, Vidya R, Kjekshus A, Fjellvag H, Eriksson O 2006 *Phys. Rev.* B **74** 224412

[110] Ederer C and Spaldin N A 200*5 Phys. Rev.* B **71** 060401

[111] Bai F, Wang J, Wuttig M, Li J F, Wang N, Pyatakov A P, Zvezdin A K, Cross L E and Viehland D 2005 *Appl. Phys. Lett*. **86** 032511

[112] http://iramis.cea.fr/LIDYL/Phocea/Vie_des_labos/Ast/ast.php?t=fait_marquant&id_ast=1012

[113] Arnold D C, Knight K S, Morrison F D and Lightfoot P 2009 *Phys. Rev. Lett.* **102** 027602

[114] Polomska M, Kaczmarek W and Pajak Z 1974 *Phys. Stat. Sol.* **23** 567

[115] Shvartsman V V, Kleemann W, Haumont R and Kreisel 2007 *Appl. Phys. Lett.* **90** 172115

[116] Lebeugle D, Colson D, Forget A, Viret M, Bonville P, Marucco J F and Fusil S 2007 *Phys. Rev.* B 76 024116

[117] Yun K Y, Ricinschi D, Kanashima T, Noda M, Okuyama M 2004 *Jpn. J. Appl. Phys.* **43** L647

[118] Neaton J B, Ederer C, Waghmare U V, Spaldin N A, Rabe K M 2005 *Phys. Rev.* B **71** 014113

[119] Park T J, Papaefthymiou G C, Viescas A J, Moodenbaugh A R and Wong S S 2007 *Nano Lett***. 7** 766

[120] Yuan G L, Or S W and Chan H L 2007 *J. Phys. D: Appl. Phys*. **40** 1196

[121] Thakuria P and Joy P A 2010 *Appl. Phys. Lett*. **97** 162504

[122] Troyanchuk I O, Karpinsky D V, Bushinsky M V, Khomchenko V A, Kakazei G N, Araujo J P, Tovar M, Sikolenko V, Efimov V and Kholkin A L 2011 *Phys. Rev.* B **83** 054109

[123] Thakuria P and Joy P A 2012. *Solid State Commun.* **152** 1609

[124] Karpinsky D V, Troyanchuk I O, Zheludkevich A L, Ignatenko O V, Silibin M V and Sikolenko V V 2016 *Phys. Solid State* **58** 1590

[125] Dai H, Li T, Chen Z, Liu D, Xue R, Zhao C, Liu H and Huang N 2016 *J. Alloys Compd.* **672** 182

[126] Khomchenko V A, Kiselev D A, Vieira J M, Jian L, Kholkin A L, Lopes A M, Pogorelov Y G, Araujo J P and Maglione M 2008 *J. Appl. Phys.* **103** 024105

[127] Kothari D, Reddy V R, Sathe A G V, Banerjee A, Gupta S M and Awasthi A M 2007 *Appl. Phys. Lett.* **91** 202505

[128] Bhushan B, Basumallick A, Bandopadhyay S K, Vasanthacharya N Y and Das D 2009 *J. Phys. D: Appl. Phys*. **42** 065004

[129] Sardar K, Hong J, Catalan G, Biswas P K, Lees M R, Walton R I, Scott J F and Redfern S A 2012 *J. Phys. Condens. Matter* **24** 045905

[130] Sosnowska, I , Schaffer W, Kockelmann W, Andersen K H, Troyanchuk I O 2002 *Appl Phys* A **74** S1040

[131] Yang C H, Koo T Y and Jeong Y H 2005 *Solid State Commun*. **134** 299

[132] Azuma M, Kanda H, Belik A A, Shimakawa Y and Takano M 2007 *J. Magn. Magn. Mater*. **310** 1177

[133] Chen J, Wang Y and Deng Y 2014 *J. Appl. Phys.* **116** 174102

[134] Qi X, Dho J, Tomov R, Blamire M G and MacManus-Driscoll J L 2005 *Appl. Phys. Lett.* **86** 062903

[135] Kumar M and Yadav K L 2006 *J. Appl. Phys.* **100** 74111

[136] Wang B, Tian X, Song X, Ma L, Yu S, Hao C, Chen K and Lei Q 2014 *Colloids Surf.* A **461** 184

[137] Shannigrahi S R, Huang A, Chandrasekhar N, Tripathy D and Adeyeye A O 2007 *Appl. Phys. Lett*. **90** 022901

[138] Popov Y F, Kadomtseva A M, Vorob'Ev G P and Zvezdin A K 199*4 Ferroelectrics* 1994 **162** 135

[139] Ruette B, Zvyagin S, Pyatakov A P, Bush A, Li J F, Belotelov V I, Zvezdin A K and Viehland D 2004 *Phys. Rev.* B **69** 064114

[140] Shrout T R and Zhang S J 2007 *J. Electroceram*. **19** 113

[141] Jun Y K and Hong S H 2007 *Solid State Commun.* **144** 329

[142] Singh S K, Maruyama K and Ishiwara H 2007 *Appl. Phys. Lett*. **91** 112913

[143] Zheng X, Xu Q, Wen Z, Lang X, Wu D, Qiu T and Xu M X 2010 *J Alloys Compd.* **499** 108

[144] Basith M A, Billah A, Jalil M A, Yesmin N, Sakib M A, Ashik E K, Yousuf S E, Chowdhury S S, Hossain M S, Firoz S H and Ahmmad B 2017 *J. Alloys Compd.* **694** 792

[145] Chakrabarti K, Das K, Sarkar B, Ghosh S, De S K, Sinha G and Lahtinen J 2012 *Appl. Phys. Lett*. **101** 042401

Chapter 2

Experimental methods

2.1. Synthesis

The most common method used for the preparation of bulk polycrystalline material is the solid-state reaction or ceramic or the high-temperature method [1-4]. In the solid state reaction involving a mixture of starting components, ions leave their respective positions and diffuse into another lattice thus forming a new composition. To overcome the lattice energy and to leave the lattice, high energy is required and hence high temperature is required for the completion of the reaction. Initially, the reaction takes place at the interfaces of the solid reactants and then the ions move from the bulk to the interface. Grinding of the reactants homogeneously mixes the components, increases the surface area and thus maximizes the contact area of the reactants thus making the reaction more feasible [5].

The co-substituted bismuth ferrite bulk samples, with the general formula $Bi_{1-x}A_xFe_{1-y}Mn_yO_3$, were prepared by the solid-state reaction method. Synthesis of single phase $BiFeO_3$ and related systems by the solid-state method is rather difficult due to the kinetics and metastability of the system [6,7] and hence extra precautions were taken during the synthesis. Bi_2O_3, $CaCO_3$/$SrCO_3$/$BaCO_3$, Mn_2O_3, and Fe_2O_3 (all from Aldrich) were weighed in the required stoichiometric ratio and ground well in an agate mortar for 1 hour using high purity acetone as a medium. Extra Bi_2O_3 (5 wt%) was added in order to compensate for the evaporation of bismuth during the heating process, as reported in the literature [8]. This avoids the formation of bismuth deficient impurity $Bi_2Fe_4O_9$. The mixed powder was pressed into circular disks of 13 mm diameter and 5 mm thickness, by applying a pressure of 25 MPa. The pressed pellets were then heated at 850 °C in air, in a programmable furnace, at a heating rate of 5 degrees/minute. The samples were heated for 12 hours and then furnace-cooled to room temperature. The samples were kept in a closed alumina crucible in order to avoid the evaporation of Bi_2O_3. In the case of the synthesis of the unsubstituted $BiFeO_3$, the temperature was fixed at 800 °C, since higher temperature will cause melting, evaporation and dissociation of $BiFeO_3$.

2.2. Powder X-ray diffraction

Powder X-ray diffraction (XRD) is the basic characterization technique used in solid-state chemistry [9,10]. Each crystalline solid material can be identified by its own characteristic powder XRD pattern, and hence an XRD patterns is a “fingerprint” of the material. A PANalytical X’PERT Pro X-ray diffractometer with Cu-K_α radiation (1.5418 Å)

is used to record the X-ray diffraction patterns of the samples. The voltage and current applied were 40 kV and 30 mA respectively, to produce the X-rays. K_β X-rays were filtered using a nickel filter. Samples were scanned in the 2θ range of 10 to 80 degrees at a scan rate of 1°/minute. The incident X-rays contain both the $K_{\alpha1}$ and $K_{\alpha2}$ components. The diffracted beams were detected using a Pixel detector. The 'Powder Cell for Windows (PCW)' software was used to simulate the XRD patterns of the compositions and to compare with the experimental patterns for the initial identification of phases [11]. Structural parameters such as space group, unit cell parameters and atomic positions were taken from the literature to simulate the patterns. Detailed structural analysis was carried out by the Rietveld refinement method.

XRD pattern of a certain compound carries much information about the crystal structure such as its lattice parameters, crystal symmetry, atomic positions, etc. The peak positions, peak width, splitting and intensity of the peaks are signatures of a particular crystal structure. In 1967 Hugo Rietveld made the first programme for the analysis of powder neutron diffraction data and later in 1969, it was fully developed to solve crystal structures [12,13]. Young and Wiles used this method for refining the powder XRD patterns to solve crystal structures [14]. Generally a high-intensity pattern is required for the refinement analysis. The Rietveld refinement is based on the least-squares method to obtain the minimum difference between the experimental and calculated patterns or the best fit. The residual S_y is minimized in the least-squares method, where S_y is given as

$$S_y = \sum_i w_i \ (y_i - y_{ci})^2$$

where y_i is the observed intensity at the ith step, y_{ci} is the calculated intensity at the ith step and $w_i = \frac{1}{y_i}$, is the statistical weight assigned to each observation point, y_i. For refinement of the XRD pattern to obtain the structural information, a good starting model is required.

The Rietveld method can precisely determine the crystal structure as it can virtually separate the overlapping reflections. Another important advantage of the Rietveld refinement is the key feedback during the refinements between improving structural understanding and improving the allocation of experimental intensity to overlapping individual Bragg reflections. During the Rietveld refinement process, the refinable parameters get adjusted until the residual is minimized and the refinement process is continued until the best fit of the

entire calculated pattern to the entire observed pattern is obtained. The following residual factors or R factors indicate the goodness of fit

$$\text{R-structure factor, } R_{F^2} = \frac{\sum I_k^{1/2} - I_{ck}^{1/2}}{\sum I_k^{1/2}}$$

$$\text{R-Bragg factor, } R_B = \frac{I_k - I_{ck}}{\sum I_{ck}}$$

$$\text{R-pattern, } R_p = \sqrt{\frac{\sum (y_i - y_{ci})}{\sum y_i}}$$

$$\text{R-weighted pattern, } R_{wp} = \sqrt{\frac{\sum w_i ((y_i - y_{ci})^2}{\sum w_i y_i^2}}$$

$$\text{R-expected, } R_e = \sqrt{\frac{M - m}{\sum w_i y_i^2}}$$

where I_k is the intensity of the kth Bragg reflection and I_{ck} is the calculated intensity of the kth Bragg reflection, M is the number of steps in the pattern and m is the number of refinable parameters. Among these R factors, R_{wp} is the most meaningful, as its numerator is the residual which is being minimized. χ-factor is another goodness of the fit indicator which is given by

$$\chi^2 = {R_{wp}}/{R_e}$$

In the present work, the General Structure Analysis System (GSAS-EXPGUI) software was used for the Rietveld refinement analysis of the powder X-ray diffraction data [15]. The recorded raw XRD data was used as such without any data smoothening, background correction or $K_{\alpha 2}$ stripping. A reasonably good starting model is required for the refinement. If the initial model is not close to the true model, it may lead to a false minimum by a non-linear relationship between the adjustable parameters and the intensities. Therefore known structural parameters of the corresponding compounds were used for the refinement. For the Rietveld refinement of the XRD pattern, the reported procedure is followed.

At the first step, scaling factor and the background functions were refined. Secondly, the lattice parameters were refined which almost fix the positions and intensity of the reflections. Using the pseudo-Voigt function, profile and symmetry parameters were refined. Pseudo-Voigt function is mixture of Gaussian and Lorentzian functions. Finally, the atomic

coordinates were refined. The refinement was performed until the best fit and lowest χ^2 values are obtained.

2.3 . Raman spectroscopy

Raman spectroscopy is another important experimental technique to evaluate the structural properties of materials. It is a non-contact non-destructive spectroscopic technique based on the vibrational transitions. Raman spectra can probe even local symmetry changes [16]. The sample is irradiated by a high-intensity laser beam and the scattered light is detected. The main principle of Raman spectroscopy is the change in polarizability of a molecule when it interacts with light [17,18]. The elastically scattered light having the same frequency (energy) as the incident light is called as Rayleigh scattering. Inelastically scattered rays with higher frequency than the incident rays are called as stokes line and the lower frequency rays are known as anti-stokes lines. In Raman spectroscopy, vibration frequencies of different bonds are measured as the frequency shift with respect to the incident rays. Raman spectroscopy can be used to identify an unknown substance, to differentiate different polymorphs, and to track the changes in the molecular structure and crystal structure. Stress and orientation of molecules can also be determined using Raman spectroscopy. In crystalline materials, the photon interacts with the lattice vibrations or phonons. The first derivative of polarizability is nonzero for a Raman active phonon. The number of Raman active modes depends on the space group of the materials. In this work, Raman spectra were recorded on a Lab RAM HR micro Raman spectrometer (HORIBA JOBIN YVON, Model No.HR 800) using a 632.8 nm He-Ne laser.

2.4. Scanning Electron Microscopy

The scanning electron microscope (SEM) technique is used to get information about the topography, morphology and microstructure of materials [19]. High-resolution surface imaging with three dimensional characteristics can be obtained using SEM. Tungsten or LaB_6 cathodes are used to create thermionic electrons which are accelerated to an anode using very high potential. Typically, an electron beam with energy of 100 eV to 50 keV is produced. Electromagnetic lenses are used to focus the beam of electrons to the sample. Secondary electrons and backscattered electrons from the sample are detected by photomultiplier detector to produce images. In the present work, a FEI Quanta 200 3D ESEM is used for collecting the micrographs. The samples in pellet forms were fixed on stubs using a carbon

tape and to avoid charging of the specimen, a thin layer of gold was coated on the sample surface using the sputtering technique. The cross-section of the broken faces of the pellets was imaged.

2.5. X-ray Photoelectron Spectroscopy

X-ray Photoelectron Spectroscopy (XPS) or Electron Spectroscopy for Chemical Analysis (ESCA) can give chemical information on the surface of materials [20,21]. Working principle of XPS is the photoelectric effect, where electrons (photoelectrons) are emitted from atoms when excited with X-rays. Both the elemental and chemical environment information of a material can be obtained from XPS analysis. Electron spectrometer measures the kinetic energy (*KE*) of the emitted electron and the binding energy (*BE*) of the electron is calculated using the formula,

$$BE = hv - (KE + \phi)$$

Where ϕ is the work function and hv is the energy of the X-rays used. XPS is a surface sensitive technique since the typical penetration depth of X-rays is less than 10 nm. A VG Microtech Multilab ESCA 3000 X-ray Photoelectron Spectrometer with a non-monochromatized Mg-Kα X-ray source (1253.6 eV) and a Thermo Fisher Kalpha+ Spectrometer with monochromated Al-Kα radiation with energy 1486.6 eV were used to record the spectra. Binding energies are corrected with respect to the adventitious carbon 1s peak at 284.6 eV as reference.

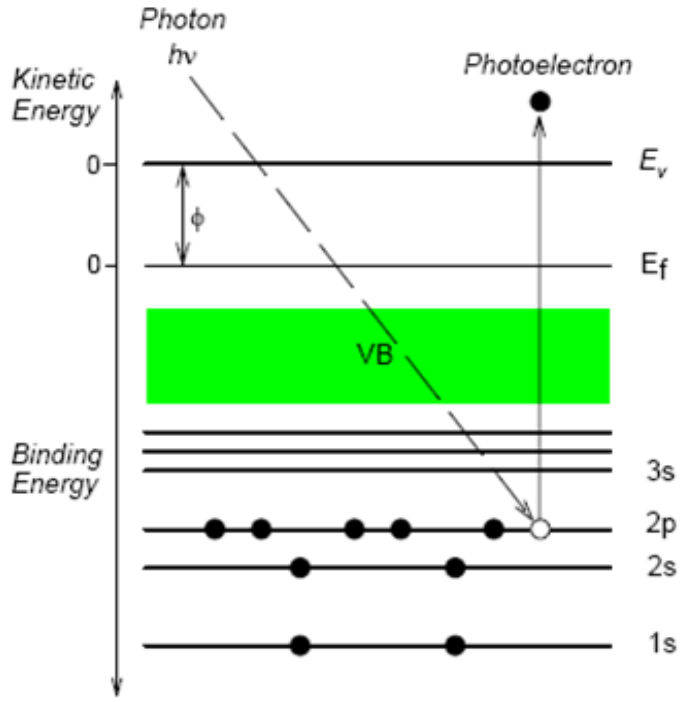

Figure 2.1. Energy level diagram showing the photoelectron emission by X-rays [22].

2.6. Magnetic measurements

The magnetization of samples can be measured as a function of field or temperature to know the magnetic characteristics of the material [23]. A vibrating sample magnetometer (VSM) was used for these measurements. VSM works based on the principle of Faraday's law, which states that a change in magnetic flux induces an electromotive force (emf) on a conductor that is proportional to the rate of change in flux [24, 25]. In a VSM, the sample is vibrated in a uniform magnetic field, and that induces a voltage on the pickup coils located near the sample. The emf on the pickup coil is directly proportional to the magnetic moment of the sample. Superconducting quantum interference device (SQUID) sensors can enhance the sensitivity of the measurements. SQUID works based on the Josephson junction, where a non-superconducting layer is placed in-between two superconducting layers and the electrons tunnel through the non-superconducting layer indefinitely [26]. SQUID has high sensitivity up to 10^{-8} emu in zero field [27].

In the present work, magnetic measurements at low temperatures were carried out on a Quantum Design make MPMS SQUID VSM DC Magnetometer. Helium-cooled superconducting magnets, which can go up to 7 T, were used. The sample chamber was cooled using liquid helium, down to a temperature of 1.8 K. Sample filled cups were fixed in

a gold plated brass sample holder attached to a sample rod which vibrated at a frequency of 13.8 Hz. Temperature-dependent magnetization measurement was carried out using both the zero field cooled (ZFC) and field cooled (FC) protocols. In the ZFC protocol, the sample was cooled to the lowest temperature in zero field and the magnetization was measured while warming up the sample back to room temperature in a constant magnetic field. In the FC protocol, the sample was cooled in the presence of a field and magnetization was measured while warming the sample in the same field. The cooling rate used was 20 K/ minute whereas the magnetization was recorded at a heating rate of 2 K/minute. For field-dependent magnetization measurements, the sample was allowed to stabilize at a particular temperature for sufficient time and magnetization was recorded by varying the field at a rate of 250 Oe/s. The instrument was calibrated using standard palladium samples with known weight whose susceptibility is taken as 5.25×10^{-6} emu/g Oe at 298 K. Temperature calibration was done using an indium sample which shows a superconducting transition at 3.4 K.

To determine the magnetic transition temperature, magnetization as a function of temperature was measured in the temperature range 30–500^{o}C, on an EG&G PAR 4500 Vibrating Sample Magnetometer, in a magnetic field of 5000 Oe (0.5 T). The sample taken in a boron nitride cup was heated at the rate of 2 ^{o}C/min, and magnetization was recorded while heating the sample from room temperature.

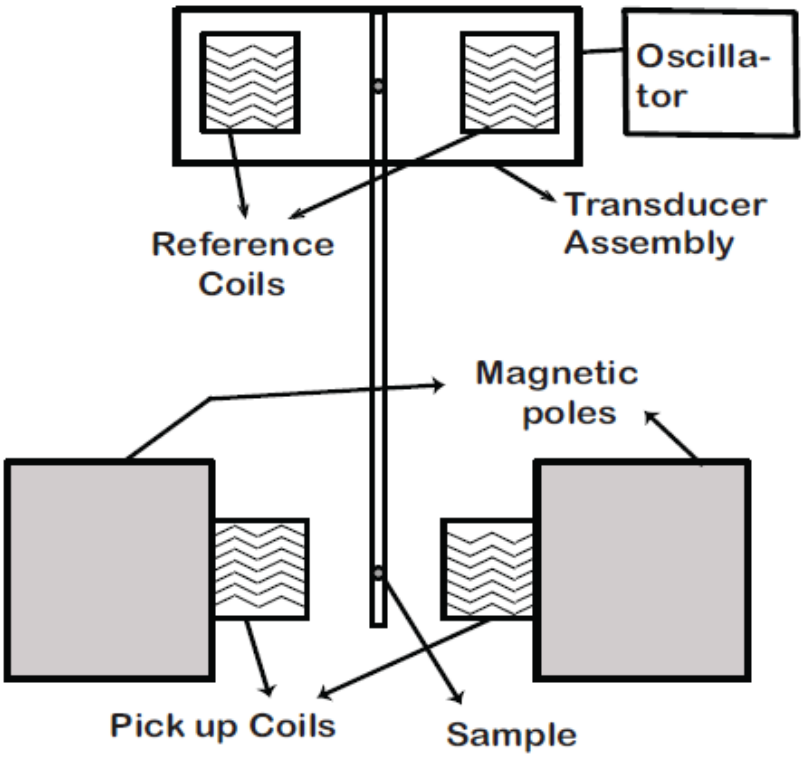

Figure 2.2. Schematic diagram of the VSM components [24].

2.7. Dielectric measurements

For the dielectric measurements, the sintered cylindrical pellets (13 mm x 1 mm) were used. Silver paste was applied on the surfaces of pellets for better electrical contact and was placed in-between two disc-shaped electrodes of almost 13 mm diameter. In the present work, a Novocontrol Beta N Impedance Analyser was used to measure the dielectric constant of the materials in the range of 1 kHz to 1 MHz at an applied voltage of 1 V.

For the magnetodielectric measurements, a General Radio 1608-A Impedance Bridge was used. The silver paste applied pellets were placed in a home-built sample holder and the holder was placed at the center of a DC magnet poles. Parallel capacitance at 1 kHz was measured using the impedance bridge, at an applied magnetic field of 10 kOe. Dielectric constant (ε_r) was calculated from the formula [28]

$$\varepsilon_r = \frac{C_p t}{\varepsilon_0 A}$$

where C_p is the capacitance of the sample, t is the sample thickness, A is the surface area of the conducting plate and ε_0 is the permittivity of air. Measurements were repeated many times in order to get a good reproducibility for the measurement.

2.8. Estimation of Mn^{4+} content

Due to the substitution of the divalent ion, Ca^{2+}, in place of the trivalent ion Bi^{3+} in $BiFeO_3$, equivalent amount of the substituted Mn will exist as Mn^{4+} inorder to maintain charge neutrality. Moreover, due to the presence of oxygen vacancies, some of the substituted Mn ions are expected to be present as Mn^{3+}. Therefore, to estimate the Mn^{3+}/Mn^{4+} content, permanganometric redox titration was carried out, which is commonly used in the case of the perovskite manganates [29-31]. Here the Mn^{3+} and Mn^{4+} get reduced to Mn^{2+} in an acidic solution in the presence of Fe^{2+} which is oxidized to Fe^{3+}. Solutions (around 0.02 N) of oxalic acid ($H_2C_2O_4.2H_2O$), potassium permanganate ($KMnO_4$), and Mohr's salt (ferrous ammonium sulphate, $FeSO_4.(NH_4)_2SO_4.6H_2O$) were prepared. $KMnO_4$ was standardized using standard oxalic acid solution which in turn was used to standardize the Mohr's salt solution. About 20 mg of the finely powdered sample was weighed accurately and dissolved in sufficient amount of a known volume (excess) of ferrous ammonium sulphate solution. Titration of this solution against the standard potassium permanganate solution gave the amount of unreacted Fe^{2+} after the reduction. The total amount of Fe^{2+} consumed for the reduction of Mn ions can be back-calculated from the titre values. One mole of Mn^{3+} reacts with one mole of Fe^{2+}, but it takes 2 moles of Fe^{2+} to react with one mole of Mn^{4+}, and thus the amount of Mn^{4+} can be determined.

References

[1] Honig J M and Rao C N R 1981 *Preparation and Characterization of Materials*, (Academic Press, New York)

[2] Segal D 1991 *Chemical Synthesis of Advanced Ceramic Materials* (Cambridge University Press, New york)

[3] Rao C N R1986 *Chemical Approaches to the Synthesis of Inorganic Materials*, (Cambridge University press, Cambridge)

[4] Jolivet J P, Henry M and Livage J 2000 *Metal Oxide Chemistry and Synthesis: From Solution to Solid State* (John Wiley & Sons, New York)

[5] West A R 2013 *Solid State Chemistry and its Applications* (John Wiley & Sons, Singapore)

[6] Palai R, Katiyar R S, Schmid H, Tissot P, Clark S J, Robertson J, Redfern S A T, Catalan G and Scott J F 200*8 Phys. Rev.* B **77** 014110

[7] Selbach S M, Einarsrud M-A and Grande T 2009. *Chem.Mater.* **21** 169

[8] Zhu W M, Guo H Y and Ye Z G 2008 *Phys. Rev. B* **78** 014401

[9] Klug H P and Alexander L E 1954 *X-Ray Diffraction Procedures* (Wiley, New York)

[10] Cullity B D and Stock S R 2001 *Elements of X-Ray Diffraction* (Prentice Hall, New Jersey)

[11] Kraus W and Nolze G, 'Powder Cell for Windows (PCW)', version 2.4, The software is freely available from http://www.ccp14.ac.uk.

[12] Rietveld H M 1967 *Acta. Crystallogr.* **22** 151

[13] Rietveld H M 1969 *J. Appl. Crystallogr.* **2** 65

[14] Young R A1995 *The Rietveld Method* (Oxford University Press, Oxford)

[15] Toby B 2001 *J. Appl. Crystallogr.* **34** 210

[16] Banwell C N and McCash E M 1994 *Fundamentals of Molecular Spectroscopy* (McGraw-Hill, London)

[17] Ferraro J R 2003 *Introductory Raman Spectroscopy* (Academic press, New York)

[18] Fateley W G, Dollish F R, McDevitt N T and Bentley F *1972 Infrared and Raman Selection Rules for Molecular and Lattice Vibrations: The Correlation Method* (John Willey and Sons, New York)

[19] Zhou W, Apkarian R, Wang Z L and Joy D 2007 *Fundamentals of Scanning Electron Microscopy (SEM)* (Springer, New York)

[20] Watts J F and Wolstenholme J 2003 *An introduction to surface analysis by XPS and AES* (John Wiley and Sons Inc, Chichester)

[21] Lowell S, Shields J E, Thomas M A and Thommes M 2012 *Characterization of porous solids and powders: surface area, pore size and density* (Springer Science & Business Media, New York)

[22] http://subato.blogspot.in/2011/05/material-surface-analysis-with-x-ray.html

[23] Hatscher S, Schilder H, Lueken H and Urland W 2005 *Pure Appl. Chem.* **77** 497

[24] Foner S 1959 *Rev. Sci. Inst.* **30** 548

[25] Cullity B D and Graham C D 2011 *Introduction to Magnetic Materials* (John Wiley & Sons, Canada)

[26] Anderson P and Rowell J, 1963 *Phys. Rev. Lett.* **10** 230

[27] Greenberg Y S 1998 *Rev. Mod. Phys.* **70** 175

[28] Kumar A and Sharma S 2007 *Prog. Electromagn. Res.* **69** 47

[29] Yakel H L 1955 *Acta Cryst.* **8** 394

[30] Jeffery G H, Bassett J, Mendham J, Denney R C 1989 *Vogel's Textbook of Quantitative Chemical Analysis*, 5*th* ed (ELBS with Longman, Singapore)

[31] Anil K P S, Alias J P and Date S 1998 *J. Mater. Chem.* **8** 1219

Chapter 3

Structural, magnetic and dielectric properties of $Bi_{1-x}A_xFe_{1-x}Mn_xO_3$ (A = Ca, Sr, Ba)

3.1. Introduction

Substitution of divalent metal ions at the bismuth-site in $BiFeO_3$ (BFO) can induce weak ferromagnetism due to size mismatch leading to structural distortion as well as the creation of Fe^{4+} and/or oxygen vacancy to compensate for the charge neutrality, where both destroys the spin periodicity. Khomchenko *et al.* have studied different divalent ion substituted BFO and showed that the magnetic parameters increase with an increase in the ionic radius of the substituent [1]. Kothari *et.al.* have shown an increase in the magnetization with increasing degree of substitution of Ca for Bi [2]. In the case of Fe-site substitution, magnetic properties are improved by the structural distortions which suppress the spin cycloidal structure leading to canted antiferromagnetism and from the magnetic contribution of the substituted transition metal ion. Enhanced magnetic and electrical properties are reported for Mn substituted at the Fe site of $BiFeO_3$ [3,4]. Divalent metal ion and manganese co-substituted BFO can exhibit enhanced magnetic properties due to the presence of Mn^{4+} species and/or oxygen vacancies, apart from the structural distortions.

Troyanchuk *et al.* have made detailed structural analysis of $Bi_{1-x}Ca_xFe_{1-x}Mn_xO_3$ and $Bi_{1-x}Sr_xFe_{1-x}Mn_xO_3$ ($0 \leq x \leq 0.5$) from neutron diffraction experiments. Around $x = 0.2$, a structural transition from the rhombohedral (space group: *R3c*) to orthorhombic (space group: *Pbnm*) and rhombohedral (space group: $R\bar{3}c$) is reported for Ca-Mn and Sr-Mn co-substitution, respectively [5]. Huang *et al.* have reported magnetic and ferroelectric properties for thin films of Ca-Mn co-substituted BFO, $Bi_{1-x}Ca_xFe_{1-y}Mn_yO_3$ ($0 \leq x \leq 0.1$ and $0 \leq y \leq 0.1$) and according to the authors, substitution of Fe by Mn causes a structural transition towards orthorhombic phase whereas substitution of Bi by Ca causes a tetragonal distortion in the co-substituted system [6]. Higher magnetic and ferroelectric properties are reported for $Bi_{0.90}Ca_{0.10}Fe_{0.90}Mn_{0.10}O_3$. Rout *et al*. have reported better magnetoelectric properties for $Bi_{1-x}Ba_xFe_{1-y}Mn_yO_3$ ($x = 0, 0.1, 0.2$) with a structural transition from rhombohedral *R3c* to tetragonal *P4mm* around $x = 0.2$ [7]. Kumar *et al*. studied the electrical and magnetic properties of $Bi_{1-x}Ba_xFe_{1-y}Mn_yO_3$ ($x = 0, 0.1, 0.2$) where they reported better properties for $x = 0.2$ [8].

In this chapter, we have studied and compared the structural and magnetic properties of Ca-Mn, Sr-Mn and Ba-Mn co-substituted BFO with the general formula $Bi_{1-x}A_xFe_{1-x}Mn_xO_3$ (BAFMO) with $0 \leq x \leq 0.3$. The ionic radii of Bi^{3+}, Ca^{2+}, Sr^{2+} and Ba^{2+}, for eight-fold coordination are 1.17, 1.12, 1.26, and 1.42 Å respectively [9]. Thus, Ca^{2+} has a

comparable ionic radius to Bi^{3+}, whereas Sr^{2+} and Ba^{2+} have larger ionic radii, and this can cause larger structural distortions in the Ba-Mn and Sr-Mn co-substituted systems. This is likely to lead to different structural and magnetic properties for the latter systems compared to the Ca-Mn co-substituted system, due to the large changes in the bond angles and bond lengths on substitution. The objective of this work is to investigate the effect of the ionic size of the substituted alkaline earth metal ions substituted for Bi, when co-substituted with Mn at the Fe-site, on the structural, magnetic and dielectric properties of $BiFeO_3$.

Co-substituted bismuth ferrite bulk samples, with the general formula $Bi_{1-x}A_xFe_{1-x}Mn_xO_3$, ($0 \leq x \leq 0.3$), where A = Ca/Sr/Ba, were prepared by the solid-state reaction method as described in section 2.1. The as-prepared samples were ground well and used for different characterizations.

3.2. Structure

Powder X-ray diffraction patterns of the $Bi_{1-x}A_xFe_{1-x}Mn_xO_3$ (BAFMO) ceramic samples for $0 \leq x \leq 0.3$ are shown in figures 3.1 to 3.3. In all the three co-substituted systems, for samples with $x < 0.2$, peaks due to minor amounts of the bismuth-rich phase $Bi_{25}FeO_{40}$ are observed. Peaks due to the Fe-rich Bi_2FeO_9 impurity phase are not observed for any of the samples. In figure 3.4, the most intense peak in the XRD patterns of the BAFMO systems is compared. The splitting of the peak due to the *R3c* structure disappears from $x = 0.2$ onwards for the Ca-Mn co-substituted system, which implies a structural transition at that composition. On the other hand, the splitting due to the *R3c* structure is directly evident for both the Ba-Mn and Sr-Mn co-substituted systems even at $x = 0.3$, implying rhombohedral structure for these compositions at $x = 0.3$. A prominent shift in the positions of the XRD peaks can be observed for Ca-Mn and Sr-Mn co-substituted systems, whereas the Ba-Mn co-substituted compositions show a relatively much smaller shift. The shift in the XRD peak positions corresponds to variation in the lattice parameters. Though Ba^{2+} has a larger ionic size than that of Bi^{3+}, the smaller Mn^{4+} species formed for the charge compensation reduces the effect of the size difference between Bi^{3+} and Ba^{2+}. Hence, the much smaller shift observed for the Ba-Mn co-substituted system. Variation in the lattice parameters is discussed with respect to figure 3.6.

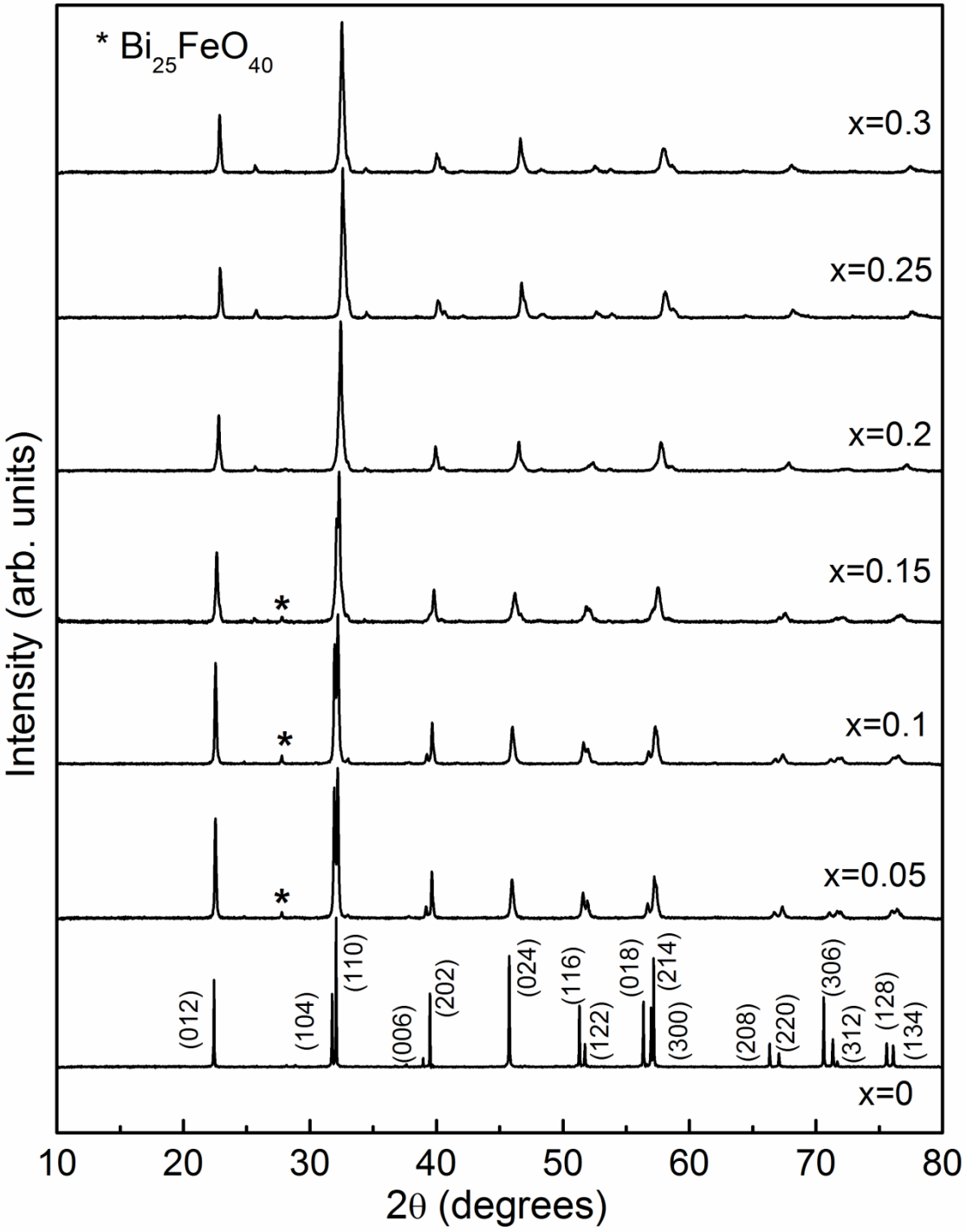

Figure 3.1. Powder XRD patterns of different compositions in $Bi_{1-x}Ca_xFe_{1-x}Mn_xO_3$. The peak from the impurity phase $Bi_{25}FeO_{40}$ is marked using the symbol '*'.

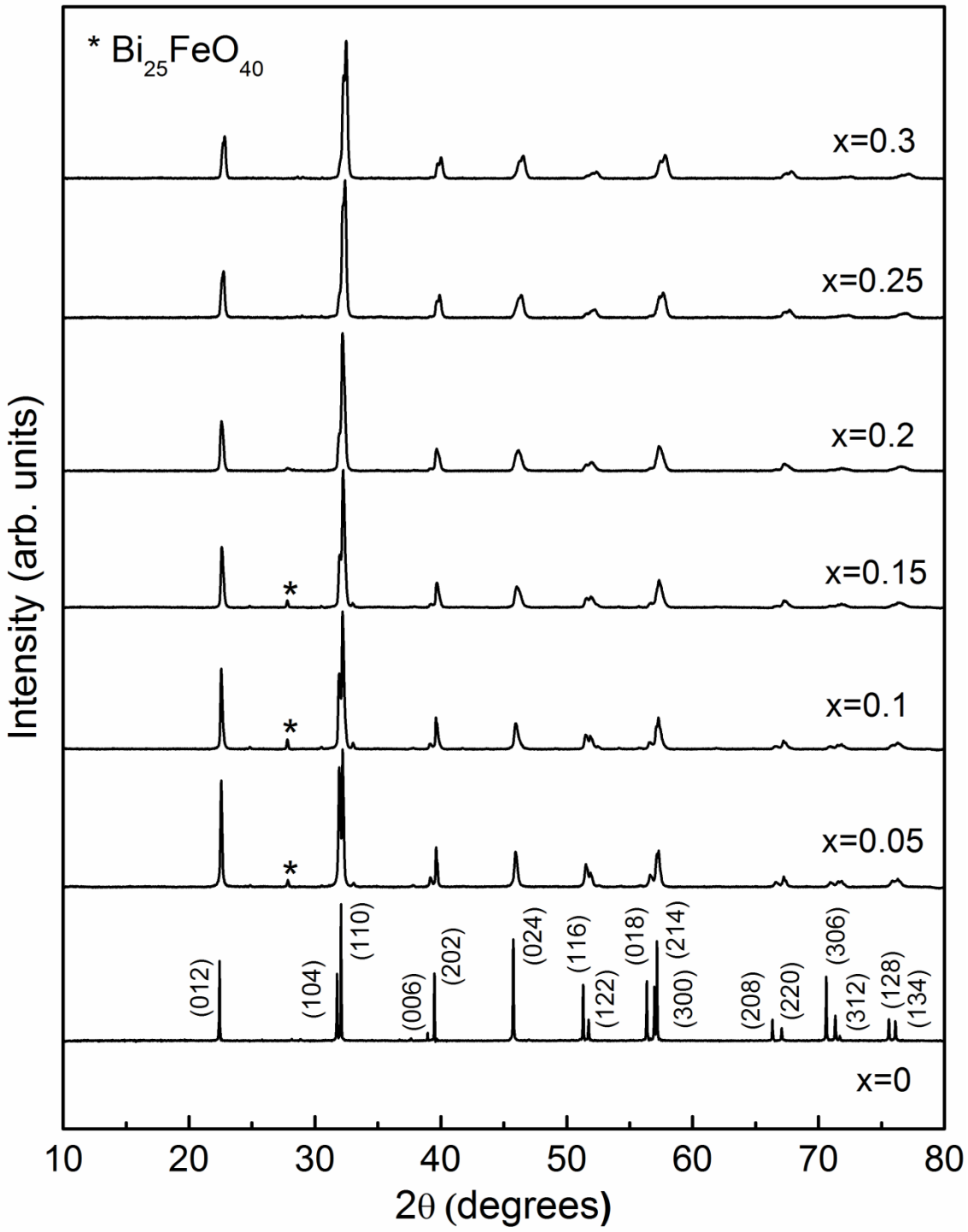

Figure 3.2. Powder XRD patterns of different compositions in $Bi_{1-x}Sr_xFe_{1-x}Mn_xO_3$. The peak from the impurity phase $Bi_{25}FeO_{40}$ is marked using the symbol '*'.

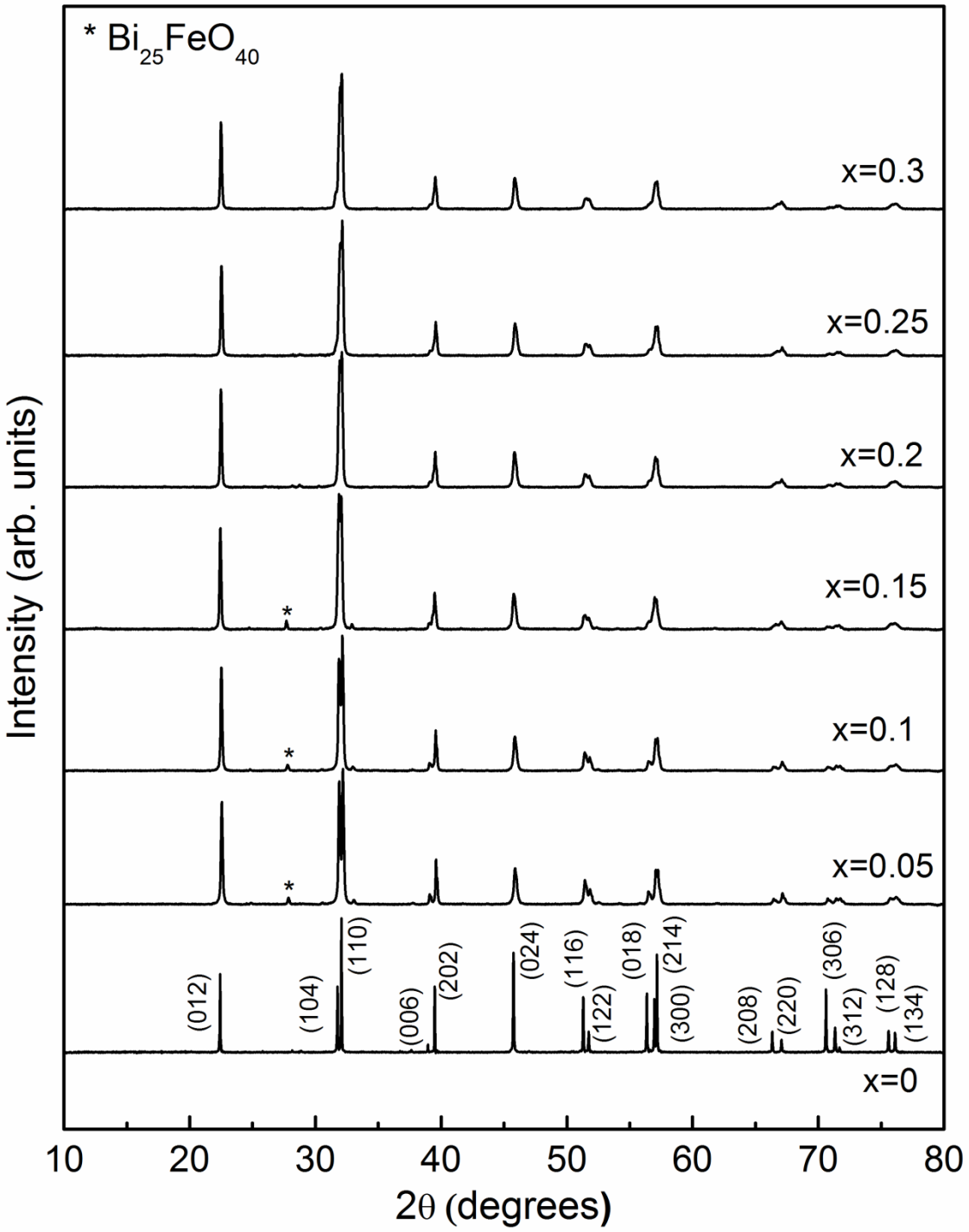

Figure 3.3. Powder XRD patterns of different compositions in $Bi_{1-x}Ba_xFe_{1-x}Mn_xO_3$. The peak from the impurity phase $Bi_{25}FeO_{40}$ is marked using the symbol '*'.

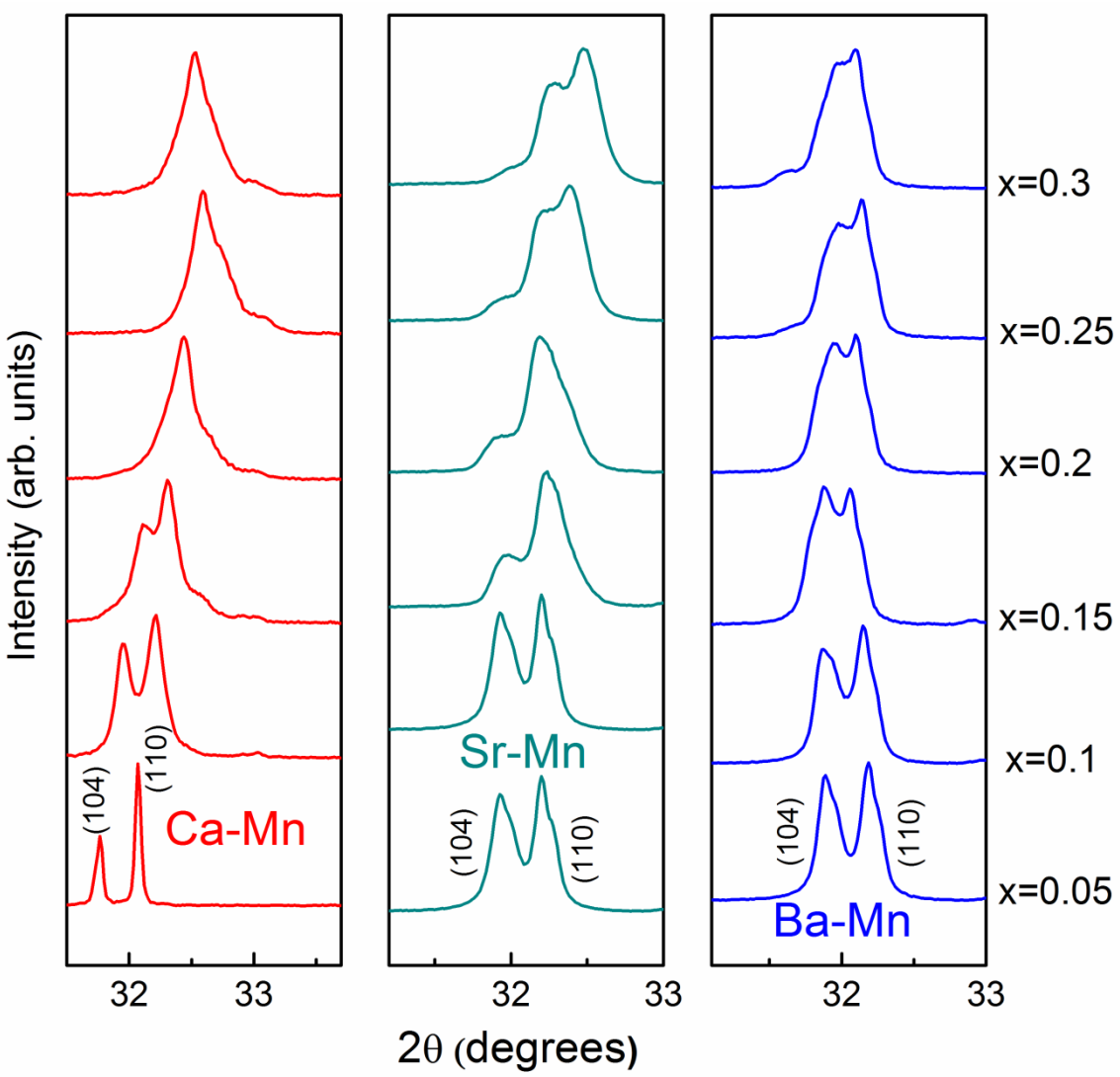

Figure 3.4. Comparison of the most intense peak in the XRD patterns of different compositions in $Bi_{1-x}A_xFe_{1-x}Mn_xO_3$ (A = Ca, Sr, Ba).

Rietveld refinement analysis of the XRD patterns reveals that, for Ca-Mn co-substitution, the compositions with $x < 0.1$ have rhombohedral structure whereas the compositions with $x > 0.2$ show orthorhombic structure, and $x = 0.15$ shows *R3c-Pbnm* mixed phase with 15% of the *Pbnm* phase. For Sr-Mn co-substitution, *R3c* to $R\bar{3}c$ structural change occurs around $x = 0.1$ and mixed phase is observed till $x = 0.3$. *R3c* and $R\bar{3}c$ are very similar space groups and its difficult to distinguish them. χ^2 value is obtained as ~4 for the XRD refinement of $Bi_{0.7}Sr_{0.3}Fe_{0.7}Mn_{0.3}O_3$ using *R3c* or $R\bar{3}c$ space groups alone, but it dropped below ~2 with a refinement considering *R3c*- $R\bar{3}c$ mixed phase and much better fit was obtained. Only 25% of *R3c* phase content was obtained for $Bi_{0.7}Sr_{0.3}Fe_{0.7}Mn_{0.3}O_3$.

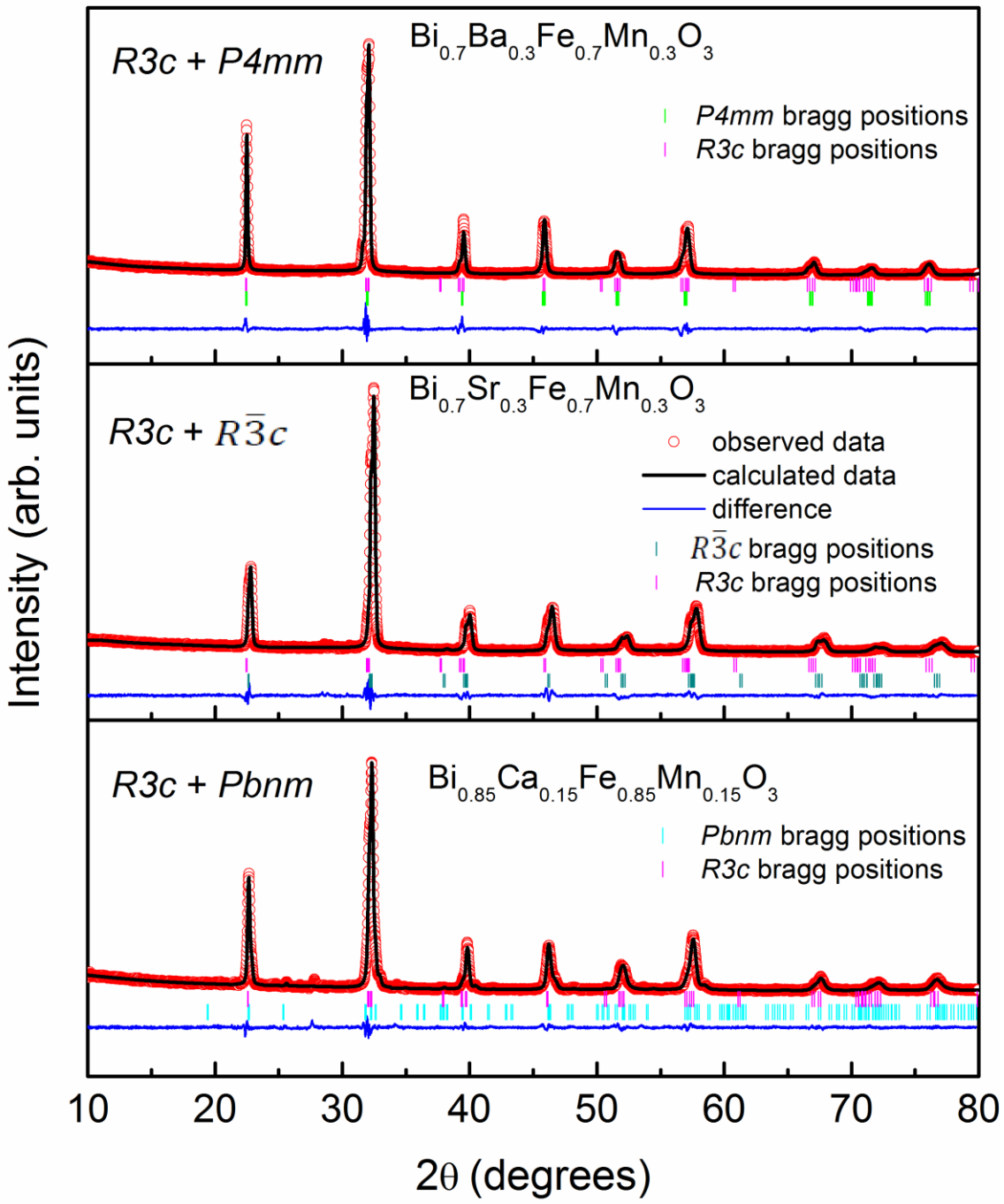

Figure 3.5. Results of the Rietveld refinement of the XRD patterns of $Bi_{1-x}A_xFe_{1-x}Mn_xO_3$ for x = 0.3 showing the presence of mixed phases (A = Ca, Sr, Ba).

For Ba-Mn co-substitution, rhombohedral (*R3c*) to tetragonal (*P4mm*) structural change occurs around x = 0.25 and shows a mixed phase of *R3c* and *P4mm* till x = 0.3. 89% of the *R3c* phase was obtained for $Bi_{0.7}Ba_{0.3}Fe_{0.7}Mn_{0.3}O_3$. Figure 3.5 shows the Rietveld refinement of the XRD patterns of $Bi_{0.85}Ca_{0.15}Fe_{0.85}Mn_{0.15}O_3$, $Bi_{0.7}Sr_{.3}Fe_{0.7}Mn_{0.3}O_3$ and $Bi_{0.7}Ba_{0.7}Fe_{0.7}Mn_{0.3}O_3$, where the compositions show mixed phase behaviour.

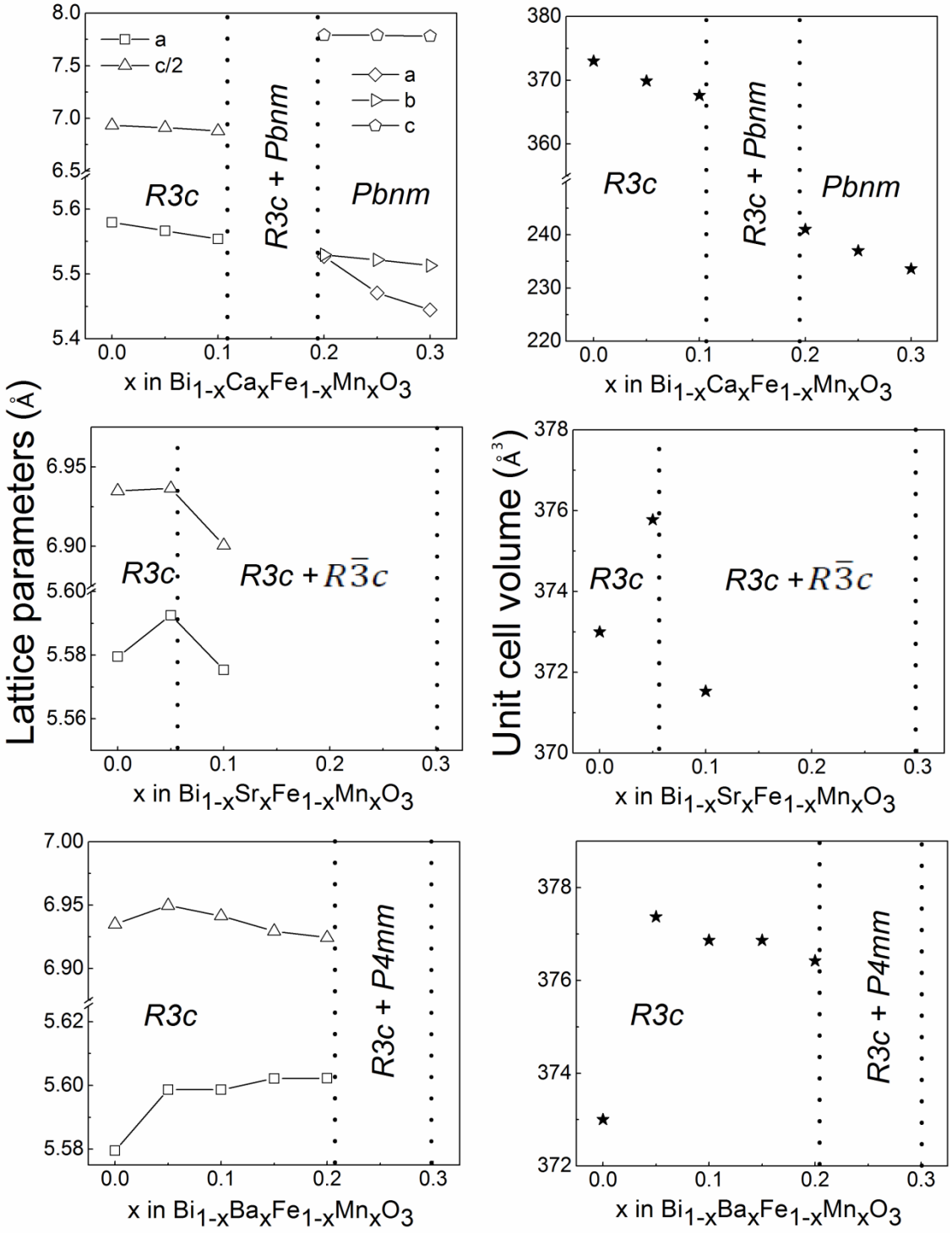

Figure 3.6. Variation of lattice parameters and unit cell volume as a function of *x* in $Bi_{1-x}A_xFe_{1-x}Mn_xO_3$ (A = Ca, Sr, Ba).

Variation of the lattice parameters and unit cell volume as a function of *x* is shown in figure 3.6, where the region between the dotted lines indicates the mixed phase region in the corresponding systems. For comparison, the *R3c* lattice parameters of $Bi_{0.9}Sr_{0.1}Fe_{0.9}Mn_{0.1}O_3$ are shown although it shows an *R3c*-$R\bar{3}c$ mixed phase. Shannon ionic radii (8-coordination)

of Bi^{3+} (1.17 Å) and Ca^{2+} (1.12 Å) are almost comparable whereas Sr^{2+} (1.26 Å) and Ba^{2+} (1.42 Å) are comparatively larger ions; ionic radii of Mn^{3+} and Fe^{3+} are 0.645 Å for 6-coordination [9]. Substitution of divalent ions should create Mn^{4+} (ionic radius = 0.53 Å) species and/or oxygen vacancies for charge neutrality. For the Ca-Mn co-substituted system, the lattice parameters decrease with increasing Ca/Mn content which is due to the lower ionic radius of the Ca^{2+} and due to formation of Mn^{4+} which is smaller than Fe^{3+} in size. In the Sr-Mn system, initially the lattice parameters increases for $x = 0.05$ and then show a decrease for $x = 0.1$. The initial increase in the lattice parameters is due to the larger size of Sr^{2+} than that of Bi^{3+} and for higher level of substitution, due to the formation of smaller $Mn^{4,+}$ the lattice parameters decrease. Difference in the ionic radius between Mn^{4+} and Fe^{3+} ($\Delta r_B = 0.115$ Å) is larger than the difference in ionic radius between Sr^{2+} and Bi^{3+} ($\Delta r_A = 0.09$ Å) which causes the decrease in the lattice parameters for $Bi_{0.9}Sr_{0.1}Fe_{0.9}Mn_{0.1}O_3$.

In the Ba-Mn system, all the co-substituted samples show larger ‘a’ lattice parameters than for the unsubstituted BFO due to the larger size of Ba^{2+}. However, with an increase in the Ba/Mn content, the lattice parameter ‘c’ shows a small decrease whereas ‘a’ remains almost constant. Here, the difference in the ionic size between Ba^{2+} and Bi^{3+}, $\Delta r_A = 0.25$ Å, is larger than the difference between Bi^{3+} and Ca^{2+}/Sr^{2+}, leading to higher lattice parameters for the Ba-Mn co-substituted compositions. However, with increasing co-substitution content, the amount of Mn^{4+} increases leading to a further smaller decrease in the lattice parameters. In all three cases, a corresponding change in the unit cell volume is also observed with the degree of substitution.

The end member of the $Bi_{1-x}A_xFe_{1-x}Mn_xO_3$ system for A = Ca, $CaMnO_3$, has the orthorhombic structure with *Pbnm* space group (a = 5.264 Å, b = 5.279 Å, c =7.448 Å) [10] whereas $SrMnO_3$ and $BaMnO_3$ exist in the hexagonal structure with $P6_3/mmc$ space group [11-16]. They also can show different crystal structures with variation in the oxygen stoichiometry [15, 16]. The Ca-Mn co-substituted system is closely related to the Ca or Mn substituted $BiFeO_3$ showing the similar crystal structure and space group. $Bi_{0.7}Ca_{0.3}Fe_{0.7}Mn_{0.3}O_3$ has the lattice parameters a = 5.448 Å, b = 5.5129 Å, and c = 7.7824 Å which are almost comparable to that of $CaMnO_3$. The Sr-Mn and Ba-Mn co-substituted systems show different crystal structures than that of their corresponding end members.

3.3. Microstructure

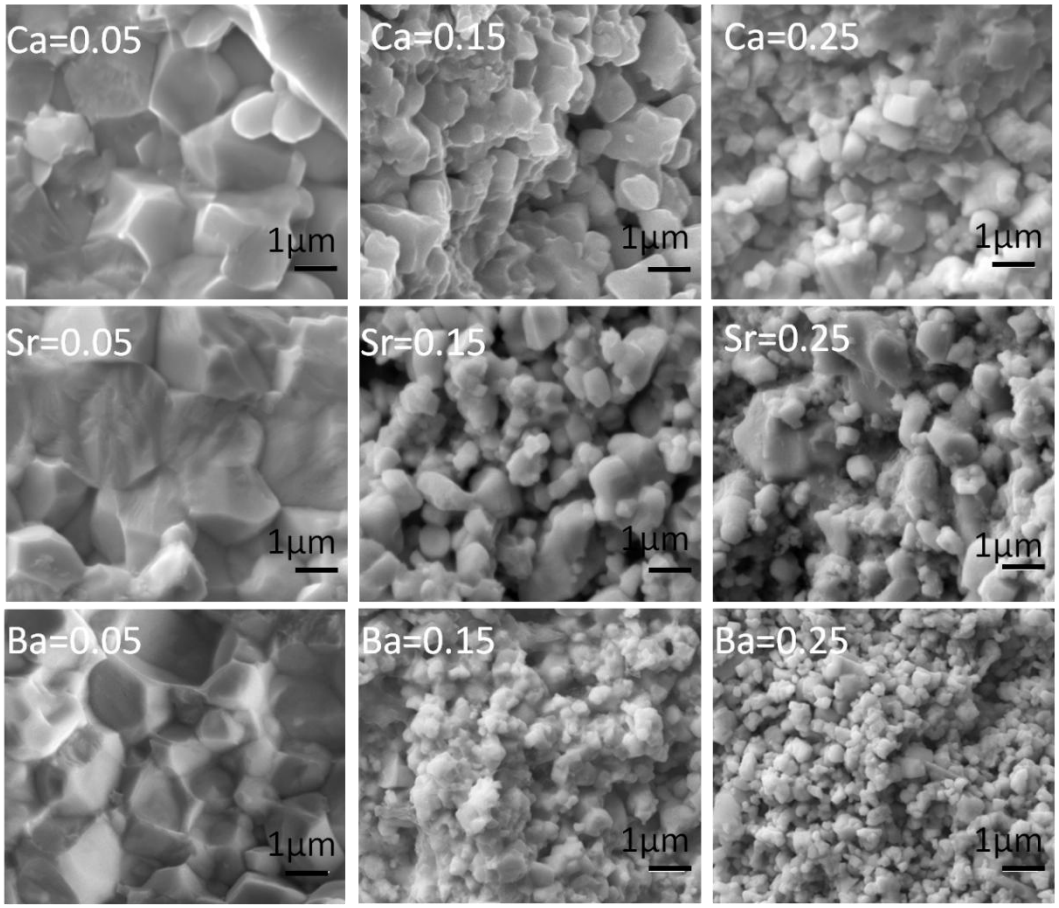

Figure 3.7. Scanning electron micrographs of different compositions in $Bi_{1-x}A_xFe_{1-x}Mn_xO_3$ (A = Ca, Sr, Ba).

SEM micrographs of the $Bi_{1-x}A_xFe_{1-x}Mn_xO_3$ samples (x = 0.05, 0.15 and 0.25) are shown in figure 3.7. Very large (> 1 μm) and fused grains are observed for x = 0.05 samples. The large fused grains of x = 0.05 samples are due to melting of these samples due to the low substitution percentage. Grain size is decreased with increasing degree of substitution in all three series, and less porosity is observed for the Ca-Mn system. $Bi_{0.85}Sr_{0.15}Fe_{0.85}Mn_{0.15}O_3$ and $Bi_{0.85}Sr_{0.25}Fe_{0.75}Mn_{0.25}O_3$ show a mixture of larger and smaller grains. This could be possibly due to the mixed phase observed for Sr-Mn and Ba-Mn co-substituted system at x = 0.25. The larger and smaller grains observed are likely to be from different phases present in these samples, as evidenced from the XRD studies. Ba-Mn co-substituted samples for higher concentrations (x > 0.05) show smaller and almost uniform sized grains than that observed for the corresponding Ca-Mn and Sr-Mn co-substituted samples.

3.4. Raman spectroscopy

Raman spectroscopy is a very good technique to distinguish different crystal structures. According to group theory calculations, Raman active modes of *R3c* structure are given by the irreducible representation, $\Gamma = 4A_1 + 9E$ [17]. Figures 3.8 to 3.11 show the Raman spectra of different compositions in $Bi_{1-x}A_xFe_{1-x}MnO_3$. The Raman bands observed for BFO are similar to that reported in the literature [2, 18]. 13 Raman modes observed for unsubstituted BFO are assigned as 143 cm^{-1} (A_1-1), 176 (A_1-2), 222 (A_1-3), 474 cm^{-1}(A_1-4) 81 (E-1), 127 (E-2), 265 (E-3), 302 (E-4), 345 (E-5), 377 (E-6), 418 (E-7), 531(E-8) and 625 cm^{-1} (E-9) (E-1 mode at 81 cm^{-1} is not shown in the figure). The low-frequency bands at 143, 176, and 222 cm^{-1} are related to Bi-O vibrations, and the high-frequency E modes are related to Fe-O vibrations. The most intense band observed for BFO is the A_1-1 mode, and this is merged with the band due to the E-2 mode.

Upon Ca-Mn co-substitution, the intensities of A_1-1 and E-2 bands are diminished, and the A_1-3 band at 222 cm^{-1} becomes more intense (figure 3.8). The band at 222 cm^{-1} is completely absent in the spectra for $x \geq 0.2$. Compositions with $x \geq 0.2$ with the orthorhombic structure show different spectral features than that for the *R3c* compositions ($x \leq 0.1$). Broad bands appearing around 480 and 620 cm^{-1} are similar to those reported for the orthorhombic $RMnO_3$ perovskites [19,20]. Even in the spectra of orthorhombic $LaFeO_3$ and other orthorhombic $BiFeO_3$ systems, the band at 620 cm^{-1} is reported [21]. However, broad and high intense band at 620 cm^{-1} is mostly observed in the Mn-substituted $BiFeO_3$ even with the rhombohedral *R3c* structure [22-25]. The intensity of this band at 620 cm^{-1} is increased due to the structural distortion caused by Mn substitution [25]. The band at 620 cm^{-1} arises from the symmetric stretching of basal oxygen of the MnO_6 octahedra and the band at 480 cm^{-1} is from the antisymmetric stretching arising from the Jahn-Teller distortion [20]. Mn^{3+} is Jahn-Teller active whereas Mn^{4+} is Jahn-Teller inactive. Raman mode at 480 cm^{-1} suggests the presence of Mn^{3+} in the samples. Low-frequency E and A_1 modes are characteristics of the stereochemical activity of Bi lone pairs and thus indicate the ferroelectric character of the compositions. Complete disappearance of the low-frequency bands for $x \geq 0.2$ suggests suppression of the stereochemical activity of the Bi lone pair of electrons and hence nonpolar nature of the compounds. These results confirm the structural change from *R3c* to *Pbnm* around $x = 0.15$, as concluded from the XRD studies on the Ca-Mn co-substituted system.

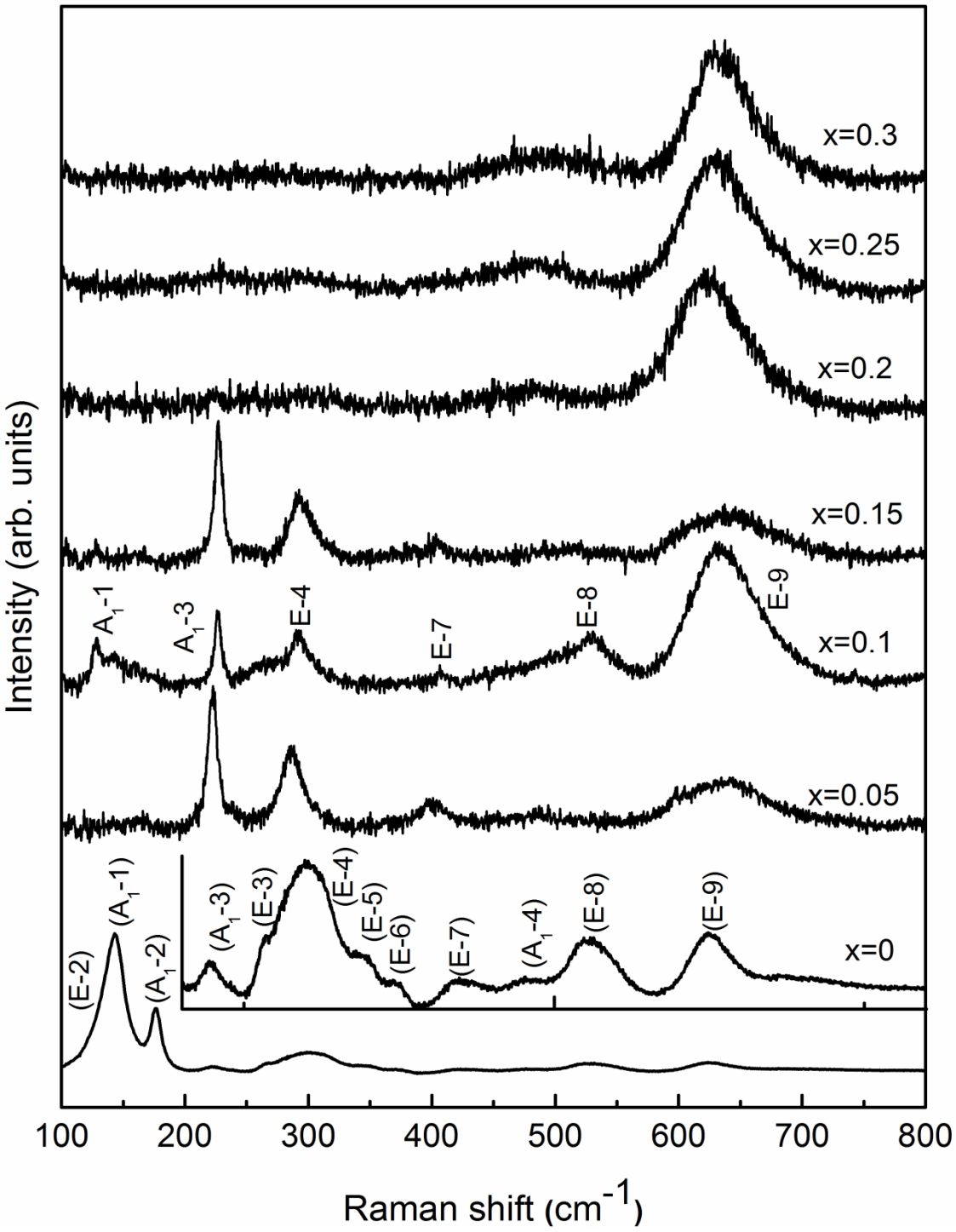

Figure 3.8. Raman spectra of $Bi_{1-x}Ca_xFe_{1-x}Mn_xO_3$. The inset shows the zoomed spectra of BFO (x = 0) in the same x-axis scale.

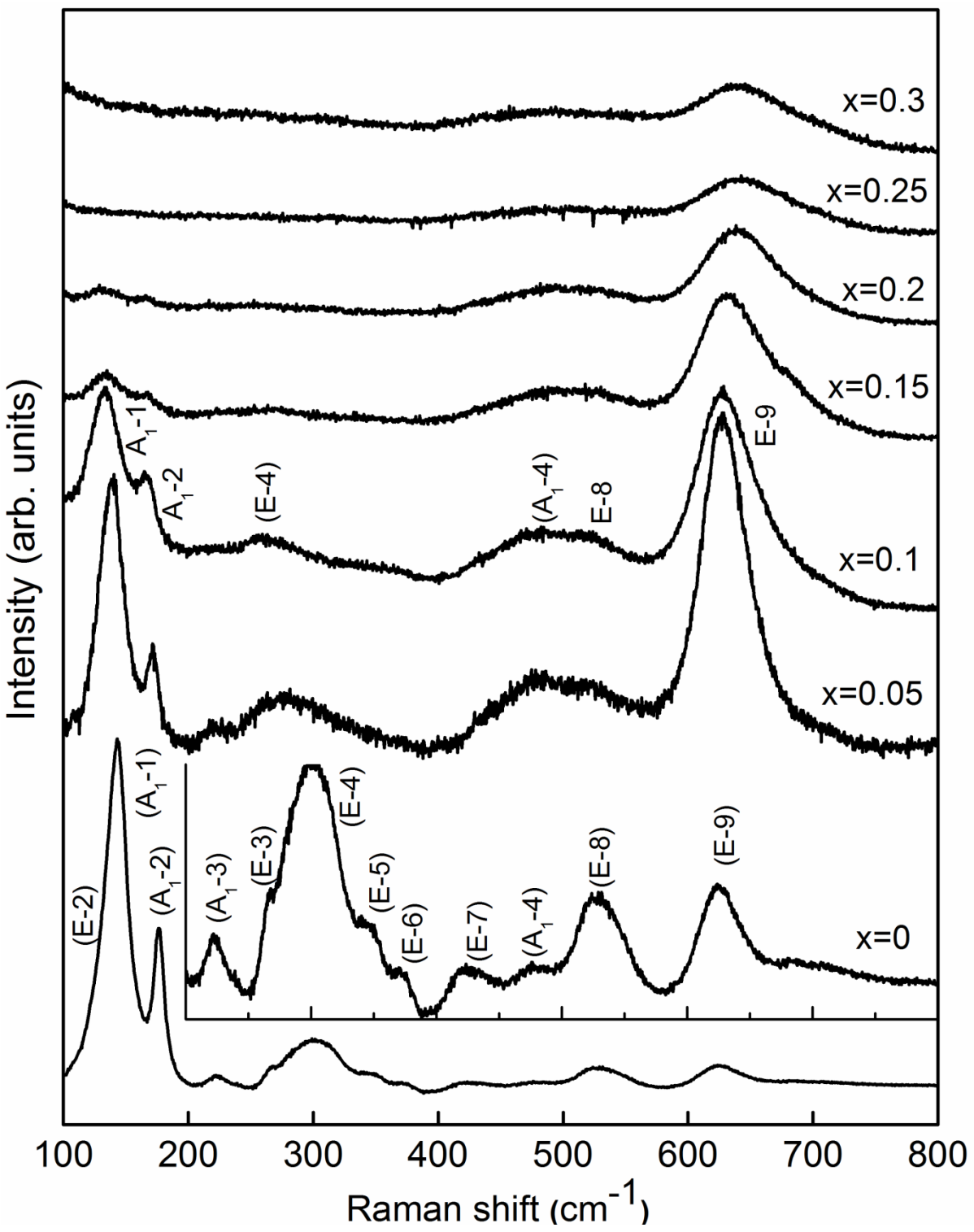

Figure 3.9. Raman spectra of $Bi_{1-x}Sr_xFe_{1-x}Mn_xO_3$. The inset shows the zoomed spectra of BFO (x = 0) in the same x-axis scale.

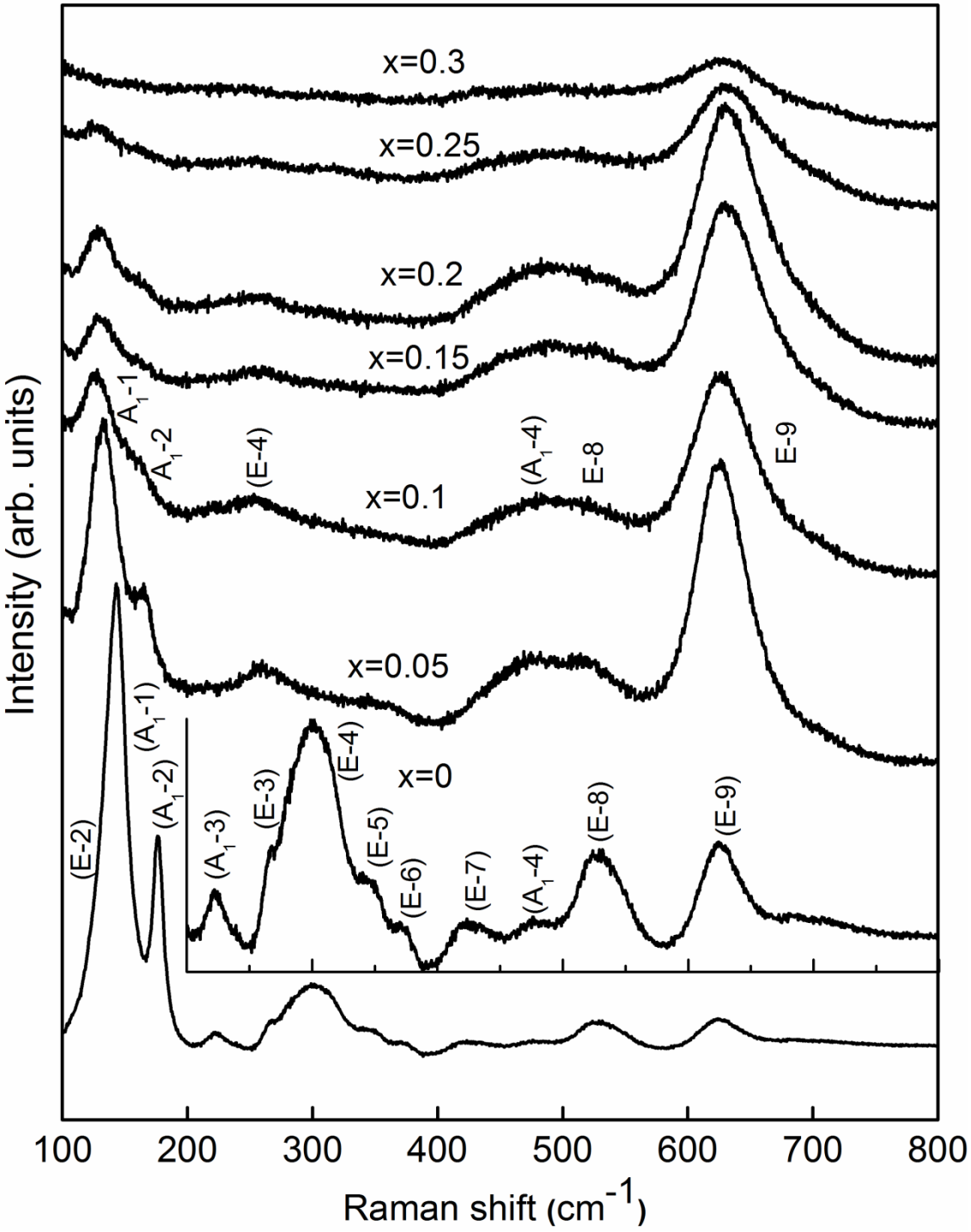

Figure 3.10. Raman spectra of $Bi_{1-x}Ba_xFe_{1-x}Mn_xO_3$. The inset shows the zoomed spectra of BFO (x = 0) in the same x-axis scale.

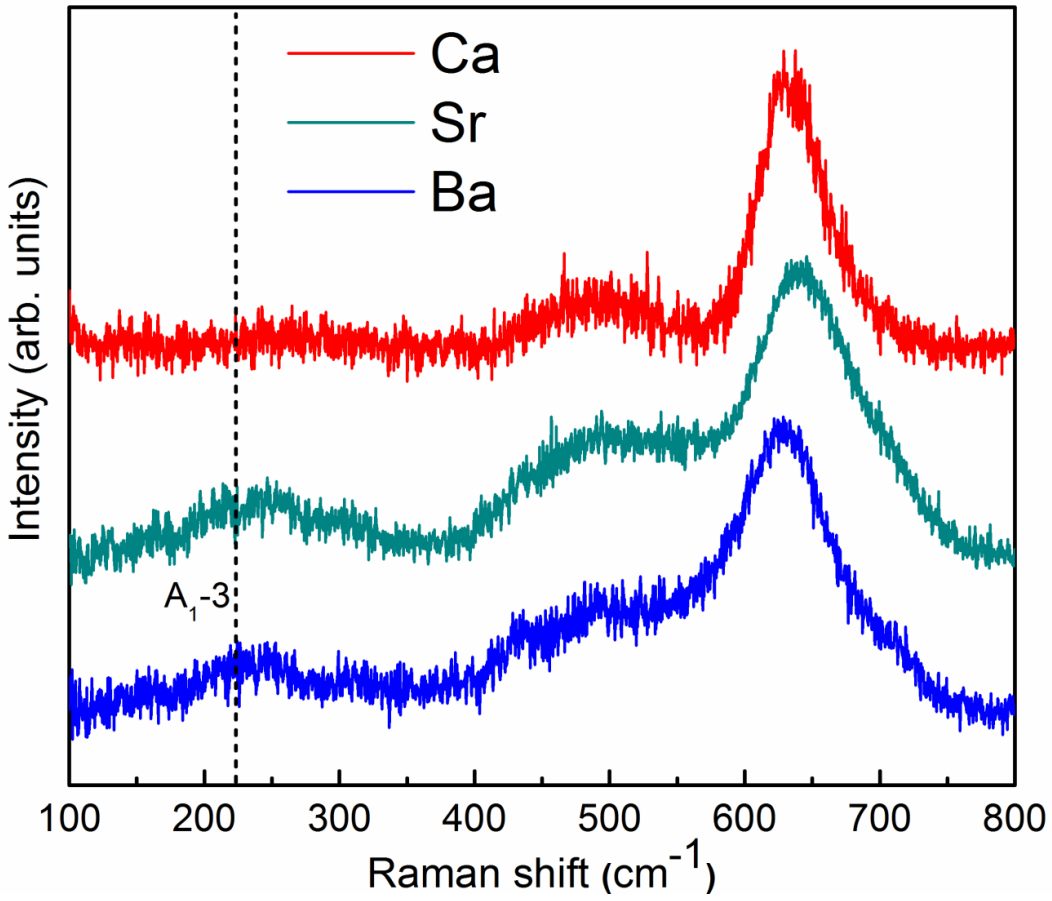

Figure 3.11. Comparison of the Raman spectra of $Bi_{0.3}A_{0.3}Fe_{0.7}Mn_{0.3}O_3$ (A = Ca, Sr, Ba).

For the Sr-Mn system, the compositions with $x \leq 0.2$ show Raman spectra similar to that of BFO. For $x \geq 0.15$, intensities of the A_1-2 and E-2 bands are decreased, and intensity of the mode at 620 cm^{-1} is increased (figure 3.9). This is possibly due to the formation of the $R\bar{3}c$ phase above x = 0.1. For $x \geq 0.25$ the bands due to the A_1-2 and E-2 modes disappear suggesting the non-ferroelectric character of the compositions. For $x \geq 0.25$, only two Raman modes at 480 and 620 cm^{-1} are observed which is in accordance with the XRD studies that for $x > 0.2$ $R\bar{3}c$ is the major phase. Ba-Mn system also shows Raman spectra similar to that of unsubstituted BFO till x = 0.25 with an increase in the intensities of the modes at 620, 480 and 530 cm^{-1} and the peak intensity of low-frequency modes decreases with the degree of co-substitution as shown in figure 3.10. XRD studies revealed a structural transition from *R3c* to *P4mm* around x = 0.25. The x = 0.25 composition show all modes of BFO in the Raman spectra, confirming that the *R3c* phase is the major phase, as confirmed from the XRD analysis. Though the x = 0.3 samples are *R3c-P4mm* mixed phase, only the bands at 620 and

480 cm^{-1} are visible implying a phase change similar to that in Ca-Mn and Sr-Mn co-substituted systems.

Normalized Raman spectra of $Bi_{0.7}A_{0.3}Fe_{0.7}Mn_{0.3}O_3$ samples are compared in figure 3.11. The A_1-3 Raman mode at 220 cm^{-1} is present for the $Bi_{0.7}Sr_{0.3}Fe_{0.7}Mn_{0.3}O_3$ and $Bi_{0.7}Ba_{0.3}Fe_{0.7}Mn_{0.3}O_3$, whereas, for $Bi_{0.7}Ca_{0.3}Fe_{0.7}Mn_{0.3}O_3$, it is absent indicating the presence of the *R3c* phase in Sr/Ba-Mn samples and absence of *R3c* phase in Ca-Mn system for x = 0.3. The other low-frequency modes are absent due to the smaller percentage of *R3c* phase in the corresponding Sr-Mn and Ba-Mn co-substituted systems. The intensity of the broad bands at 480 and 620 cm^{-1} remain almost comparable for the three co-substituted series which are mainly from the BO_6 (Fe/Mn) vibrations in $Bi_{0.7}A_{0.3}Fe_{0.7}Mn_{0.3}O_3$. This observation is in accordance with the results from the XRD studies.

3.5. Magnetic properties

3.5.1. M vs. H measurements

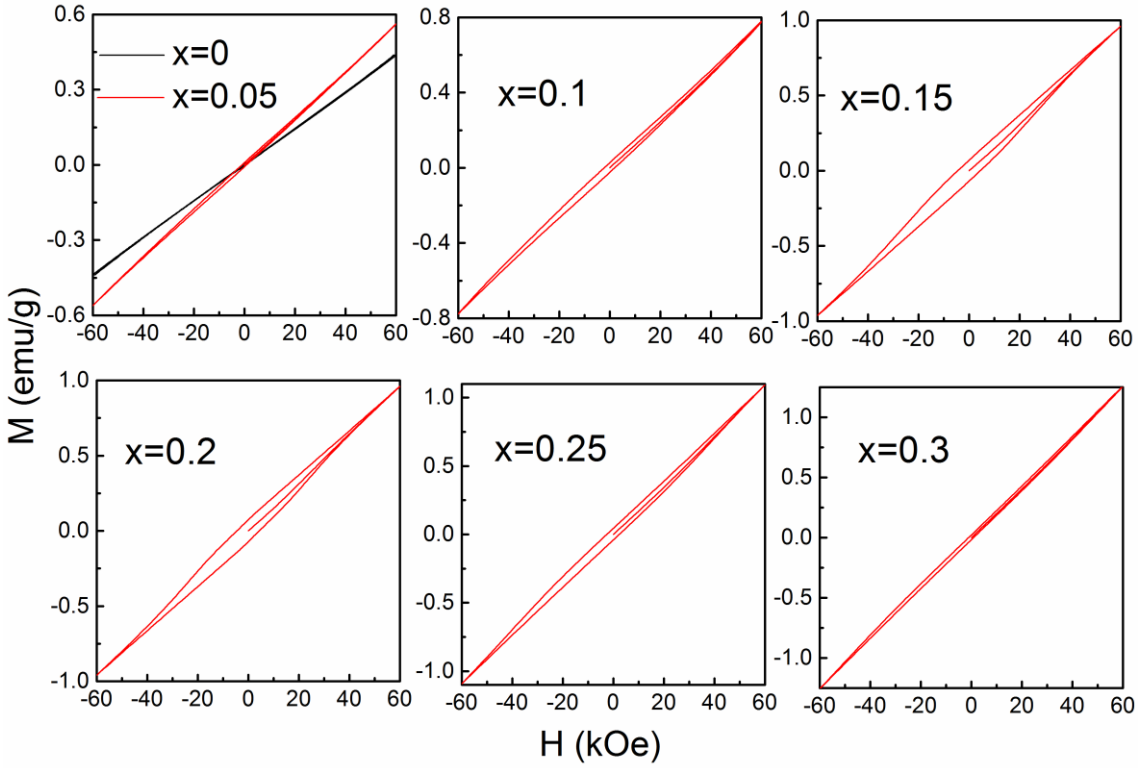

Figure 3.12. Magnetization vs. applied magnetic field curves of $Bi_{1-x}Ca_xFe_{1-x}Mn_xO_3$ measured at room temperature.

Room temperature M-H curves of BFO and the substituted compositions are shown in figures 3.12 to 3.14. BFO shows a linear variation of magnetization with the applied magnetic field, with negligible coercivity and remanence, which is the typical antiferromagnetic nature. However, with increasing the level of substitution, magnetization increases with significant coercivity and remanence, indicating the weak ferromagnetic nature of the samples on co-substitution. Upon co-substitution, magnetization increases with increasing A/Mn content, which does not saturate even at 60 kOe. BFO shows a magnetization of 0.4 emu/g at 60 kOe which is increased to ~0.6 emu/g for x = 0.05 and ~1.25 emu/g for x = 0.3 for all the three co-substituted systems.

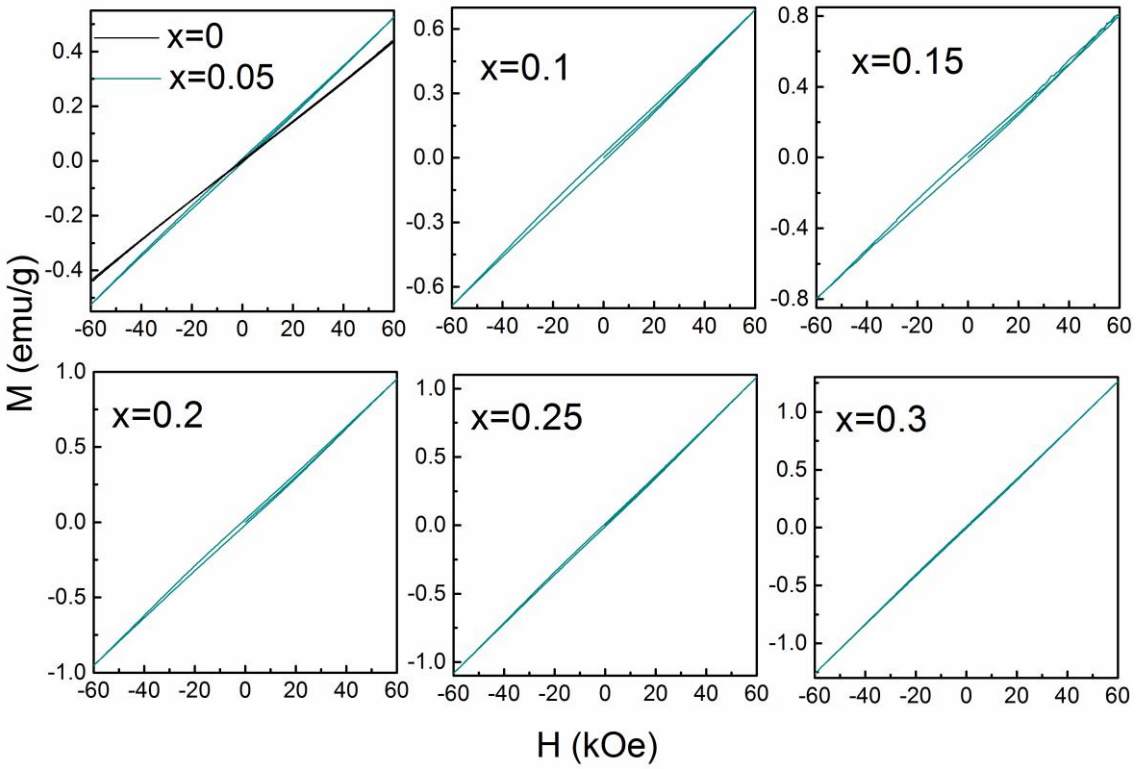

Figure 3.13. Magnetization vs. applied magnetic field curves of $Bi_{1-x}Sr_xFe_{1-x}Mn_xO_3$ measured at room temperature.

Upon co-substitution, the coercivity and remanence increase with increasing the percentage of co-substitution indicating the weak ferromagnetic nature of the co-substituted samples. Larger hysteresis loops are observed of Ca-Mn co-substituted samples than the Sr-Mn and Ba-Mn co-substituted samples as shown in figure 3.15. For x > 0.15, the loop becomes narrower in all the three co-substituted systems, and $Bi_{0.3}Sr_{0.3}Fe_{0.7}Mn_{0.3}O_3$ shows almost a linear variation of magnetization with negligible remanence and coercivity similar to

the M-H behaviour of BFO. For the Ba-Mn co-substituted samples, for $x \geq 0.2$, a weak ferromagnetic nature is observed at low magnetic fields.

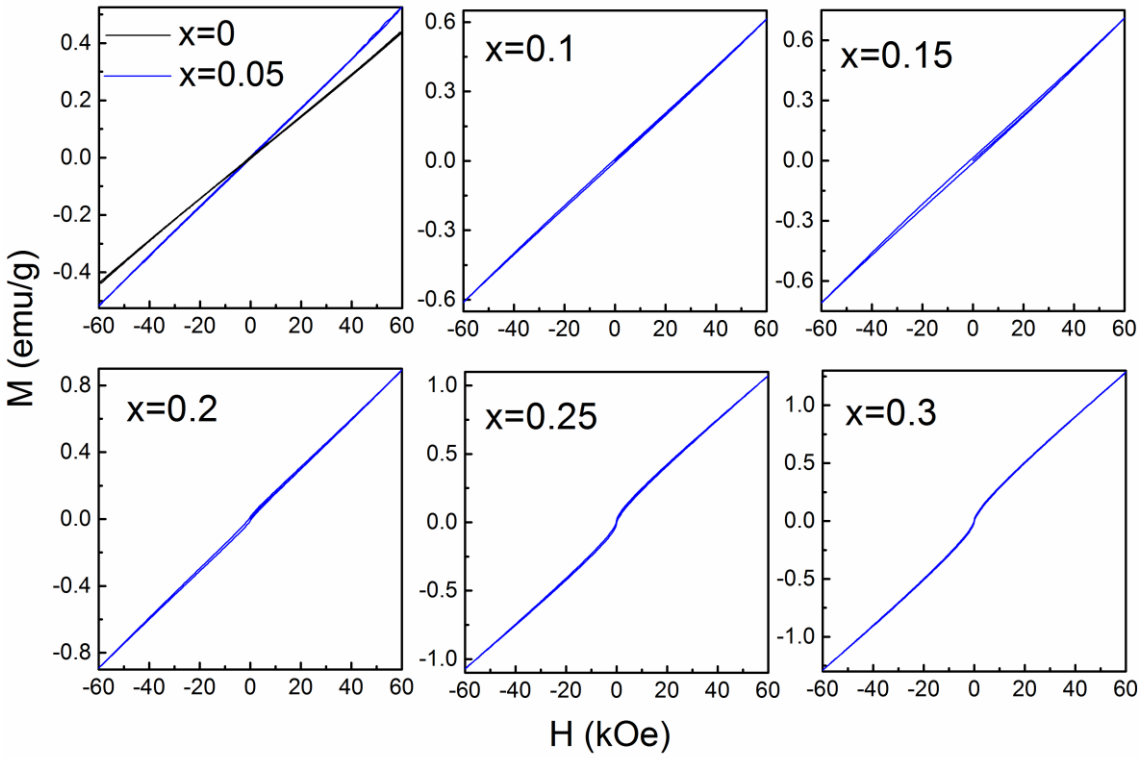

Figure 3.14. Magnetization vs. applied magnetic field curves of $Bi_{1-x}Ba_xFe_{1-x}Mn_xO_3$ measured at room temperature.

The impurity phase observed for $x < 0.2$, $Bi_{25}FeO_{40}$, is paramagnetic at room temperature [26, 27] and hence contribution from this impurity phase to the room temperature magnetization can be ruled out. Therefore, the weak ferromagnetism exhibited by different compositions is due to canted antiferromagnetism caused by the change in Fe-O-Fe bond angle and bond length due to the structural change on substitution [28-30]. Substitution of Bi^{3+} by A^{2+} in $BiFeO_3$ should create either oxygen vacancy and/or Mn^{4+} to preserve charge neutrality. Since Mn^{4+} is a stable oxidation state, Mn should exist only in the Mn^{4+} state in $Bi_{1-x}A_xFe_{1-x}Mn_xO_3$ (considering no oxygen vacancy). Contraction of the unit cell parameters and unit cell volume in all the three co-substituted system (as shown in figure 3.6) indicate the presence of Mn^{4+} in the co-substituted samples whereas the Raman bands around 480 cm^{-1} corresponding to the Jahn-Teller distortion in the compositions indicate the presence of Mn^{3+}. This suggests the mixed Mn valency in the samples leading to Mn^{3+}-O-Mn^{4+}

ferromagnetic double exchange interaction, as in the case of substituted rare earth manganites [31]. This can also contribute to the weak ferromagnetism exhibited by the Ca/Sr/Ba and Mn co-substituted $BiFeO_3$.

The magnetic parameters obtained from the room temperature magnetization curves are plotted as a function of *x* in $Bi_{1-x}A_xFe_{1-x}Mn_xO_3$ as shown in figure 3.16. For all the three systems, remanence and coercivity increase with increasing level of substitution, showing a maximum value at $x = 0.15$ and then decreases at higher values of *x*. Among the three different systems, the Ca-Mn substituted compositions show higher coercivity and remanence and the values decrease in the order Ca-Mn > Sr-Mn > Ba-Mn, corresponding the ionic size of the divalent alkaline earth metal ion. A linear increase is observed for the magnetization at 60 kOe with an increase in the substitution percentage. It is interesting to note that even in the case of the magnitude of magnetization at the highest measuring field, Ca-Mn system shows an anomaly around $x = 0.15$ which is the *R3c* to *Pbnm* structural transition region. Such an MPB assisted enhanced or anomalous magnetic properties are reported in many substituted BFO-based systems [32-35].

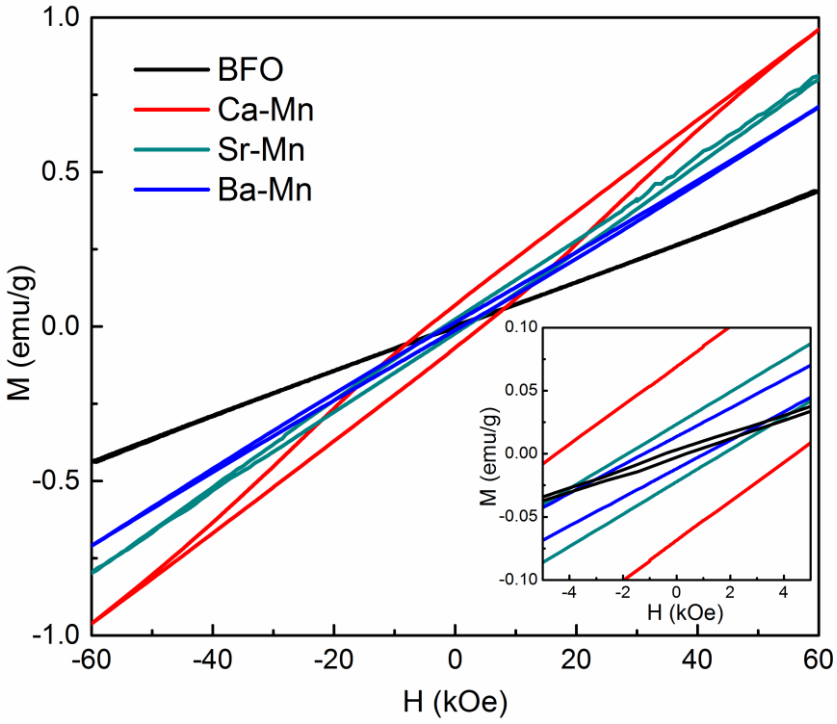

Figure 3.15. Room temperature M-H curves of $Bi_{1-x}A_xFe_{0.85}Mn_{0.15}O_3$ (A = Ca, Sr, Ba). The inset shows the zoomed curves at low magnetic fields.

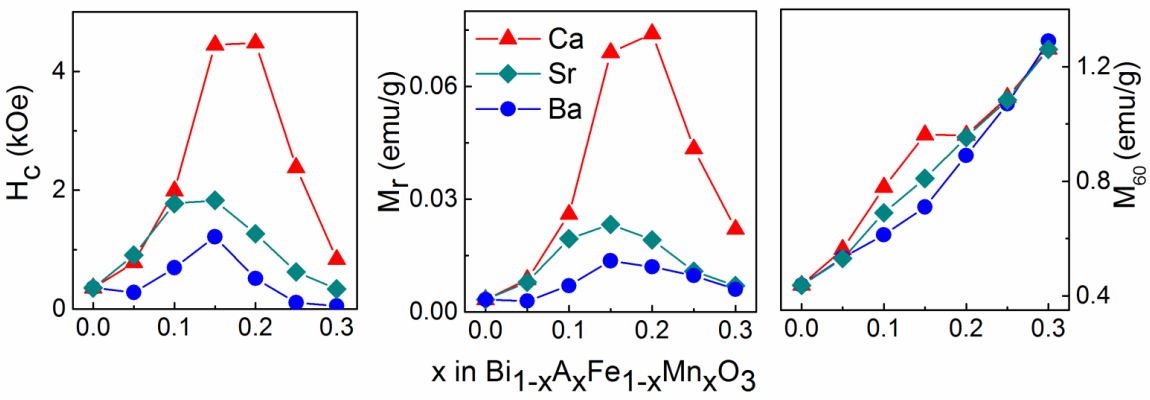

Figure 3.16. The room temperature magnetic parameters, coercivity (H_c), remnant magnetization (M_r) and magnetization at 60 kOe (M_{60}), as a function of *x* in $Bi_{1-x}A_xFe_{1-x}Mn_xO_3$ (A = Ca, Sr, Ba).

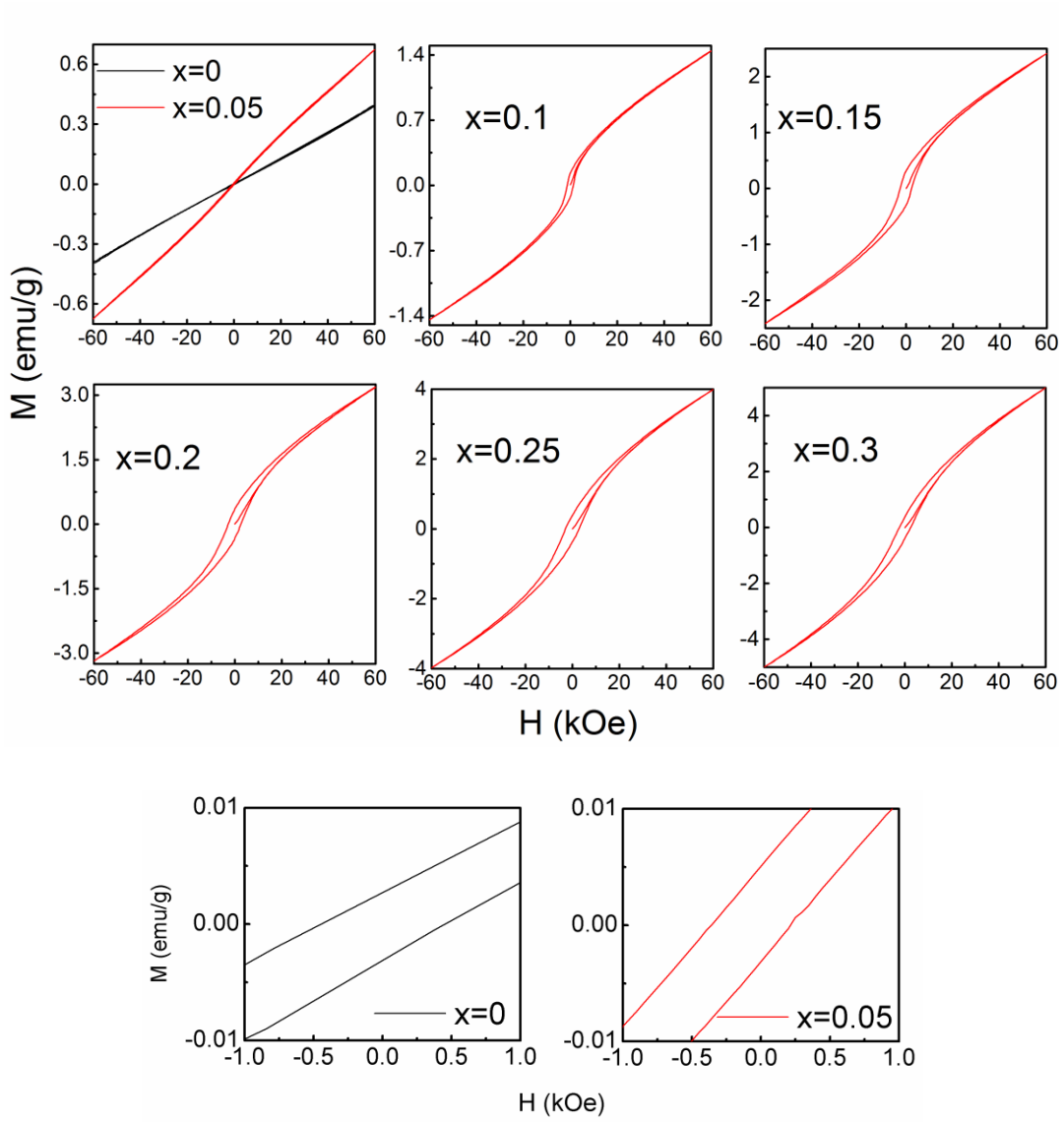

Figure 3.17. Magnetization vs. applied magnetic field curves of $Bi_{1-x}Ca_xFe_{1-x}Mn_xO_3$ at 5 K. The graphs at the bottom show the zoomed magnetization curves for $x = 0$ and $x = 0.05$

The weak ferromagnetism shown by the co-substituted samples is possibly arising from the various exchange interactions involving Fe^{3+}, Mn^{3+}, Mn^{4+}, oxygen vacancy as well as suppression of spiral spin cycloidal structure leading to canted antiferromagnetism. Since the observed changes in the magnetic parameters correlate with the size of the divalent substituted cation at the Bi-site, it can be concluded that the structural distortions on substitution are responsible for the observed weak ferromagnetism.

The M-H curves measured at 5 K for the co-substituted systems are shown in figures 3.17 to 3.19. Unsubstituted BFO shows antiferromagnetic nature with almost zero remanence. At 5 K, BFO shows a magnetization of 0.4 emu/g with a coercivity of 450 Oe. Upon co-substitution, the magnetization increases for co-substituted systems with increase in co-substitution percentage. The x = 0.05 compositions in all the three systems show similar low-temperature hysteresis curve as that of BFO with the magnitude of magnetization at the highest field almost doubled. A lower coercivity and remanence are observed for x = 0.05 than that of unsubstituted BFO. For $x \geq 0.1$, very high values of magnetization are obtained for the co-substituted systems with large hysteresis loops similar to that of a ferromagnetic system. x = 0.3 compositions show almost ten times higher values of magnetization (≈5 emu/g) than BFO.

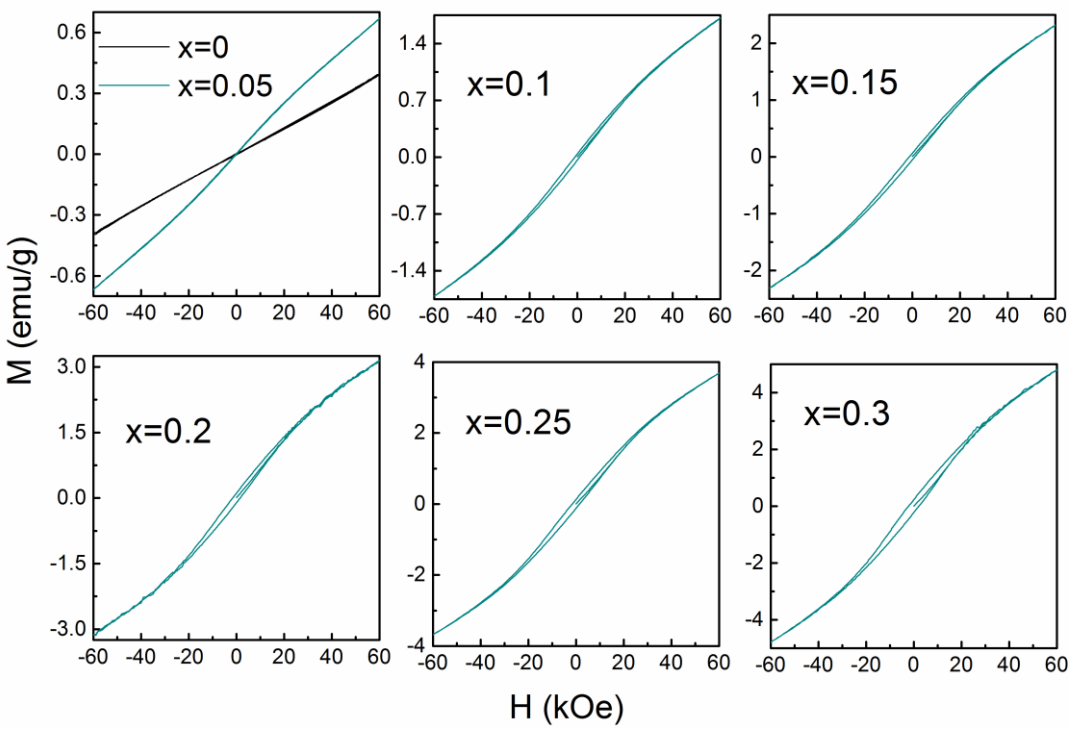

Figure 3.18. Magnetization vs. applied magnetic field curves of $Bi_{1-x}Sr_xFe_{1-x}Mn_xO_3$ at 5 K.

As in the case of the RT magnetization curves, at 5 K also a larger hysteresis loop is observed for the Ca-Mn system.

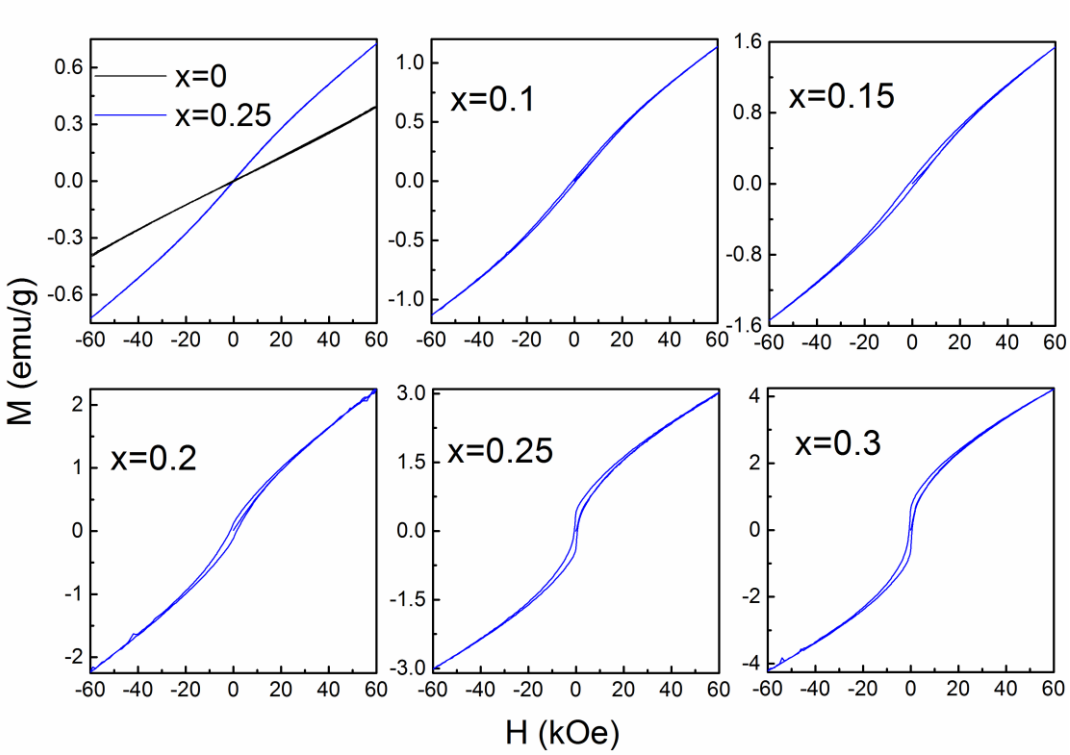

Figure 3.19. Magnetization vs. applied magnetic field curves of $Bi_{1-x}Ba_xFe_{1-x}Mn_xO_3$ at 5 K.

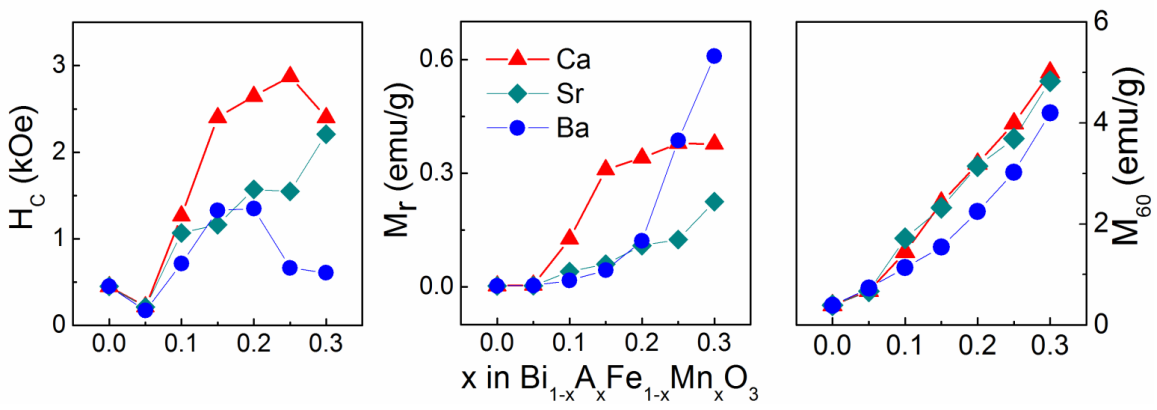

Figure 3.20. The coercivity (H_c), remnant magnetization (M_r) and magnetization at 60 kOe (M_{60}), at 5 K, as a function of *x* in $Bi_{1-x}A_xFe_{1-x}Mn_xO_3$ (A = Ca, Sr, Ba).

The magnetic parameters obtained from the magnetization curves at 5 K are plotted in figure 3.20. The coercivity increases for Ca-Mn and Sr-Mn systems with co-substitution

whereas for Ba-Mn it shows a maximum around $x = 0.15$. Remanence and magnetization at 60 kOe increase with an increase in the substitution level for all the three co-substituted systems. For $x = 0.05$, almost similar magnetic parameters are obtained for the three different co-substituted systems. For $x > 0.15$ a sudden large change in the remanence is observed for the Ba-Mn system. Ca-Mn co-substituted systems show largest magnetic parameters. For Sr-Mn co-substituted system, the magnetic parameters increase with an increase in the substitution content. The anomaly in the coercivity and remanence around $x = 0.15$ at 5 K for the Ca-Mn and Ba-Mn systems is similar to that observed at room temperatures.

3.5.2. M vs. T measurements

To understand the magnetic characteristics of the $Bi_{1-x}A_xFe_{1-x}Mn_xO_3$ co-substituted systems, the temperature dependent magnetization studies have been carried out. Both the zero field cooled (ZFC) and field cooled (FC) magnetization measurements were carried out at an applied magnetic field of 500 Oe in the temperature range of 5 to 300 K (figures 3.21 to 3.23). BFO shows a decrease in the magnetization with decreasing temperature below 300 K, due to the antiferromagnetic nature and showing a small kink around 50 K which is similar to the reported data for the bulk or single crystalline samples [36]. The anomaly around 50 K in MT curves of BFO is attributed to spin glass transition [36,37]. Upon 5% co-substitution in all the three systems, the ZFC and FC curves show a different characteristic. Magnetization increases with decreasing temperature similar to paramagnetic systems with a kink around 50 K which is probably the spin glass transition similar to that reported for BFO. For the Ca-Mn co-substituted system, a broad maximum around 40 K is observed for $x \geq 0.1$. This could be attributed to a spin-glass-like transition. For Sr-Mn co-substitution, such a spin glass transition is observed only for $x \geq 0.2$ and for Ba-Mn co-substitution, for $x \geq 0.15$. The observed spin-glass-like transitions observed for the co-substituted systems can be related to the spin glass transition reported for unsubstituted $BiFeO_3$ at 50 K [36,37].

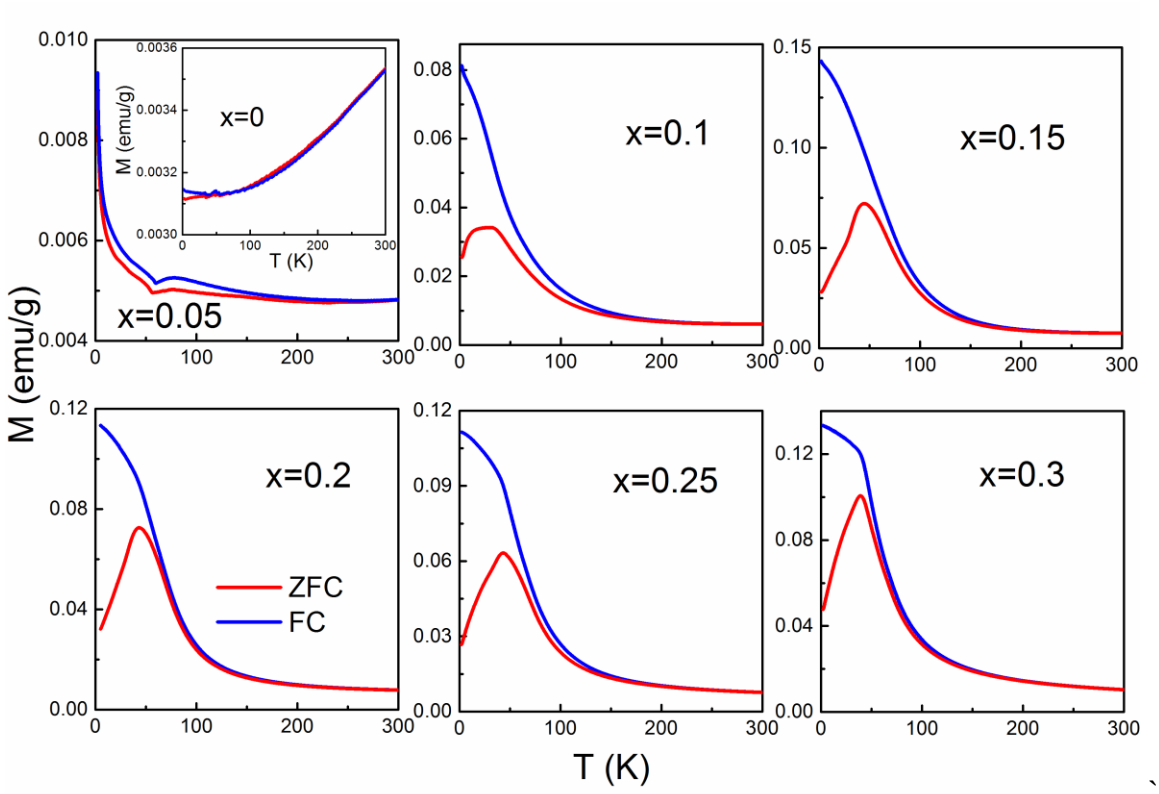

Figure 3.21. ZFC and FC magnetization curves of $Bi_{1-x}Ca_xFe_{1-x}Mn_xO_3$. The inset shows the ZFC and FC curves of BFO (x=0).

The variation in the spin glass transition temperature is likely to be due to the contributions from large structural distortions and the different possible exchange interactions between the different ions involved in the co-substituted systems. In all the co-substituted compositions, the ZFC and FC magnetization curves split around 250 K with the divergence increasing with decreasing temperature. A similar FC/ZFC divergence is reported for $BiFeO_3$ single crystal [36], suggesting the same origin for the substituted systems also.

The spin glass transition temperature, defined as the temperature at which a maximum is observed in the ZFC magnetization curve, T_p, is plotted against the substitution content for the three different co-substituted systems in figure 3.24. In the case of Ca-Mn and Ba-Mn co-substitution, T_p shows a maximum value at x = 0.15 and x = 0.25 respectively. The Ca-Mn and Ba-Mn compositions with $x \geq 0.25$ show almost similar T_p values. The Sr-Mn co-substituted system shows a different trend, where T_p increases with substitution, with a lower value (≈20 K) compared to the Ca-Mn and Ba-Mn systems. Further investigation is needed to comment on this low T_p shown by the Sr-Mn co-substitution.

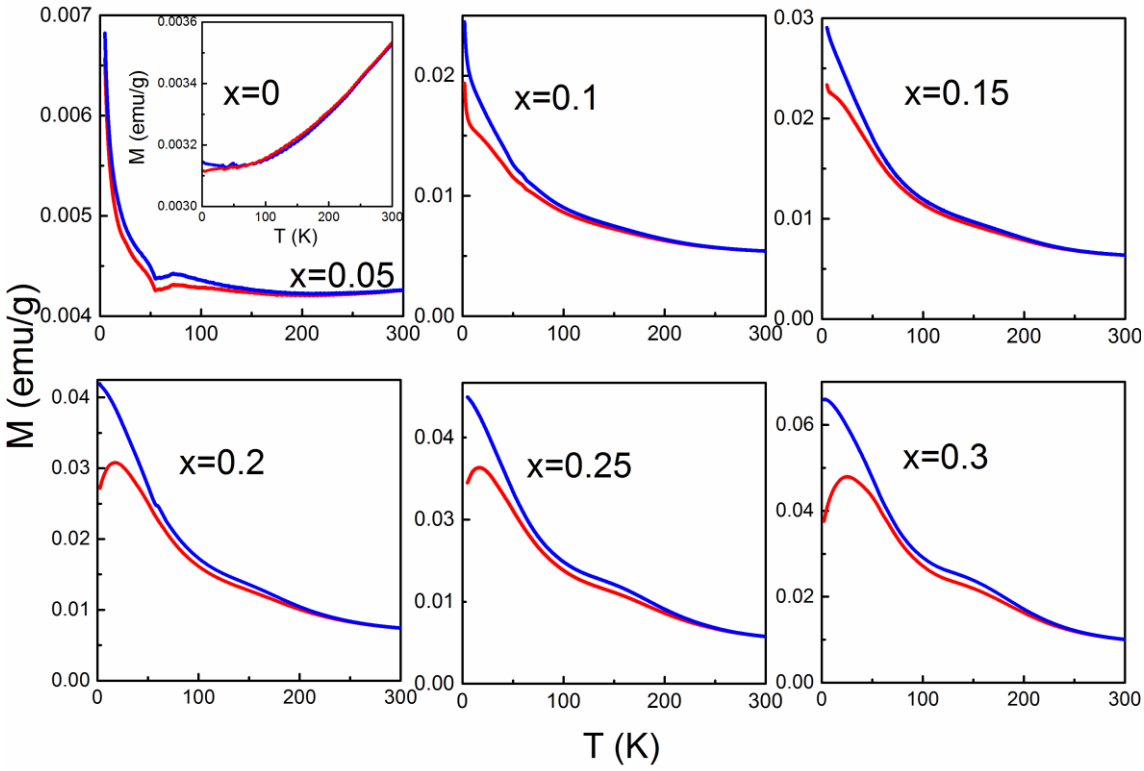

Figure 3.22. ZFC and FC magnetization curves of $Bi_{1-x}Sr_xFe_{1-x}Mn_xO_3$. The inset shows the ZFC and FC curves of BFO (x = 0)

For the Sr-Mn and Ba-Mn co-substituted compositions, a broad magnetic transition like feature, with the divergence of the FC and ZFC magnetizations is observed between 200 and 300 K, suggesting another spin-glass-like phase or a weak ferromagnetic phase in the different compositions. For the Sr-Mn and Ba-Mn compositions, this feature is observed for $x \geq 0.15$ and $x \geq 0.2$, respectively. This feature at a higher temperature is not observed for the Ca-Mn systems.

In $BiFeO_3$, low-temperature magnetic anomalies have been reported at 90, 140, 200 and 250 K [38-42]. The magnetic anomalies at 140 K and 250 K are associated with coupling with electric polarization as suggested by the Raman [38,39,41], dielectric and electromechanical studies [42]. The observed anomalies in the ZFC-FC curves around 250 K for the Ba-Mn co-substituted system and at 140 K for the Sr-Mn co-substituted system are possibly related to these anomalies shown by the unsubstituted BFO. It is possible that the magnetoelectric coupling is enhanced due to the larger structural distortions in Sr-Mn and Ba-Mn systems, due to the larger size of the substituted ions.

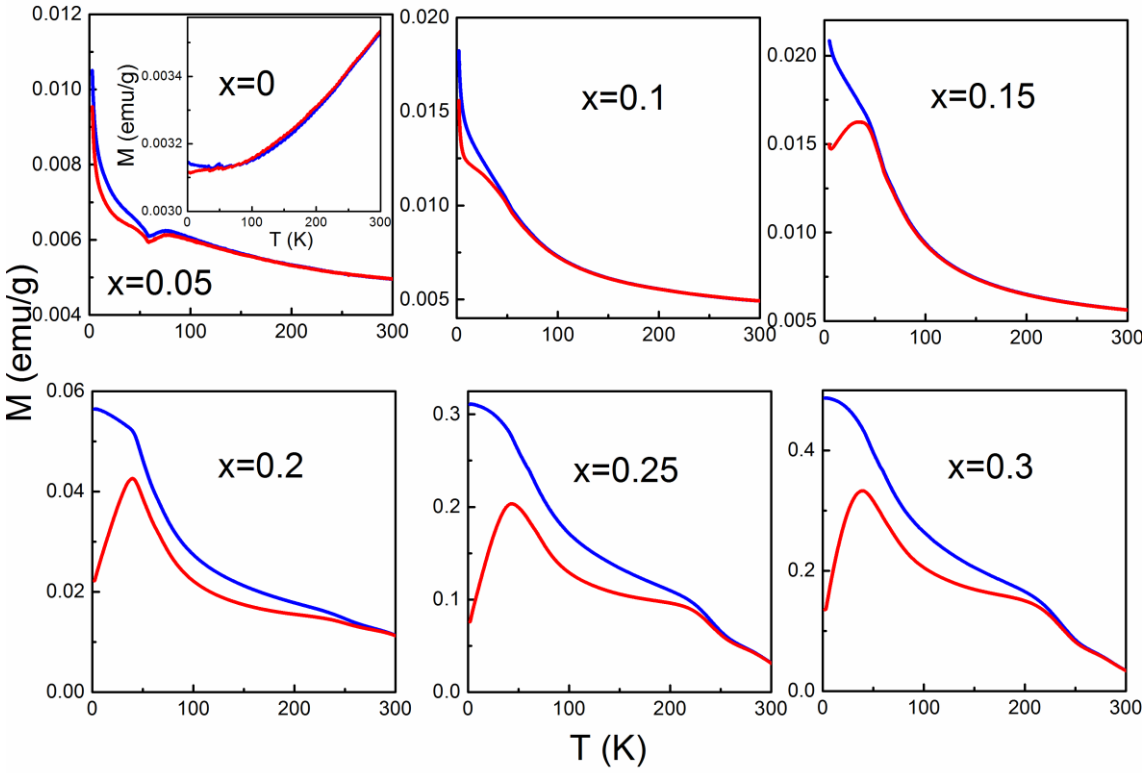

Figure 3.23. ZFC and FC curves of $Bi_{1-x}Ba_xFe_{1-x}Mn_xO_3$. Inset shows the ZFC and FC curves of BFO (*x*=0).

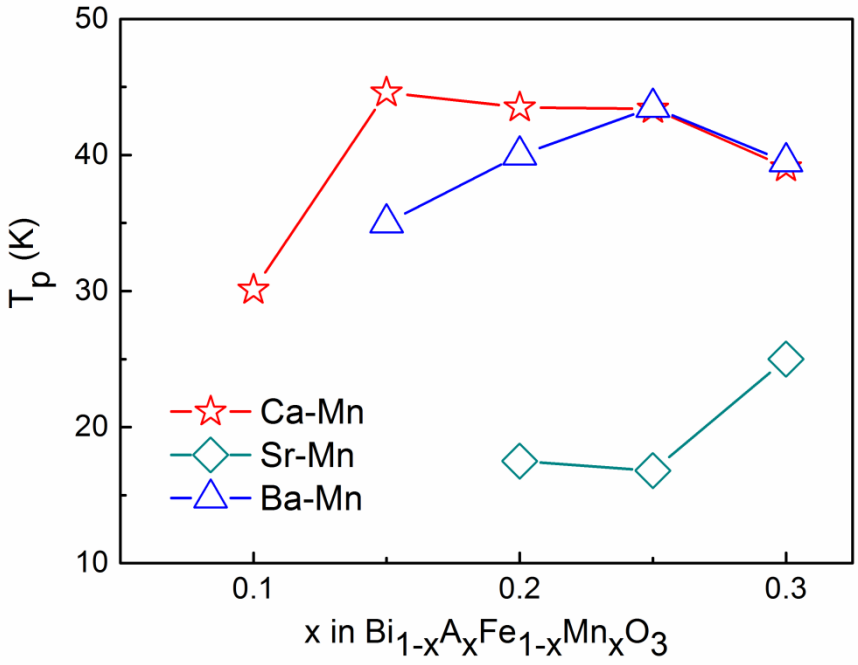

Figure 3.24. Spin glass transition temperature vs. *x* in $Bi_{1-x}A_xFe_{1-x}Mn_xO_3$ (A = Ca, Sr, Ba).

The spin-glass-like transition around 40 K observed for the Ca, Sr, Ba and Mn co-substituted compositions are reported for many similar individual compositions studied. Yin *et al*. [43] have reported this type of spin glass phase in $Bi_{0.8}Ca_{0.2}Fe_{1-x}Mn_xO_3$ and Tzankov *et al*. [44,45] for $Bi_{0.5}Ca_{0.5}Fe_xMn_{1-x}O_3$ and $Bi_{0.5}Sr_{0.5}Fe_xMn_{1-x}O_3$. Divalent ion substituted $BiMnO_3$, and Fe substituted $CaMnO_3/BiMnO_3$ are also known to show spin glass behaviour [46-49]. Fe substituted $CaMnO_3$ shows a spin glass behaviour with a T_p around 40 K. In $CaMn_{1-x}Fe_xO_3$, only for $x \geq 0.35$ spin glass behaviour is observed whereas in $SrMn_{1-x}Fe_xO_3$ $0.2 \leq x \leq 0.7$ compositions showed spin glass behaviour [49,50]. In $SrBiMTiO_6$ (M = Mn, Cr, Fe) perovskites, only Mn substitution gives a spin glass structure whereas chromium and iron substitution showed paramagnetic nature [51]. Possibly, the spin glass nature depends on the size of the substituted atom. Belik *et al*. have studied the $BiMnO_{3+\delta}$ system with varying the oxygen content. As δ is increased, the system started showing spin glass behaviour [52]. Increasing the δ values implies increasing the Mn^{4+} content. The same scenario is expected with a divalent ion substitution, where, due to the increasing Mn^{4+} content, spin-glass-like transition originates. The competing antiferromagnetic and ferromagnetic exchange interactions involving different magnetic ions such as Fe^{3+}, $Mn^{3+,}$ and Mn^{4+} possibly gives rise to a frustrated magnetic system with ferromagnetic and antiferromagnetic clusters leading to spin-glass-like nature.

3.6. Dielectric properties

Dielectric measurements have been carried on all samples in the frequency range of 1 kHz to 1 MHz (Figures 3.25 to 3.27). Compositions in all three series with $x > 0.25$ showed a high dielectric loss an hence measurements are not carried out for these compositions. The dielectric constant decreases with increasing frequency and becomes almost constant at higher frequencies. Variations of the dielectric constant at 10 kHz for the three different systems are plotted against x in figure 3.28. The Ca-Mn system shows higher dielectric constant than the Ba-Mn and Sr-Mn systems. For the Ca-Mn system, dielectric constant increases with x and reaches a maximum at $x = 0.15$, which is the *R3c* to *Pbnm* structural transition region, and then decreases. Sr-Mn co-substituted samples show a decrease in dielectric value showing an anomaly at $x = 0.1$ where *R3c* to $R\bar{3}c$ structural change occurs. $R\bar{3}c$ being a centrosymmetric space group, has no contribution towards ferroelectricity. Thus, decrease in the dielectric constant for $x > 0.1$ is due to the increase in the nonpolar $R\bar{3}c$ phase

content as observed from the XRD results as explained in section 3.3. Ba-Mn co-substituted samples shows a decrease in the dielectric constant till x = 0.15 and then becomes almost constant, though the Ba-Mn co-substituted samples show only the *R3c* phase till x = 0.2 and above which it is a mixture of the *R3c* and *P4mm* phases. The *P4mm* phase is non-centrosymmetric ferroelectric space group and thus should enhance the ferroelectric and dielectric properties. No anomaly in the dielectric constant was observed for the Ba-Mn co-substituted system at the *R3c* to *P4mm* structural transition region as shown by the Ca-Mn and Sr-Mn co-substituted systems. Dielectric properties also depend on the grain size and distribution. With decreasing grain size the dielectric constant decreases [53,54]. As evidenced from the SEM microstructural studies, low level substituted samples have large fused grains and compositions with higher levels of substitution have smaller grains. Thus, the decrease in the dielectric constant with increase in the co-substitution content is likely to be due to this grain size effect.

The higher dielectric constant of the Ca-Mn compositions could be due to the enhanced ferroelectric polarization, especially in the MPB region. Such enhanced ferroelectric properties in the MPB region have been reported for substituted $BiFeO_3$ [33,55-56]. Sun *et al.* [56] have reported higher piezoelectric properties around x = 0.1 in $Bi_{1-x}Sm_xFeO_3$ thin films, wherein rhombohedral to orthorhombic structural transition occurs. Troyanchuk *et al*. [33] also reported such an enhanced piezoresponse in $Bi_{1-x}La_xFeO_3$ around the MPB region. Enhanced piezoelectric properties are related to the enhanced ferroelectric properties in the MPB region.

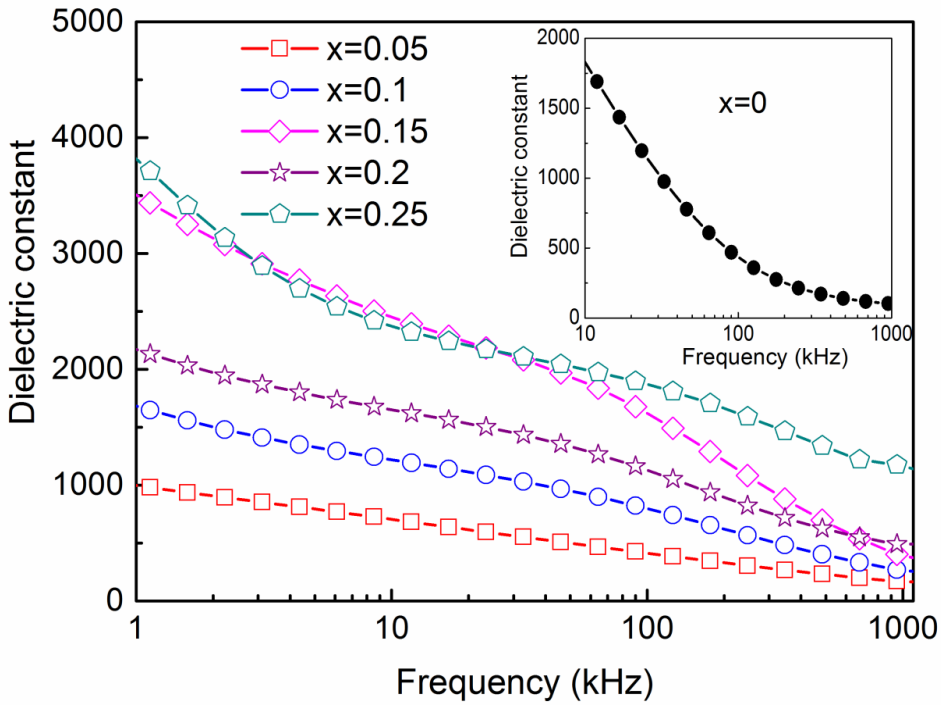

Figure 3.25. Dielectric spectra of $Bi_{1-x}Ca_xFe_{1-x}Mn_xO_3$. The inset shows the dielectric spectra of BFO (x = 0).

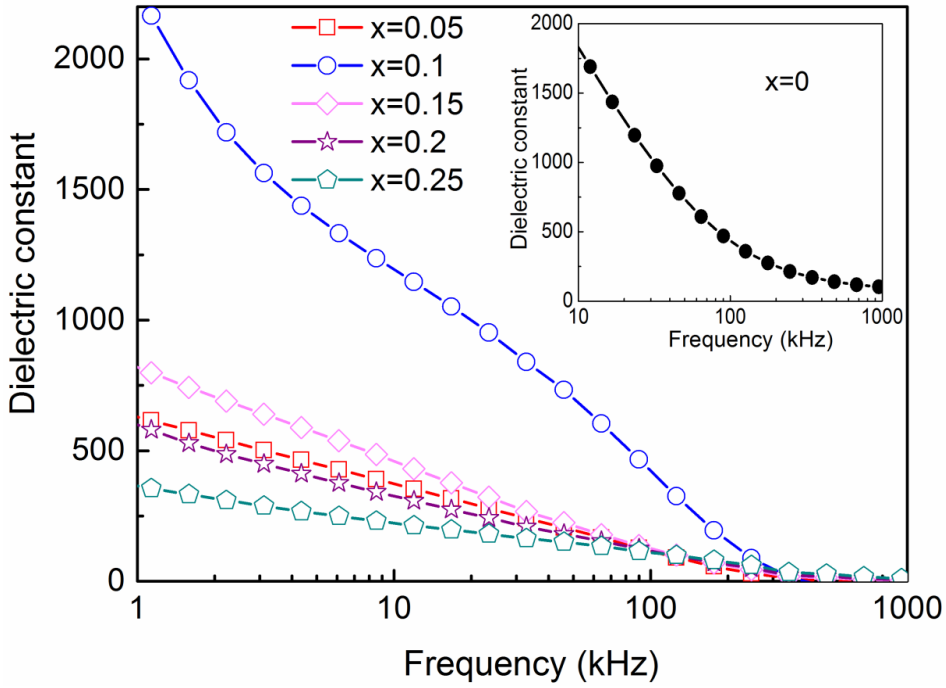

Figure 3.26. Dielectric spectra of $Bi_{1-x}Sr_xFe_{1-x}Mn_xO_3$. The inset shows the dielectric spectra of BFO (x = 0).

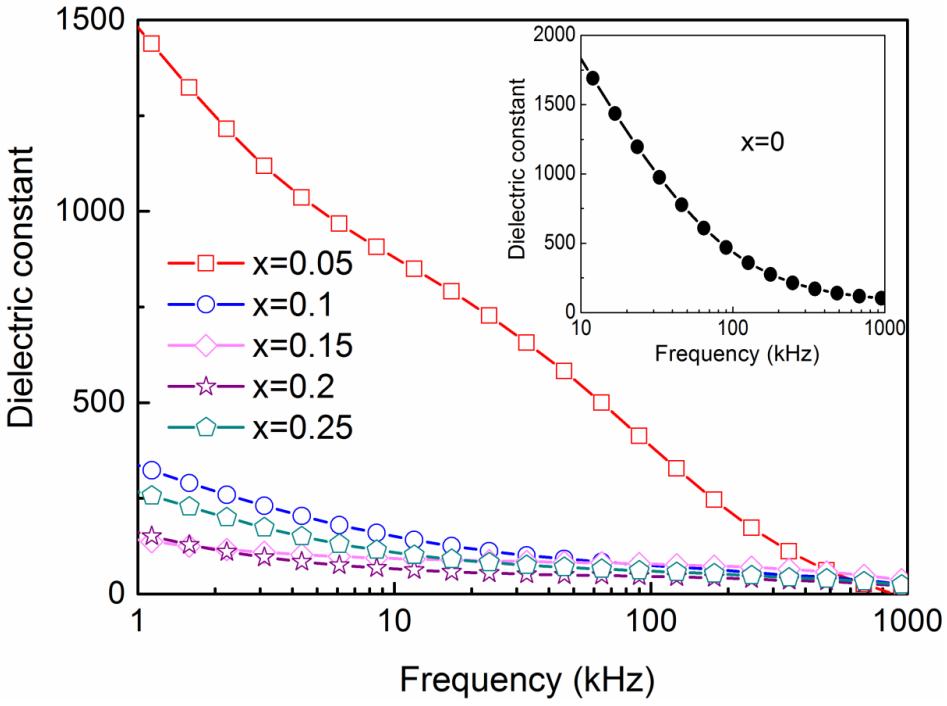

Figure 3.27. Dielectric spectra of $Bi_{1-x}Ba_xFe_{1-x}Mn_xO_3$. The inset shows the dielectric spectra of BFO (x = 0).

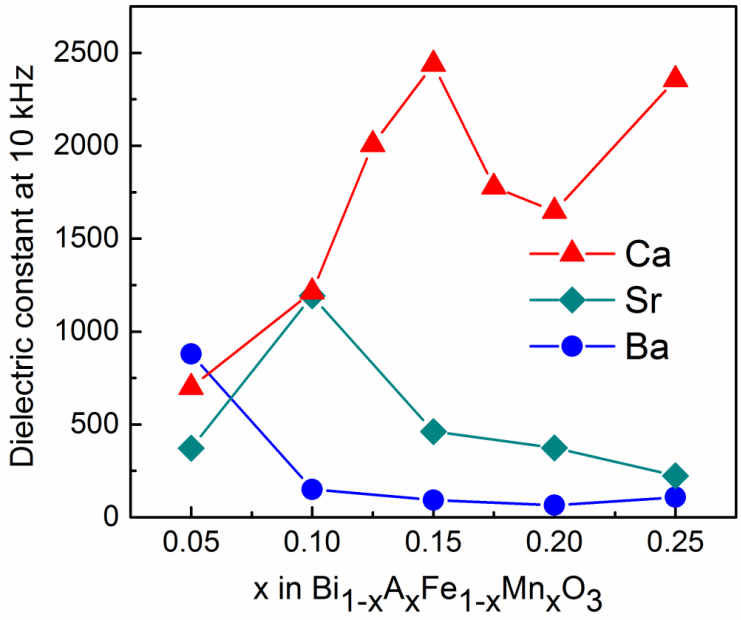

Figure 3.28. Dielectric constant at 10 kHz vs. x in $Bi_{1-x}A_xFe_{1-x}Mn_xO_3$ (A = Ca, Sr, Ba).

The divalent ion and Mn co-substituted $BiFeO_3$ exhibits enhanced magnetic and dielectric properties than the unsubstituted $BiFeO_3$. Among the three co-substituted systems analysed, Ca-Mn co-substituted compositions show better magnetic and dielectric properties.

Enhanced magnetic and dielectric properties around x = 0.15 in the $Bi_{1-x}A_xFe_{1-x}Mn_xO_3$ is possibly due to increased Fe-O-Fe bond angle and Fe-O bond distance enhancing the canted antiferromagnetism and due to the effective suppression of cycloidal spin structure. Thus, Ca-Mn co-substituted compositions around the MPB region (x = 0.15) is a promising candidate for magnetoelectric device applications due to the larger magnetic and dielectric properties.

3.7. Conclusions

Alkaline earth metal and manganese co-substituted $BiFeO_3$ compositions with the general formula, $Bi_{1-x}A_xFe_{1-x}Mn_xO_3$ are prepared by solid state method and their structural, magnetic and dielectric properties are studied, for x = 0.05, 0.1, 0.15, 0.2 and 0.3, to compare the influence of size effect of the alkaline earth metal ion on the properties. Rietveld refinement analysis of the XRD patterns revealed rhombohedral structure (space group: *R3c*) for $x \leq 0.1$ and orthorhombic structure (space group: *Pbnm*) for $x \geq 0.2$ and an *R3c–Pbnm* mixed phase for intermediate compositions in the Ca-Mn co-substituted system. Sr-Mn system shows *R3c* phase for $x \leq 0.05$, and *R3c–R*$\bar{3}$*c* mixed rhombohedral phase for $x \geq 0.1$, whereas the Ba-Mn system shows *R3c* phase till x = 0.2 and above which it shows a mixed structure with tetragonal *P4mm* phase. These structural transitions are further confirmed by Raman spectral analysis. Room temperature M-H curves showed that the samples have antiferromagnetic behaviour with weak ferromagnetic characteristics. At room temperature, high coercivity and remanence are observed at x = 0.15 for all three co-substituted systems. Low-temperature magnetization studies revealed spin-glass-like behaviour for the compositions at higher levels of co-substitution. In all the three systems, both the room temperature and low-temperature magnetization increases with increase in the amount of co-substitution. Ca-Mn co-substituted compositions show better magnetic and dielectric parameters than the Ba-Mn and Sr-Mn co-substituted compositions. The weak ferromagnetism shown by the different compositions is possibly by the combined effect of the weak ferromagnetism induced by the structural distortions which destroy the spin cycloid apart from the possible Mn^{3+}-Mn^{4+} double exchange interaction. Higher dielectric properties were also observed for Ca-Mn system (with a maximum around x = 0.15) than the Ba-Mn and Sr-Mn systems. Higher magnetic and dielectric properties around x = 0.15 suggest higher magnetoelectric coupling for the Ca-Mn system.

References

[1] Khomchenko V A, Kiselev D A, Vieira J M, Jian L, Kholkin A L, Lopes A M, Pogorelov Y G, Araujo J P and Maglione M 2008 *J. Appl. Phys.* **103** 024105

[2] Kothari D, Reddy V R, Sathe A G V, Banerjee A, Gupta S M and Awasthi A M 2007 *Appl. Phys. Lett.* **91** 202505

[3] Yang C H, Koo T Y and Jeong Y H 2005 *Solid State Commun*. **134** 299

[4] Azuma M, Kanda H, Belik A A, Shimakawa Y and Takano M 2007 *J. Magn. Magn. Mater*. **310** 1177

[5] Troyanchuk I O, Karpinskiĭ D V, Bushinskiĭ M V, Chobot A N, Pushkarev N V, Prohnenko O, Kopcewicz M and Szymczak R 2009 *Crystallogr. Rep.* **54** 1172

[6] Huang J-Z, Shen Y, Li M and Nan C-W 2011 *J. Appl. Phys.* **110** 094106

[7] Rout J and Choudhary R N 2016 *Phys. Lett.* **380** 288

[8] Kumar K S, Venkateswaran C, Kannan D, Tiwari B and Rao M R 2012 *J. Phys. D: Appl. Phys.* **45** 415302

[9] Shannon R D 1976 *Acta Cryst. A* **32** 751

[10] Poeppelmeier K R, Leonowicz M E, Scanlon J C, Longo J M and Yelon W B 1982 *J. Solid State Chem.* **45** 71

[11] Kuroda K, Ishizawa N, Mizutani N and Kato M 1981 *J. Solid State Chem.* **38** 297

[12] Negas T and Roth R S 1970 *J. Solid State Chem.* **1** 409

[13] Chamberland B L, Sleight A W and Weiher J F 1970 *J. Solid State Chem.* **1** 506

[14] Belik A A, Matsushita Y, Katsuya Y, Tanaka M, Kolodiazhnyi T, Isobe M and Takayama-Muromachi E 2011 *Phys. Rev.* B **84** 094438

[15] Negas T and Roth R S 1971 *J. Solid State Chem.* **3** 323

[16] Adkin J J and Hayward M A 2007 *Chem. Mater.* **19** 755

[17] Haumont R, Kreisel J, Bouvier P and Hippert F 2006 *Phys. Rev.* B **73** 132101

[18] Fukumura H, Harima H, Kisoda K, Tamada M, Noguchi Y and Miyayama M 2007 *J. Magn. Magn. Mater*. **310** e367

[19] Martín-Carrón L, De Andres A, Martínez-Lope M J, Casais M T and Alonso J A 2002 *Phys. Rev. B.* **66** 174303

[20] Lahmar A, Habouti S, Dietze M, Solterbeck CH and Es-Souni M 2009 *Appl. Phys. Lett*. **94** 12903

[21] Bielecki J, Svedlindh P, Tibebu D T, Cai S, Eriksson S G, Börjesson L and Knee C S 2012 *Phys. Rev.* B **86** 184422

[22] Varshney D, Kumar A and Verma K 2011 *J. Alloys Compd.* **509** 8421

[23] Ghosh A K, Dwivedi G D, Chatterjee B, Rana B, Barman A, Chatterjee S and Yang H D 2013 *Solid State Comm.* **166** 22

[24] Gupta S, Tomar M and Gupta V 2013 *J. Exp. Nanosci.* **8** 261

[25] Fukumura H, Matsui S, Tonari N, Nakamura T, Hasuike N, Nishio K, Isshiki T, Harima H and Kisoda K 2009 *Acta Phys. Pol.* **116** 47

[26] Nalwa K S and Garg A 2008 *J. Appl. Phys.* **103** 044101

[27] Chen Y, Wu Q and Zhao J 2009 *J. Alloys Compd.* **487** 599

[28] Kumar M M, Srinath S, Kumar G S and Suryanarayana S V 199*8 J. Magn. Magn. Mater***. 188** 203

[29] Ederer C and Spaldin N A 2005 *Phys. Rev.* B **71** 060401

[30] Kumar M and Yadav K L 2006 *J. Appl. Phys.* **100** 74111

[31] Coey J M, Viret M and Von Molnar S 2009 *Adv. Phys.* **58** 571

[32] Yuan G L, Or S W and Chan H L 2007 *J. Phys. D: Appl. Phys*. **40** 1196

[33] Troyanchuk I O, Karpinsky D V, Bushinsky M V, Khomchenko V A, Kakazei G N, Araujo J P, Tovar M, Sikolenko V, Efimov V and Kholkin A L 2011 *Phys. Rev.* B **83** 054109

[34] Thakuria P and Joy P A 2012. *Solid State Commun.* **152** 1609

[35] Karpinsky D V, Troyanchuk I O, Zheludkevich A L, Ignatenko O V, Silibin M V and Sikolenko V V 2016 *Phys. Solid State* **58** 1590

[36] Singh M K, Prellier W, Singh M P, Katiyar R S and Scott J F 2008 *Phys. Rev.* B **77** 144403

[37] Singh M K, Katiyar R S, Prellier W and Scott J F 2008 *J. Phys. Condens. Matter.* **21** 042202

[38] Scott J F, Singh M K and Katiyar R S 2008 *J. Phys. Condens. Matter.* **20** 322203

[39] Singh M K, Katiyar R S and Scott J F 2008 *J. Phys. Condens. Matter.* **20** 252203

[40] Vijayanand S, Mahajan M B, Potdar H S and Joy P A 2009 *Phys. Rev.* B **80** 064423

[41] Cazayous M, Gallais Y, Sacuto A, De Sousa R, Lebeugle D and Colson D 2008 *Phys. Rev. Lett.* **101** 037601

[42] Redfern S A, Wang C, Hong J W, Catalan G and Scott J F 2008 *J. Phys. Condens. Matter*. **20** 452205

[43] Yin L H, Sun Y P, Zhang F H, Wu W B, Luo X, Zhu X B, Yang Z R, Dai J M, Song W H and Zhang R L 2009 *J. Alloys Compd.* **488** 254

[44] Tzankov D, Kovacheva D, Krezhov K, Puźniak R, Wiśniewski A, Sváb E and Mikhov M 2005 *J. Phys. Condens. Matter*. **17** 4319

[45] Tzankov D, Kovacheva D, Krezhov K, Puźniak R, Wiśniewski A, Sváb E and Mikhov M 2008 *J. Appl. Phys.* **103** 053910

[46] Troyanchuk I O, Mantytskaya O S and Chobot A N 2002 *Phys. Solid State* **44** 2266

[47] Troyanchuk I O, Karpuk M K, Mantytskaya O S and Szymczak H 2004 *Crystallogr. Rep.* **49** 626

[48] Mantytskaya O S, Troyanchuk I O, Chobot A N and Szymczak H 2004 *Low Temp. Phys.* **30** 218

[49] Liu X J, Li Z Q, Wu P, Bai H L and Jiang E Y 2007 *Solid State Commun*. **142** 525

[50] Kolesnik S, Dabrowski B, Mais J, Brown D E, Feng R, Chmaissem O, Kruk R and Kimball C W 2003 *Phys. Rev.* B **67** 144402

[51] Yao C, Meng F, Liu X, Han L, Meng J, Liang Q and Meng J 2014 *Ceram. Int.* **40** 13339

[52] Belik A A, Kolodiazhnyi T, Kosuda K and Takayama-Muromachi E 2009 *J. Mater. Chem.* C **19** 1593

[53] Tang X G, Wang J, Wang X X and Chan H L 2004 *Solid State Commun*. **131** 163

[54] Zhao Z, Buscaglia V, Viviani M, Buscaglia M T, Mitoseriu L, Testino A, Nygren M, Johnsson M and Nanni P 2004 *Phys. Rev.* B **70** 024107

[55] Zhang S T, Pang L H, Zhang Y, Lu MH and Chen Y F 2006 *J. Appl. Phys.* **100** 114108

[56] Sun W, Li J F, Yu Q and Cheng L Q 2015 *J. Mater. Chem. C* **3** 2115

Chapter 4

Structure-property correlation of $Bi_{1-x}Ca_xFe_{1-x}Mn_xO_3$ near the MPB region

4.1. Introduction

In **chapter 3**, we have discussed the structural, magnetic and dielectric properties of $Bi_{1-x}A_xFe_{1-x}Mn_xO_3$ (A = Ca, Sr, and Ba). The comparative studies on the three co-substituted systems showed that the Ca-Mn co-substituted system exhibits better magnetic and dielectric properties than the Sr-Mn and Ba-Mn co-substituted series. Ca^{2+} has almost the same size as that of Bi^{3+} whereas Sr^{2+} and Ba^{2+} ions are larger than Bi^{3+}. Thus, the comparable sizes of Bi^{3+} and Ca^{2+} ions possibly give better structural stability for the Ca-Mn co-substituted system. Also, it was found that all the three systems show enhanced properties around $x \approx 0.15$. For the Ca-Mn co-substituted system $x \approx 0.15$ is in the rhombohedral (space group: *R3c*) to orthorhombic (space group: *Pbnm*) structural transition region. At $x = 0.15$, a mixed phase of rhombohedral and orthorhombic phases is found to coexist.

To understand the structural phase transition in detail in the Ca-Mn co-substituted system, we have carried out a systematic study involving a large number of compositions of bulk $Bi_{1-x}Ca_xFe_{1-x}MnO_3$ (BCFMO) for $0 \leq x \leq 0.4$, in the MPB region, using powder X-ray diffraction, Raman spectroscopy, and XPS. The magnetic, dielectric and magnetodielectric properties are studied, and the correlations between the structure and properties are carried out.

Calcium and manganese co-substituted bismuth ferrite bulk samples, with the general formula $Bi_{1-x}Ca_xFe_{1-x}Mn_xO_3$ (x = 0, 0.05, 0.08, 0.1, 0.11, 0.12, 0.125, 0.15, 0.175, 0.2, 0.25, 0.3, 0.4), were prepared by the solid-state reaction method as described chapter 2, section 2.1. The as-prepared samples were ground well and used for X-ray diffraction, magnetic measurements, Raman spectroscopy, microstructural studies. Mn^{4+} content in the samples was determined by redox titrations, as explained in chapter 2, section 2.8.

4.2. Structure

Figure 4.1 shows comparison of the powder XRD patterns of $Bi_{1-x}Ca_xFe_{1-x}Mn_xO_3$ for x = 0, 0.1, 0.2, 0.3 and 0.4. Simulated patterns of $BiFeO_3$ for the reported rhombohedral [1] and orthorhombic [2] structures are shown in the figure for comparison. Magnified views of the selected peaks in the XRD patterns of different compositions are shown in figure 4.2. Figure 4.2(a) shows the 2θ region where the most intense peak is observed. The peaks in this region correspond to the rhombohedral structure for $x < 0.2$ and orthorhombic structure for $x \geq 0.2$. Figure 4.2(b) shows the emergence of the (111) reflection of the orthorhombic phase in

the pattern for x = 0.12 and above. Similarly, figure 4.2(c) shows the (104) and (110) reflections from the rhombohedral structure up to x = 0.175. Thus, figure 4.2 suggests the co-existence of the rhombohedral (*R3c*) and orthorhombic (*Pbnm*) phases in the compositional region $0.12 \leq x \leq 0.175$.

Rietveld refinement analysis of the XRD patterns of all the compositions is carried out considering rhombohedral phase for $x < 0.12$, orthorhombic phase for $x \geq 0.2$ and mixture of the two phases for $0.12 \leq x \leq 0.175$. The results of the refinement are shown in figure 4.3 for selected compositions. Inset of figure 4.3(b) shows the fits of the most intense peak of x = 0.15 using only the *R3c* structure and using both *R3c* and *Pbnm* structures. It is clear that using *R3c*+*Pbnm* mixed phase gives a better fit. Percentage of the *R3c* phase obtained from the Rietveld analysis is shown in figure 4.3(d) as a function of x.

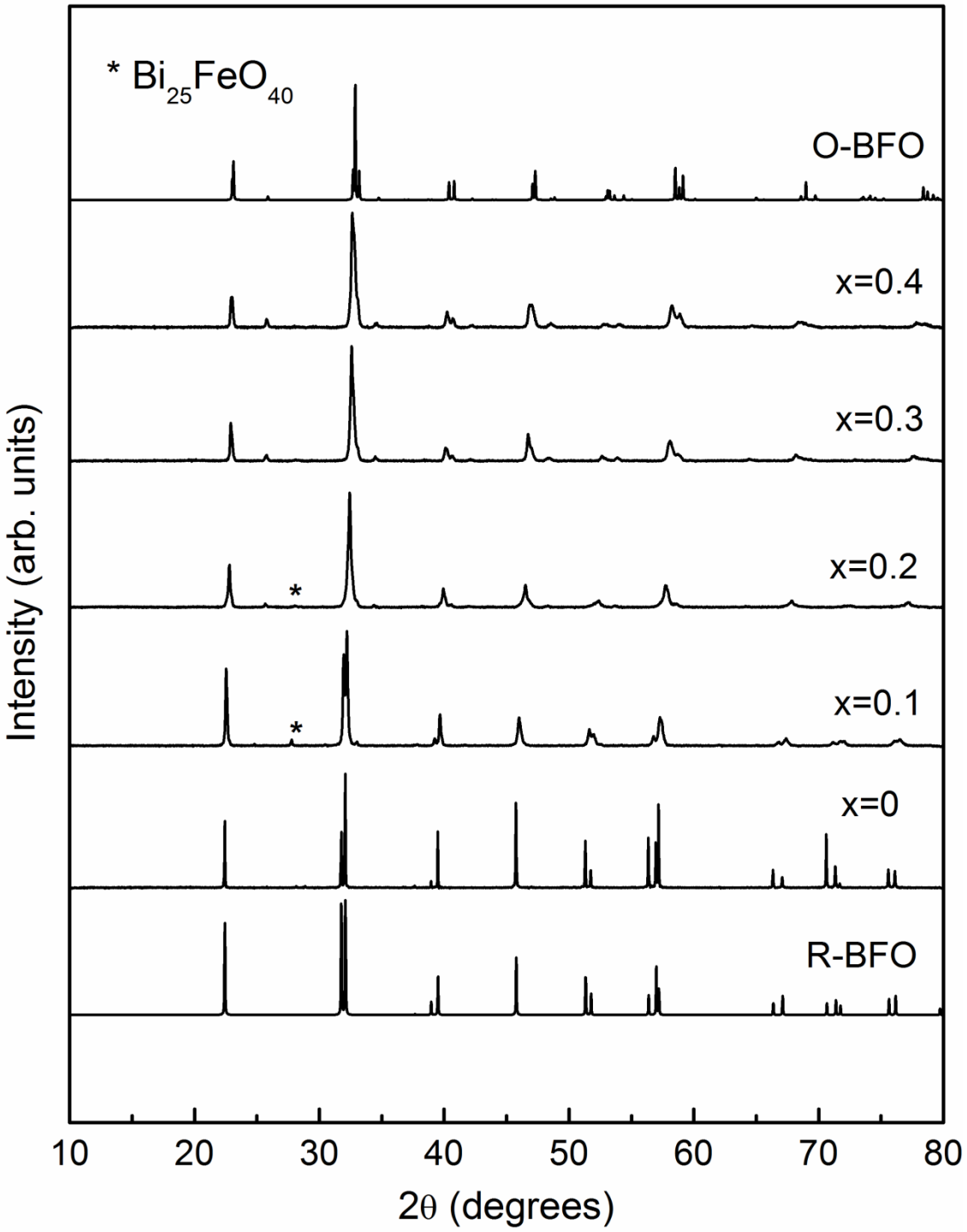

Figure 4.1. Powder X-ray diffraction patterns of $Bi_{1-x}Ca_xFe_{1-x}Mn_xO_3$. The simulated patterns of $BiFeO_3$ for the rhombohedral (R-BFO) and orthorhombic (O-BFO) structures are compared at the bottom and top, respectively. The peak from the impurity phase $Bi_{25}FeO_{40}$ is marked using the symbol '*'.

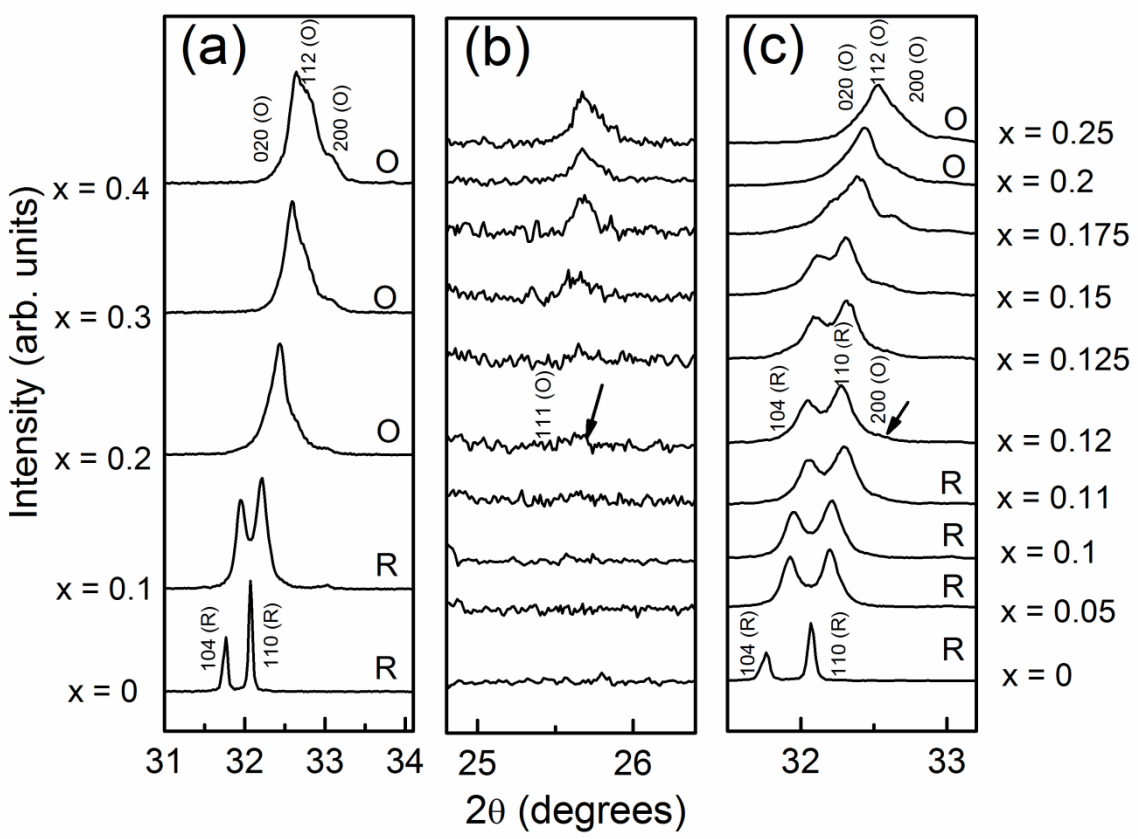

Figure 4.2. Magnified view of the XRD patterns of $Bi_{1-x}Ca_xFe_{1-x}Mn_xO_3$. (a) Selected compositions showing the peaks for rhombohedral (R) and orthorhombic (O) phases, (b) and (c) show patterns for close compositions.

Variation of the lattice parameters and unit cell volume, obtained from the refinement analysis, as a function of *x*, is shown in figure 4.4. The shaded region in the figures indicates the mixed phase region ($0.12 \leq x \leq 0.175$) in the system where the *R3c* and *Pbnm* phases co-exist. Lattice parameters are found to decrease with increasing substitution in both the rhombohedral as well as the orthorhombic region. The decreasing lattice parameters, as well as the unit cell volume, are due to the relatively smaller size of Ca^{2+} compared to that of Bi^{3+} as well as the smaller ionic size of Mn^{4+} compared to that of Fe^{3+}, as discussed in the previous chapter.

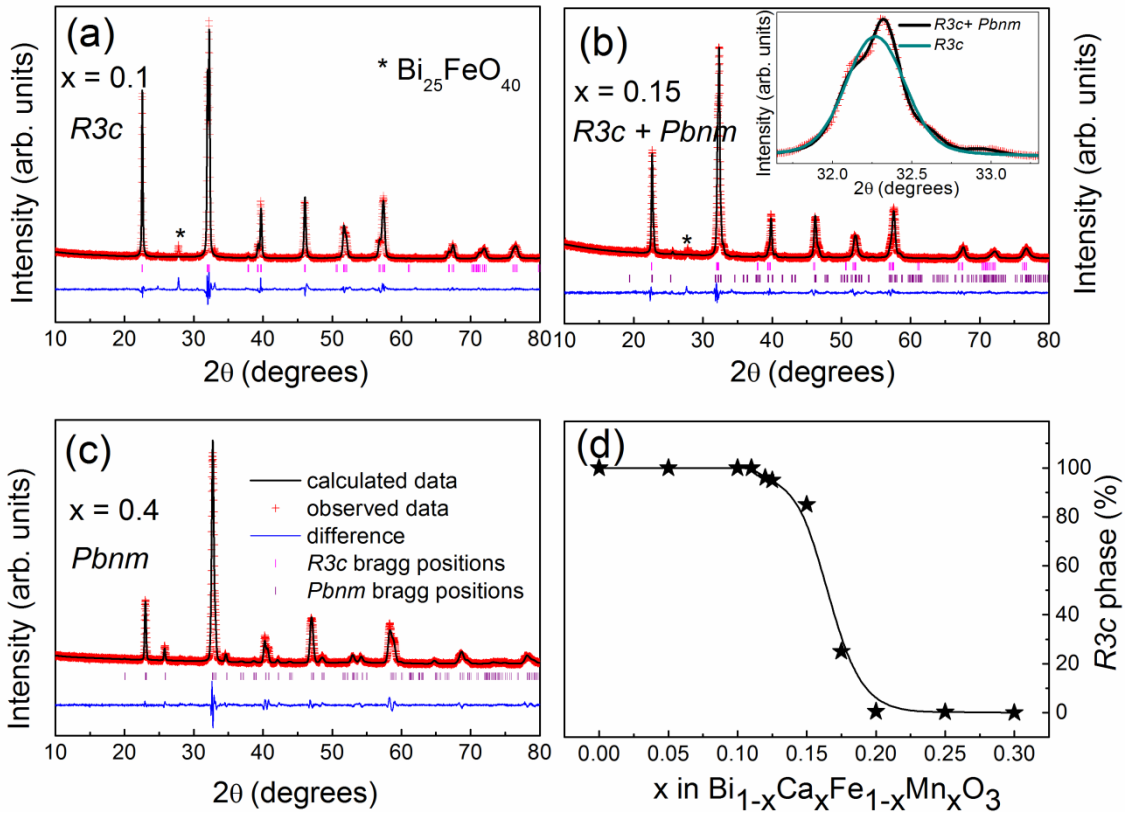

Figure 4.3. Results of the Rietveld refinement of $Bi_{1-x}Ca_xFe_{1-x}Mn_xO_3$ for (a) x = 0.1, (b) x = 0.15, and (c) x = 0.4, along with (d) the variation of the rhombohedral (*R3c*) phase content as a function of x. Inset shows the refined pattern of the peak at 2θ = 32° using *R3c* phase (green curve) and *R3c*+*Pbnm* phases (black curve) for x = 0.15. The peak from the impurity phase $Bi_{25}FeO_{40}$ is marked using the symbol '*'.

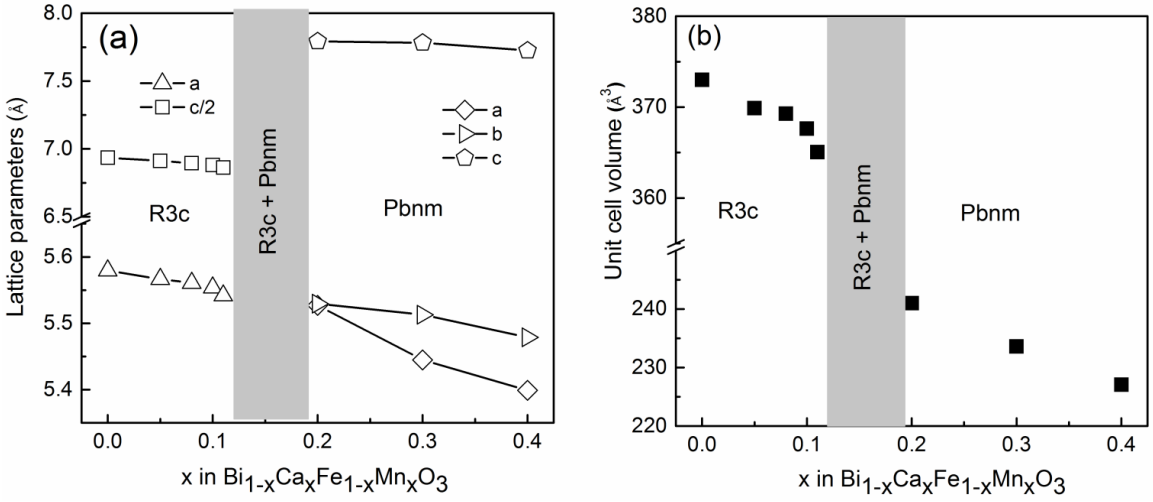

Figure 4.4. Variation of (a) lattice parameters, and (b) unit cell volume as a function of x in $Bi_{1-x}Ca_xFe_{1-x}Mn_xO_3$.

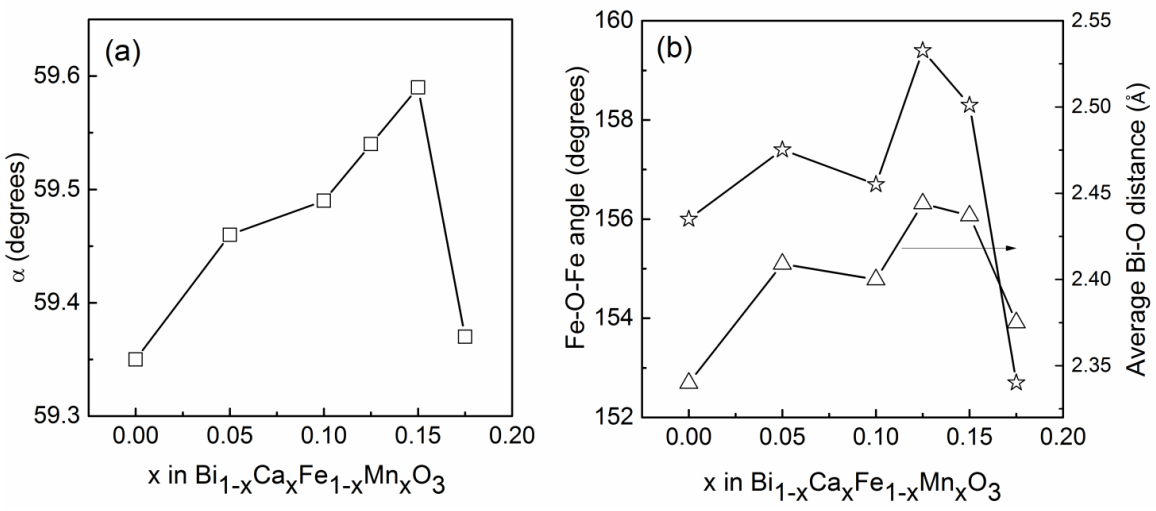

Figure 4.5. Variation of (a) rhombohedral angle, α, and (b) Fe-O-Fe bond angle and Bi-O bond length, for the rhombohedral phase, as a function of *x* in $Bi_{1-x}Ca_xFe_{1-x}Mn_xO_3$.

The rhombohedral angle (α) obtained from the Rietveld refinement is plotted against *x* in figure 4.5(a). α increases almost linearly with increasing substitution and shows a maximum around *x* = 0.15, suggesting decreased rhombohedral distortion. This is also evidenced from the increasing average Fe-O-Fe bond angle and the average Bi-O distance as shown in figure 4.5(b). Both the parameters show a maximum around *x* = 0.125.

Megaw and Darlington have derived certain geometrical and structural parameters for rhombohedral perovskites with polar space groups, including *R3c* [3]. Four important structural parameters are the octahedral tilt (*ω*), the octahedral distortion (*d*), and the atomic displacement parameters of the A (*s*) and B (*t*) cations in the ABO_3 perovskite lattice. These parameters are defined as, $A_z = s+0.25$, $t = B_z$, $O_y = 1/3–4d$ and $O_x = (1/6)–2e–2d$, where A_z, B_z, O_x, and O_y are the atomic positions of the respective elements. The octahedral distortion parameter, *d*, occurs only in polar space groups like *R3c* and is absent in non-polar space groups like *Pbnm*. '*d*' is usually observed with a negative sign and have a smaller value (10^{-2} to 10^{-4}). '*e*' describes another octahedral tilt parameter given by $\mathrm{Tan}\,\omega = 4e\sqrt{3}$ and the parameter, *e*, denotes the rotation of the octahedral faces resulting in a tilt of the octahedra in the *R3c* system. In the perovskite systems, such as in $BaTiO_3$, ferroelectric properties are usually observed due to the displacement of the B atom and a larger displacement parameter, *t*, indicates larger ferroelectric properties [4]. However, in BFO, since the ferroelectric contribution comes from Bi (A-site), the parameter, *s*, also should be considered for

explaining the ferroelectric properties. Selbech *et al.* [5] proposed that (*s*-*t*) is directly proportional to polarization in unsubstituted BFO.

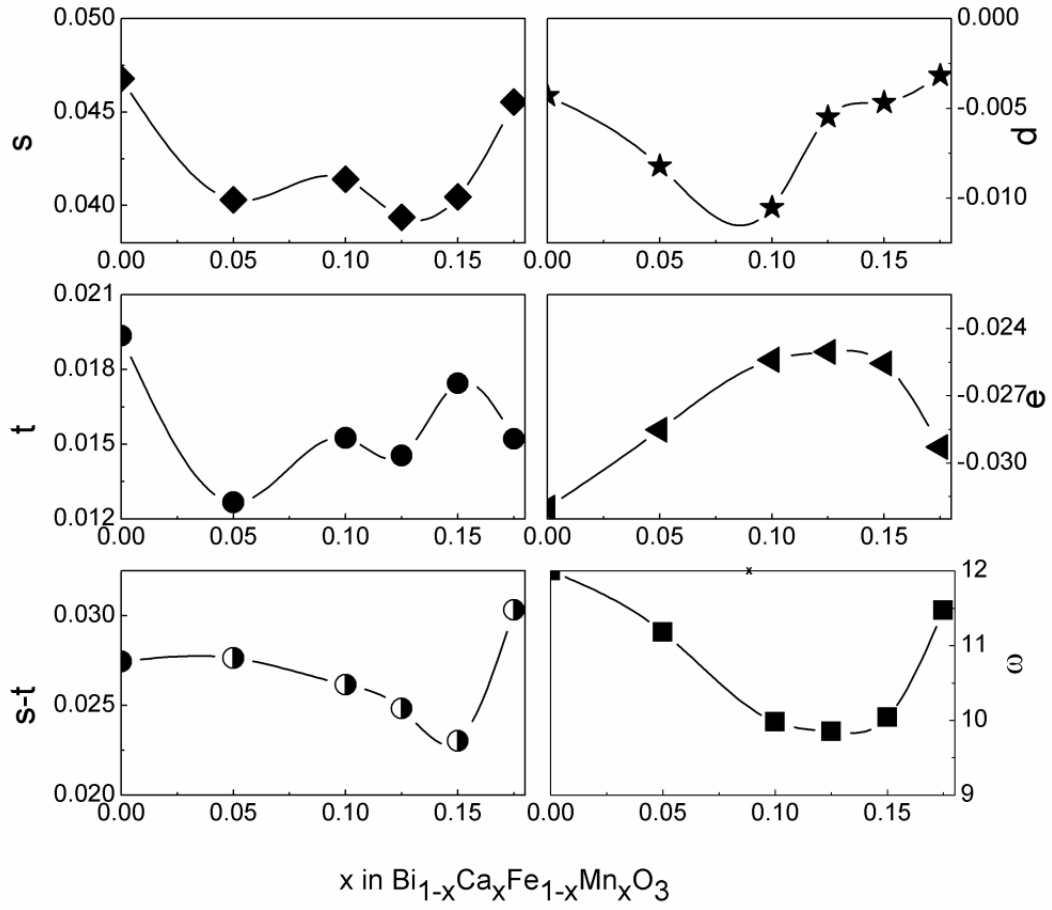

Figure 4.6. Different crystallographic parameters as a function of *x* in $Bi_{1-x}Ca_xFe_{1-x}Mn_xO_3$.

From the positions of the respective atoms obtained from the Rietveld analysis for the *R3c* space group, *s*, *t*, *s*-*t*, *d*, *e*, and ω have been calculated. The variation of these parameters as a function of *x* in $Bi_{1-x}Ca_xFe_{1-x}MnO_3$ for $0 \leq x \leq 0.175$ is shown in figure 4.6. The parameter, *s*, shows a minimum around $x = 0.125$ and then increases. The increase of *s* above $x = 0.125$ is probably due to the mixed phase behaviour in this region. '*t*' shows a maximum around $x = 0.15$. '*s*-*t*' clearly shows a distinct variation, showing a minimum at $x = 0.15$. Similarly, the octahedral distortion parameter, *d*, decreases, shows a minimum around $x = 0.1$ and then increases towards zero. This implies the stability of the *R3c* structure by Ca and Mn co-substitution till $x = 0.1$. Increase in the value of *d* above $x = 0.1$ also indicates a possible

structural phase transition towards a more symmetric phase. The octahedral tilting parameters, ω and e, show minimum and maximum, respectively, at $x = 0.125$. The combined effect of the octahedral distortion and octahedral tilt gives rise to a maximum Fe-O-Fe bond angle around $x = 0.125$. From these results, it can be concluded that all the derived structural parameters show an anomaly in the compositional region $0.1 \leq x \leq 0.175$ which correspond to a morphotropic phase boundary (MPB) region.

4.3. Microstructure

SEM images of the $Bi_{1-x}Ca_xFe_{1-x}MnO_3$ samples ($x = 0$ to 0.25) are shown in figure 4.7. Very large (> 1 μm) and fused grains are observed for $x = 0$ and 0.05, whereas large isolated grains are observed for $x = 0.1$. The microstructures are entirely different for $0.125 \leq x \leq 0.175$, showing the presence of larger and smaller grains. Almost well-separated grains are visible for $x > 0.175$, with average grain size around 0.5 μm. Thus, larger sized grains are observed for the rhombohedral phase, smaller grains for the orthorhombic phase and non-uniform grain size and dense microstructure for the mixed phase region.

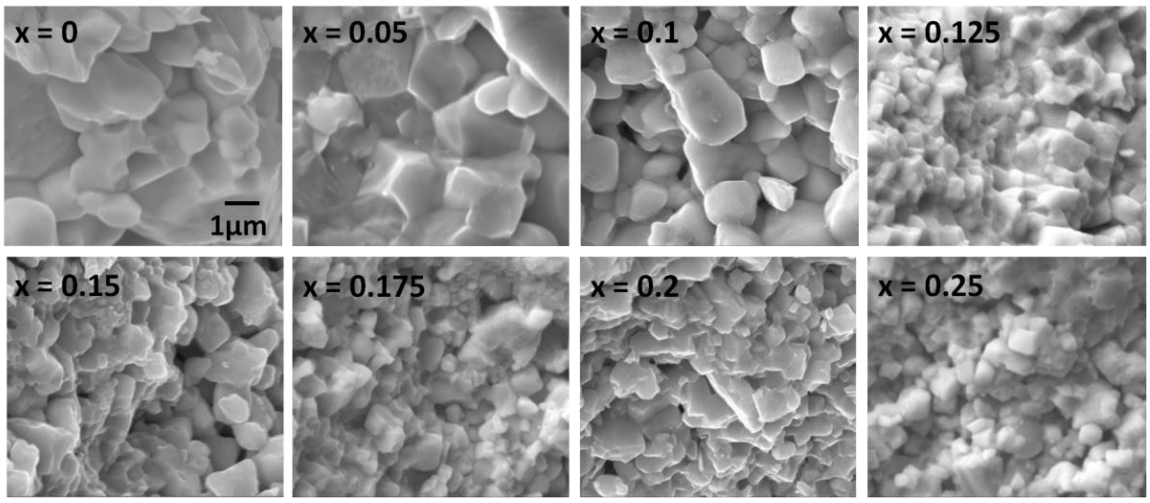

Figure 4.7. Scanning electron micrographs of different compositions in $Bi_{1-x}Ca_xFe_{1-x}Mn_xO_3$. The scale shown is common for all images.

4.4. Raman spectroscopy

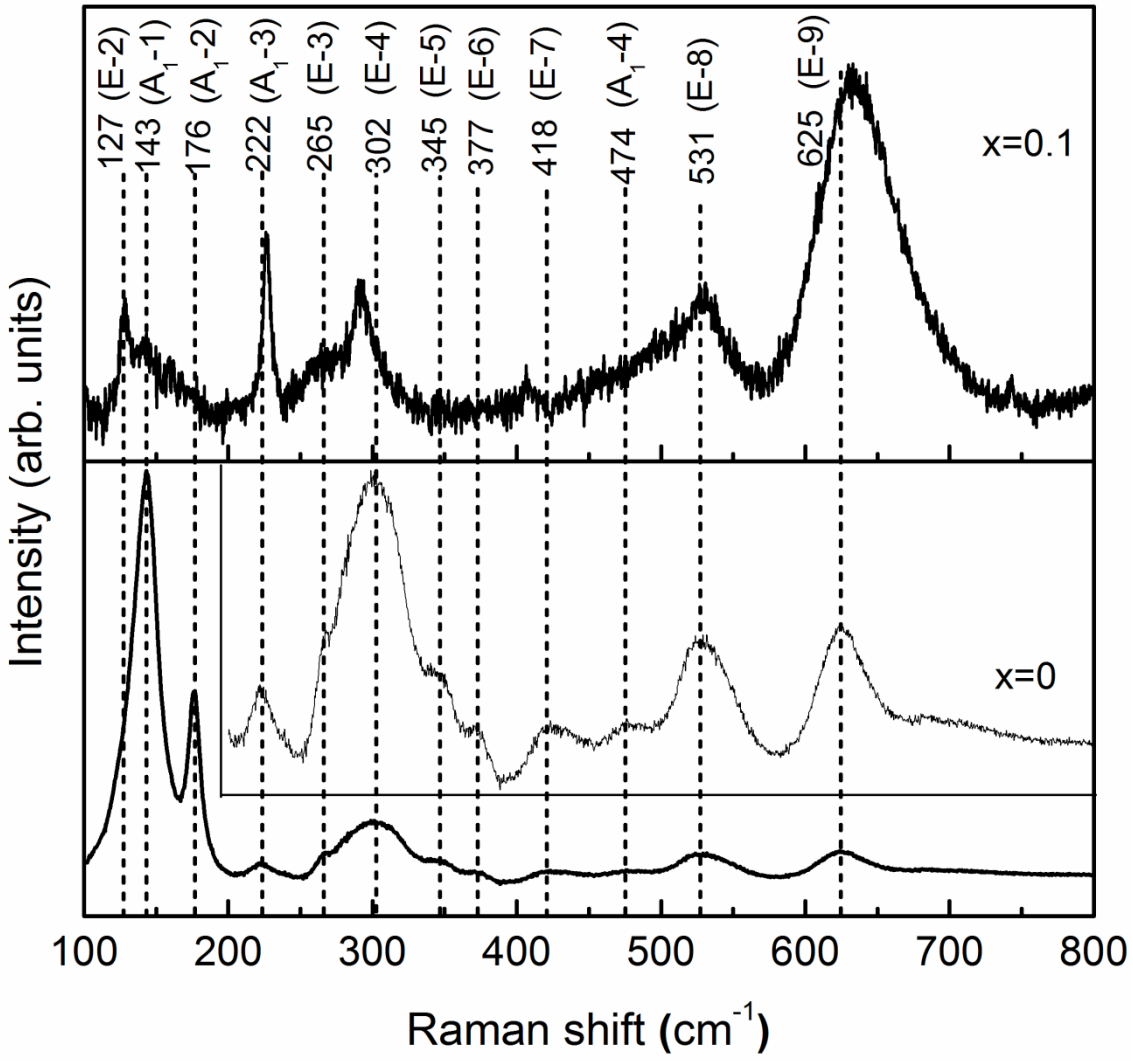

Figure 4.8. Raman spectra of $BiFeO_3$ and $Bi_{0.9}Ca_{0.1}Fe_{0.9}Mn_{0.1}O_3$. The inset shows the zoomed spectra of $BiFeO_3$ on the same *x*-axis scale.

Figures 4.8 and 4.9 show the Raman spectra of different compositions in $Bi_{1-x}Ca_xFe_{1-x}MnO_3$. Details of the Raman spectrum of BFO are discussed in chapter 3, section 3.4. From figure 4.8, it is clear that the spectra of $x = 0.1$ shows all modes of vibrations shown by BFO confirming its *R3c* structure. Raman spectra of different compositions are compared in figure 4.9. A clear shift towards higher frequency is observed for the A_1-3, E-4 and E-7 modes. The shift in the peak positions and the changes in the relative intensities of different bands are due to the structural distortion caused by the substitution. The blue shift is due to the lower atomic mass of Ca substituted at the heavier Bi-site since the frequencies of

the Raman modes depend on the mass of the atom. A weak, broad, band at 480 cm^{-1} is observed for $x \geq 0.125$ indicating the presence of orthorhombic phase in these samples and intensity of this mode increases with increasing the degree of substitution. Presence of this band along with the Raman bands of BFO confirms the *R3c-Pbnm* mixed phase nature for $0.125 \leq x \leq 0.175$.

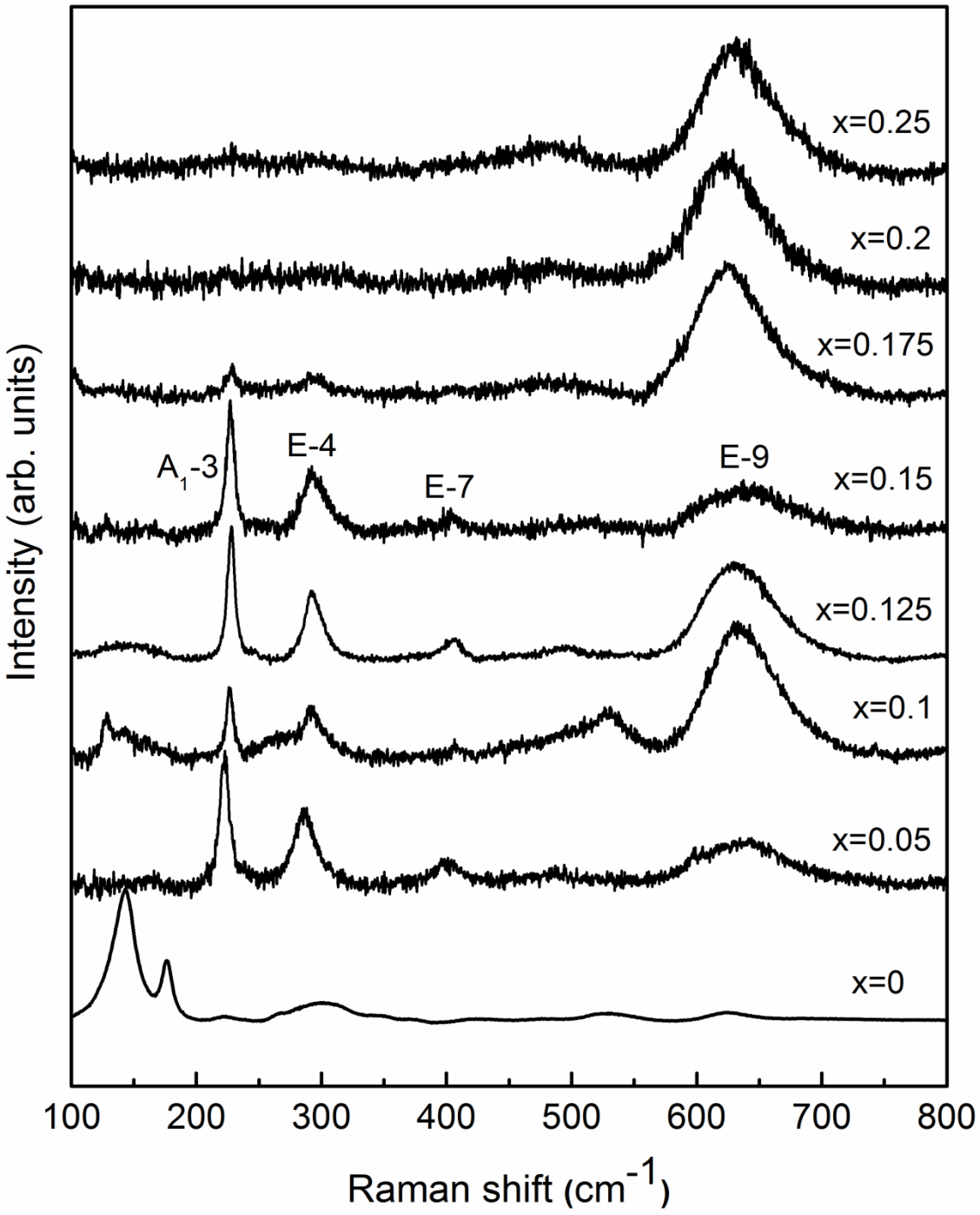

Figure 4.9. Raman spectra of different compositions in $Bi_{1-x}Ca_xFe_{1-x}Mn_xO_3$.

Intensities of all the major bands remain comparable till x = 0.15, and for x = 0.175, intensities of all bands, except those at 480 and 625 cm^{-1} are diminished. This is due to the low percentage of *R3c* phase in x = 0.175. The band at 222 cm^{-1} is completely absent in the spectra for $x > 0.175$. Compositions with $x \geq 0.2$ with the orthorhombic structure show different spectral features than that for the compositions with *R3c* structure ($x \leq 0.175$). The compositions with $x \geq 0.2$ show two major broad bands around 480 and 620 cm^{-1}. Ghosh *et al.* [6] have reported similar Raman spectra for $Bi_{0.8}La_{0.2}FeO_3$ and $Bi_{0.8}La_{0.2}Fe_{0.9}Mn_{0.1}O_3$ with orthorhombic structure. These results confirm the structural change from *R3c* to *Pbnm* around x = 0.175, as concluded from the XRD studies

4.5. Oxygen stoichiometry

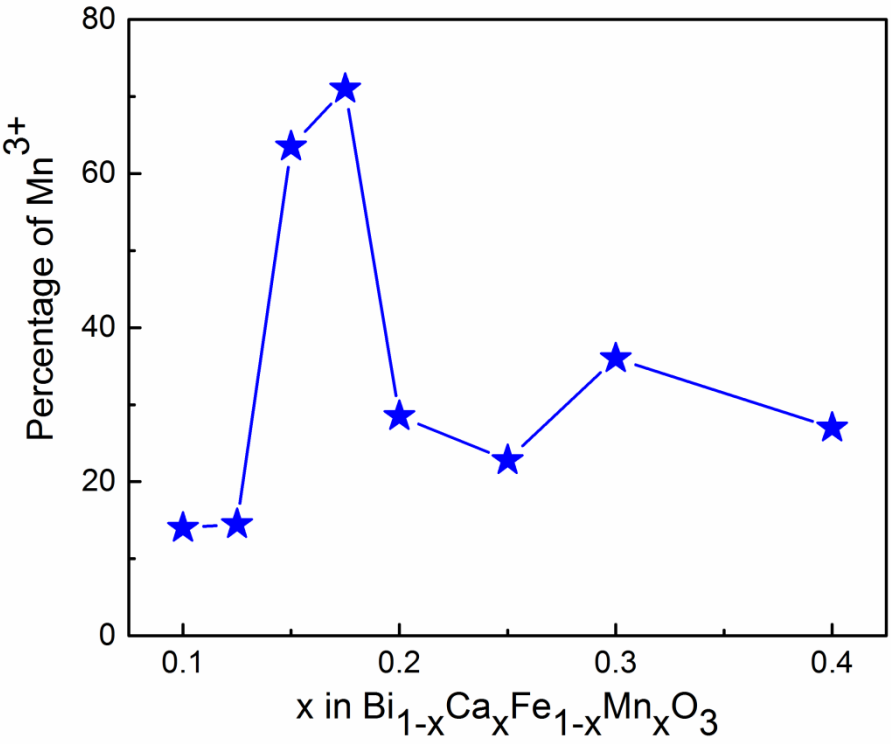

Figure 4.10. Mn^{3+} percentage obtained from the redox titration vs x in $Bi_{1-x}Ca_xFe_{1-x}Mn_xO_3$.

In $Bi_{1-x}Ca_xFe_{1-x}Mn_xO_3$, to preserve charge neutrality, all the substituted Mn in $Bi_{1-x}Ca_xFe_{1-x}Mn_xO_3$ is expected to be in the tetravalent state due to the replacement of trivalent Bi by divalent Ca ions. Large amounts of oxygen non-stoichiometry have been reported for $Bi_{1-x}Ca_xFeO_{3-\delta}$ [7-10], and deviation from oxygen stoichiometry is very common

in the substituted perovskites [11]. Therefore, the Mn^{3+}/Mn^{4+} contents (figure 4.10) in the samples are obtained from permanganometric redox titration analysis which is a reliable and accurate analytical method to estimate the oxygen stoichiometry in substituted manganites [12]. For $Bi_{0.9}Ca_{0.1}Fe_{0.9}Mn_{0.1}O_3$, around 15% Mn was observed as Mn^{3+} which increases with the degree of substitution, and Mn^{3+} content reaches around 70% for x = 0.175 and which is decreased for higher compositions. For x = 0.4, around 30% of Mn^{3+} was observed. It is interesting to note that barring the compositions in the MPB region, the Mn^{3+} content increases almost linearly with x, and large amounts of Mn^{3+} are present in the compositions in the MPB region. Thus, both Mn^{3+} and Mn^{4+} are present in all samples, suggesting oxygen non-stoichiometry.

4.6. X-ray Photoelectron Spectroscopy

X-ray photoelectron spectroscopy (XPS) is used to further look at the valency of Mn and oxygen stoichiometry. Oxygen 1s XPS peak of the $Bi_{1-x}Ca_xFe_{1-x}Mn_xO_3$ compositions is analyzed to find out the number of oxygen vacancies in the samples. Oxygen 1s spectra of different compositions are shown in figure 4.11. The spectra could be deconvoluted to three peaks at 529.6 (O_l), 531.6 (O_c) and 533.9 eV (O_p), where O_l is due to crystallite oxygen species, O_c is due to chemisorbed water species, and O_p is due to physisorbed water species, respectively, as reported in the literature [13]. As x increases, intensities of O_c and O_p increase indicating an increase in the number of vacancies at higher compositions. The ratio of the area of the peaks due to O_l and O_c gives a rough estimation of the oxygen vacancy (O_v) in the samples, as reported [14]. The variation of the amount of oxygen vacancy, O_v, as a function of x is shown in the inset of figure 4.14. The oxygen vacancy remains about 30% for all compositions up to x = 0.3.

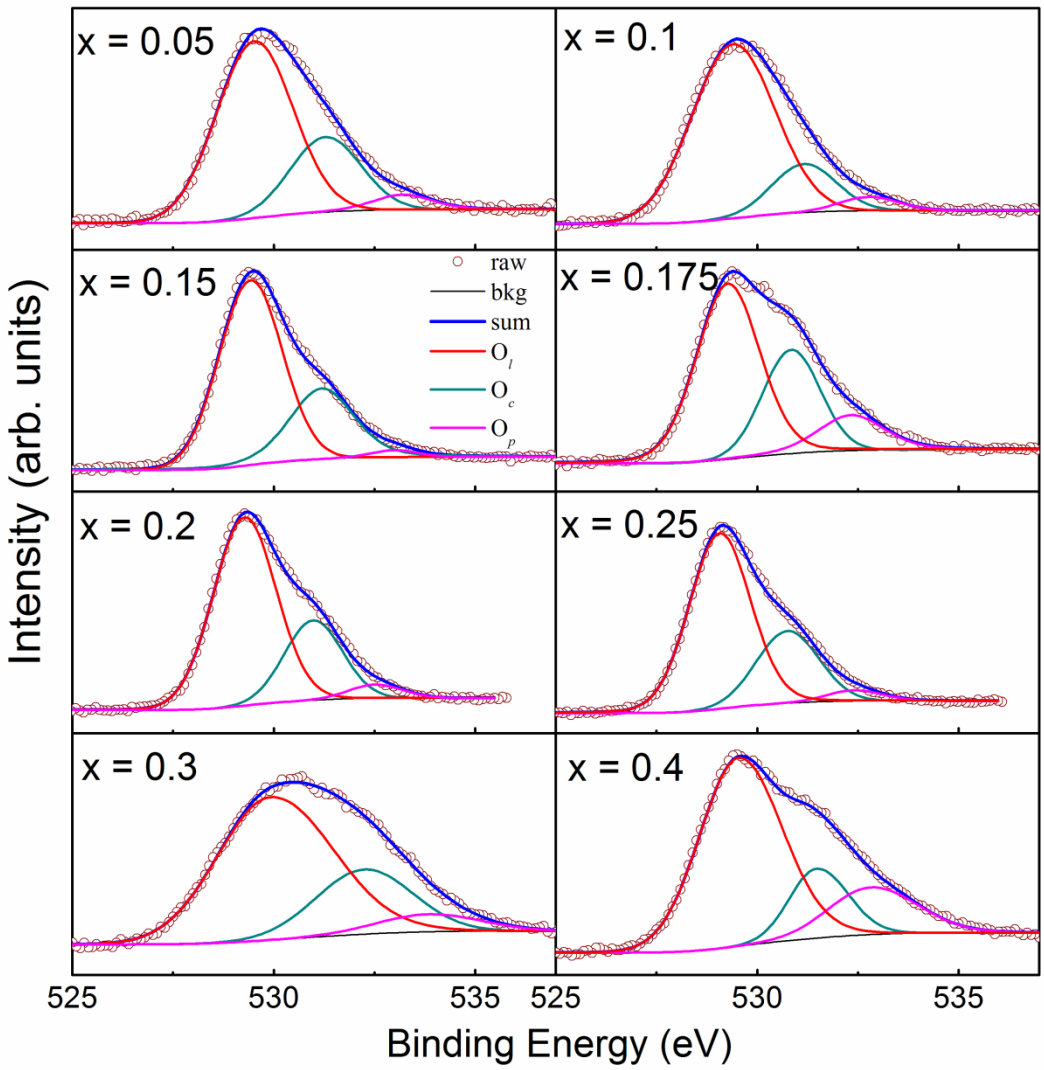

Figure 4.11. Deconvoluted oxygen 1s XPS spectra of different compositions of $Bi_{1-x}Ca_xFe_{1-x}Mn_xO_3$.

The Mn 2p XPS spectra (Mn $2p_{1/2}$ and Mn $2p_{3/2}$) of different compositions in $Bi_{1-x}Ca_xFe_{1-x}Mn_xO_3$ are shown in figure 4.12. Mn $2p_{3/2}$ XPS peaks are analyzed to find the oxidation state of manganese in the system (figure. 4.13). Deconvolution of the peak gives the binding energies as 641.6 and 642.6 eV, respectively, for Mn^{3+} and Mn^{4+}. The percentages of the two oxidation states are calculated by taking the ratio of the area obtained under each fitted peak corresponding to Mn^{3+} and Mn^{4+} [14]. Percentage of Mn^{3+} obtained from the XPS fitting is plotted against the degree of substitution in figure 4.14. The results obtained are concurrent with the amount of Mn^{3+} obtained from the titration experiments. Both the percentage of Mn^{3+} and oxygen vacancy show a maximum around $x = 0.175$.

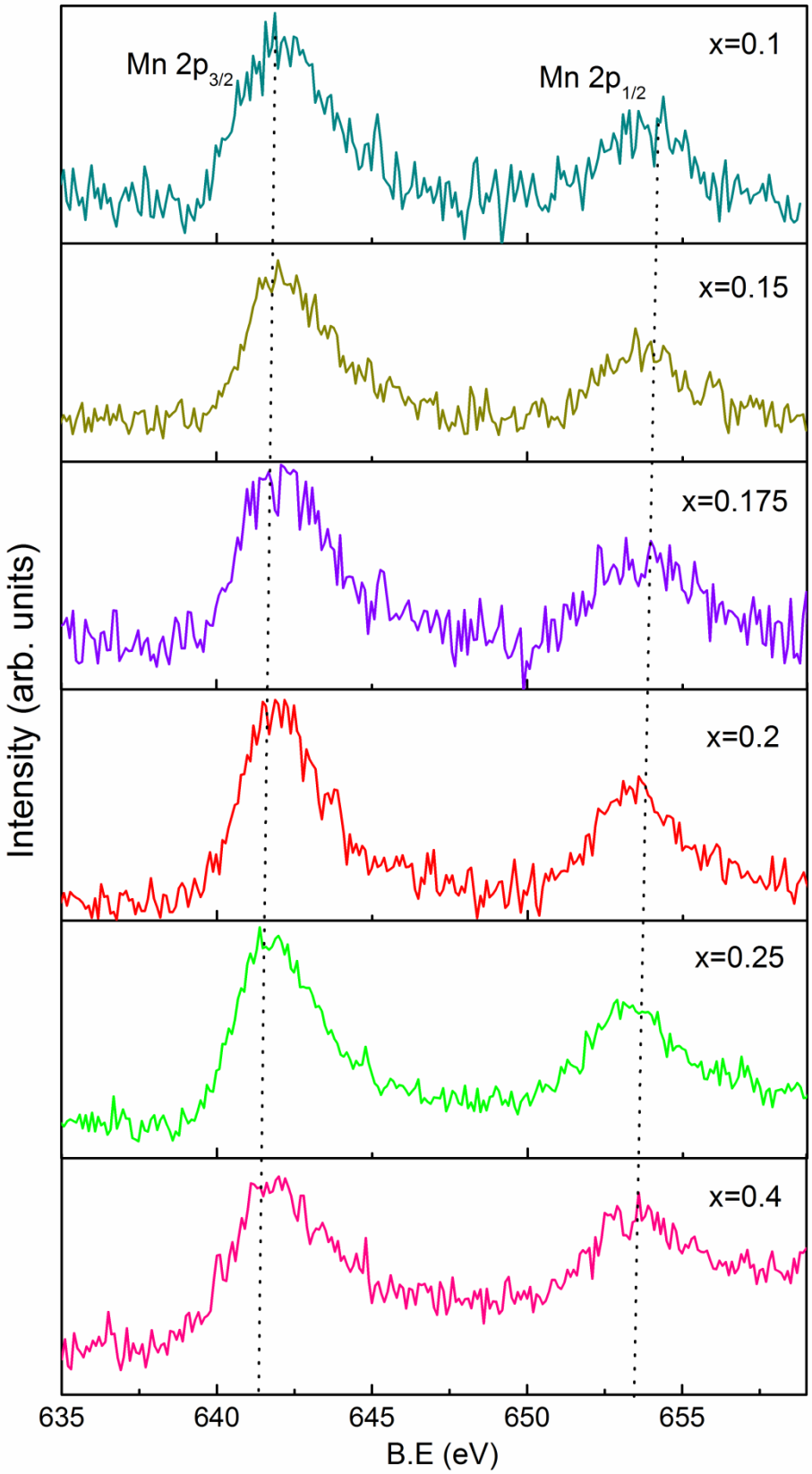

Figure 4.12. Mn 2p XPS spectra of the $Bi_{1-x}Ca_xFe_{1-x}Mn_xO_3$ samples.

Thus, XPS and redox titration analysis suggest that apart from the formation of Mn^{4+}, both oxygen vacancies and Mn^{3+} are created to compensate for the charge neutrality by the divalent ion substitution at the Bi^{3+} site.

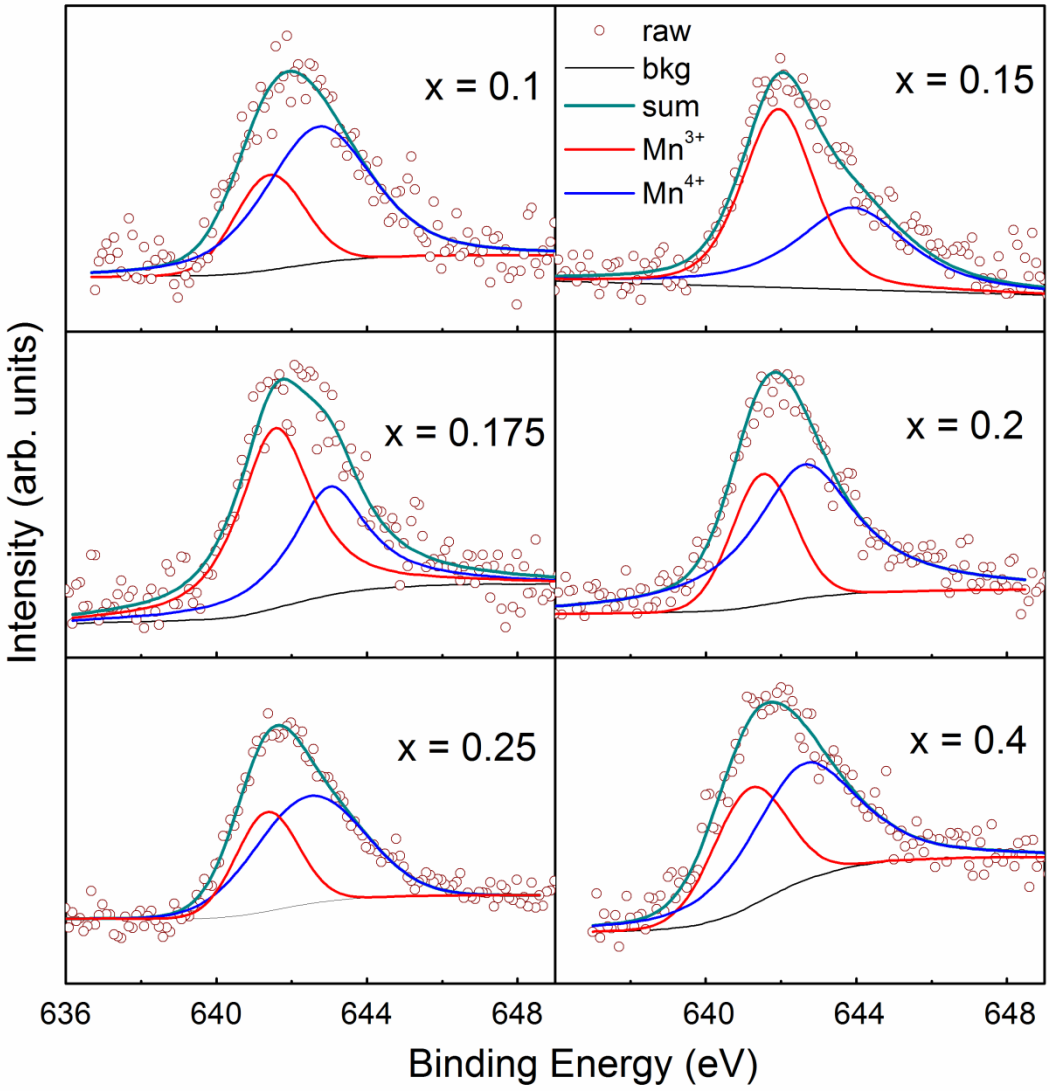

Figure 4.13. Deconvoluted Mn $2p_{3/2}$ XPS spectra of different compositions in $Bi_{1-x}Ca_xFe_{1-x}Mn_xO_3$.

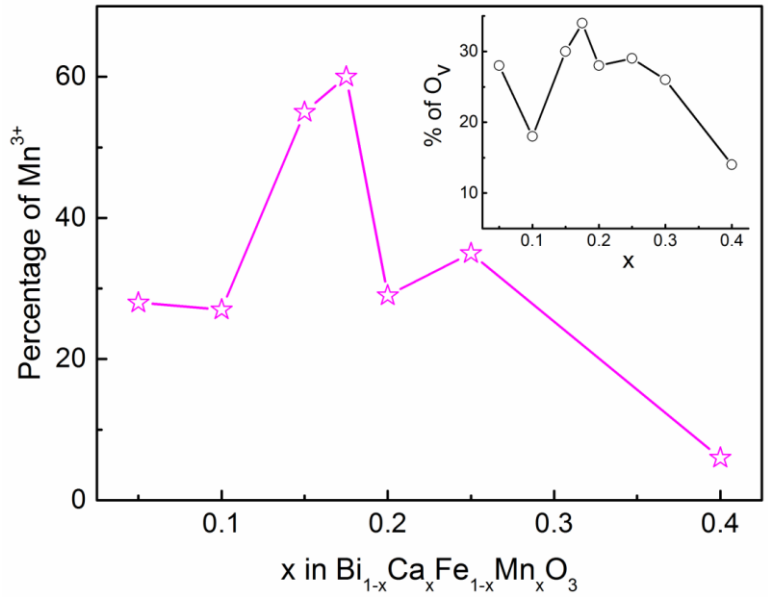

Figure 4.14. Percentage of Mn^{3+} vs. *x* in $Bi_{1-x}Ca_xFe_{1-x}Mn_xO_3$. The inset shows the percentage of oxygen vacancy vs. *x* in $Bi_{1-x}Ca_xFe_{1-x}Mn_xO_3$.

4.7. Magnetic properties

4.7.1. M vs. H measurements

Room temperature M-H curves of BFO and the co-substituted compositions are shown in figure 4.15. Magnetic properties of the unsubstituted BFO are discussed in chapter 3. BFO shows a magnetization of 0.4 emu/g (at 60 kOe) which is increased to 0.6 emu/g for *x* = 0.05 and the magnetization increases with the degree of substitution, showing a value of 1.4 emu/g for *x* = 0.4. Magnetic hysteresis loop with increasing coercivity and remanence is observed for the compositions in the mixed phase region, as shown in the upper inset of figure 4.15. A very high coercivity around 6 kOe is obtained for the composition *x* = 0.175, with a remnant magnetization of 0.09 emu/g. All the substituted compositions, except *x* = 0.4, show magnetic hysteresis loops indicating weak ferromagnetism. Surprisingly, for *x* = 0.4, the weak ferromagnetism is completely disappeared without any remanence and coercivity, suggesting paramagnetic or antiferromagnetic nature of the composition.

Fe-O-Fe superexchange interaction depends on the Fe-O-Fe angle. As discussed in section 4.2, the Fe-O-Fe angle increases with increasing level of substitution, and hence the increasing magnetization with substitution is due to the enhanced ferromagnetic superexchange interactions. Sati *et al.* [15] have discussed such enhanced magnetization with

an increase in the Fe-O-Fe bond angle in Dy-substituted BFO, where the Fe-O-Fe angle increases with increasing the amount of Dy substitution. Similar results are reported in the literature for co-substituted systems also [16, 17]. Contraction of the unit cell parameters and unit cell volume (as shown in figure 4.4) indicate the presence of Mn^{4+} in the co-substituted samples whereas the redox titration and XPS results revealed the presence of both Mn^{3+} and Mn^{4+} in the samples. This observation suggests that Mn^{3+}-O-Mn^{4+} ferromagnetic double exchange interaction, as in the case of substituted rare earth manganites [18], can also contribute to the weak ferromagnetism exhibited by the Ca and Mn co-substituted BFO. The Ca and Mn co-substituted samples contain mostly Mn^{4+} with a small amount of Mn^{3+} for the compositions with only *R3c* ($x \leq 0.11$) and only *Pbnm* phase ($x \geq 0.2$), whereas in the mixed phase MPB region, Mn^{3+} content, and oxygen vacancies were found to be higher.

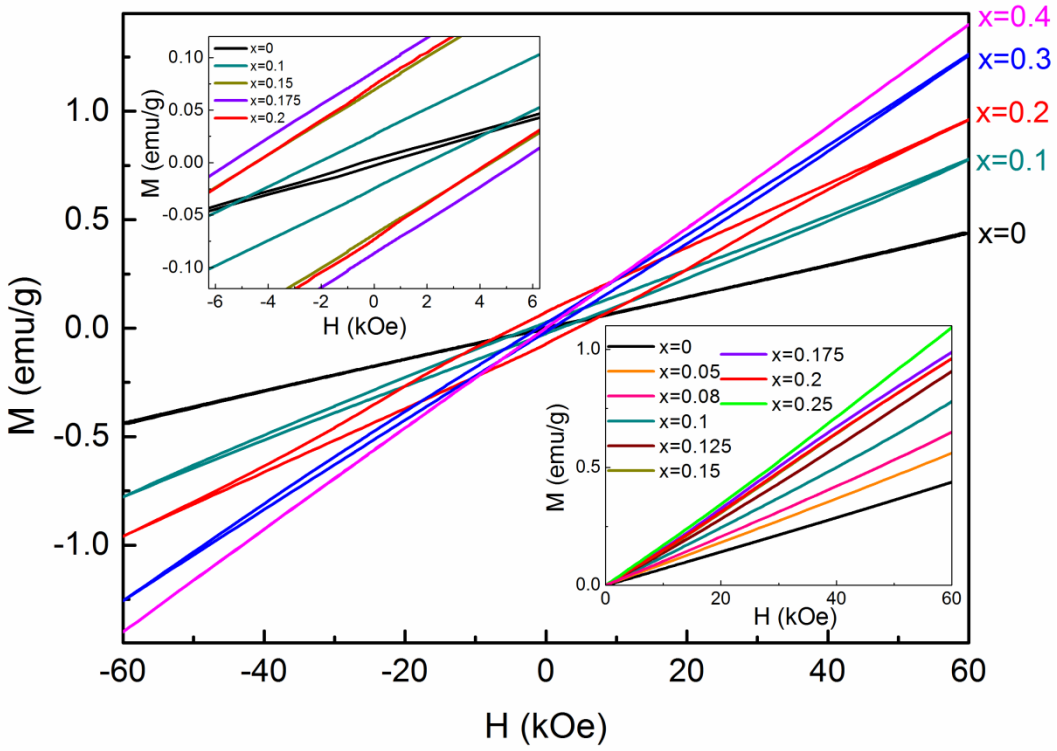

Figure 4.15. M-H curves of $Bi_{1-x}Ca_xFe_{1-x}Mn_xO_3$ measured at room temperature. The upper inset shows the zoomed curves at low field, and the lower inset shows the initial magnetization curves of different samples.

The magnetization at 60 kOe (M_{60}) increases with substitution (figure 4.16(c)), showing a broad anomaly between x = 0.1 and 0.2. The higher rhombohedral angle and higher Fe–O–Fe angle observed in this compositional region (as explained based on figure 4.5) could be leading to the higher magnetization in this compositional region. Since the

Mn^{3+} content increases with the degree of substitution, the increased ferromagnetic contribution from the double exchange interaction involving Mn^{3+} and Mn^{4+} also is a possibility. Higher Fe–O–Fe angle (for the rhombohedral phase) around the MPB region suggests less distorted FeO_6 octahedra, favoring a strong magnetic interaction. Such enhanced magnetic properties around the structural phase transition region have been reported in many substituted BFO systems [19-22]. Thus, the weak ferromagnetism shown by the co-substituted compositions can be arising from the various exchange interactions involving Fe^{3+}, Mn^{3+}, Mn^{4+}, oxygen vacancy, as well as due to the suppression of spiral spin cycloidal structure leading to canted antiferromagnetism.

Unlike the changes in the magnetization, figures 4.16(a) and (b) shows that coercivity (H_c) and remanence (M_r) increase with increasing substitution, showing a maximum value at $x = 0.175$ and then these parameters decrease at higher values of x. Both the parameters show similar variation, suggesting a common origin, other than the contributions to magnetization from Fe–O–Fe bond angle and Fe–O bond distance. Apart from the contribution from magnetocrystalline anisotropy, coercivity and remnant magnetization of sintered polycrystalline materials are known to depend on the microstructure [23,24]. The shape, size and orientation of the grains, which affect the domain structure, contribute to these parameters. Structural studies indicated mixed phase behaviour for $0.12 < x < 0.2$, showing an increasing contribution of the orthorhombic phase, and for $x > 0.175$, only orthorhombic phase exists. Thus, the changes in the remanence and coercivity are likely to be due to the changes in the microstructure associated with the presence of mixed phases, as evidenced from the SEM images shown in figure 4.7. For $x \geqslant 0.2$, the decreasing coercivity and remanence could be due to the changes in the Fe–O–Fe angle and Fe–O bond distance of the orthorhombic phase, apart from the microstructure.

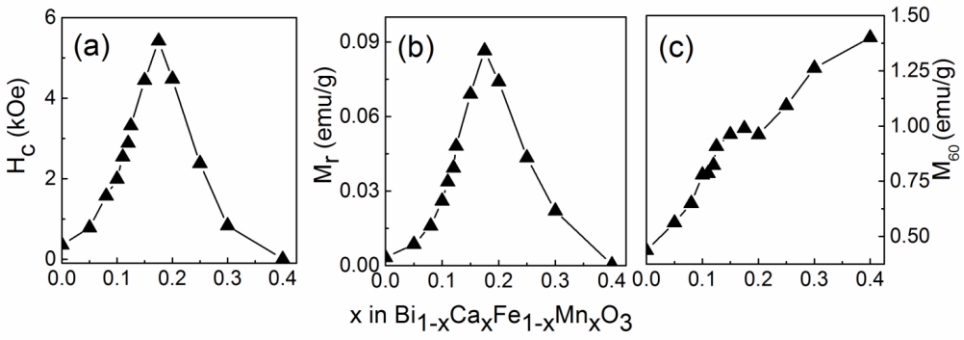

Figure 4.16. (a) Coercivity (H_c), (b) remnant magnetization (M_r), and (c) magnetization at 60 kOe (M_{60}) as a function of x in $Bi_{1-x}Ca_xFe_{1-x}Mn_xO_3$.

Low-temperature M-H curves (measured at 5 K) of the samples are shown in figure 4.17. The composition with x = 0.05 shows a linear variation of magnetization with the field as shown in the lower inset in figure 4.17. Compositions with $x \geq 0.1$ exhibit large hysteresis loops and higher magnetization which increases with the degree of substitution. x = 0.1 show a magnetization around 1.5 emu/g and coercivity and remanence of 1.5 kOe and 0.15 emu/g, respectively. x = 0.4 sample shows a low-temperature magnetization of 7 emu/g with a remanence of 0.45 emu/g. The magnetic hysteresis loops with large coercivity akin to a ferromagnetic behavior shown by the compositions can be an intrinsic property rather than from magnetic impurities or phase separation. Magnetic parameters obtained from the low-temperature magnetization curves are plotted against substitution content x in figure 4.18.

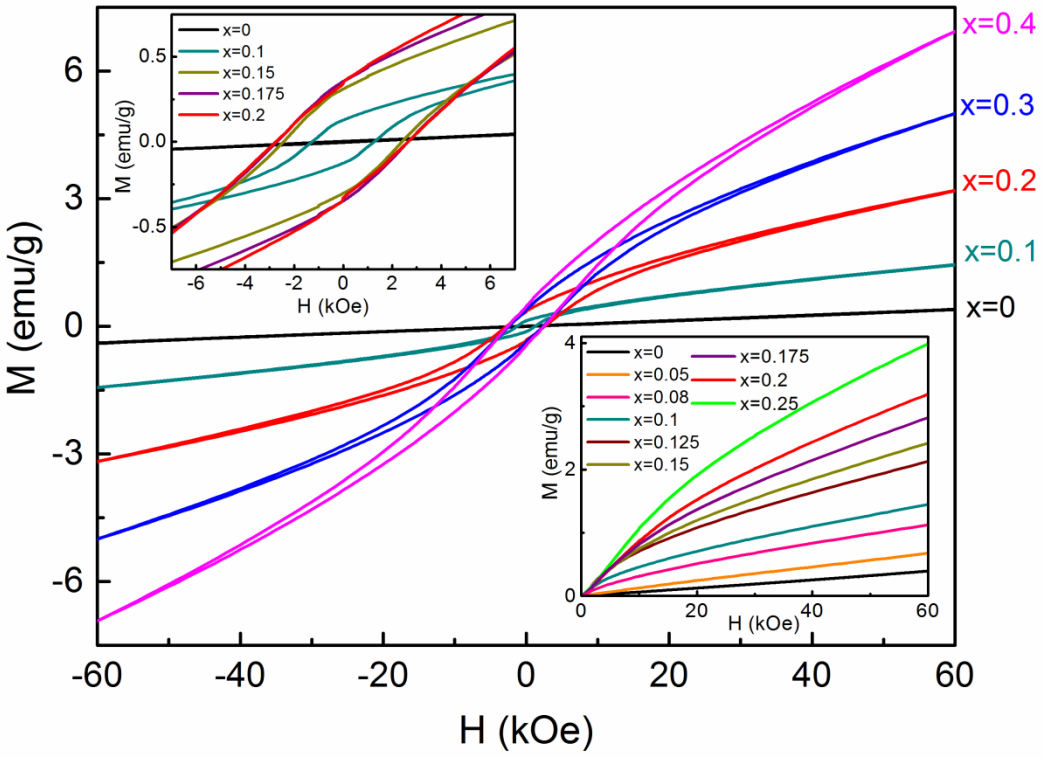

Figure 4.17. Magnetization vs. applied magnetic field curves of $Bi_{1-x}Ca_xFe_{1-x}Mn_xO_3$ at 5 K. Upper inset shows the magnified image, and the lower inset shows the initial magnetization curves.

Coercivity increases with substitution and shows a maximum in the region x = 0.175–0.25 and then decreases. Similarly, remanence also increases with substitution and shows a shoulder for x = 0.175–0.3 and then increases for x= 0.4. Thus, both the remanence

and coercivity show a broad anomaly around the structural transition region similar to that reflected in the RT magnetic parameters. Magnetization value at 60 kOe increases linearly with substitution but shows a small anomaly around the MPB region.

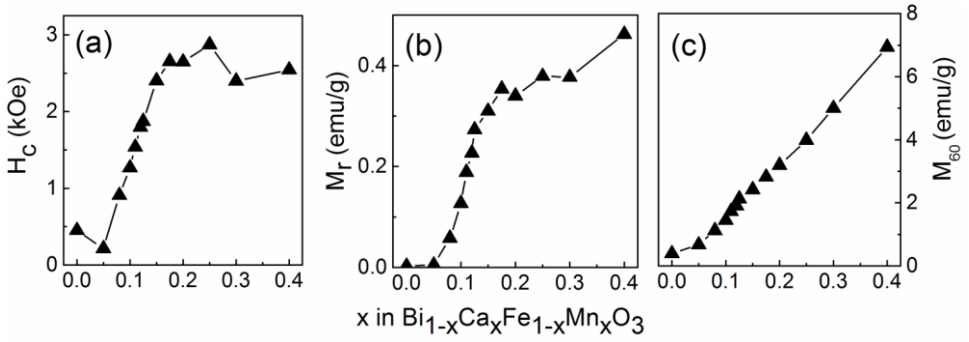

Figure 4.18. (a) Coercivity (H_c), (b) remnant magnetization (M_r), and (c) magnetization at 60 kOe (M_{60}), at 5 K, as a function of *x* in $Bi_{1-x}Ca_xFe_{1-x}Mn_xO_3$.

Since the *x* = 0.4 composition (having only *Pbnm* phase) showed a paramagnetic behaviour at room temperature, M-H curves of the sample are measured at different temperatures, as shown in figure 4.19. Opening up of a magnetic hysteresis loop is observed below 275 K, suggesting weak ferromagnetism in the composition at low temperatures (figure 4.19 (b)). M-H measurements for the *x* = 0.1 composition having only the *R3c* phase and *x* = 0.175 containing both *R3c* and *Pbnm* mixed phases are also carried out and compared as shown in figure 4.20. Both the samples showed a magnetic hysteresis loop at room temperature.

Variation of the remanence, coercivity, and magnetization at 60 kOe as a function of temperature is shown in figure 4.21. For *x* = 0.4 (*Pbnm* phase) all the magnetic parameters increase with decreasing temperature, where coercivity clearly shows a broad maximum around 100 K and a minimum around 50 K. The coercivity increases drastically below 50 K. For *x* = 0.1 with *R3c* phase, magnetization and remanence increase with decreasing temperature similar to *x* = 0.4 whereas coercivity decreases till 50 K and below which it increases sharply. For *x* = 0.175 (MPB region), remanence and magnetization almost remain unchanged down to 150 K and increases below this temperature. Coercivity shows a larger drop till 50 K and below which it increases rapidly. Similar to *x* = 0.4, a broad maximum in the coercivity around 100 K is observed for the *x* = 0.1 samples whereas such an anomaly is absent for *x* = 0.175. Below 50 K, coercivity shows almost comparable values for the three

compositions implying composition independent nature of the coercivity in the $Bi_{1-x}Ca_xFe_{1-x}Mn_xO_3$ system below 50 K. This suggests a common origin for the coercivity for all three compositions. Since the microstructures of all the three compositions are widely different the parameter may have its origin from domain wall pinning. It is also possible that electronic phase separation [25-27], as observed in different related systems may be responsible for the changes in the coercivity.

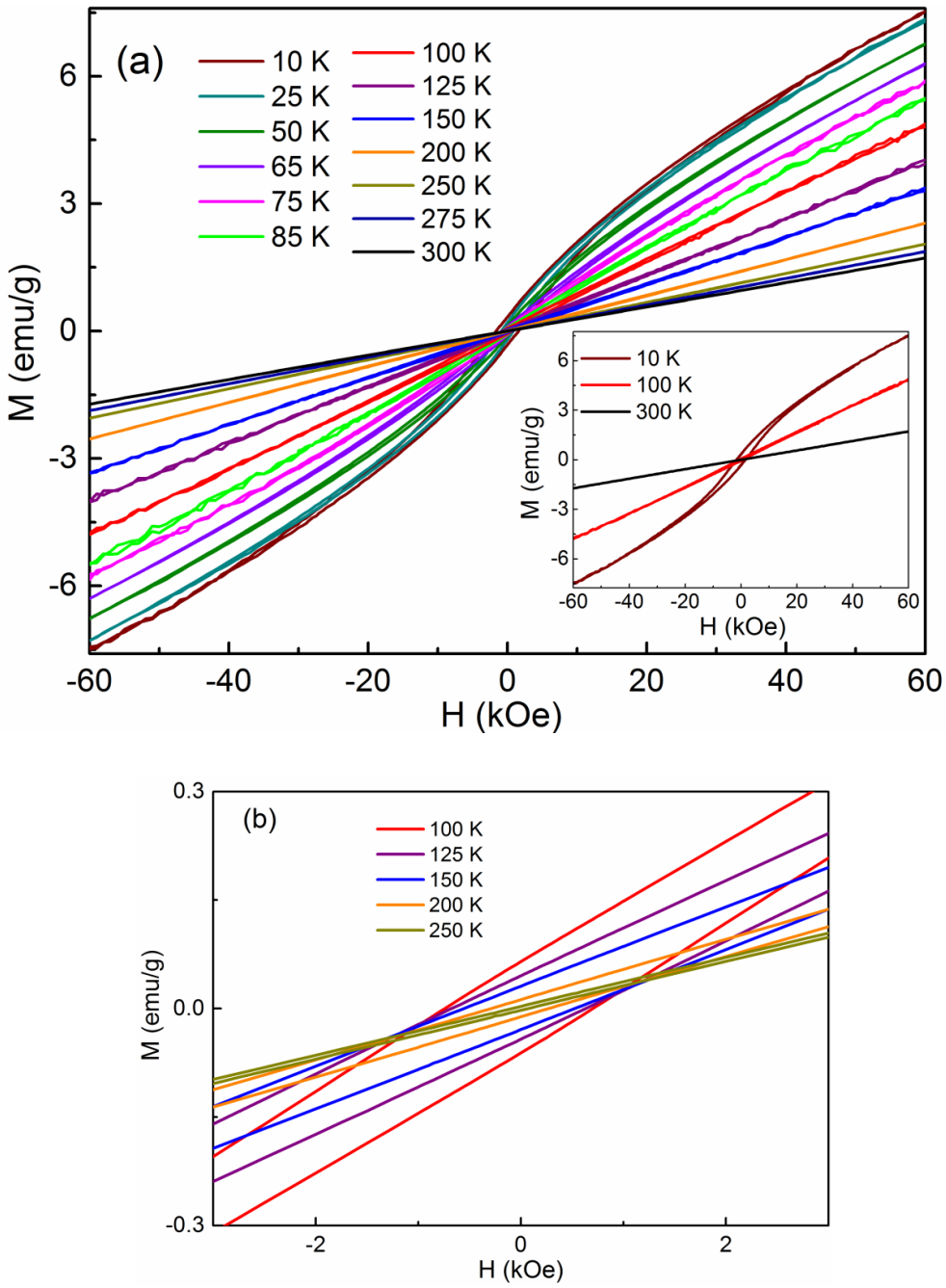

Figure 4.19. (a) M-H curves of x = 0.4 taken at different temperatures. The inset shows M-H curves at 300, 100, and 10 K. (b) Magnified view of the M-H curves in the 100–250 K temperature region.

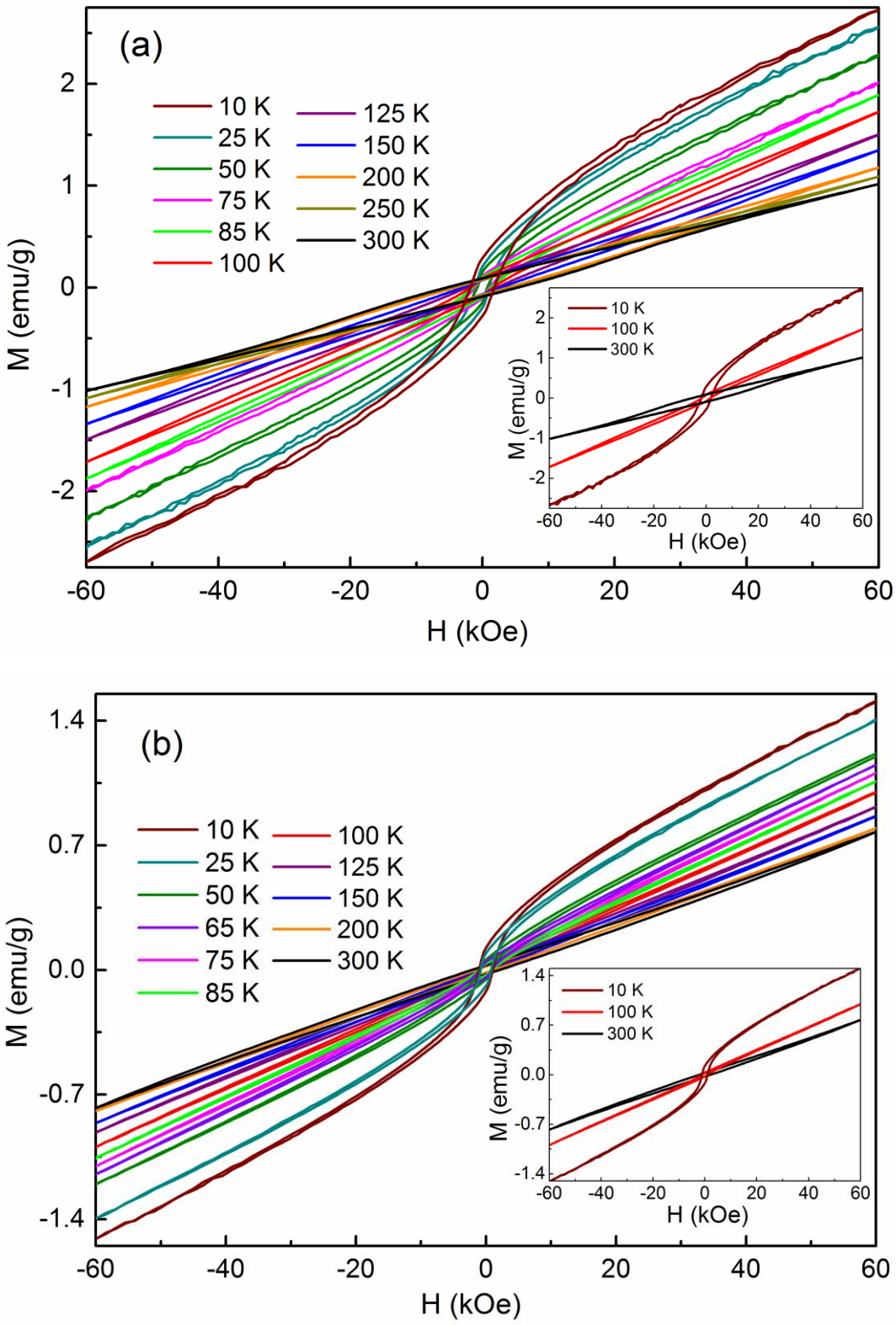

Figure 4.20. (a) M-H curves of x = 0.175 taken at different temperatures. The inset shows M-H curves at 300, 100 and 10 K. (b) M-H curves of x = 0.1 taken at different temperatures. The inset shows M-H curves at 300, 100 and 10 K.

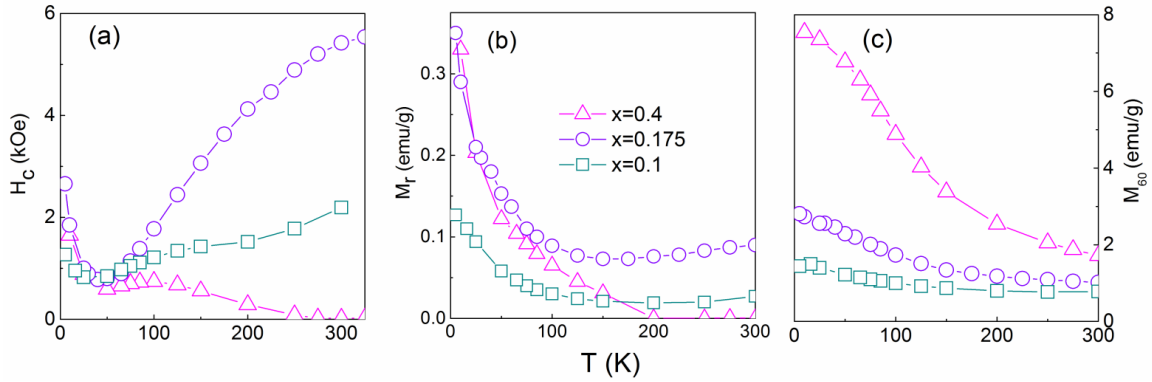

Figure 4.21. Magnetic parameters of x = 0.1 (*R3c phase*), x = 0.175 (*R3c-Pbnm* mixed phase) and x = 0.4 (*Pbnm phase*) at different temperatures.

4.7.2. M vs. T measurements

The anomalies in the coercivity at 100 and 50 K suggest changes in the anisotropy or a different magnetic phase such as a spin glass phase. Therefore, to get more information on the magnetic nature of the materials, the temperature variation of magnetization has been measured for all compositions below room temperature. Figure 4.22 shows the ZFC and FC magnetization curves, measured in a constant magnetic field of 500 Oe. The detailed low-temperature M-T behavior of BFO and some of the co-substituted compositions is explained in chapter 3, section 3.5.2. For comparison, only the ZFC curves of the samples for $0.05 \leq x \leq 0.175$ are shown in figure 4.23. As discussed in the previous chapter, a divergence between the FC and ZFC magnetization curves is observed below 50 K. A spin glass transition at 50 K has been reported from studies on thin films and single crystals of $BiFeO_3$ [28,29]. The temperature at which a maximum is observed in the ZFC magnetization curve has been found to follow $H^{2/3}$ dependence according to the well-known Almeida-Thouless line corresponding to a mean-field spin glass system [28].

A drastic difference in the nature of the M-T curve is observed after substitution. The zero field cooled magnetization of x = 0.05 shows a large decrease in the magnetization with increasing temperature, down to 55 K, close to the spin glass transition temperature reported for BFO. Apart from this, a minimum in the ZFC magnetization is observed around 240 K. It may be recalled that a divergence between FC and ZFC magnetizations is reported below 240 K for single crystal BFO, ascribed to the spin glass behavior [29]. On the other hand, the x = 0.08 sample shows a well-defined peak (T_p) around 12 K indicating a spin-glass-like behavior. The x = 0.1 sample shows a broader peak compared to that for x = 0.08 with T_p

around 30 K. However, a close examination of the peak (as shown in the inset of figure 4.23) suggests a broad maximum with a clear slope change around 12 K showing a shoulder and another maximum at 32 K. For samples with $0.1 \leq x \leq 0.125$ the shoulder (T_{max1}) is still observed at 12 K with a T_{max2} around 40 K is observed as shown in figure 4.24. It is interesting to note that T_{max1} is almost constant with the degree of substitution whereas the T_{max2} shows a shift with substitution as shown in figure 4.24. ZFC curves for the compositions with *Pbnm* structure is shown in figure 4.25 for comparison. In the *R3c* region, T_p (T_{max2}) shifts towards higher temperature with the degree of substitution whereas in the *Pbnm* region, T_p shifts towards lower temperatures. T_p vs x in $Bi_{1-x}Ca_xFe_{1-x}Mn_xO_3$ is shown in figure 4.26. T_p increases with substitution and shows a maximum (44 K) at x = 0.15 then decreases for higher compositions. x = 0.4 sample shows a T_p = 37 K. It should be noted that x = 0.15 falls within the MPB region and around which enhanced magnetic parameters are observed. M_{max} (M at T_p) from the ZFC magnetization curves is plotted in the inset of figure 4.26, which also show a similar trend showing a maximum at x = 0.175.

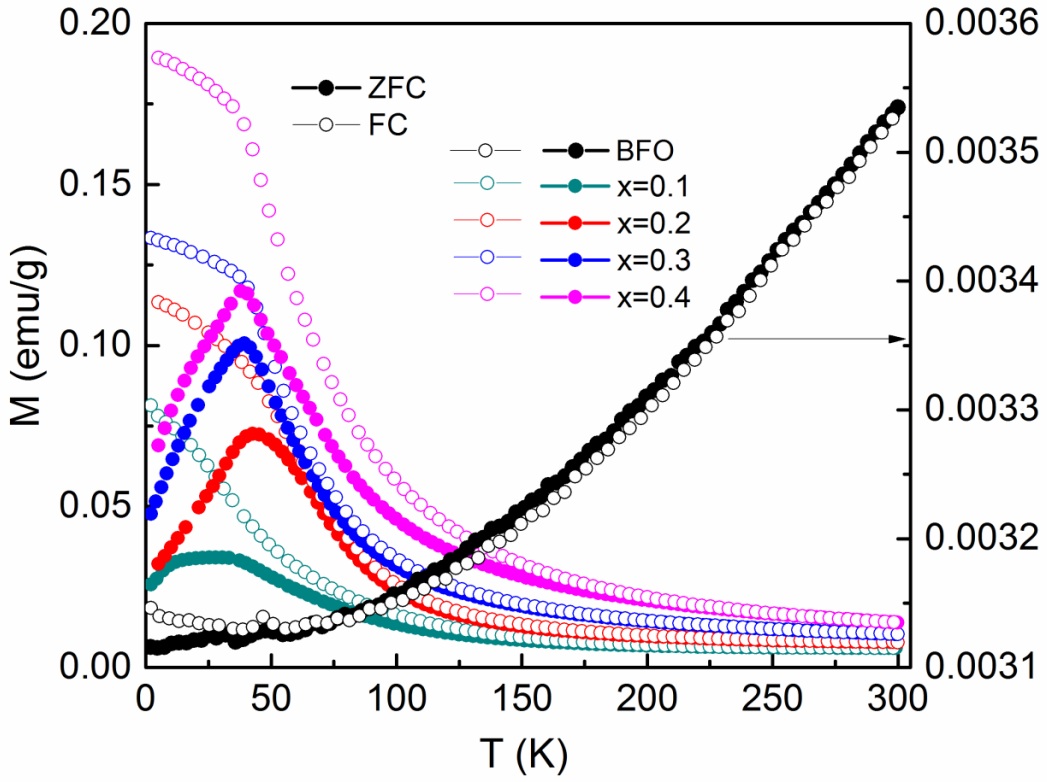

Figure 4.22. FC and ZFC magnetization curves of $Bi_{1-x}Ca_xFe_{1-x}Mn_xO_3$.

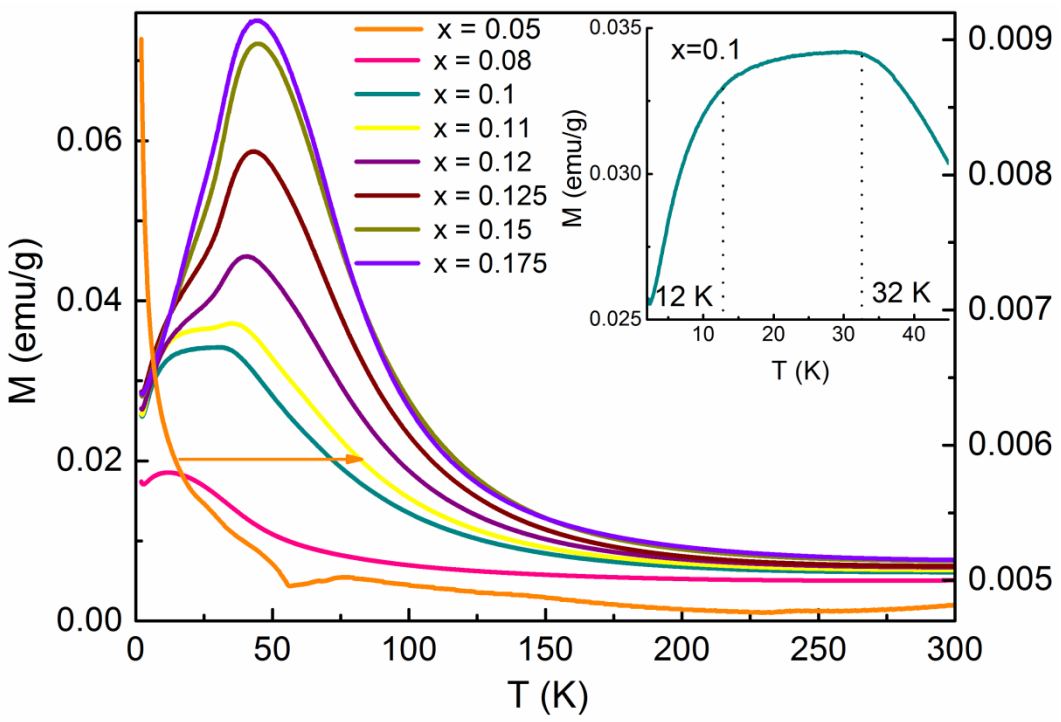

Figure 4.23. ZFC magnetization curves of $Bi_{1-x}Ca_xFe_{1-x}Mn_xO_3$ for $0.05 \leq x \leq 0.175$.

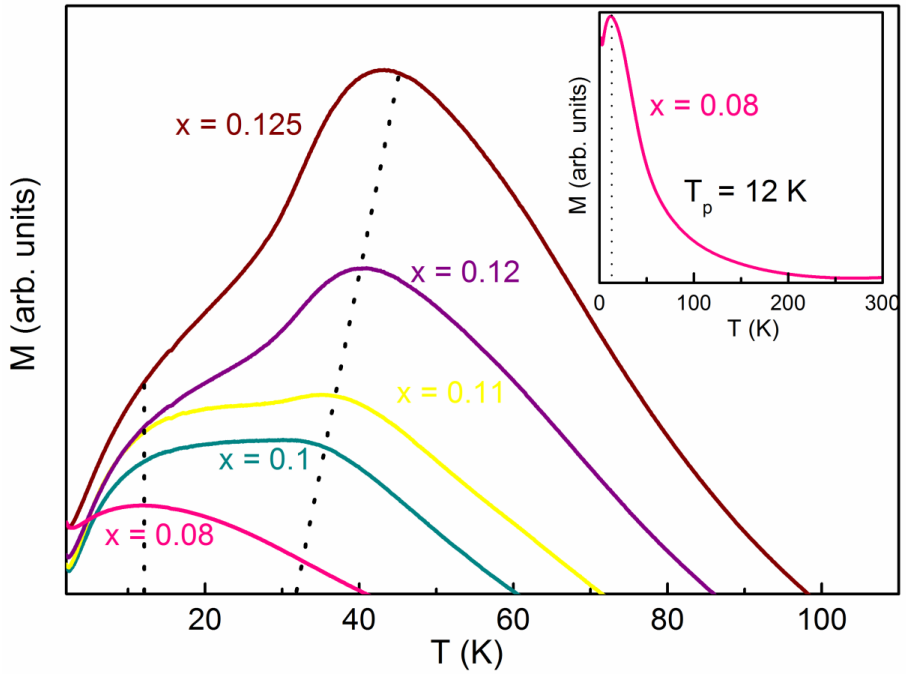

Figure 4.24. Magnified view of the ZFC magnetization curves of x = 0.1, 0.11, 0.12, and 0. 125, showing the two different peaks.

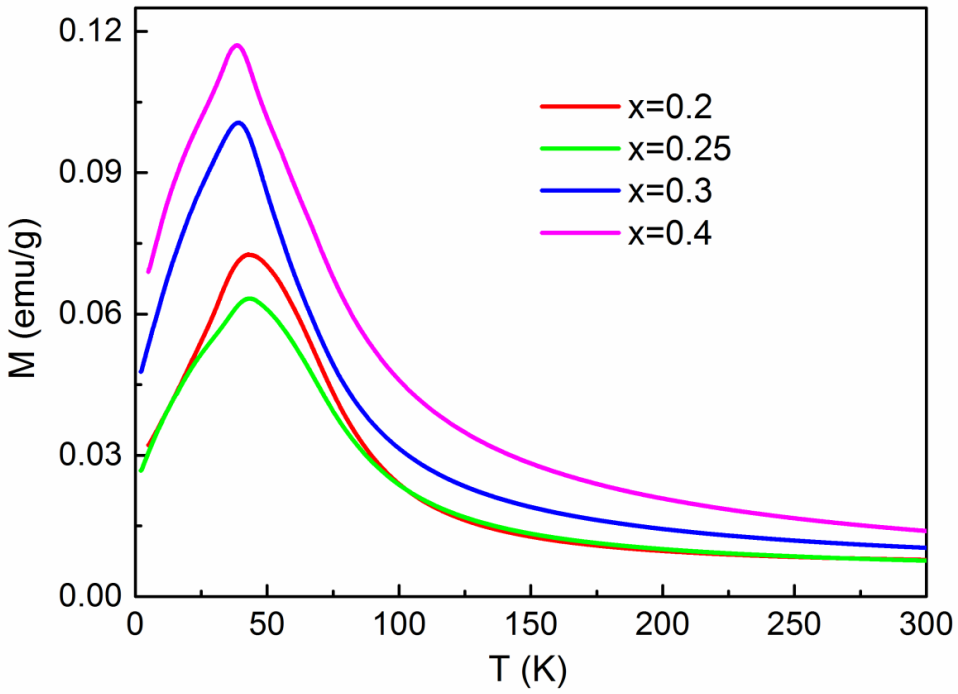

Figure 4.25. ZFC magnetization curves of $Bi_{1-x}Ca_xFe_{1-x}Mn_xO_3$ for $0.2 \leq x \leq 0.4$ having the *Pbnm* structure.

Bifurcation of ZFC and FC magnetizations much above the T_p (close to room temperature) implies some kind of magnetic interaction in the samples above T_p. The two transitions observed indicate a re-entrant spin-glass-like behavior of the system. Re-entrant spin glass system can be defined as systems, where more than one magnetic transition occurs, like the paramagnetic state to ferro(FM)/antiferromagnetic(AFM) state and FM/AFM to spin glass state [30-33]. In $Bi_{1-x}Ca_xFe_{1-x}Mn_xO_3$, the re-entrant spin glass state occurs possibly due to the competing FM and AFM exchange interactions among Mn^{3+}, $Mn^{4+,}$ and Fe^{3+}.

It is possible that the spin glass transition shown by the samples probably depends on the Mn^{3+}/Mn^{4+} ratio. As discussed in section 4.5 and 4.6, higher Mn^{3+} content is observed around the structural transition region which could be leading to the higher T_p around this region. It is difficult to conclude on this spin glass transition observed with the current data. AC susceptibility measurements and neutron diffraction analysis can give more information on the origin of the spin glass nature of the different systems.

Various possibilities for the observed spin glass transition in $Bi_{1-x}Ca_xFe_{1-x}Mn_xO_3$ systems have been discussed in section 3.5.2. Additionally, Sundaresan *et al.* [34] have reported that stoichiometric $BiMnO_3$ is not ferromagnetic and shows a spin-glass-like transition at very low temperatures. Belik *et al.* [35] suggested that in $BiMnO_3$, there is a

low-temperature anomaly below 20 K. Thus, it is possible that in the $Bi_{1-x}Ca_xFe_{1-x}Mn_xO_3$ compositions, the anomaly in the ZFC curves below 20 K, which is independent of *x*, could be due to phase segregation, that is, the presence of Bi- and Mn-rich phases similar to that of $BiMnO_3$. Similar results are reported, due to the presence of $TbMnO_3$-rich phase, in the case of $(La,Tb)_{2/3}Ca_{1/3}MnO_3$ [36].

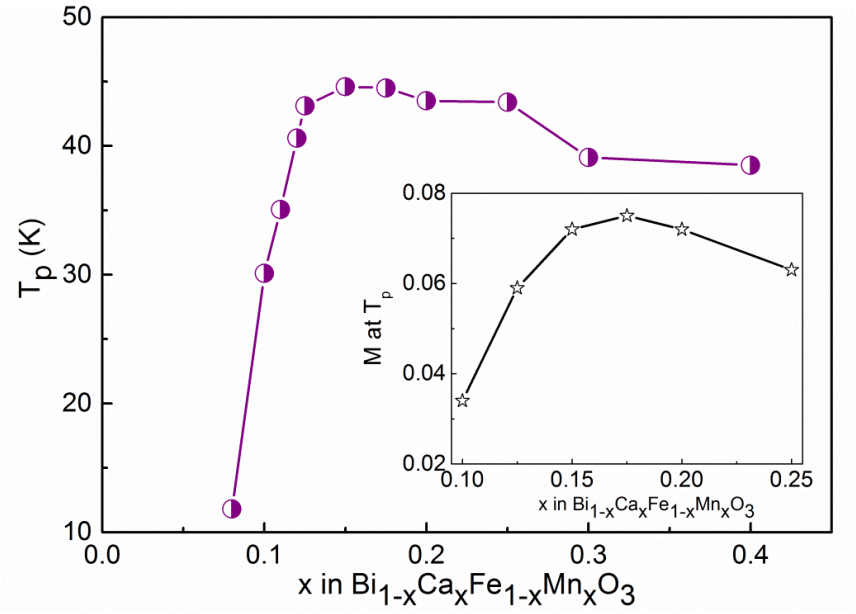

Figure 4.26. T_p vs *x* of $Bi_{1-x}Ca_xFe_{1-x}Mn_xO_3$. The inset shows M_{max} (M at T_p) vs. *x*.

Figures 4.27 and 4.29 show the ZFC magnetization curves measured at different magnetic fields for the compositions $x = 0.08$ and 0.1 in the rhombohedral structural region, respectively. These two compositions showed a wide difference in the nature of the ZFC magnetization curves measured at 500 Oe (see figure 4.24). With increasing the magnetic field, T_p is shifted towards lower temperatures, and the maximum is almost disappeared at higher measuring field (for $x = 0.08$, H = 3000 Oe and for $x = 0.1$, H = 5000 Oe). At lower fields, $x = 0.1$ shows a broad peak which becomes sharper with increasing the field. Figures 4.28 and 4.30 show the variation of T_p with H. The variation follows the Almeida-Thouless (A-T) line corresponding to the equation,

$$H \; \alpha \; (1-T_p/T_f)^{3/2}$$

where T_p is the peak temperature, and T_f is the spin glass freezing temperature at H = 0 [37,38]. A linear decrease in the value of T_p is observed as a function of $H^{2/3}$ for both $x = 0.08$ and $x = 0.1$, according to the A-T equation, suggesting spin glass nature of the compositions.

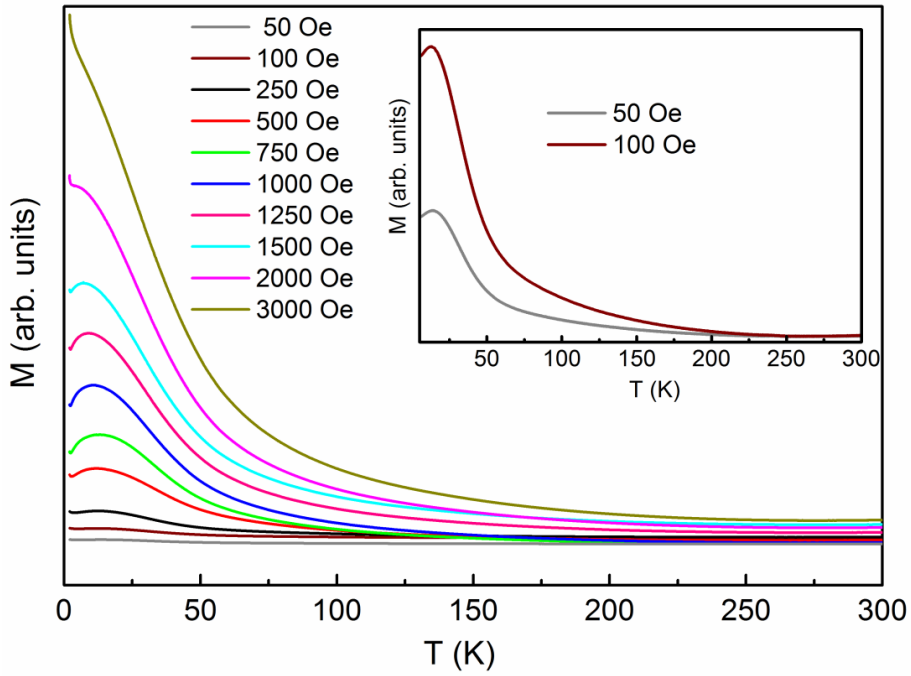

Figure 4.27. ZFC magnetization curves of x = 0.08 at different magnetic fields. The inset shows the magnified view for H= 50 and 100 Oe.

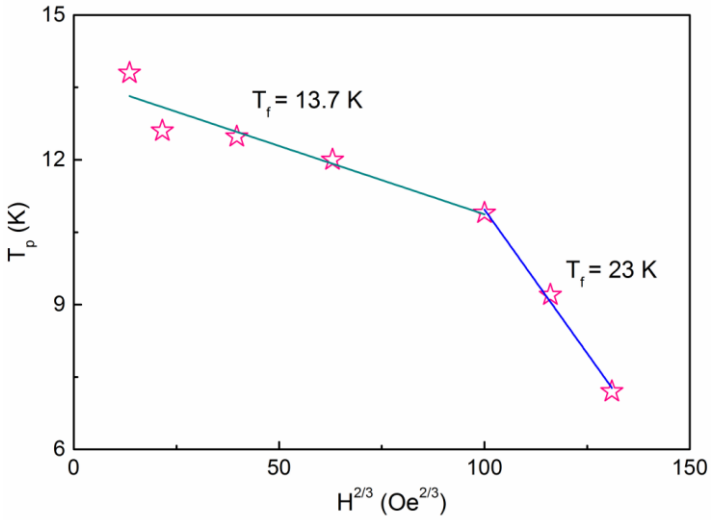

Figure 4.28. Variation of T_p vs applied magnetic field for x = 0.08. The green and blue lines are the A-T fit at low- and high-field regions, respectively.

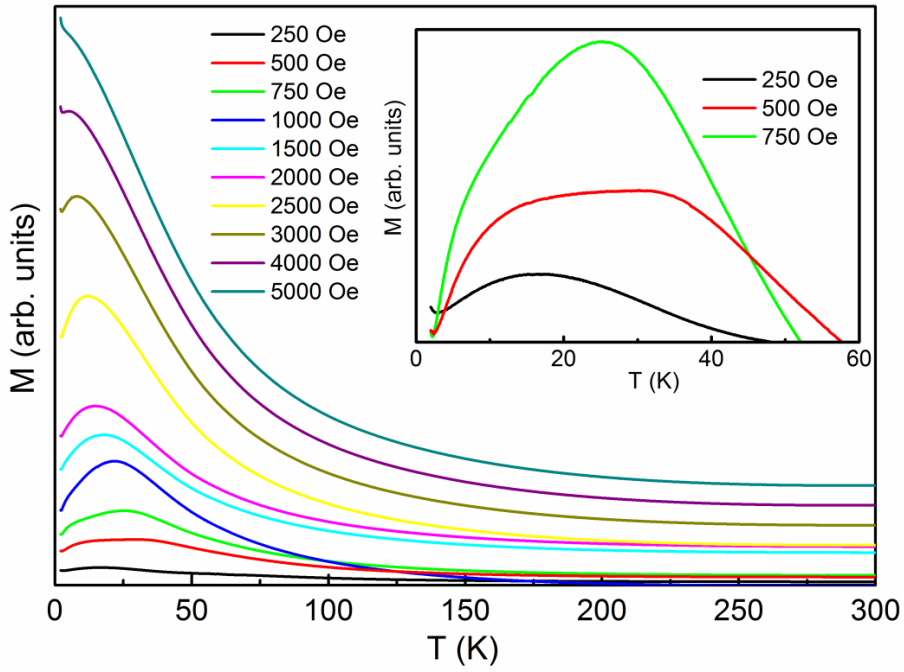

Figure 4.29. ZFC magnetization curves of x = 0.1 at different magnetic fields. Inset shows the magnified view for H= 250, 500, and 750 Oe.

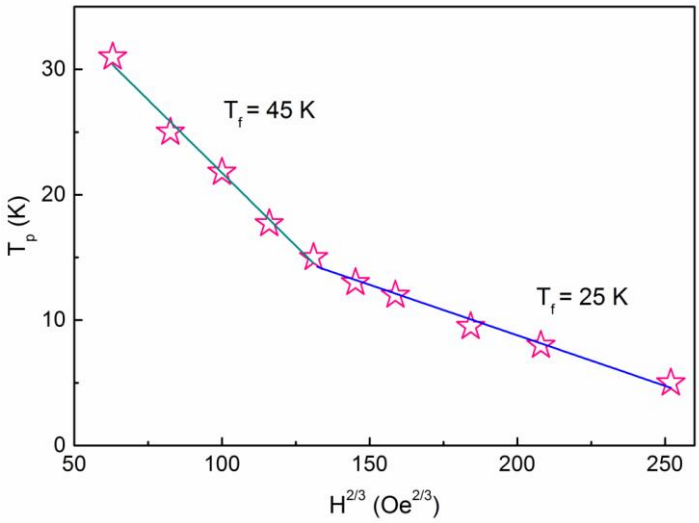

Figure 4.30. Variation of T_p vs applied magnetic field for x = 0.1. The green and blue lines are the AT fit at low- and high-field regions, respectively.

For both the compositions, two linear regions are observed in the low-field and high-field regions. Singh M K *et al* [28] have observed such two linear regions for undoped BFO wherein they have fitted the AT line only for the high field region. There are similar reports where such two linear regions are reported in other spin glass/cluster glass systems [39-43]. As explained, x = 0.1 sample shows a broad peak at 500 Oe, possibly due to the overlapping

of the peak around 10 K and one around 30 K whereas x = 0.08 show only one peak at 12 K within the measurement range (5 to 300 K). We have fitted two AT lines in order to check the contribution from these two peaks. Almost comparable T_f is obtained for x = 0.08 (T_f = 23 K) and x = 0.1 (T_f = 25 K) in the high-field region whereas in the low-field region, x = 0.08 shows a T_f = 14 K and x = 0.1 shows a higher T_f = 45 K.

4.7.3. High-temperature M-T measurements

M-T measurements above the room temperature have been carried out (figure 4.31) in an applied magnetic field of 5000 Oe to find out the magnetic transition temperatures of the different samples. Unsubstituted BFO shows a very weak ferromagnetic transition at the Neel temperature of 650 K, similar to that reported in the literature [44]. Due to the low magnetic moment of BFO, a clear transition could not be observed. The x = 0.05 sample shows a magnetic transition at 620 K and x = 0.25 shows a transition at 610 K. For x = 0.175 (T_N = 585 K), M-H curves are measured above and below the Neel temperature (figure 4.32) to confirm that transition observed is a magnetic transition. M-H curve at 525 K below the transition temperature shows a large magnetic hysteresis loop whereas the M-H curve measured at 600 K (above T_N) shows a linear variation with the field, suggesting paramagnetic nature. This confirms that the large increase in the magnetization below 585 K is a weak ferromagnetic transition. The magnetic transition temperatures obtained from the M-T measurements are plotted against the composition in figure 4.33 (the transition temperature is taken as the point of slope change in the M-T curve). Upon co-substitution, T_N varies almost linearly with substitution, with a relatively lower value for x = 0.175 in the MPB region. No visible magnetic transition is observed for the x = 0.3 and x = 0.4 compositions and the magnetization continuously decreases with increasing temperature. The x = 0.4 sample showed a linear variation of magnetization with the magnetic field at 300 K (see figure 4.15) which suggested its paramagnetic nature. The observed magnetic transitions in the x < 0.3 compositional region further confirms the single phase nature and suggest the absence of any impurity phase. Very high coercivity for the Ca-substituted $BiFeO_3$ at room temperature can be due to the impurity phase of calcium hexaferrite (T_C = 718 K) [45]. However, we did not observe any other magnetic transition in the high-temperature region which confirms that the higher magnetic parameters at room temperature are intrinsic.

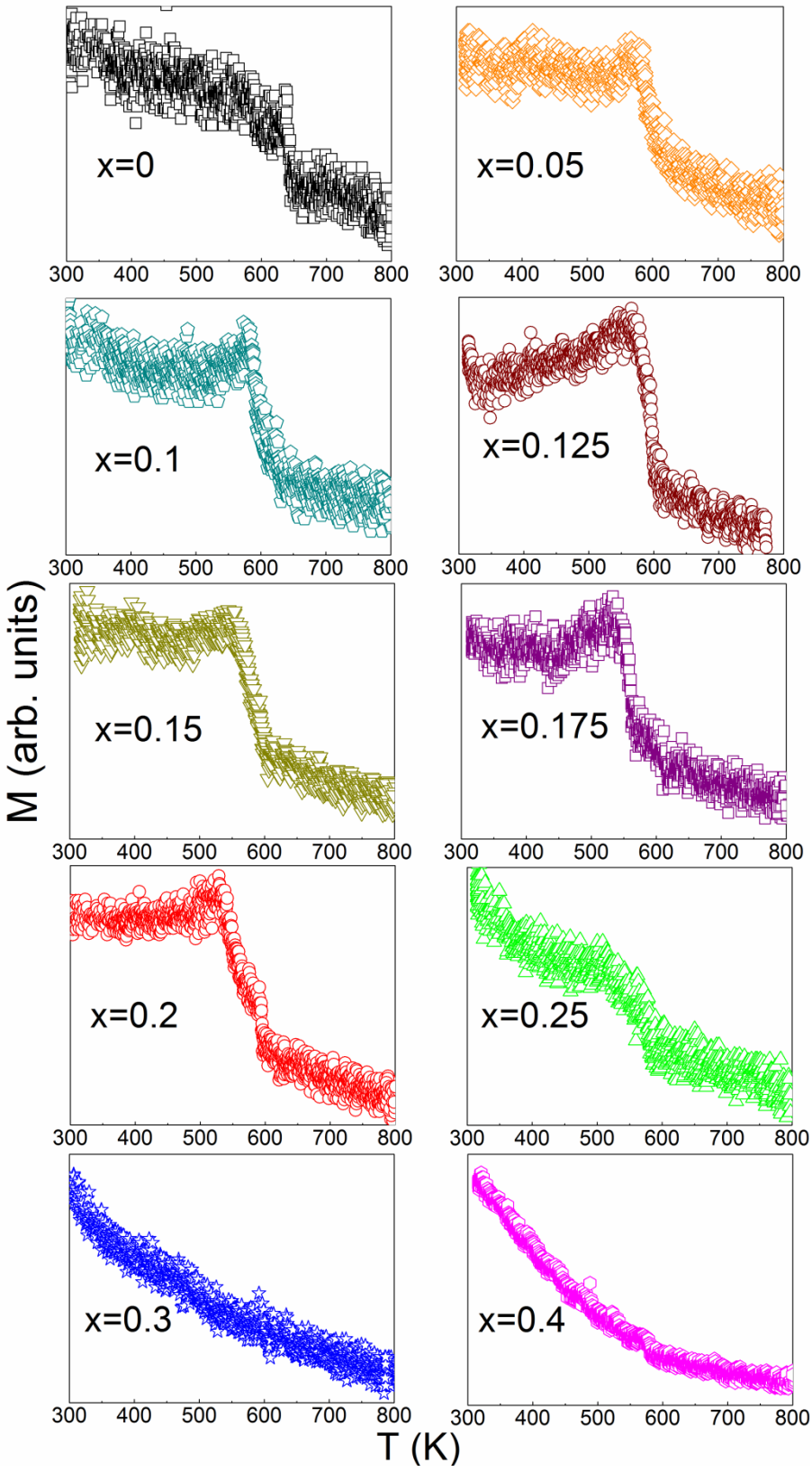

Figure 4.31. M-T curves of $Bi_{1-x}Ca_xFe_{1-x}Mn_xO_3$ measured above room temperature.

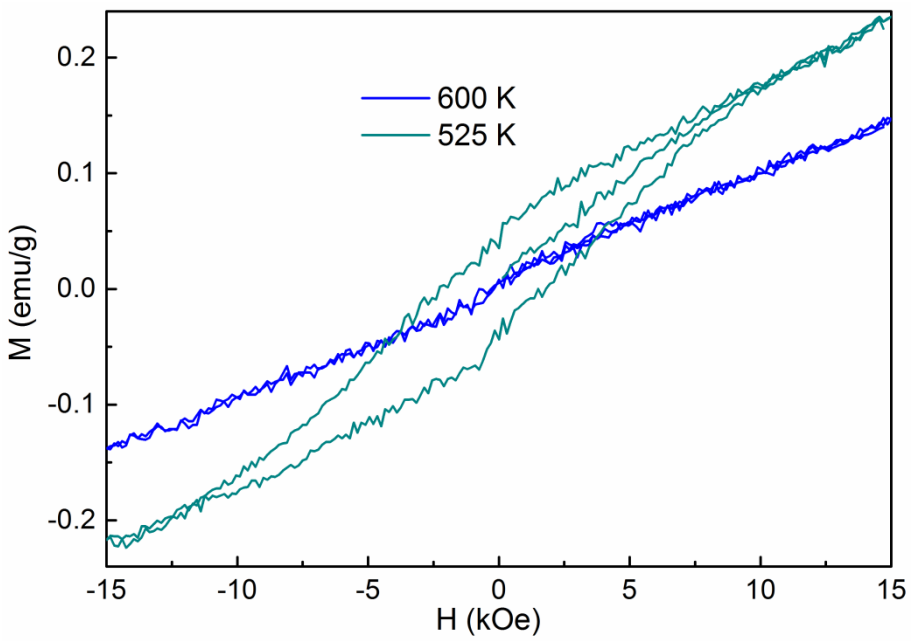

Figure 4.32. M-H curves of x = 0.175 above (600 K) and below (525K) the T_N (585 K).

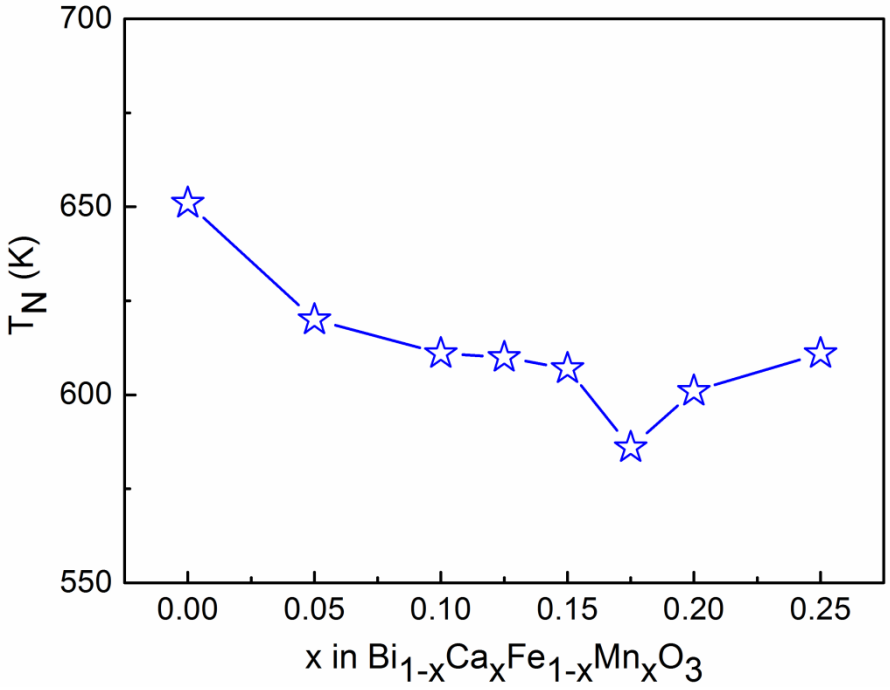

Figure 4.33. T_N vs x of $Bi_{1-x}Ca_xFe_{1-x}Mn_xO_3$.

4.8. Dielectric properties

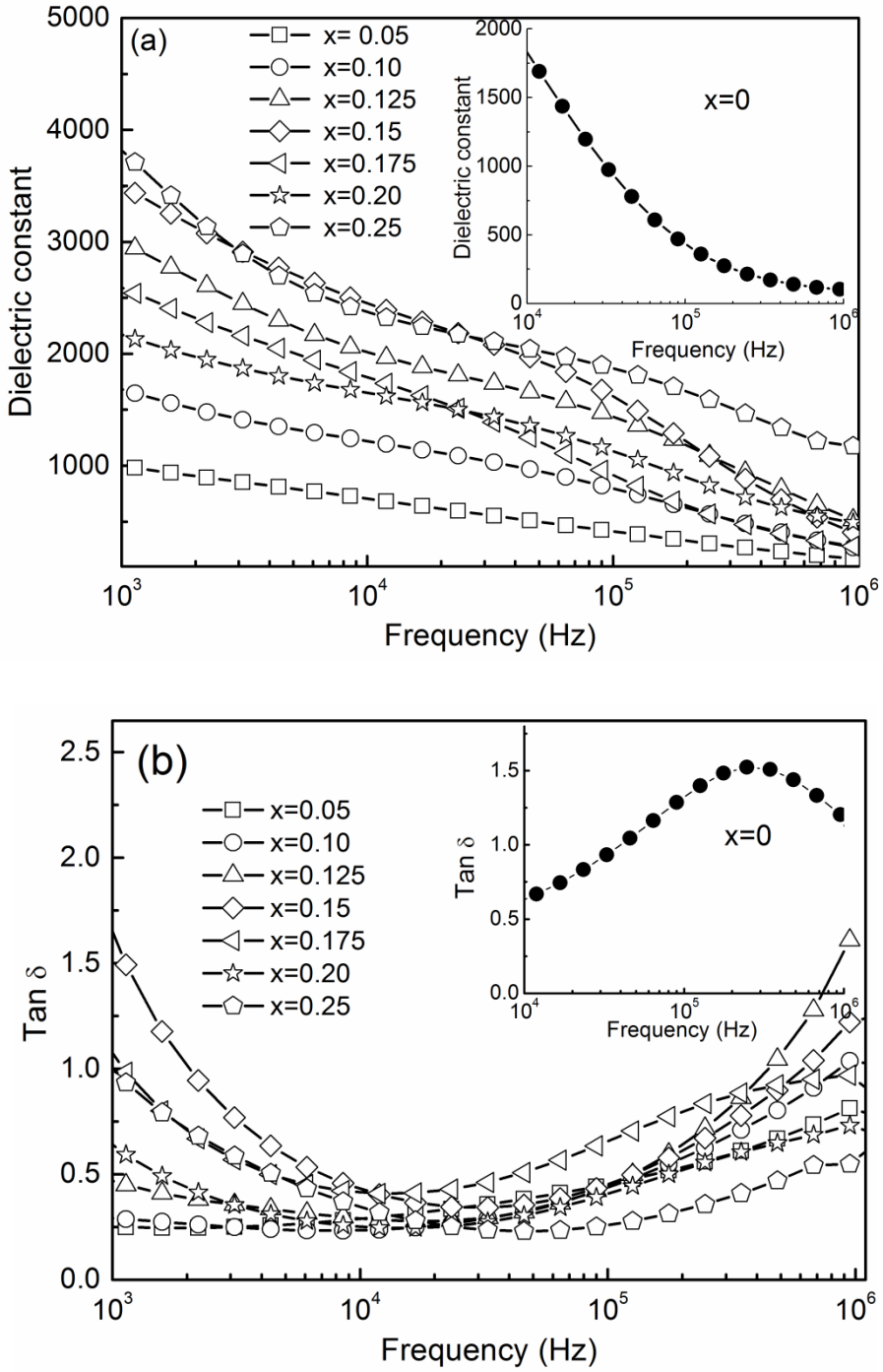

Figure 4.34. (a) Dielectric constant and (b) dissipation factor of $Bi_{1-x}Ca_xFe_{1-x}Mn_xO_3$, measured as a function of frequency. The insets show the dielectric spectra and dissipation factor of BFO (x = 0).

Dielectric measurements are carried on all samples in the frequency range of 1 kHz to 1 MHz. Figure 4.34(a) shows that the dielectric constant decreases with increasing frequency for all the compositions. Compositions with $x > 0.25$ showed a high dielectric loss, and hence measurements are not carried out for these compositions. The dielectric constant decreases with increasing frequency and becomes almost constant at higher frequencies. The dielectric loss factor (Tan δ) initially decreases with frequency and then increases at higher frequencies (figure 4.34(b)), showing a minimum in the 10^4-10^5 Hz frequency region for all the substituted compositions. Increase in the loss factor at higher frequencies implies contribution from the charge carriers and influence of space charges at the interface [46].

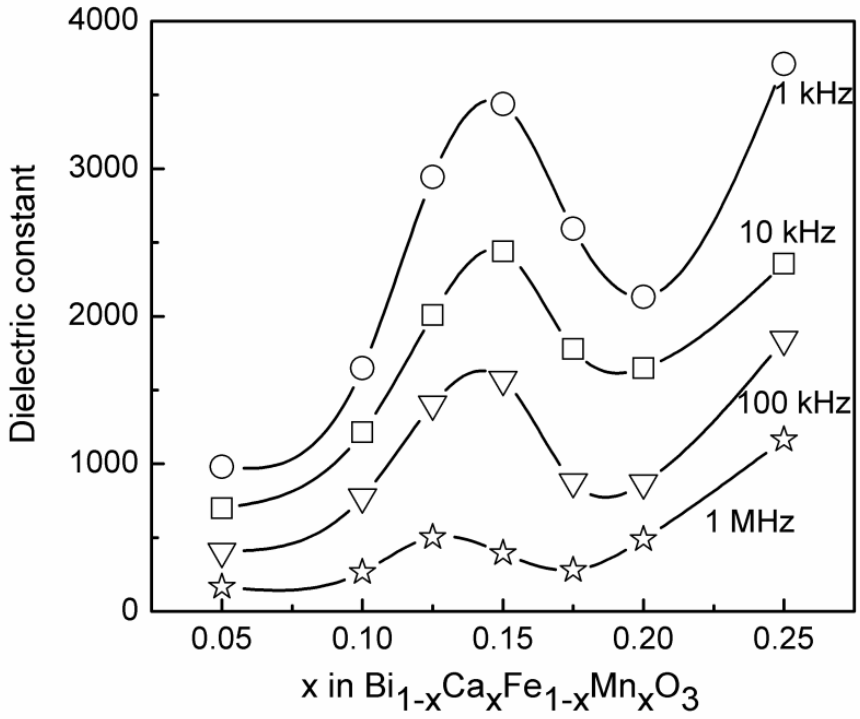

Figure 4.35. The dielectric constant of $Bi_{1-x}Ca_xFe_{1-x}Mn_xO_3$ as a function of x at 1 kHz, 10 kHz,100 kHz, and 1 MHz.

Variation of the dielectric constant at 1 kHz, 10 kHz, 100 kHz and 1 MHz are plotted against x in figure 4.35. Dielectric constant increases with x and reaches a maximum at $x = 0.15$ (MPB region) and then decreases. Higher dielectric constant at $x = 0.15$ can be explained based on the structural parameter, *s-t*, which is the combined effect of the displacement of Fe/Mn and Bi atoms from their actual positions. *s-t*, which is a measure of the polarization, showed a minimum at $x = 0.15$ (figure 4.6). Apart from this, the dielectric constant is also known to depend on the density and microstructure of the materials [47,48].

SEM images of samples (figure 4.7) suggested a dense microstructure in the MPB region which could also contribute to the higher dielectric properties observed in this region. Many ferroelectric compositions are known to exhibit higher polarization in the MPB region [49]. Thus, the higher dielectric constant in the MPB region is likely to be due to higher ferroelectric polarization, as already reported for some substituted $BiFeO_3$ [20,50,51]

4.9. Magnetodielectric properties

Magnetodielectric (MD) constant or magnetocapacitance (MC) is an indirect indication for the coupling of the electric and magnetic orders in magnetoelectrics [52,53]. Due to the higher magnetic parameters and dielectric constant of the substituted compositions, a higher magnetoelectric coupling is expected for the studied compositions. The dielectric constants of the different compositions are measured in a magnetic field of 10 kOe at 1 kHz, and the results are shown in the figure. 4.36. The Magnetodielectric percentage (MD%) is calculated using the formula $[\varepsilon_{(H)} - \varepsilon_{(0)}]/ \varepsilon_{(0)}*100\%$, where $\varepsilon_{(H)}$ is the dielectric constant measured in a field of 10 kOe and $\varepsilon_{(0)}$ is the dielectric constant at zero field [53]. BFO showed almost zero (negligible) value of MD. MD increases with *x* for the rhombohedral structure, and a maximum positive MD of 0.86% is obtained for $x = 0.1$ for the rhombohedral phase. MD decreases in the mixed phase region, with increasing substitution, until $x = 0.175$ and then shows negative values for $x \geq 0.2$ for the orthorhombic structure. The sign of MD depends on the sign of the magnetoelectric coupling coefficient [54]. Also, change in the dielectric constant by the application of a magnetic field implies a change in the polarization of the samples [55]. In multiferroics, electric and magnetic orders are coupled, and hence the strain produced by the magnetic field produces a stress in the material which in turn induces an electric field and thus changes the dielectric property [56].

From the present study, it is inferred that in Ca and Mn co-substituted $BiFeO_3$, positive MD is shown when the structure is rhombohedral and negative MD effect is exhibited by the orthorhombic system. In the MPB region, as the orthorhombic phase content increases, competition between the positive MD by rhombohedral phase and negative MD by the orthorhombic phase occurs and thus the overall MD decreases. Such a composition dependent MD has been reported by Dixit *et al.* [57] for hexagonal $YMn_{1-x}In_xO_3$, where positive and negative MD values are obtained at lower and higher substitution levels, respectively. The sign and magnitude of MD also depend on the magnetic field, temperature, and frequency at which it is measured [58-61]. Kimura *et al.* [58] have shown a maximum

MD with respect to the magnetic field in $TbMnO_3$, which shifts with temperature. Similarly, in $BiMnO_3$, MD (at low temperature) is positive at low fields and shows a negative value at higher fields [54]. Ramachandran *et al.* [61] have reported a maximum MD of +0.2% (at 30 kHz, 80 kOe) at $x = 0.1$ in $Bi_{1-x}Ca_xFeO_3$ and Yang *et al.* [62] have reported +0.3% MD for $BiFe_{1-x}Mn_xO_3$ (at 90 kOe for $x = 0.3$) whereas the present Ca-Mn co-substituted system shows higher MD% at lower magnetic field and frequency.

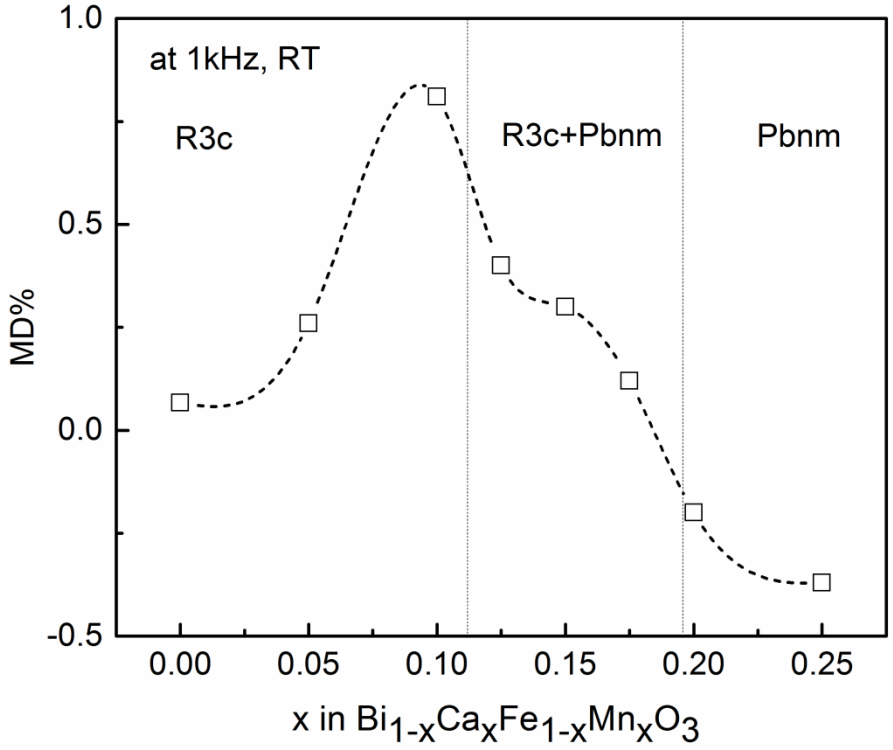

Figure 4.36. Magnetodielectric data (MD%) of $Bi_{1-x}Ca_xFe_{1-x}Mn_xO_3$ measured at a frequency of 1 kHz and in a field of 10 kOe. The height of the symbol represents the error in the value of MD.

The reported values for MD in the literature are very low, compared to the value shown by the Ca-Mn co-substituted system in the present work (at 1 kHz, 10 kOe). The magnetodielectric value of ~1% at 10 kOe reported in this work for bulk BFO based system is relatively larger when compared to that reported for other single phase materials and composites. In conclusion, strong correlations are found between the structure and the properties exhibited by Ca and Mn co-substituted bulk $BiFeO_3$. Maximum magnetic and dielectric parameters are observed in the morphotropic phase boundary region $0.12 \leq x \leq 0.175$ in $Bi_{1-x}Ca_xFe_{1-x}Mn_xO_3$. Therefore, the enhanced magnetic and dielectric properties of bulk $Bi_{1-x}Ca_xFe_{1-x}Mn_xO_3$ in the MPB region is expected to show enhanced magnetoelectric coupling.

Table 4.1. Comparison of MD values, taken from literature, for the various substituted BFO systems at the Bi- or Mn-site.

Substituent	**MD(%), magnetic field and frequency**	**Reference**
Ca (10%)	+ *0.2* at 80 kOe and 30 kHz	61
Mn (30%)	+ *0.3* at 90 kOe and 100 kHz	62
Sc (30%)	+ *3.36* at 8 kOe and 10 kHz	63
Ba (25%)	+ *0.1* at 60 kOe and 10 kHz	64
La (15%)	+*0.14* at 80 kOe and 10 kHz	65
Ba-Ti co-substitution (20%)	- *0.25* at 9 kOe and 1 kHz	66
Pr-Cr co-substitution (10%)	+*1* at 6 kOe and 1kHz	67
Ca-Mn co-substitution (10%)	***+0.86*** at 10 kOe and 1kHz	***Present study***

4.10. Conclusions

Bulk polycrystalline $Bi_{1-x}Ca_xFe_{1-x}Mn_xO_3$ compositions for $0 \leq x \leq 0.4$ are prepared by solid state method and their structural, magnetic and dielectric properties are studied. Rietveld refinement analysis of the XRD patterns revealed rhombohedral structure for $x \leq 0.11$ and orthorhombic structure for $x \geq 0.2$. Compositions with $0.12 \leq x \leq 0.175$ showed mixed phase behaviour with both rhombohedral and orthorhombic phases. Raman spectral studies also supported complete structural transformation above $x = 0.175$. XPS analysis and redox titration studies showed that Mn^{4+} is the major species in the co-substituted system for the *R3c* and *Pbnm* phases, whereas higher Mn^{3+} content was observed for $x = 0.15$ and $x = 0.175$ (mixed phase/MPB). The number of oxygen vacancies derived from oxygen 1s XPS spectra also showed a similar trend. Room temperature M-H curves showed that the

samples have antiferromagnetic behaviour with weak ferromagnetic characteristics. High coercivity, remanence, and magnetization are observed in the MPB region which is possibly due to the higher Fe-O-Fe angle observed, apart from the microstructure. Weak ferromagnetism obtained in the samples can be attributed to canted antiferromagnetism and Mn^{3+}-Mn^{4+} double exchange interaction. Low-temperature M-H curves have a ferromagnetic behavior with a high magnetization values showing anomaly around the structural phase transition region. Low-temperature ZFC-FC magnetic measurements of the samples indicated a spin-glass-like behavior of the samples showing a peak around 40 K for all the compositions. The spin glass transition temperature was found to be composition dependent showing a maximum at $x = 0.15$ which is within the MPB region. The observed magnetic transition from the high-temperature magnetization measurements confirmed the intrinsic magnetic nature of the samples. Similar to the magnetic properties, higher dielectric constants are also observed in the MPB region. Magnetodielectric studies showed positive values for the rhombohedral structure and negative values for the orthorhombic structure, with a maximum MD for the rhombohedral structure closer to the onset of the MPB region, with relatively less rhombohedral distortion. The relatively higher magnetodielectric effect, with enhanced magnetic parameters and higher dielectric properties in the MPB region of bulk Ca-Mn co-substituted $BiFeO_3$, suggest better magnetoelectric coupling suitable for applications.

References

[1] Sosnowska I, Schafer W, Kockelmann W, Andersen K H and Troyanchuk I O 2002 *Appl. Phys.* A **74** S1040

[2] Arnold D C, Knight K S, Morrison F D and Lightfoot P 2009 *Phys. Rev. Lett*. **102** 027602

[3] Megaw H D and Darlington C N W 1975 *Acta Cryst.* A **31** 161

[4] Kwei G H, Lawson A C, Billinge S J and Cheong S W 1993 *J. Phys. Chem.* **97** 2368

[5] Selbach S M, Tybell T, Einarsrud M A and Grande T 2007 *Chem. Mater*. **19** 6478

[6] Ghosh A K, Dwivedi G D, Chatterjee B, Rana B, Barman A, Chatterjee S and Yang H D 2013 *Solid State Comm.* **166** 22

[7] Ramachandran B, Dixit A, Naik R, Lawes G and Ramachandra Rao M S 2012 *J. Appl. Phys.***111** 023910.

[8] Feng Y N, Wang H C, Luo Y D, Shen Y and Lin Y H 2013 *J. Appl. Phys.* **113** 146101

[9] Schiemer J A, Withers R L, Liu Y and Carpenter M A 2013 *Chem. Mater*. **25** 4436

[10] Schiemer J, Withers R, Noren L, Liu Y, Bourgeois L and Stewart G 2009 *Chem. Mater*. **21** 4223

[11] Galasso F S 1968 *Structure Properties and Preparation of Perovskite-Type Compounds* (Oxford, London)

[12] Anil K P S, Alias J P and Date S K 1998 *J. Mater. Chem.* **8** 1219

[13] Mocherla P S, Karthik C, Ubic R, Ramachandra Rao M S and Sudakar C 2013 *Appl. Phys. Lett.* **103** 022910

[14] Ponce S, Pena M A and Fierro J L 2000 *Appl. Catal.* B **24** 193

[15] Sati P C, Arora M, Chauhan S, Kumar M and Chhoker S 2014 *J. Phys. Chem. Solids* **75** 105

[16] Singh H and Yadav KL 2011 *J. Phys. Condens. Matter*. **23** 385901

[17] Dahiya R, Agarwal A, Sanghi S, Hooda A and Godara P 2015 *J. Magn. Magn. Mater*. **385** 175

[18] Coey J M, Viret M and Von Molnar S 2009 *Adv. Phys.* **58** 571

[19] Yuan G L, Or S W and Chan H L 2007 *J. Phys. D: Appl. Phys*. **40** 1196

[20] Troyanchuk I O, Karpinsky D V, Bushinsky M V, Khomchenko V A, Kakazei G N, Araujo J P, Tovar M, Sikolenko V, Efimov V and Kholkin A L 2011 *Phys. Rev.* B **83** 054109

[21] Thakuria P and Joy P A 2012. *Solid State Commun.* **152** 1609

[22] Karpinsky D V, Troyanchuk I O, Zheludkevich A L, Ignatenko O V, Silibin M V and Sikolenko V V 2016 *Phys. Solid State* **58** 1590

[23] Herzer G 1990 *IEEE Trans. Mag.* **26** 1397

[24] Day R, Fuller M and Schmidt V A 1977 *Phys. Earth. Planet. Inter.***13** 260

[25] Acharya S, Sutradhar S, Mandal J, Mukhopadhyay K, Deb A K and Chakrabarti P K 2012 *J. Magn. Magn. Mater*. **324** 4209.

[26] Dagotto E, Hotta T and Moreo A 2001 *Phys. Rep.* **344** 1.

[27] Wu T, Ogale S B, Garrison J E, Nagaraj B, Biswas A, Chen Z, Greene R L, Ramesh R, Venkatesan T and Millis A J 2001 *Phys. Rev. Lett*. **86** 5998.

[28] Singh M K, Katiyar R S, Prellier W and Scott J F 2008 *J. Phys. Condens. Matter.* **21** 042202

[29] Singh M K, Prellier W, Singh M P, Katiyar R S and Scott J F 2008 *Phys. Rev.* B **77** 144403

[30] Mukherjee S, Ranganathan R, Anilkumar P S and Joy P A 1996 *Phys. Rev.* B **54** 9267

[31] Nam D N, Mathieu R, Nordblad P, Khiem N V and Phuc N X 2000 *Phys. Rev.* B **62** 8989

[32] Dho J, Kim W S and Hur N H 2002 *Phys. Rev. Lett.* **89** 027202

[33] Viswanathan M and Kumar P A 2009 *Phys. Rev.* B **80** 012410

[34] Sundaresan A, Mangalam R V, Iyo A, Tanaka Y and Rao C N R 2008 *J. Mater. Chem.* C **18** 2191

[35] Belik A A and Takayama-Muromachi E 2006 *Inorg. Chem.* **45** 10224

[36] Sankar C R, Vijayanand S and Joy P A 2009 *Solid State Sci.* **11** 714

[37] Martinez B, Obradors X, Balcells L, Rouanet A and Monty C *1998 Phys. Rev. Lett.* **80** 181

[38] Sankar C R, Vijayanand S, Verma S and Joy P A 2007 *Solid State Commun.* **141** 307

[39] Hassnain Jaffari G, Rizwan Ali S, Hasanain S K, Güntherodt G and Ismat Shah S 2010 *J. Appl. Phys.* **108** 06392.

[40] Kremenovic A, Antic B, Spasojevic V, Vucinic-Vasic M, Jaglicic Z, Pirnat J and Trontelj Z 2005 *J. Phys. Condens. Matter*. **17** 4285.

[41] Kumar A, Katiyar R S, Rinaldi C, Lushnikov S G and Shaplygina T A 2008 *Appl. Phys. Lett.* **93** 232902.

[42] Chandra S, Khurshid H, Li W, Hadjipanayis G C, Phan M H and Srikanth H 2012 *Phys. Rev.* B **86** 014426.

[43] Topkaya R, Akman Ö, Kazan S, Aktaş B, Durmus Z, Baykal A 2012 *J. Nanoparticle Res* **14** 1156.

[44] Fischer P, PoIomska M, Sosnowska I and Szymanski 1980 *J. Phys. C: Solid State Phys.* **13** 1931

[45] Lanje N Y and Kulkarni D K 2001 *J. Magn. Magn. Mater.* **234** 114

[46] Yan F, Zhu T J, Lai M O and Lu L 2010 *Scripta Mater.* **63** 780

[47] Tang X G, Wang J, Wang X X and Chan H L 2004 *Solid State Commun*. **131** 163

[48] Zhao Z, Buscaglia V, Viviani M, Buscaglia M T, Mitoseriu L, Testino A, Nygren M, Johnsson M and Nanni P 2004 *Phys. Rev.* B **70** 024107

[49] Jaffe B, Cook W R and Jaffe H 1971 *Piezoelectric Ceramics* (Academic, New York)

[50] Eitel R E, Randall C A, Shrout T R, Rehrig P W, Hackenberger W and Park S E 2001 *Jpn. J. Appl. Phys***. 40** 5999.

[51] Zhang S T, Pang L H, Zhang Y, Lu MH and Chen Y F 2006 *J. Appl. Phys.* **100** 114108

[52] Kamba S, Nuzhnyy D, Savinov M, Sebek J, Petzelt J, Prokleska J, Haumont R and Kreisel J 2007 *Phys. Rev.* B **75** 024403

[53] Hur N, Park S, Sharma P A, Guha S and Cheong S W 2004 *Phys. Rev*. B **93** 107207

[54] Kimura T, Kawamoto S, Yamada I, Azuma M, Takano M and Tokura Y 2003 *Phys. Rev*. B **67** 180401

[55] Tirupathi P and Chandra A 2013 *J. Alloys Compd*. 2013 **564** 151

[56] Kumar M and Yadav K L 2006 *J. Appl. Phys.* **100** 74111

[57] Dixit A, Smith A E, Subramanian M A and Lawes G 2010 *Solid State Commun.* **150** 746

[58] Kimura T, Goto T, Shintani H, Ishizaka K, Arima T and Tokura Y 2003 *Nature* **426** 55

[59] Koo Y S, Bonaedy T, Sung K D, Jung J H, Yoon J B, Jo Y H, Jung M H, Lee H J, Koo T Y and Jeong Y H 2007 *Appl. Phys. Lett.* **91** 212903

[60] Yin L H, Yang J, Zhao B C, Liu Y, Tan S G, Tang X W, Dai J M, Song W H and Sun Y P 2013 *J. Appl. Phys.* **113** 214104

[61] Ramachandran B, Dixit A, Naik R, Lawes G and Rao M S R 2012 *Appl. Phys. Lett.* **100** 252902

[62] Yang C H, Koo T Y and Jeong Y H 2005 *Solid State Commun*. **134** 299

[63] Shannigrahi S R, Huang A, Chandrasekhar N, Tripathy D and Adeyeye A O 2007 *Appl. Phys. Lett*. **90** 022901

[64] Singh P and Jung J H 2010 *Physica* B **405** 1086

[65] Le Bras G, Colson D, Forget A, Genand-Riondet N, Tourbot R and Bonville P. 2009 *Phys. Rev.* B **80** 134417

[66] Singh H, Kumar A and Yadav K L 2011 *Mat. Sci. Eng.* B **176** 540

[67] Das R, Gopal Khan G and Mandal K 2012 *J. Appl. Phys.* **111** 104115

Chapter 5

Structural and magnetic properties of $Bi_{1-x}Ca_xFe_{1-y}Mn_yO_3$ ($x \neq y$)

5.1. Introduction

Ca and Mn co-substitution in $BiFeO_3$ was first reported by Tzankov *et al.* in 2005 wherein the structural and magnetic properties of Fe-substituted $Bi_{0.5}Ca_{0.5}MnO_3$ were discussed [1]. Later, the authors reported similar studies in the $Bi_{0.5}Sr_{0.5}Fe_yMn_{1-y}O_3$ system. In both the cases, a decrease in the magnetization with increasing Fe content has been reported [2].Yin *et al.* have reported enhanced magnetic and electrical properties of bulk $Bi_{0.8}Ca_{0.2}Fe_{1-y}Mn_yO_3$ for $0 \leq x \leq 0.5$ [3]. Huang *et al.* have studied the structural and electrical properties of $Bi_{1-x}Ca_xFe_{1-y}Mn_yO_3$ (x = 0, 0.05, 0.10; y = 0, 0.05, 0.10) thin films prepared by sol-gel spin coating method and found that the ferroelectric properties enhanced with increase in the substitution level [4]. Khomchenko *et al.* have reported the structural and magnetic properties of $Bi_{0.9}Ca_{0.1}Fe_{1-y}Mn_yO_3$ ($0 \leq y \leq 0.5$) where it is found that the magnetization increases but with decreasing remanence on increasing the Mn content [5]. In the above reported studies, the Bi-site and Fe-site in $BiFeO_3$ are substituted unequally.

In **chapter 3** we have shown that among the Ca-Mn, Sr-Mn, and Ba-Mn co-substituted $BiFeO_3$ systems, Ca-Mn co-substitution showed better magnetic and dielectric properties. In **chapter 4**, we have discussed the detailed structure-property correlation studies on $Bi_{1-x}Ca_xFe_{1-x}Mn_xO_3$, with equal amounts of substitution at the Bi and Fe sites. $Bi_{1-x}Ca_xFe_{1-x}Mn_xO_3$ showed a rhombohedral *R3c* to orthorhombic *Pbnm* structural transition around x = 0.15 and around this MPB region higher magnetic and dielectric properties are observed. In $Bi_{1-x}Ca_xFe_{1-x}Mn_xO_3$, although manganese is expected only as Mn^{4+} for the charge neutrality, presence of both Mn^{3+} and Mn^{4+} was established from XPS and titration analyses, which could be leading to the higher magnetic properties in this system.

In this chapter, we discuss the structural and magnetic properties of $Bi_{1-x}Ca_xFe_{1-y}Mn_yO_3$ for $x \neq$ y. Different compositions of the Ca-Mn co-substituted system with the general formula $Bi_{1-x}Ca_xFe_{1-y}Mn_yO_3$ ($0 \leq x \leq 0.4$; y = 0.1, 0.2, 0.3, 0.4, 0.5) have been studied (In y = 0.5 series, x = 0.5 and x = 0.6 compositions are synthesised additionally). The objectives are to investigate whether (i) any other combinations of Ca and Mn could show enhanced magnetic properties other than for $x = y$ = 0.15 as discussed in the previous chapter and (ii) any MPB region exists in the $x \neq y$ co-substituted system as found in the $x = y$ system. By varying the calcium and/or manganese substitution content, one can vary the Mn^{3+}/Mn^{4+} ratio and thus alter the structural and magnetic properties of the system. Also, there are no systematic studies reported in the literature on the effect of divalent ion (Ca/Sr/Ba/Pb)

substitution in $BiFe_{1-y}Mn_yO_3$ or the effect of Mn substitution in $Bi_{1-x}A_xFeO_3$. Different compositions in $Bi_{1-x}Ca_xFe_{1-y}Mn_yO_3$ were prepared by the solid state reaction method, as discussed in chapter 2, section 2.1.

5.2. Structure

Powder X-ray diffraction patterns of the different compositions in $Bi_{1-x}Ca_xFe_{1-y}Mn_yO_3$ compositions are shown in figures 5.1 to 5.5. Figures showing the Rietveld refined XRD patterns of selected compositions for different values of *x* and *y* are shown in figures A.1 to A.5 in the Appendix. For the $y = 0.1$ series ($Bi_{1-x}Ca_xFe_{0.9}Mn_{0.1}O_3$), Rietveld refinement analysis of the XRD patterns revealed rhombohedral *R3c* phase for $x \leq 0.1$ and orthorhombic *Pbnm* phase for $x \geq 0.2$ compositions. A mixed phase with *R3c* and *Pbnm* structures is observed for $x = 0.15$. Such a phase transition from *R3c* to *Pbnm* is reported for La and Mn co-substituted $BiFeO_3$ [9]. As shown in figure 5.1(b), the orthorhombic (110) reflection is visible for $x \geq 0.15$, suggesting the presence of the orthorhombic *Pbnm* phase. Similarly, the rhombohedral splitting is found up to $x = 0.1$, with increasing Ca substitution, as evident from figure 5.1(c) and the rhombohedral peaks are absent for $x \geq 0.2$. A small decrease in the splitting of the rhombohedral peaks is observed. The decrease in the *R3c* splitting with Ca substitution in $BiFe_{1-y}Mn_yO_3$ has been reported to be due to the decrease in the rhombohedral distortion [6-8]. The $x = 0.15$ composition shows a broad peak, with a shoulder corresponding to the rhombohedral peak, which is due to the contribution from the reflections of the *R3c* and *Pbnm* phases, suggesting mixed phase behaviour. The $x \geq 0.2$ compositions show a single peak without any splitting, due to the orthorhombic phase.

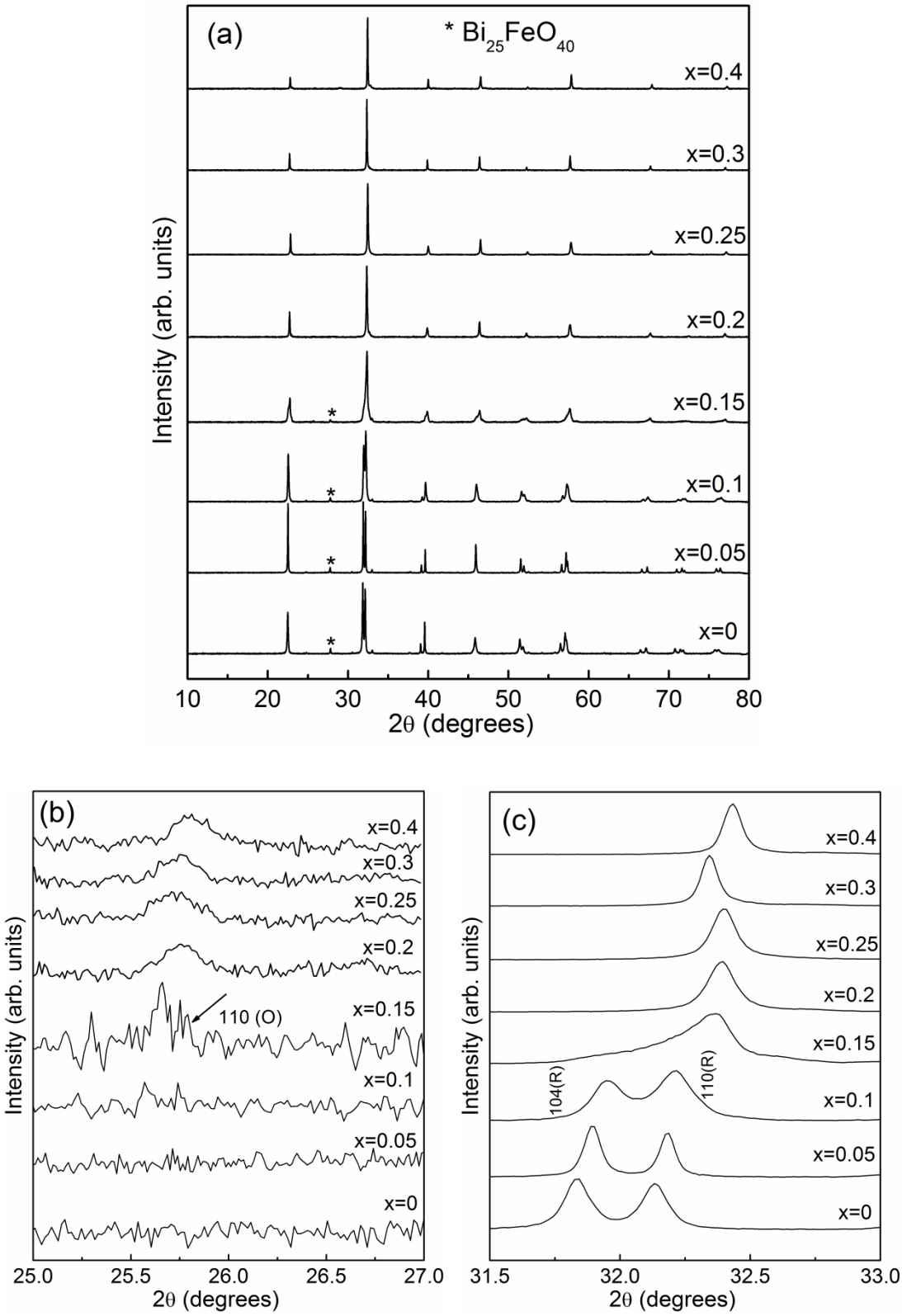

Figure 5.1. (a) X-ray diffraction patterns of $Bi_{1-x}Ca_xFe_{0.9}Mn_{0.1}O_3$. Magnified view of the XRD patterns of $Bi_{1-x}Ca_xFe_{0.9}Mn_{0.1}O_3$ showing (b) the evolution of the (110) orthorhombic reflection around $2\theta = 26°$, and (c) the most intense peak around $2\theta = 32°$ showing the structural change from rhombohedral to orthorhombic. The peak from the impurity phase $Bi_{25}FeO_{40}$ is marked using the symbol '*'.

For the y = 0.2 series ($Bi_{1-x}Ca_xFe_{0.8}Mn_{0.2}O_3$), Rietveld refinement analysis revealed *R3c* phase for $x \leq 0.1$ and *Pbnm* phase for $x \geq 0.2$ and a mixed phase nature for x = 0.15, similar to that observed for the $Bi_{1-x}Ca_xFe_{0.9}Mn_{0.1}O_3$ series (y = 0.1). The orthorhombic (110) reflection is observed for $x \geq 0.15$, as shown in figure 5.2(b), indicating the existence of the *Pbnm* phase The rhombohedral splitting disappears for $x \geq 0.2$ as shown in figure 5.2(c).

In the $Bi_{1-x}Ca_xFe_{0.7}Mn_{0.3}O_3$ series, Rietveld refinement revealed *R3c* phase for $x \leq 0.15$ and *Pbnm* phase for $x \geq 0.25$ with the x = 0.2 composition showing a mixed phase behaviour. Figure 5.3(b) shows that the orthorhombic (110) reflection is present for $x \geq 0.2$. Similarly, the reflections corresponding to the orthorhombic (020), (112), and (200) planes are clearly visible in figure 5.3(c). The composition $Bi_{0.8}Ca_{0.2}Fe_{0.7}Mn_{0.3}O_3$ shows reflections from both the *R3c* and *Pbnm* phases. Unlike the y = 0.1 and 0.2 series, the *R3c* to *Pbnm* structural transformation is clearly visible in the XRD patterns for the y = 0.3 series. The shift in the position of the peaks is more prominent than in the y = 0.1 and 0.2 systems.

It is not possible to prepare single phase $BiFe_{0.6}Mn_{0.4}O_3$ by ordinary solid-state synthesis method. High-pressure synthesis techniques are required for the synthesis of manganese substituted compositions with $x \geq 0.4$ [9,10]. Thus, the broad asymmetric peak in the XRD pattern of $BiFe_{0.6}Mn_{0.4}O_3$ (x = 0 in figure 5.4(c)) could be due to phase separation and/or formation of a different phase for the higher manganese substitution at the Fe site which lowers the rhombohedral distortion [11].). Rietveld refinement analysis of the XRD patterns of different compositions in the $Bi_{1-x}Ca_xFe_{0.6}Mn_{0.4}O_3$ series revealed *R3c* phase for $x \leq 0.1$ and *Pbnm* phase for $x \geq 0.2$. A mixed phase behaviour was observed for x = 0.15 as in the y = 0.1 and y = 0.2 series. With 5% Ca substitution in $BiFe_{0.6}Mn_{0.4}O_3$, the intensity of the rhombohedral (104) reflection increases (figure 5.4(c)). Thus, $Bi_{0.9}Ca_{0.1}Fe_{0.6}Mn_{0.4}O_3$ shows the signatures of the rhombohedral splitting indicating the increase in the structural stability for the *R3c* phase (higher rhombohedral distortion) with Ca substitution. Such an enhanced stability of the *R3c* phase is reported for La and Mn co-substituted $BiFeO_3$ [12]. As evident in figure 5.4(c), $Bi_{0.85}Ca_{0.15}Fe_{0.6}Mn_{0.4}O_3$ (x = 0.15) clearly shows peaks due to both the *R3c* and *Pbnm* phases whereas x = 0.2 shows peaks corresponding to the *Pbnm* phase only. Similarly, the orthorhombic (110) reflection is observed for x = 0.15 as shown in figure 5.4(b).

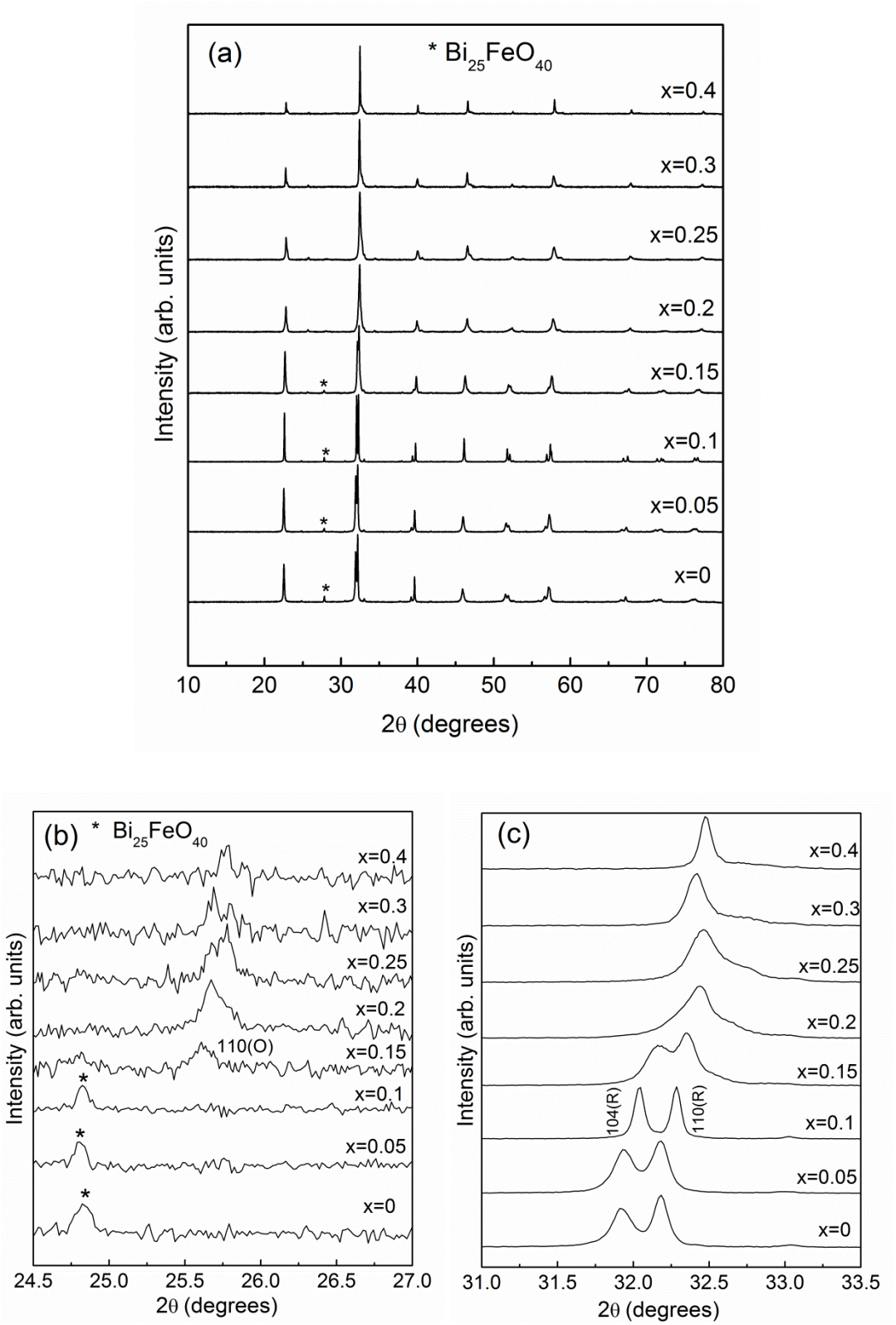

Figure 5.2. (a) X-ray diffraction patterns of $Bi_{1-x}Ca_xFe_{0.8}Mn_{0.2}O_3$. Magnified view of the XRD patterns of $Bi_{1-x}Ca_xFe_{0.8}Mn_{0.2}O_3$ showing (b) the evolution of the (110) orthorhombic reflection around $2\theta = 26°$, and (c) the most intense peak around $2\theta = 32°$ showing structural change from rhombohedral to orthorhombic. The peak from the impurity phase $Bi_{25}FeO_{40}$ is marked using the symbol '*'.

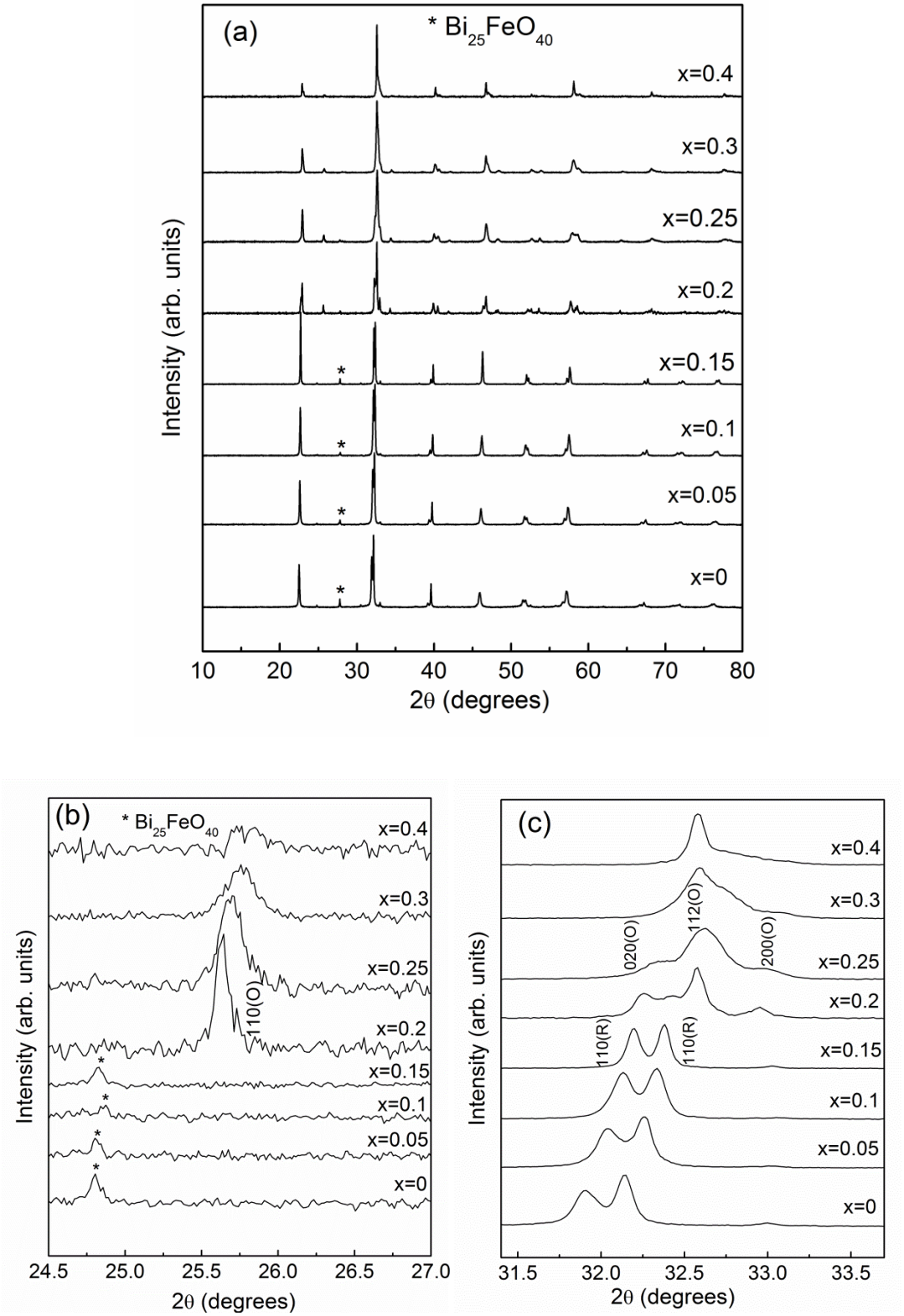

Figure 5.3. (a) X-ray diffraction patterns of $Bi_{1-x}Ca_xFe_{0.7}Mn_{0.3}O_3$. Magnified view of the XRD patterns of $Bi_{1-x}Ca_xFe_{0.7}Mn_{0.3}O_3$ showing (b) the evolution of the (110) orthorhombic reflection around $2\theta = 26°$, and (c) the most intense peak around $2\theta = 32°$ showing the structural change from rhombohedral to orthorhombic. The peak from the impurity phase $Bi_{25}FeO_{40}$ is marked using the symbol '*'.

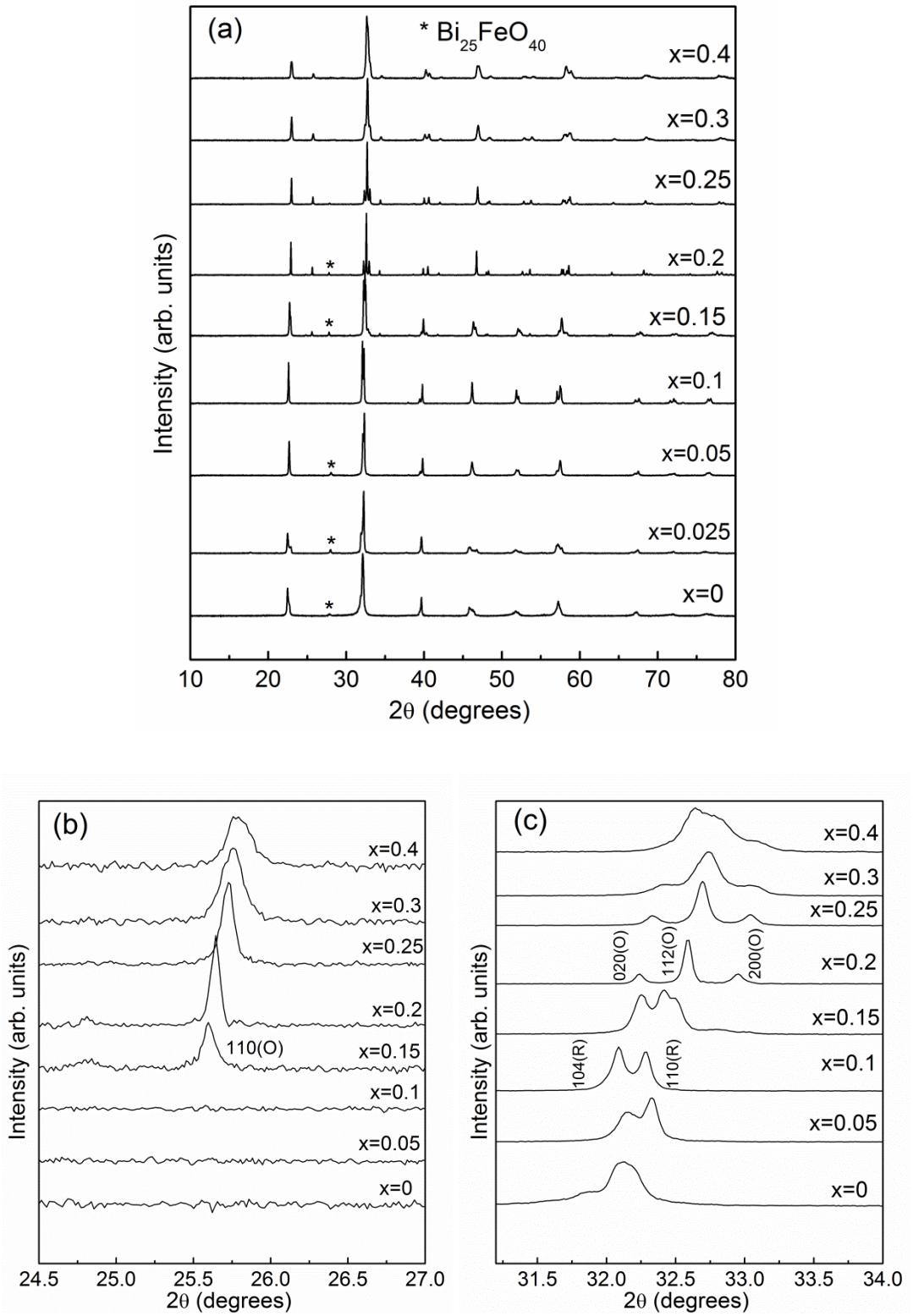

Figure 5.4. (a) X-ray diffraction patterns of $Bi_{1-x}Ca_xFe_{0.6}Mn_{0.4}O_3$. Magnified view of the XRD patterns of $Bi_{1-x}Ca_xFe_{0.4}Mn_{0.6}O_3$ showing (b) the evolution of the (110) orthorhombic reflection around $2\theta = 26°$, and (c) the most intense peak around $2\theta = 32°$ showing structural change from rhombohedral to orthorhombic. The peak from the impurity phase $Bi_{25}FeO_{40}$ is marked using the symbol '*'.

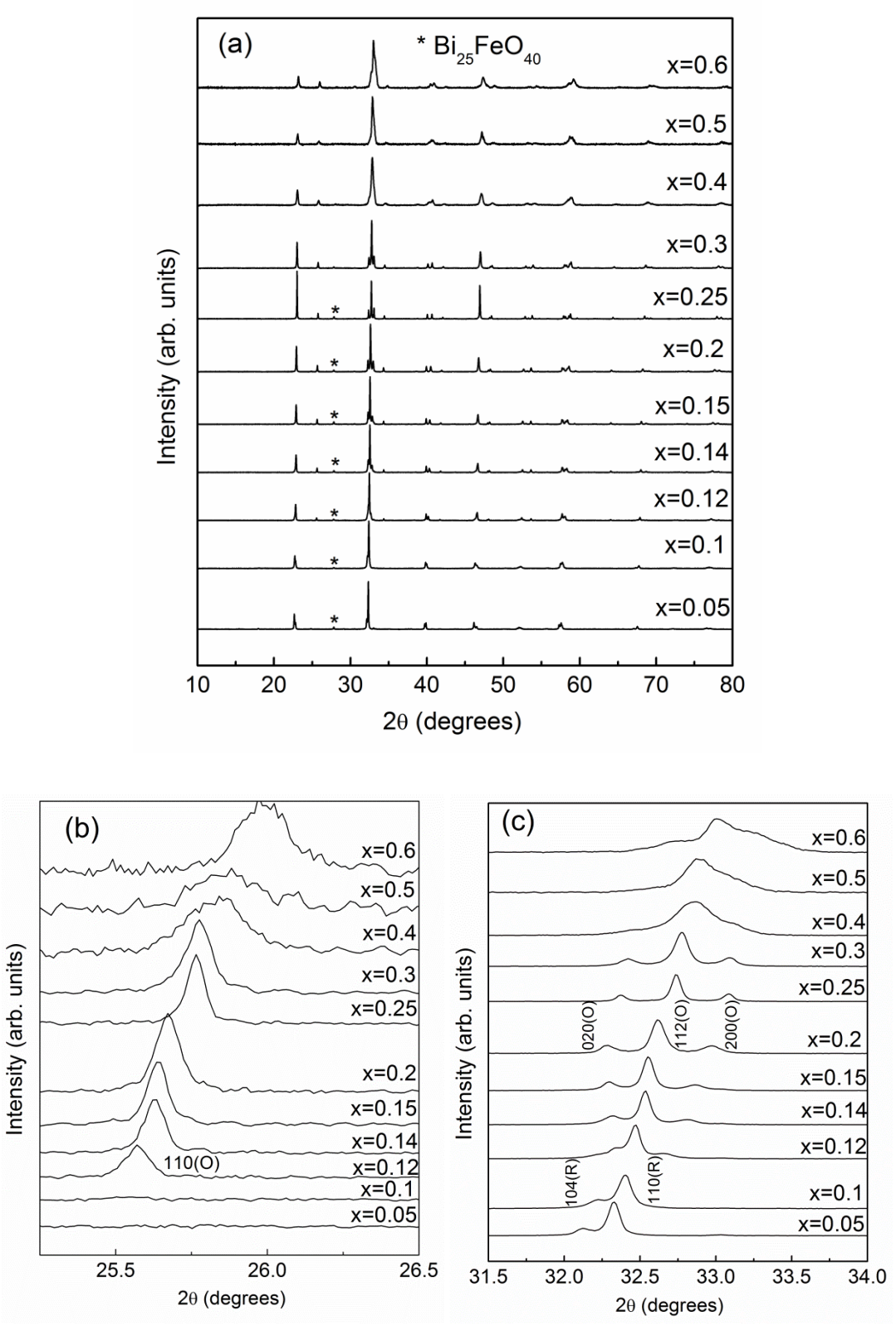

Figure 5.5. (a) X-ray diffraction patterns of $Bi_{1-x}Ca_xFe_{0.5}Mn_{0.5}O_3$. Magnified view of the XRD patterns of $Bi_{1-x}Ca_xFe_{0.5}Mn_{0.5}O_3$ showing (b) the evolution of the (110) orthorhombic reflection around $2\theta = 26°$, and (c) the most intense peak around $2\theta = 32°$ showing structural change from rhombohedral to orthorhombic. The peak from the impurity phase $Bi_{25}FeO_{40}$ is marked using the symbol '*'.

$Bi_{1-x}Ca_xFe_{0.6}Mn_{0.4}O_3$ co-substituted compositions indicated that Ca-substitution helps to stabilize the *R3c* phase in the $BiFe_{1-x}Mn_yO_3$ system. Catalan *et al*. have shown that Ca-substitution internally produces a large chemical pressure which is equivalent to the GPa pressure scale [13] and this chemical pressure in the system can help stabilizing the higher Mn substituted structures. Thus, the co-substituted compositions of 50% Mn substitution could be synthesized with only 5% Ca substitution and the only impurity phase formed is $Bi_{25}FeO_{40}$. As shown in figure 5.5(b,c), $Bi_{0.95}Ca_{0.05}Fe_{0.5}Mn_{0.5}O_3$ and $Bi_{0.1}Ca_{0.9}Fe_{0.5}Mn_{0.5}O_3$ showed less rhombohedral distortion similar to $Bi_{0.95}Ca_{0.05}Fe_{0.6}Mn_{0.4}O_3$ due to the higher Mn content. Orthorhombic (110) reflection is observed for $x > 0.1$. Rietveld refinement revealed *R3c* phase for $x \leq 0.1$ and *Pbnm* phase for $x \geq 0.2$ with a mixed phase for $0.1 < x < 0.2$.

Variation of the lattice parameters and unit cell volume as a function of x is shown in figure 5.6 for all compositions, where the shaded region indicates the mixed phase region in the systems. For all the five series of compositions studied, lattice parameters and unit cell volume decrease with increasing the Ca concentration similar to the $x = y$ co-substituted system, discussed in chapter 4. Decrease in the unit cell volume in a particular series (i.e., with constant Mn content) with increasing the Ca substitution is due to the smaller ionic radius of Ca^{2+} and the formation of Mn^{4+}. In $Bi_{1-x}Ca_xFe_{0.9}Mn_{0.1}O_3$ ($y = 0.1$ series), the unit cell volume drops from 243 $Å^3$ (for $x = 0.2$) to 240 $Å^3$ (for $x = 0.4$) whereas for the $y = 0.5$ series, a large drop in the cell volume from 237 $Å^3$ (for $x = 0.2$) to 228 $Å^3$ (for $x = 0.4$) is observed suggesting the presence of relatively larger amount of Mn^{4+} in $Bi_{1-x}Ca_xFe_{0.5}Mn_{0.5}O_3$. If the decrease in the unit cell volume was only due to the effect of substitution of smaller Ca^{2+}, both the $Bi_{1-x}Ca_xFe_{0.9}Mn_{0.1}O_3$ and the $Bi_{1-x}Ca_xFe_{0.5}Mn_{0.5}O_3$ compositions should show similar unit cell volume values since both Mn^{3+} and Fe^{3+} have similar ionic radii.

For the $y = 0.1$ and 0.2 series, the orthorhombic cell parameters ‘a’ and ‘b’ have almost comparable values. Due to this close lattice parameters, the orthorhombic splitting of the XRD peaks is not observed for the $x > 0.2$ compositions in these two series. This is probably due to the relatively lesser amount of Mn and correspondingly a lesser orthorhombic distortion caused by it. Unlike the $Bi_{1-x}Ca_xFe_{0.9}Mn_{0.1}O_3$ and $Bi_{1-x}Ca_xFe_{0.8}Mn_{0.2}O_3$ compositions, where the orthorhombic cell parameters ‘a’ and ‘b’ show closer values, for $y \geq 0.3$ series, the orthorhombic cell parameters clearly show distinct values which is due to the higher percentage of Mn in these systems which cause more orthorhombic distortion. Except for $y = 0.3$, the *R3c* to *Pbnm* structural transition occurs around $x = 0.15$ in the $Bi_{1-x}Ca_xFe_{1-y}Mn_yO_3$ system. For the $y = 0.3$ series, structural transition occurs around $x = 0.2$.

In $Bi_{0.85}Ca_{0.15}Fe_{0.9}Mn_{0.1}O_3$, the *Pbnm* phase content is obtained as ~48% whereas in $Bi_{0.85}Ca_{0.15}Fe_{0.5}Mn_{0.5}O_3$, ~90% *Pbnm* phase is observed which suggests that higher the Mn content, higher the orthorhombic distortion. This is likely to be due to the larger Jahn-Teller distortion (of the Mn^{3+} octahedra) in the $y = 0.5$ series.

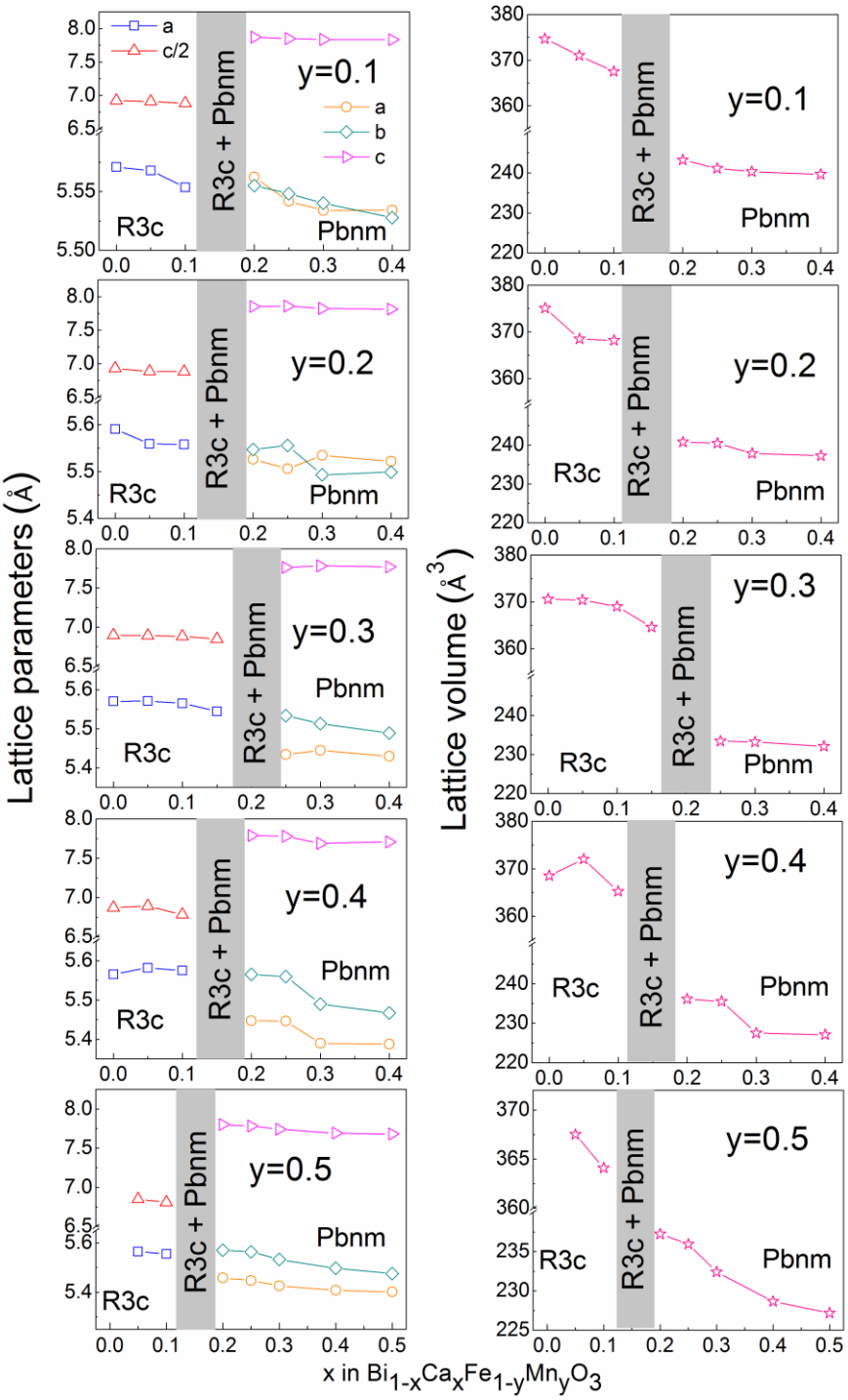

Figure 5.6. Variation of the lattice parameters and unit cell volume as a function of x in $Bi_{1-x}Ca_xFe_{1-y}Mn_yO_3$.

Variation of the rhombohedral angle (α) as a function of Ca substitution content is shown in figure 5.7. α increases with increasing Ca substitution implying a smaller rhombohedral distortion at x = 0.15 [14]. With the increase in the Mn content, α increases which suggest why the lesser *R3c* splitting is observed for the y = 0.4 and y = 0.5 series. It can be concluded from the XRD analysis that, in the $BiFe_{1-y}Mn_yO_3$ system, Ca substitution up to a certain limit ($x \approx 0.15$) can stabilize the *R3c* phase and above which *R3c* to *Pbnm* structural transition occurs.

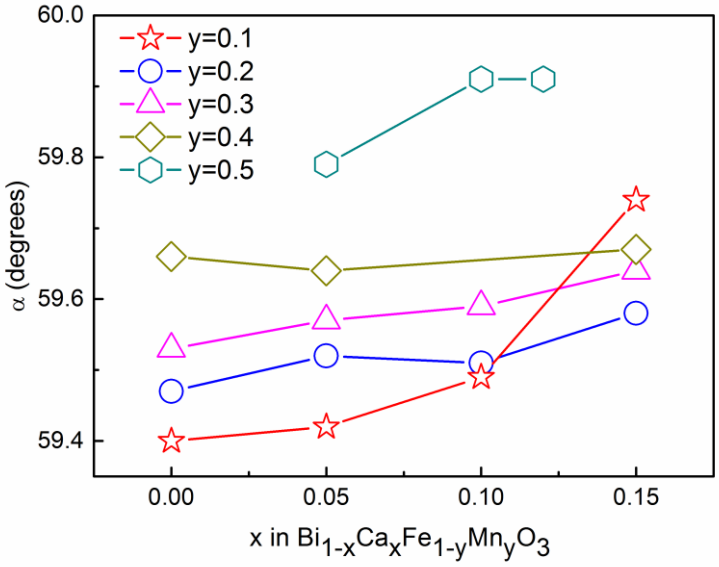

Figure 5.7. Variation of the rhombohedral angle, α, as a function of x in $Bi_{1-x}Ca_xFe_{1-y}Mn_yO_3$.

5.3. Raman spectroscopy

Figure 5.8 shows the Raman spectra of different compositions in $Bi_{1-x}Ca_xFe_{1-y}Mn_yO_3$. Detailed Raman analysis of $BiFeO_3$ and $Bi_{1-x}Ca_xFe_{1-x}Mn_xO_3$ ($x = y$) is discussed in the previous chapters. For $BiFe_{0.9}Mn_{0.1}O_3$, intense Raman bands are observed at 135 cm^{-1} and 170 cm^{-1} corresponding to the A_1-1 and A_1-2 modes, which is similar to the Raman spectra shown by $BiFeO_3$ (BFO in figure 5.8). With increasing Mn substitution content in $BiFeO_3$, the intensity of the band at 620 cm^{-1} is increased, as observed by Zheng *et al.* in La and Mn co-substituted $BiFeO_3$ [15]. With the increase in the Mn content, intensities of the bands due to the A_1-1 and A_1-2 modes are diminished, and for $BiFe_{0.6}Mn_{0.4}O_3$, the intensities of these bands are very low. This can be correlated with the XRD data where a less rhombohedral

splitting was observed for $BiFe_{0.6}Mn_{0.4}O_3$. Upon Ca substitution in $BiFe_{1-x}Mn_xO_3$, the intensities of the A_1-1 and A_1-2 bands are diminished and the Raman band at 620 cm^{-1} (E-9) becomes more intense. In all the five series, the bands due to the A-O vibrations related to the rhombohedral phase start disappearing from x = 0.15, corresponding to the structural transition around this composition as in the $x = y$ series. The $x \geq 0.2$ compositions with orthorhombic phase show Raman bands only at 480, 530 and 620 cm^{-1} similar to that for the $RMnO_3$ orthorhombic phase (as discussed in section 4.4).

For the *R3c* compositions with $x < 0.2$, the low-frequency bands due to the E and A_1 modes are present in the spectra of all the five series, implying the ferroelectric nature of these compositions. Complete disappearance of the low-frequency bands for $x \geq 0.2$ suggests suppression of the stereochemical activity of the Bi lone pair of electrons and hence nonferroelectric nature of the compositions. The information obtained on the structural phase transition observed from the Raman spectra is in accordance with the results from the XRD studies.

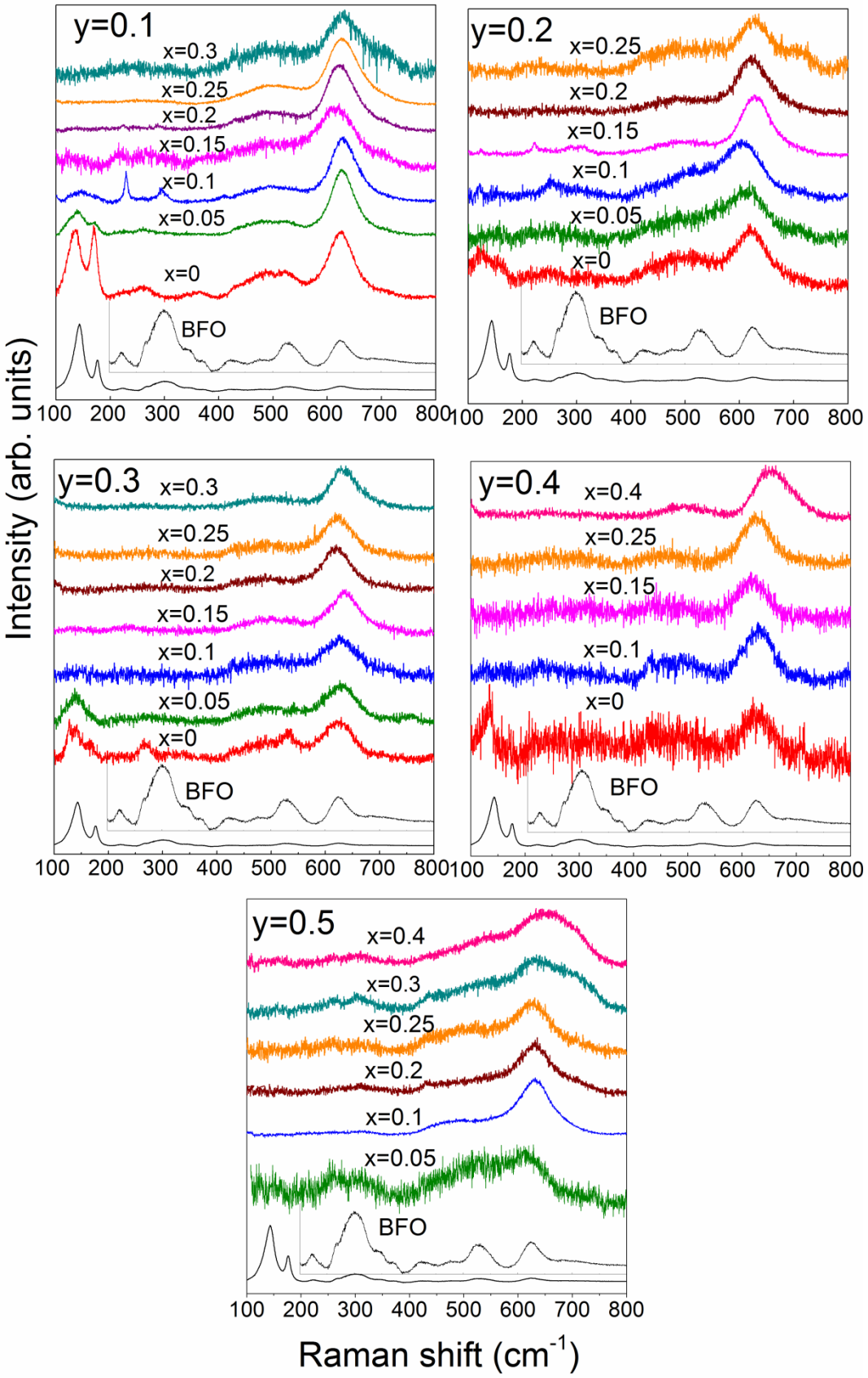

Figure 5.8. Raman spectra of different compositions in $Bi_{1-x}Ca_xFe_{1-y}Mn_yO_3$. Lower inset in all graphs shows the magnified spectra of $BiFeO_3$ (BFO) on the same *x*-axis scale.

5.4. XPS studies

Oxygen 1s XPS spectra of the samples are analyzed in order to find out the amount of oxygen vacancies in the samples (figures 5.9-5.13). The XPS studies are performed using two different instruments, as mentioned in section 2.5, chapter 2. The spectra recorded on the VG Microtech instrument (source: Mg-Kα) are very broad compared to the ones recorded on Thermo Fisher Kalpha+ spectrometer (source: Al-Kα). The widths of the peaks are not used for any comparison. In most of the compositions analyzed, with increase in the amount of Ca substitution, the intensities of the peaks due to O_c and O_p (where O_c is due to chemisorbed water species, and O_p is due to physisorbed water species, as discussed in chapter 4, section 4.6) increase indicating an increase in the number of oxygen vacancies at higher levels of substitution. With the increase in the Mn content also, an increase in the number of oxygen vacancies is observed. The presence of oxygen vacancies indicates the presence of Mn^{3+} in the compositions.

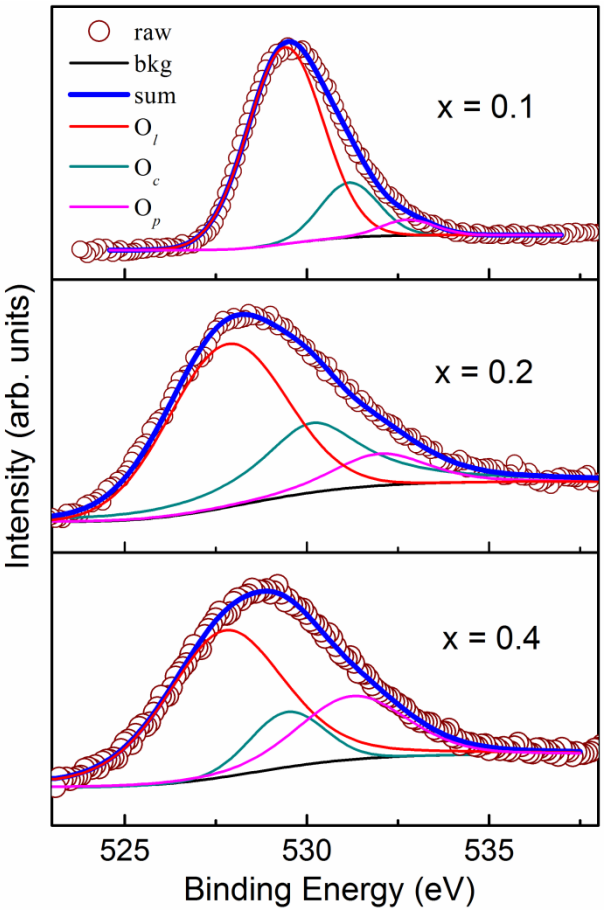

Figure 5.9. Deconvoluted oxygen 1s XPS spectra of selected compositions in $Bi_{1-x}Ca_xFe_{0.9}Mn_{0.1}O_3$.

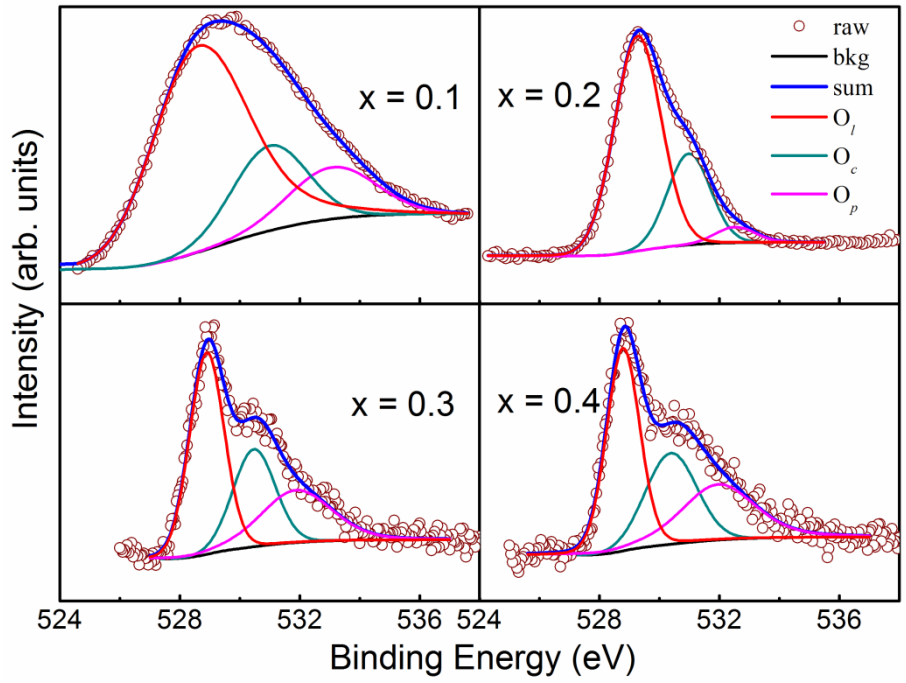

Figure 5.10. Deconvoluted oxygen 1s XPS spectra of selected compositions in $Bi_{1-x}Ca_xFe_{0.8}Mn_{0.2}O_3$.

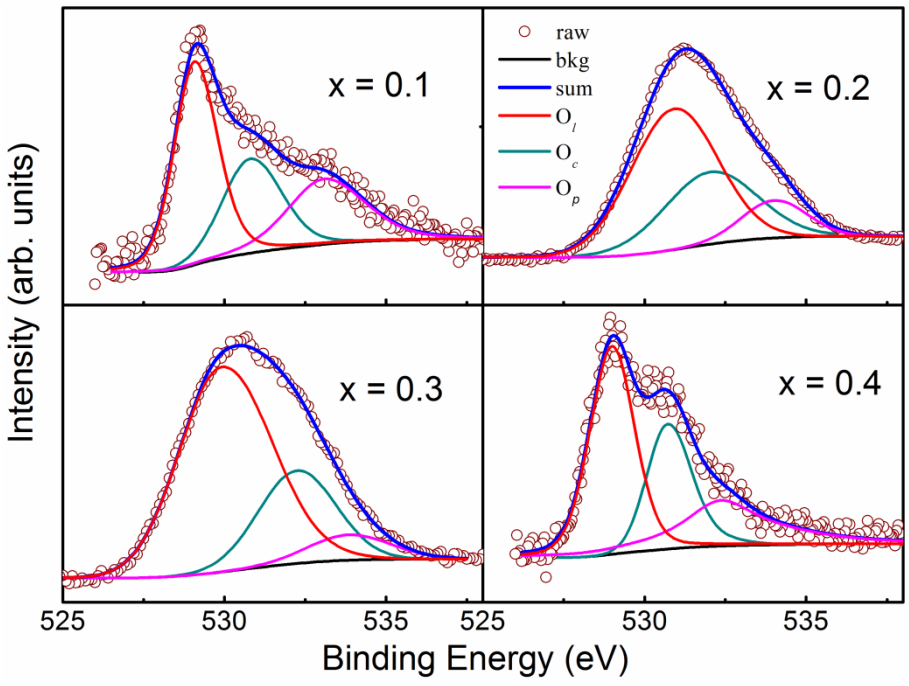

Figure 5.11. Deconvoluted oxygen 1s XPS spectra of selected compositions in $Bi_{1-x}Ca_xFe_{0.7}Mn_{0.3}O_3$.

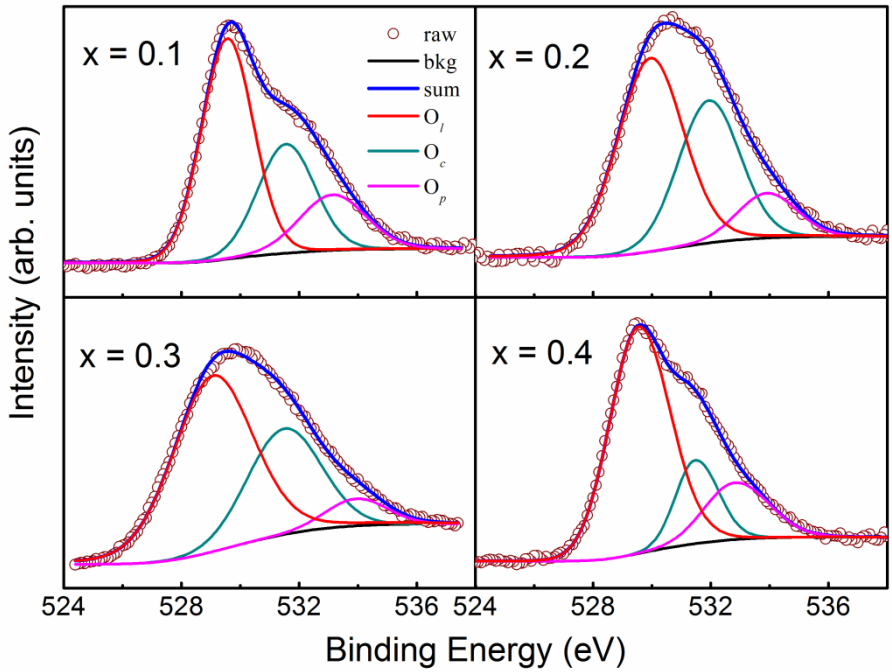

Figure 5.12. Deconvoluted oxygen 1s XPS spectra of selected compositions in $Bi_{1-x}Ca_xFe_{0.6}Mn_{0.4}O_3$.

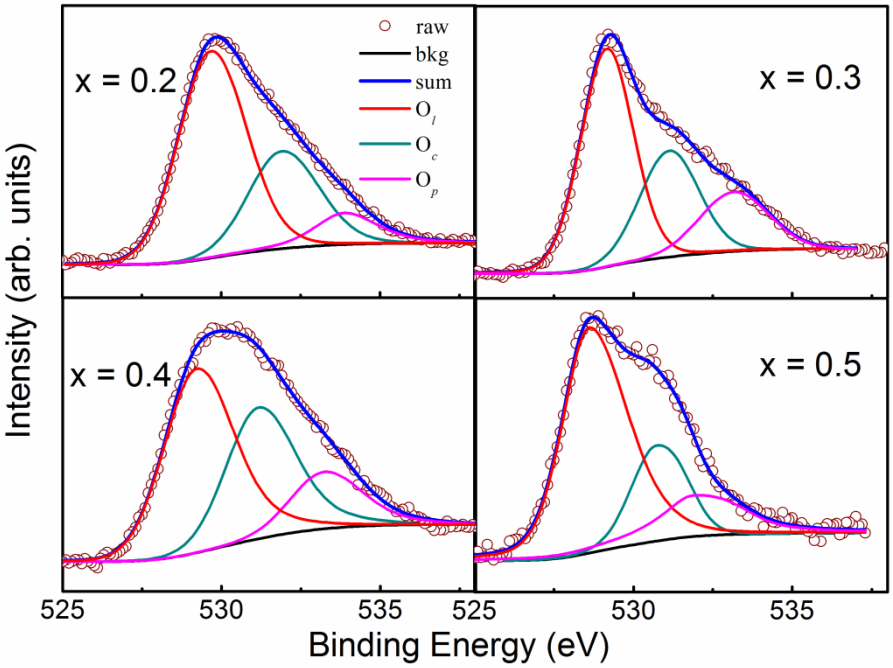

Figure 5.13. Deconvoluted oxygen 1s XPS spectra of selected compositions in $Bi_{1-x}Ca_xFe_{0.5}Mn_{0.5}O_3$.

Mn $2p_{3/2}$ XPS peaks are analyzed in order to get information on the oxidation state of manganese in the $Bi_{1-x}Ca_xFe_{1-y}Mn_yO_3$ system (figures 5.14-5.17). Mn XPS signals for the

y = 0.1 series are very weak and hence no fitting could be done for these samples. For all the other compositions analyzed, presence of a mixture of Mn^{3+} and Mn^{4+} is observed.

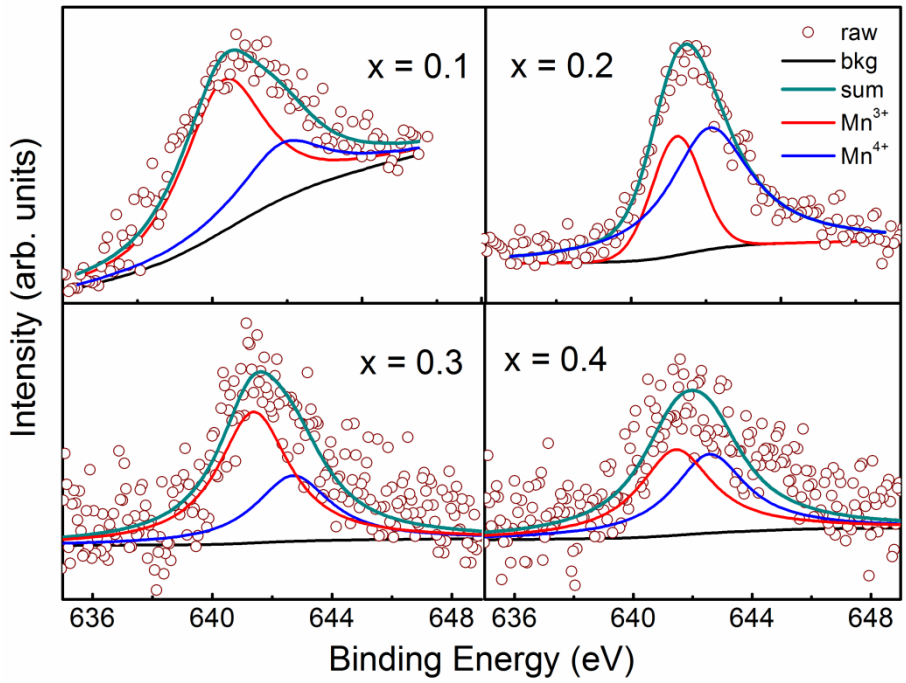

Figure 5.14. Deconvoluted Mn $2p_{3/2}$ XPS spectra of different compositions in $Bi_{1-x}Ca_xFe_{0.8}Mn_{0.2}O_3$.

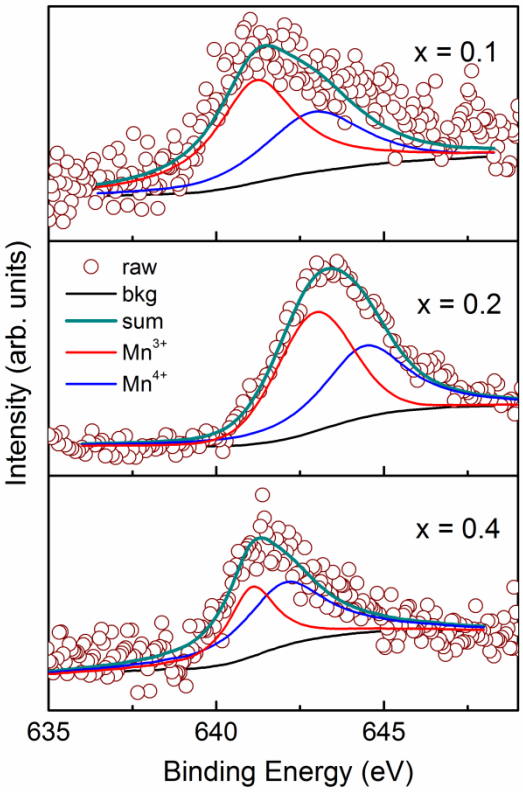

Figure 5.15. Deconvoluted Mn $2p_{3/2}$ XPS spectra of different compositions in $Bi_{1-x}Ca_xFe_{0.7}Mn_{0.3}O_3$.

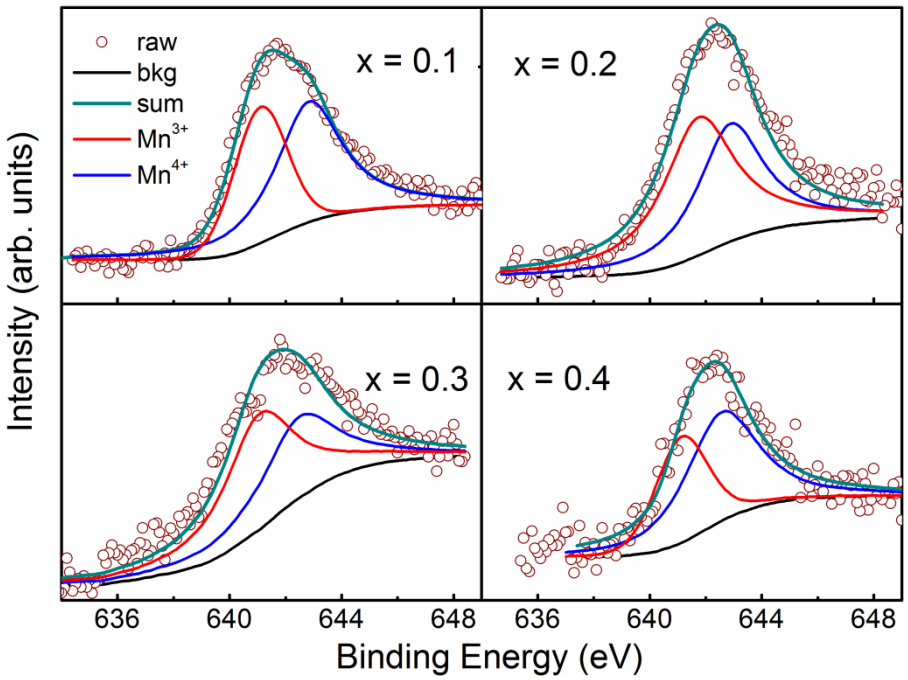

Figure 5.16. Deconvoluted Mn $2p_{3/2}$ XPS spectra of different compositions in $Bi_{1-x}Ca_xFe_{0.6}Mn_{0.4}O_3$.

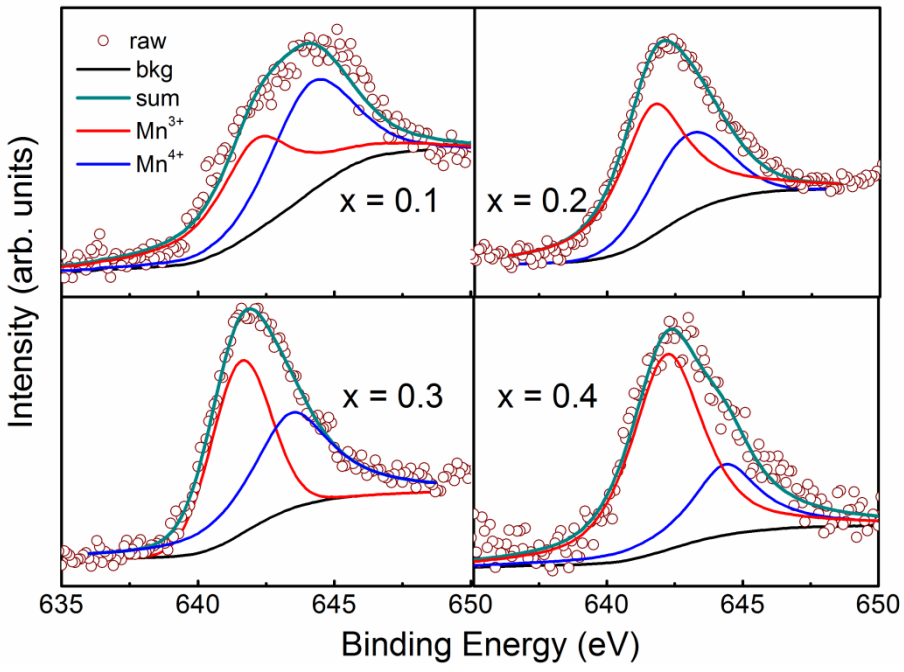

Figure 5.17. Deconvoluted Mn $2p_{3/2}$ XPS spectra of different compositions in $Bi_{1-x}Ca_xFe_{0.5}Mn_{0.5}O_3$.

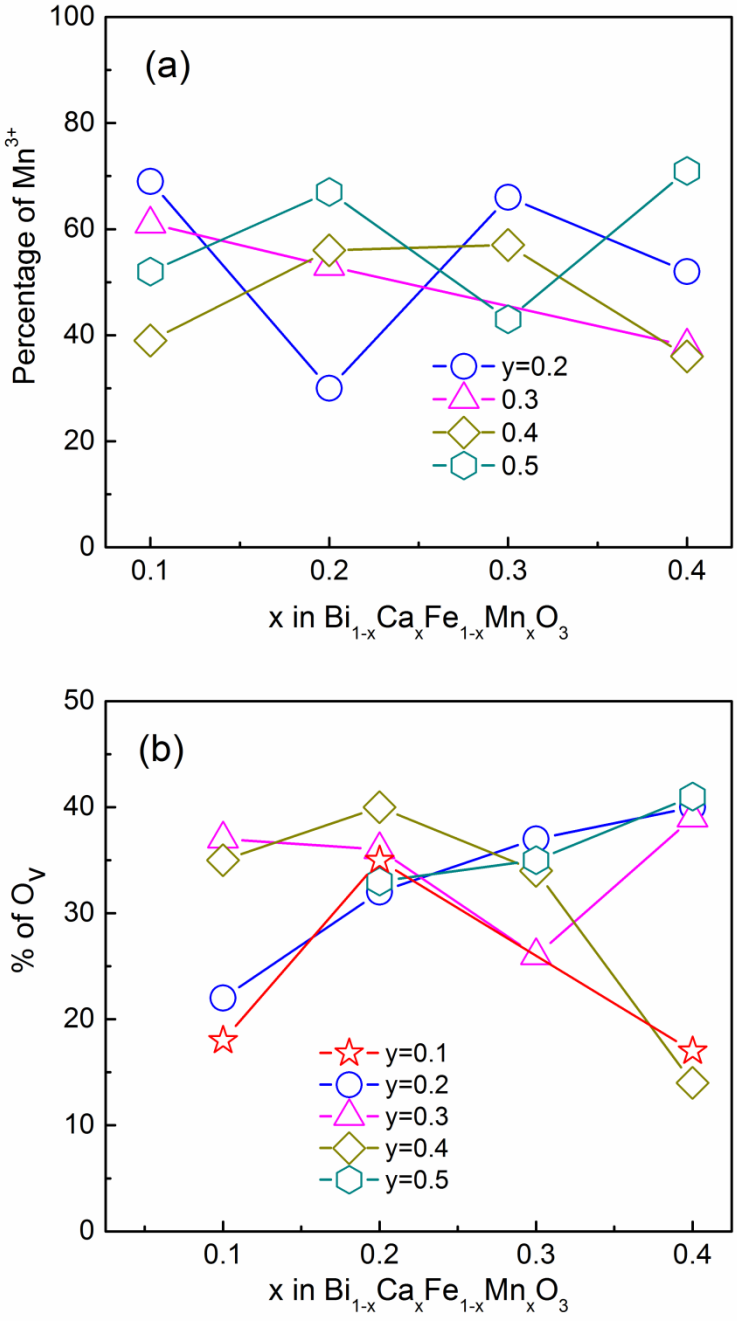

Figure 5.18. (a) Percentage of Mn^{3+}, and (b) percentage of oxygen vacancy (O_v) as a function of *x* in $Bi_{1-x}Ca_xFe_yMn_{1-y}O_3$.

Figure 5.18 shows the percentage of Mn^{3+} and oxygen vacancy obtained from the XPS analysis as a function of Ca concentration in $Bi_{1-x}Ca_xFe_yMn_{1-y}O_3$. It is noticed that in most of the compositions analysed, around 40% to 60% of Mn exists as Mn^{3+} and oxygen vacancies vary from 20% to 40%.

5.5. Magnetic properties

5.5.1. M vs. H measurements

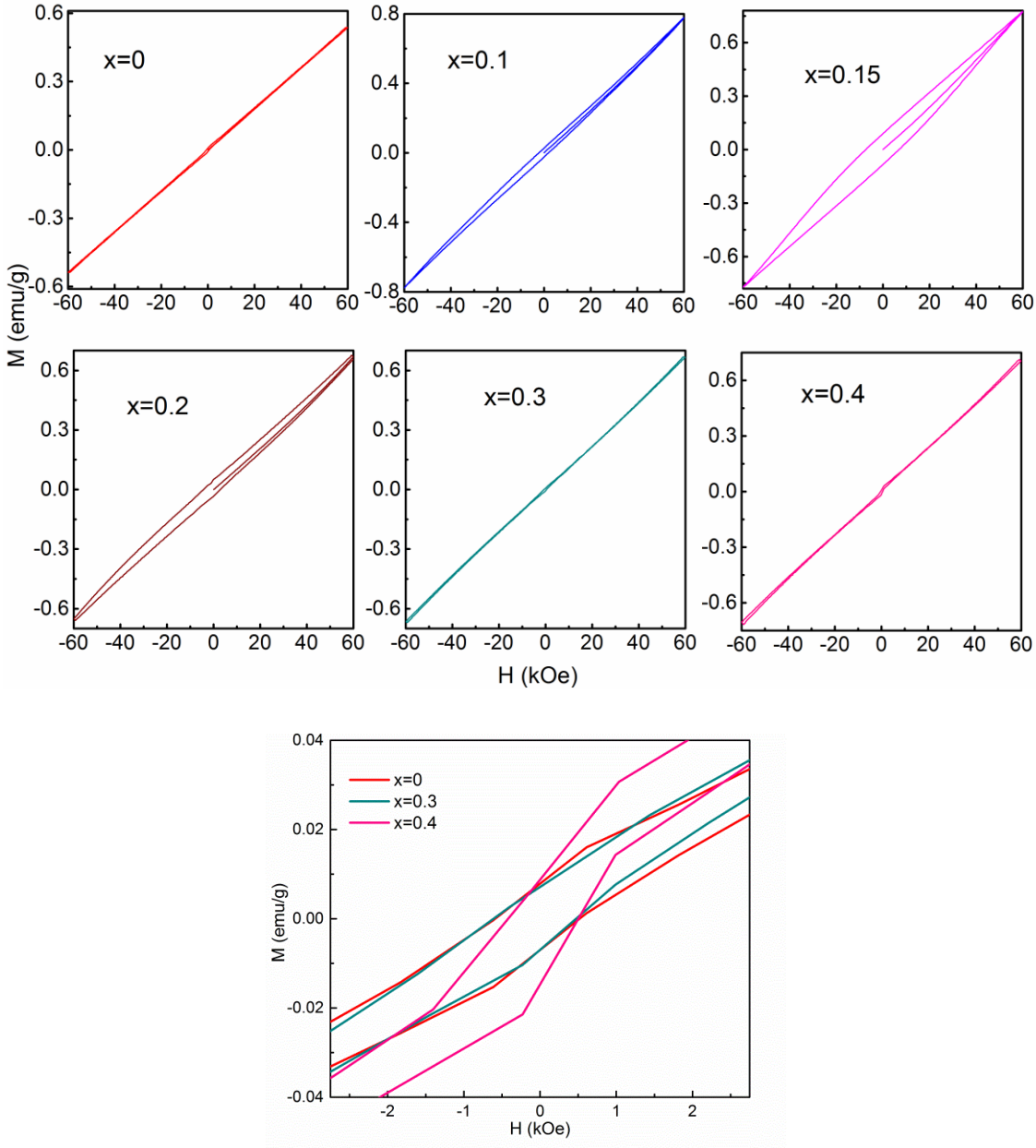

Figure 5.19. Room temperature magnetization curves of $Bi_{1-x}Ca_xFe_{0.9}Mn_{0.1}O_3$. The figure at the bottom shows the zoomed magnetization curves of selected compositions.

Room temperature magnetization curves of the different compositions in $Bi_{1-x}Ca_xFe_yMn_{1-y}O_3$ are shown in figures 5.19 to 5.23 and the magnetic parameters obtained from the M-H curves are plotted in figures 5.25 to 5.27. $BiFe_{0.9}Mn_{0.1}O_3$ (x = 0) shows negligible hysteresis loop (figure 5.19). However, on co-substitution with Ca, the magnetization of the samples increases. A very wide hysteresis loop is observed for x = 0.15

and the coercivity decreases for higher degree of Ca substitution. $Bi_{0.6}Ca_{0.4}Fe_{0.9}Mn_{0.1}O_3$ shows a linear variation of magnetization with negligible remanence and coercivity. Remanence, coercivity and magnetization increase (as shown in figures 5.25 to 5.27) with Ca substitution showing a maximum at x = 0.15 (MPB region) as in the $x = y$ co-substituted system. However, unlike the $x = y$ co-substituted system, here, even the magnetization at 6 T shows a maximum at x = 0.15.

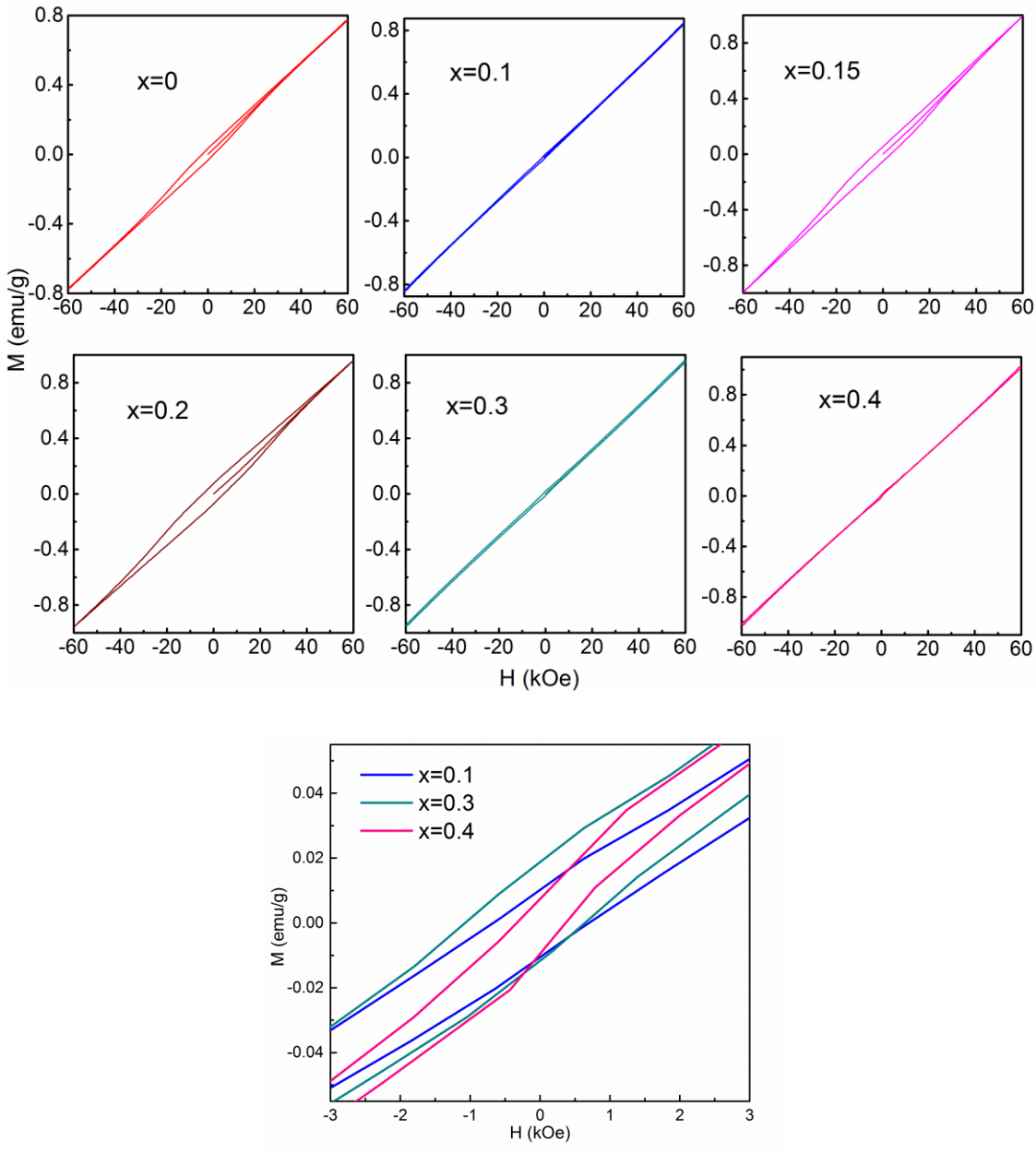

Figure 5.20. Room temperature magnetization curves of $Bi_{1-x}Ca_xFe_{0.8}Mn_{0.2}O_3$ The figure at the bottom shows the zoomed magnetization curves of selected compositions.

$Bi_{0.85}Ca_{0.15}Fe_{0.9}Mn_{0.1}O_3$ shows the highest coercivity around 8 kOe which is even larger than that observed for $Bi_{0.825}Ca_{0.175}Fe_{0.825}Mn_{0.175}O_3$ (see figure 4.15, chapter 4).

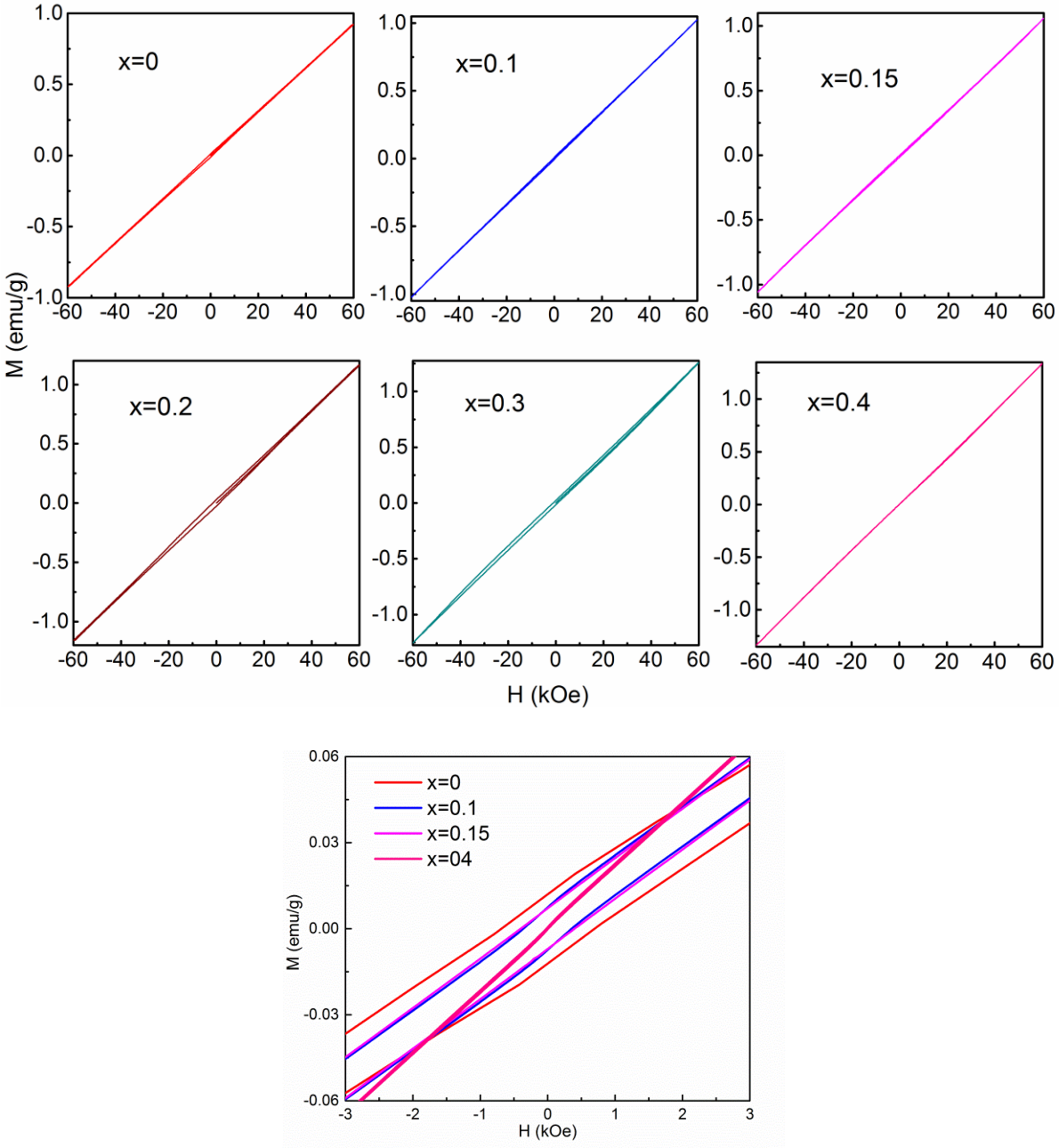

Figure 5.21. Room temperature magnetization curves of $Bi_{1-x}Ca_xFe_{0.7}Mn_{0.3}O_3$. The figure at the bottom shows the zoomed magnetization curves of selected compositions.

Compared to $BiFe_{0.9}Mn_{0.1}O_3$, $BiFe_{0.8}Mn_{0.2}O_3$ shows a wider hysteresis loop (figure 5.20). In the $Bi_{1-x}Ca_xFe_{0.8}Mn_{0.2}O_3$ series, the loop becomes wider till x = 0.2 and then becomes narrower for higher amount of Ca substitution. Remanence and coercivity increase

with increasing Ca substitution and show a maximum at x = 0.2. Magnetization at 60 kOe increases with Ca substitution with an anomaly around x = 0.15 which is the structural transition region in the $Bi_{1-x}Ca_xFe_{0.8}Mn_{0.2}O_3$ system.

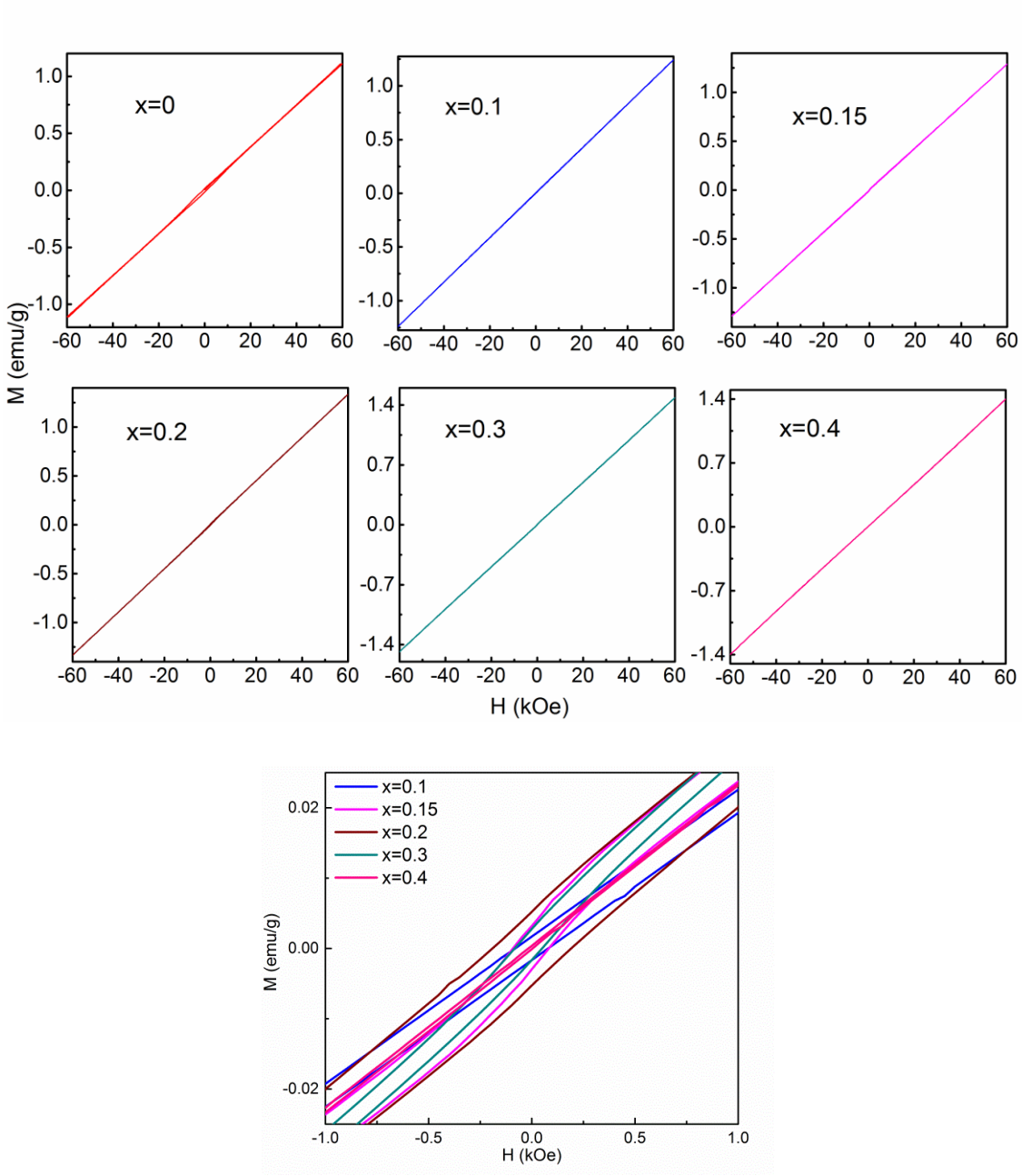

Figure 5.22. Room temperature magnetization curves of $Bi_{1-x}Ca_xFe_{0.6}Mn_{0.4}O_3$. The figure at the bottom shows the zoomed magnetization curves of selected compositions.

$BiFe_{0.7}Mn_{0.3}O_3$ shows almost negligible hysteresis loop whereas comparatively a wider hysteresis loop is observed for x = 0.2 and then again the loop becomes narrower and shows paramagnetic-like nature for x = 0.4 (figure 5.21). However, the zoomed curves showed a narrow hysteresis loop with very low coercivity and remanence. With calcium

co-substitution, magnetization of the samples increases in the y = 0.3 series as in the case of the y = 0.1 and 0.2 series. Remanence and coercivity show a sudden jump for x = 0.05 and then decrease for x = 0.1. Remanence and coercivity show a maximum at x = 0.2. Magnetization at 60 kOe increases with increasing the Ca content, without showing any anomaly at the structural transition region.

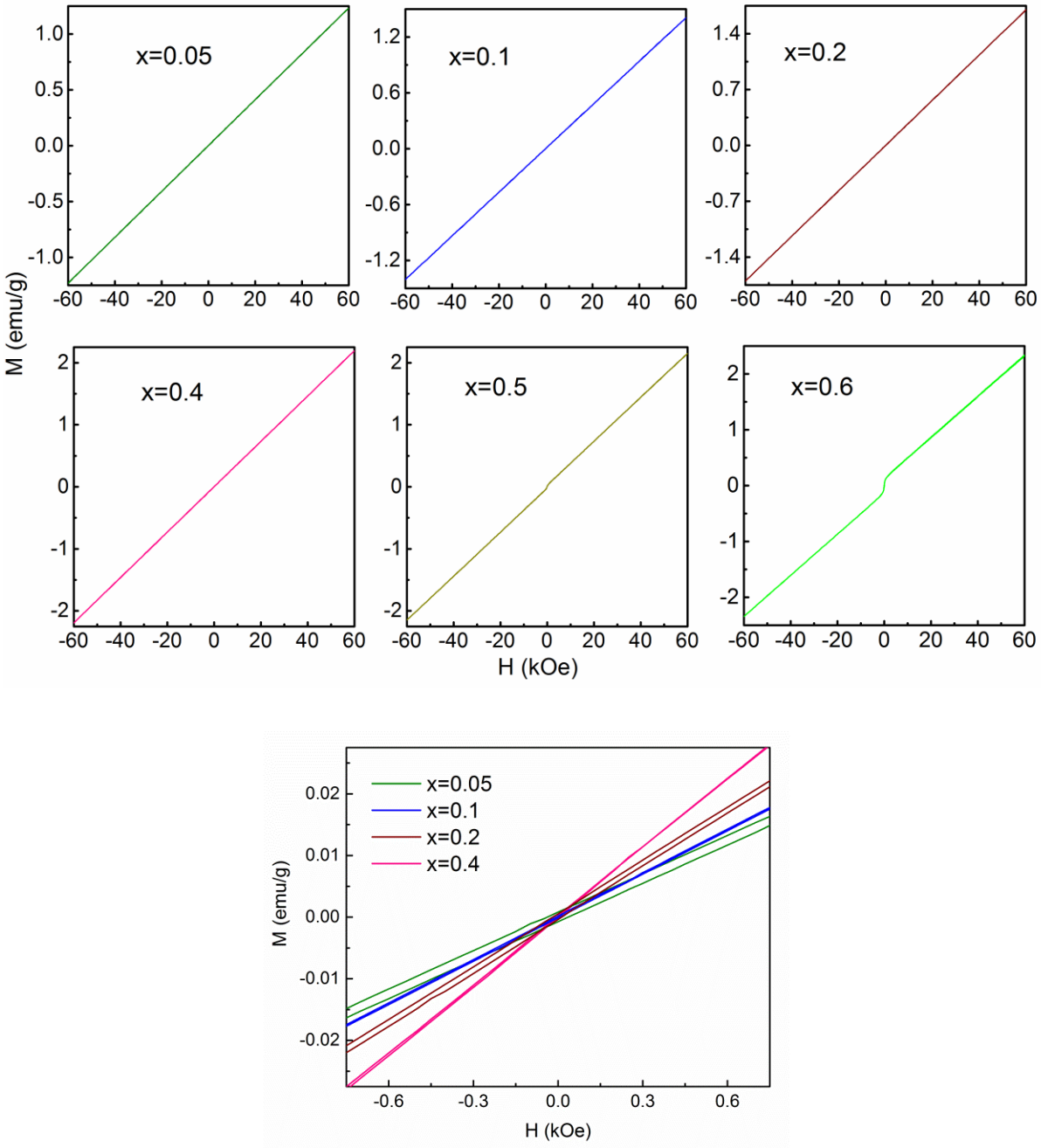

Figure 5.23. Room temperature magnetization curves of $Bi_{1-x}Ca_xFe_{0.5}Mn_{0.5}O_3$. The figure at the bottom shows the zoomed magnetization curves of selected compositions.

In the y = 0.4 system, all compositions show a paramagnetic-like nature, and the magnetization increases with Ca content. Unlike for the other co-substituted series, remanence and coercivity are maximum for x = 0 in $Bi_{1-x}Ca_xFe_{0.6}Mn_{0.4}O_3$ as shown figure 5.25 (b) and figure 5.26(b). A clear anomaly in the remanence and coercivity can be observed at x = 0.25.

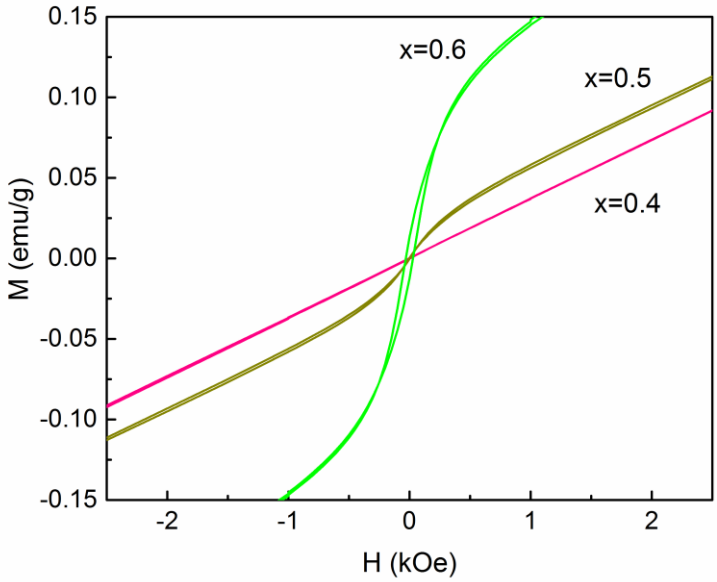

Figure 5.24. Zoomed magnetization curves of x = 0.4, x = 0.5 and x = 0.6 in $Bi_{1x}Ca_xFe_{0.5}Mn_{0.5}O_3$ at room temperature.

In the $Bi_{1-x}Ca_xFe_{0.5}Mn_{0.5}O_3$ system, for $x \leq 0.4$, a linear M-H curve with almost zero remanence and coercivity are observed which is the typical paramagnetic/antiferromagnetic character. However, the zoomed curves showed a narrow hysteresis loop with very low coercivity and remanence. For x = 0.5 and x = 0.6, a weak ferromagnetic loop is observed at low magnetic fields as shown in figure 5.24. Magnetization increases with increase in the Ca substitution content as in the case of other four systems. For the y = 0.5 system, remanence and coercivity show very low value as compared to the compositions in the $y \leq 0.4$ series. As seen in figure 5.25(c), coercivity shows an anomaly around x = 0.25 whereas remanence shows values which is within the error limit of the measurement as shown in figure 5.26 (c).

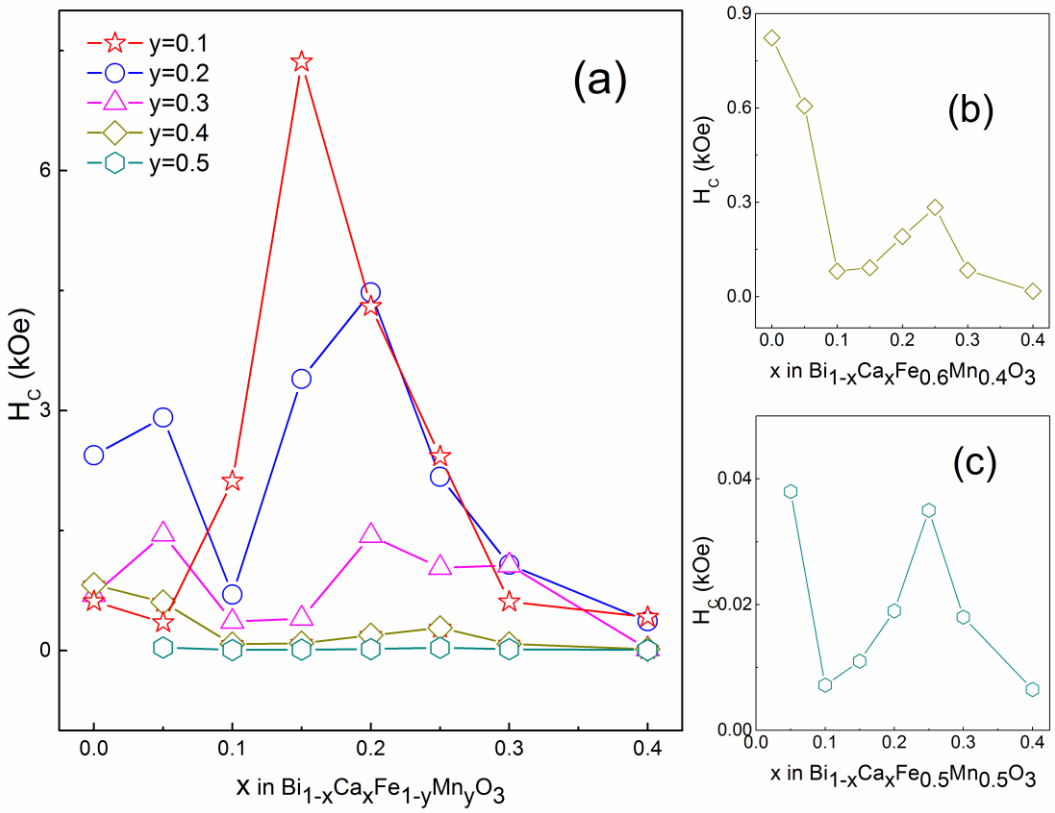

Figure 5.25. (a) Variation of room temperature coercivity (H_c) as a function of x in $Bi_{1-x}Ca_xFe_{1-y}Mn_{1-y}O_3$. Variation of H_c for (b) y = 0.4 and (c) y = 0.5.

It is possible that the weak ferromagnetism shown by the co-substituted compositions is due to the D-M interaction assisted canted antiferromagnetic structure [16,17]. Furthermore, the co-substitution can efficiently suppress the spin cycloid structure which allows weak ferromagnetism in the *R3c* phase. Upon co-substitution, the Fe-O-Fe bond angle changes and this can also contribute to the higher magnetic properties observed, as illustrated for the $x = y$ system. In all the five different series studied, higher magnetic properties are observed around the structural transition region as in the $x = y$ system where an MPB assisted enhancement occurs, as reported for the rare earth substituted $BiFeO_3$ [18-20]. In addition to these structural changes, the presence of both the Mn^{3+} and Mn^{4+} species (as confirmed by the contraction in unit cell volume and XPS analysis) can lead to double exchange interaction resulting in ferromagnetism. For all the different series, magnetization increases with increase in the Ca (Mn) content as shown figure 5.27. Such an increase in the magnetization with increase in the Mn/Ca content in $BiFeO_3$ is reported in the literature [21-23]. Within a particular series with constant Mn content, when Ca substitution is increased, possibly more Mn^{4+} species along with oxygen vacancies are created to attain the charge neutrality.

Anomaly in magnetization shown by $Bi_{1-x}Ca_xFe_{0.9}Mn_{0.1}O_3$ and $Bi_{1-x}Ca_xFe_{0.8}Mn_{0.2}O_3$ around the structural transition region (x = 0.15) could be due to the MPB assisted enhancement as discussed in the case of the $x = y$ system. Both the coercivity and remanence decrease with increase in the manganese substitution content. Compositions in $Bi_{1-x}Ca_xFe_{0.9}Mn_{0.1}O_3$ exhibit highest coercivity and remanence whereas the compositions in $Bi_{1-x}Ca_xFe_{0.5}Mn_{0.5}O_3$ show the lowest. For y = 0.5, the coercivity and remanence are almost negligible.

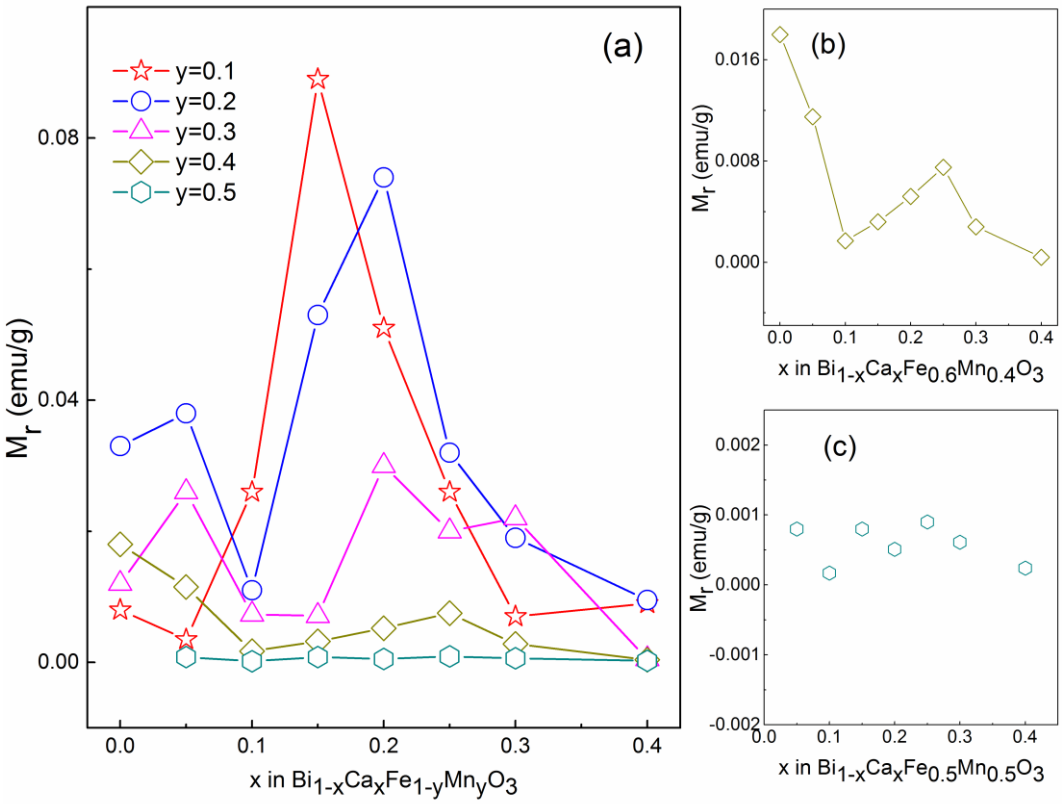

Figure 5.26. Variation of room temperature remnant magnetization (M_r) as a function of x in $Bi_{1-x}Ca_xFe_{1-y}Mn_{1-y}O_3$. (b) Variation of M_r for (b) y = 0.4 and (c) y = 0.5.

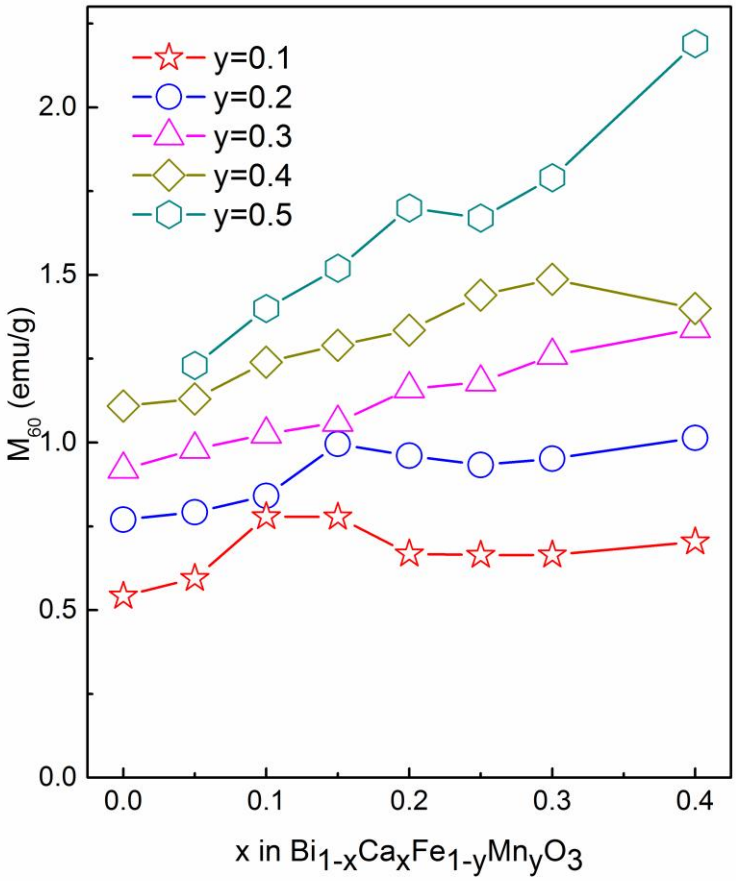

Figure 5.27. Room temperature magnetization at 60 kOe (M_{60}) as a function of x in $Bi_{1-x}Ca_xFe_{1-y}Mn_yO_3$ for different values of y.

The magnetization curves measured at 5 K are shown in figures 5.28–5.32 and the low-temperature magnetic parameters are plotted in figures 5.33–5.35. Very low remanence and coercivity are observed for $BiFe_{0.9}Mn_{0.1}O_3$. Upon Ca substitution, a clear magnetic hysteresis loop is observed for $x \geq 0.1$. Remanence, coercivity and magnetization at 60 kOe increase with Ca substitution showing a maximum around the MPB region, $x = 0.15$ (maximum coercivity at $x = 0.2$) as in the case of the room temperature hysteresis curves and then decrease. Similar to the $x = y$ system, in the $y = 0.1$ series also coercivity observed at 5 K is less than that observed at room temperature whereas the remanence and magnetization show larger values.

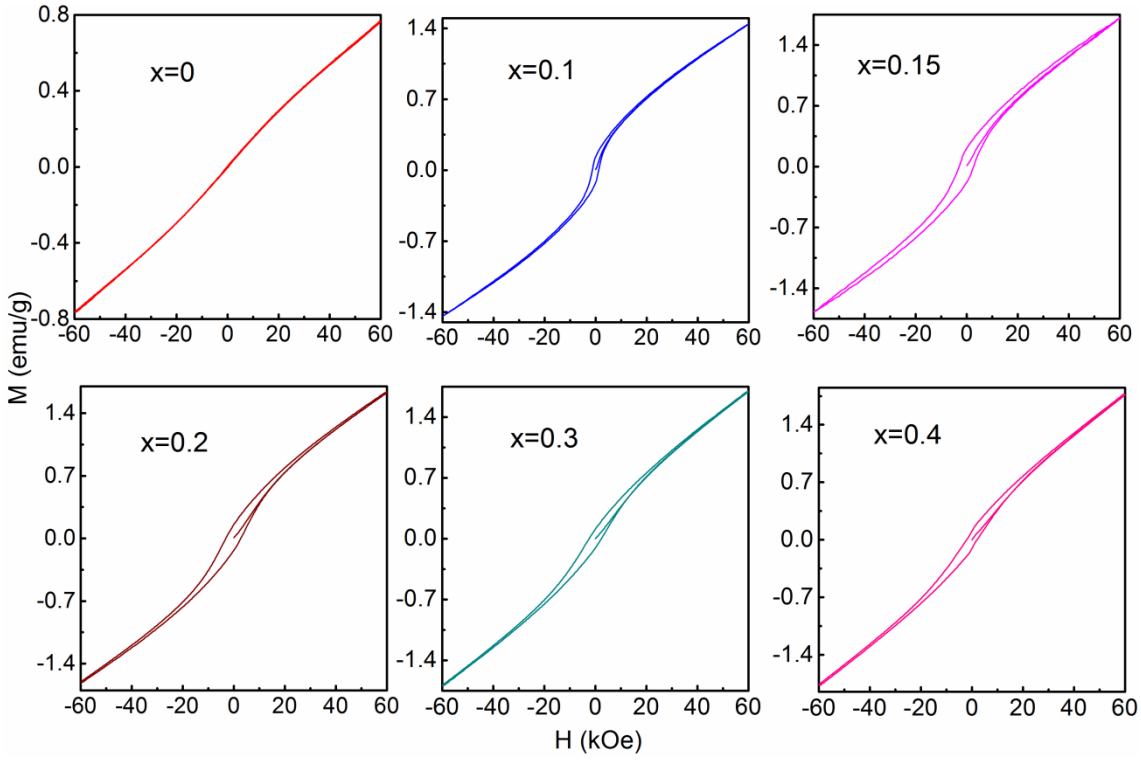

Figure 5.28. Magnetization vs applied magnetic field curves of $Bi_{1-x}Ca_xFe_{0.9}Mn_{0.1}O_3$ at 5 K.

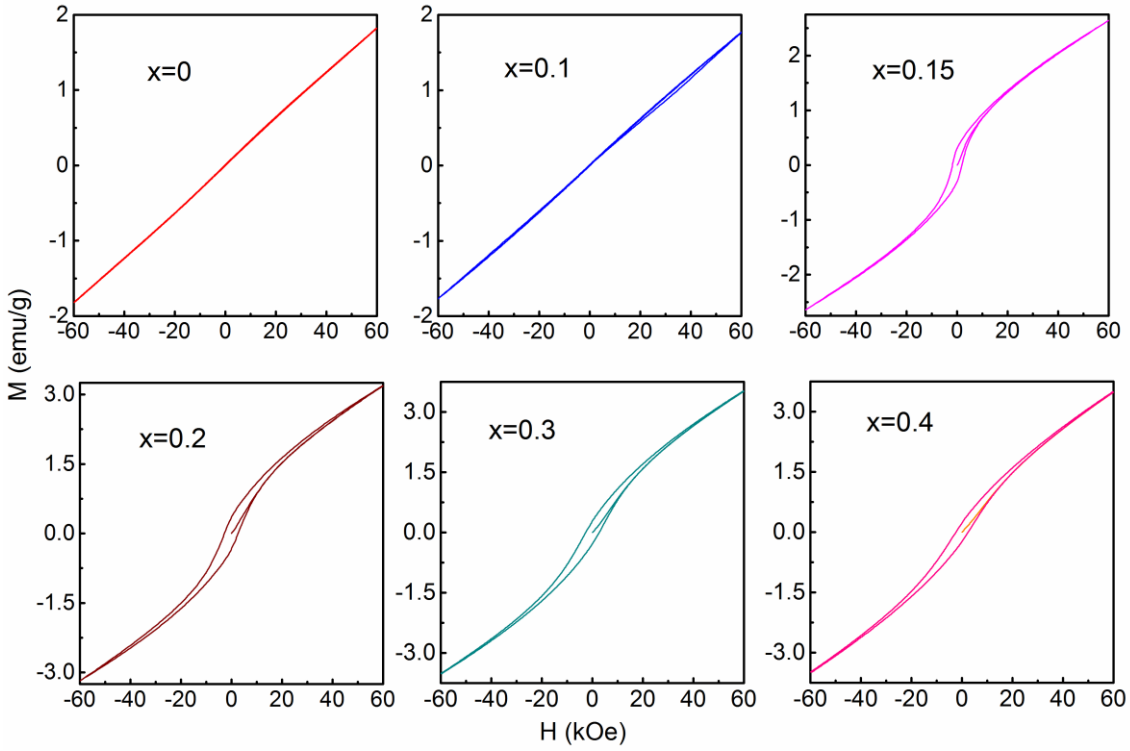

Figure 5.29. Magnetization vs applied magnetic field curves of $Bi_{1-x}Ca_xFe_{0.8}Mn_{0.2}O_3$ at 5 K.

Negligible coercivity and remanence are observed for $BiFe_{0.8}Mn_{0.2}O_3$ at 5 K similar to $BiFe_{0.9}Mn_{0.1}O_3$. With Ca substitution, $x \geq 0.15$ compositions show ferromagnetic-like hysteresis loop. Maximum remanence and coercivity are observed around the MPB region, whereas as the magnetization at 60 kOe increases with co-substitution. As in the $Bi_{1-x}Ca_xFe_{0.1}Mn_{0.9}O_3$ system, for the y = 0.2 system also the low-temperature coercivity values are less than the corresponding room temperature coercivity.

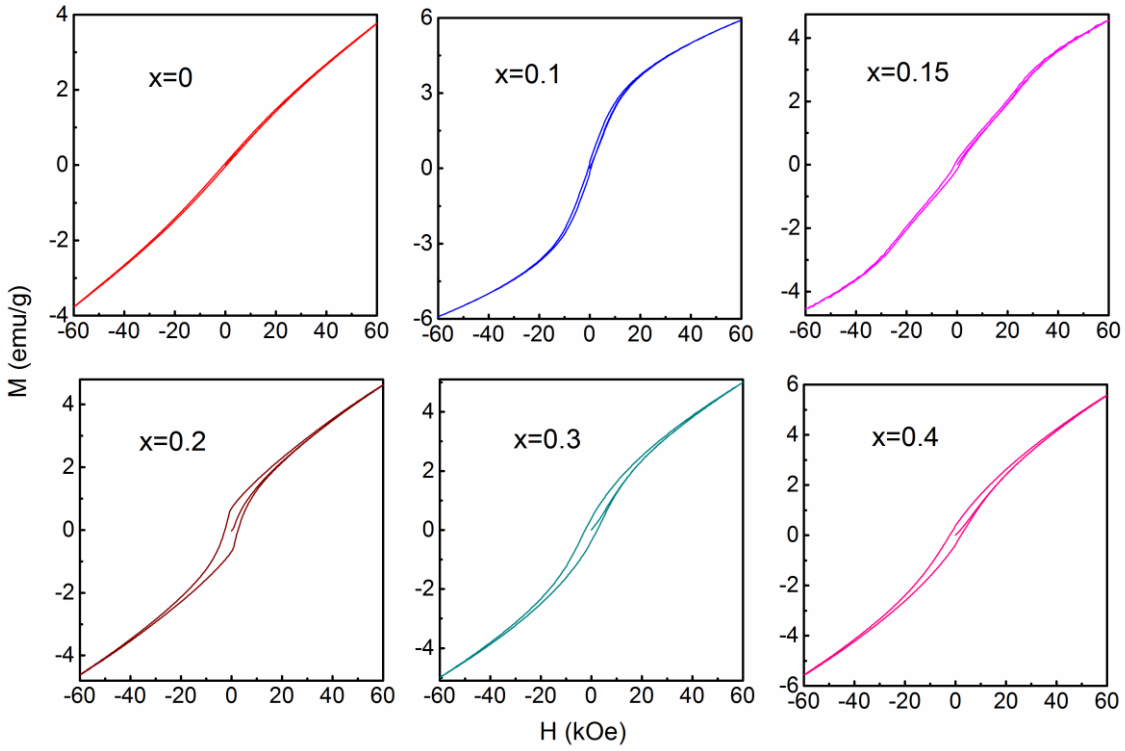

Figure 5.30. Magnetization vs applied magnetic field curves of $Bi_{1-x}Ca_xFe_{0.7}Mn_{0.3}O_3$ at 5 K.

In the $Bi_{1-x}Ca_xFe_{0.7}Mn_{0.3}O_3$ system, a narrow hysteresis loop is observed till x = 0.15. Compositions with $x \geq 0.2$ show a wider hysteresis loop. Remanence show a maximum at x = 0.2 and coercivity show a maximum at x = 0.25, whereas the magnetization at 60 kOe shows anomalously high value for x = 0.1. The low-temperature coercivity values are higher than the room temperature coercivity unlike in the case of the $Bi_{1-x}Ca_xFe_{0.1}Mn_{0.9}O_3$ and $Bi_{1-x}Ca_xFe_{0.2}Mn_{0.8}O_3$ co-substituted systems.

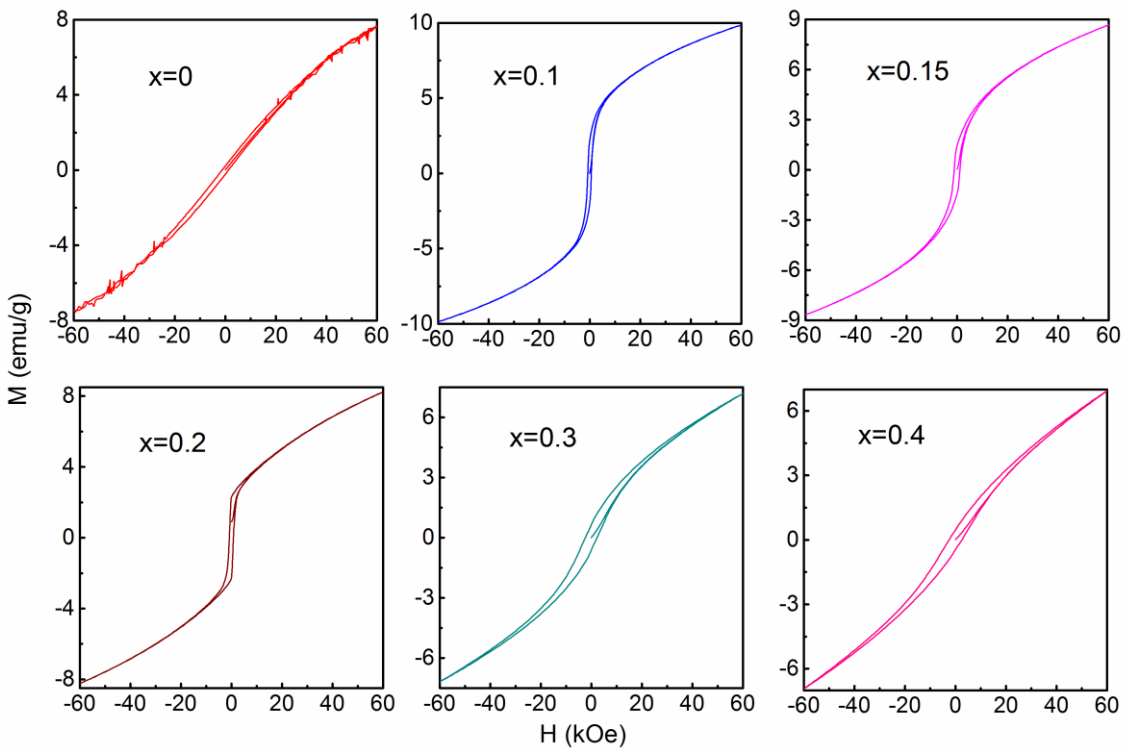

Figure 5.31. Magnetization vs applied magnetic field curves of $Bi_{1-x}Ca_xFe_{0.6}Mn_{0.4}O_3$ at 5 K.

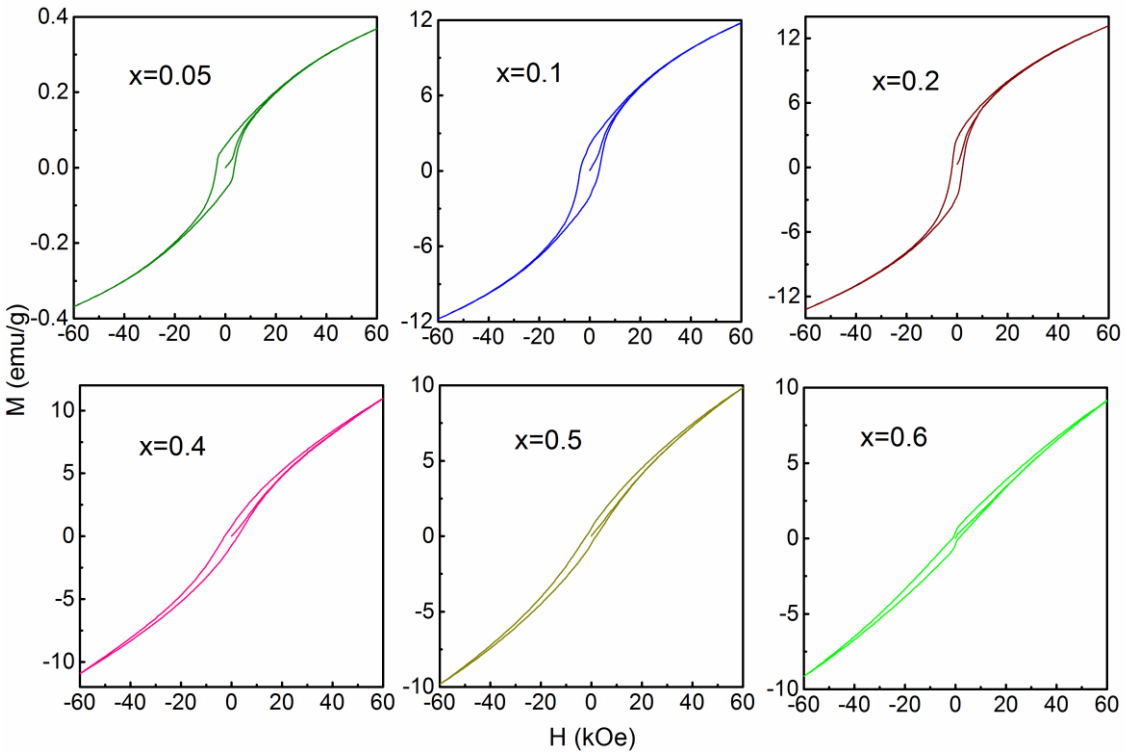

Figure 5.32. Magnetization vs applied magnetic field curves of $Bi_{1-x}Ca_xFe_{0.5}Mn_{0.5}O_3$ at 5 K.

For the y = 0.4 system, ferromagnetic like hysteresis loop is observed from x = 0.05. Remanence show a maximum at x = 0.2 and coercivity at x = 0.25. Magnetization at 60 kOe shows a highest value around x = 0.1 and then decreases continuously till x = 0.4. The low-temperature coercivity values are higher than the room temperature coercivity like that for the y = 0.3 co-substituted system. For the y = 0.5 system, ferromagnetic loops are observed for all the compositions. Remanence, coercivity and magnetization at 60 kOe show a clear anomaly around x = 0.2 as in the case of the room temperature magnetic parameters. Remanence and magnetization show a maximum at x = 0.2 whereas coercivity shows a dip.

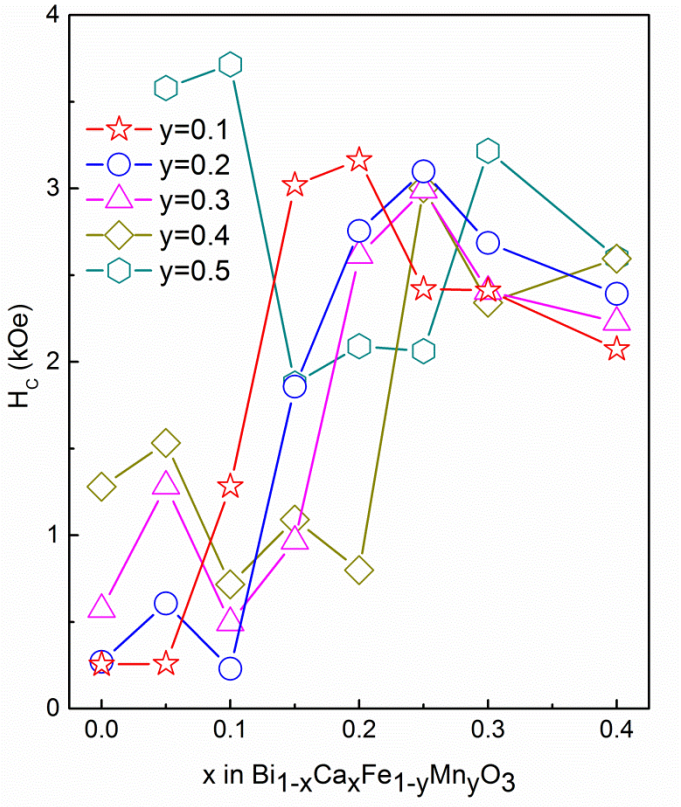

Figure 5.33. Coercivity (H_c) at 5 K as a function of x in $Bi_{1-x}Ca_xFe_{1-y}Mn_yO_3$.

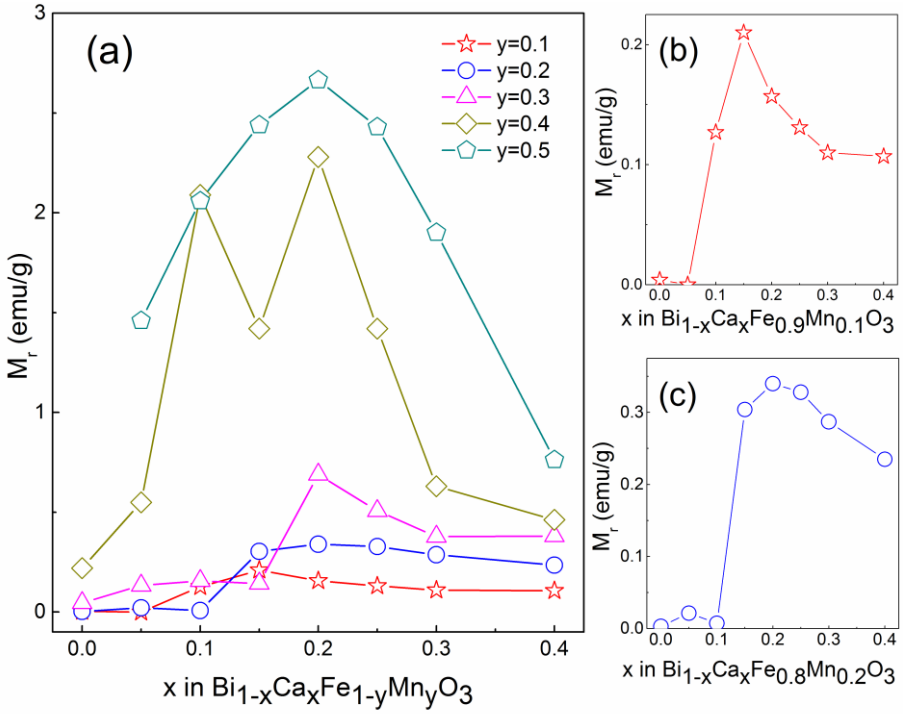

Figure 5.34. (a) Remnant magnetization (M_r) at 5 K as a function of x in $Bi_{1-x}Ca_xFe_{1-y}Mn_yO_3$. Zoomed M_r curves for (b) y = 0.1, and (c) y = 0.2

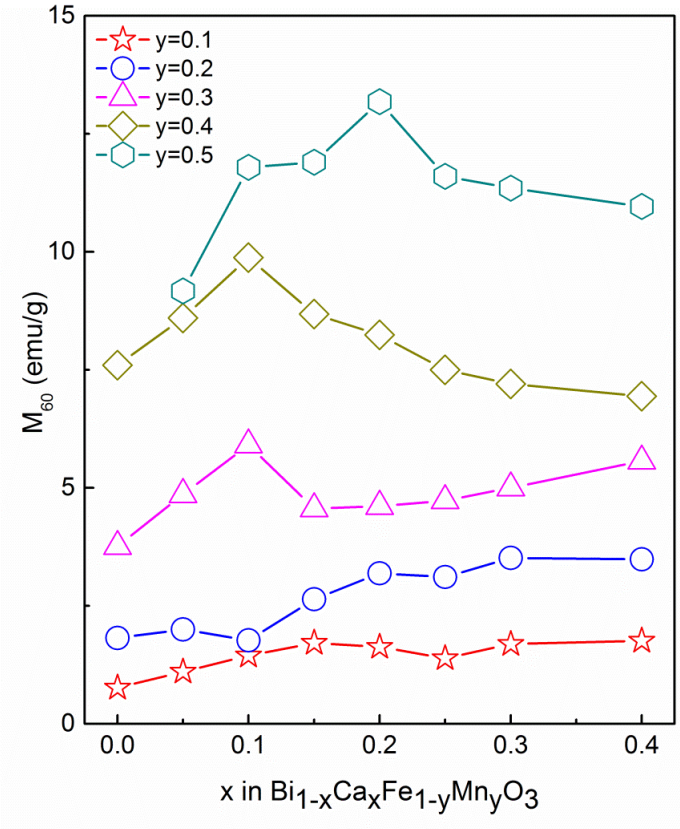

Figure 5.35. Magnetization at 5 K at the field of 60 kOe (M_{60}) as a function of x in $Bi_{1-x}Ca_xFe_{1-y}Mn_yO_3$.

It is observed that, in a particular series (with constant Mn content), room temperature and low-temperature magnetic parameters exhibit anomaly around the same values of *x*, which vary from $x = 0.15$ to $x = 0.25$ for different *y* (Mn) values. In $Bi_{1-x}Ca_xFe_{1-y}Mn_yO_3$, the structural transition is observed around $x = 0.1–0.2$. The anomalous magnetic parameters observed in the compositional region $x = 0.1$ to $x = 0.25$ could be due to the MPB assisted enhanced properties similar to that observed for the $Bi_{1-x}Ca_xFe_{1-x}Mn_xO_3$ series. Another possibility for these enhanced properties is the Mn^{3+}/Mn^{4+} content, though such a trend was not observed from the XPS analysis.

5.5.2. M vs. T measurements

The ZFC and FC magnetization curves of different compositions in $Bi_{1-x}Ca_xFe_{1-y}Mn_yO_3$, measured in an applied magnetic field of 500 Oe, are shown in figures 5.36–5.40. For $BiFe_{0.9}Mn_{0.1}O_3$, both the FC and ZFC magnetizations decrease with increasing temperature showing a kink around 26 K and 195 K as shown in figure 5.36. On the other hand, upon Ca substitution, these kinks disappear, and a broad peak is observed in the ZFC curve, with the FC magnetization decreasing continuously, suggesting a spin glass transition. The spin glass transition is observed for $x = 0.1$ at a T_p around 30 K. The spin glass transition temperature increases with increasing Ca substitution and show the maximum vlaue at $x = 0.25$ with $T_p = 45$ K and then decreases for higher compositions. Such a spin-glass-like behaviour is reported in calcium and manganese co-substituted systems $Bi_{0.5}Ca_{0.5}Fe_{1-y}Mn_yO_3$ and $Bi_{0.8}Ca_{0.2}Fe_{1-y}Mn_yO_3$ [1-3]. The ferromagnetic loop observed at 5 K for $x \geq 0.1$ in $Bi_{1-x}Ca_xFe_{0.9}Mn_{0.1}O_3$ could be due to the spin glass state of the system since such loops are absent for $x \leq 0.05$.

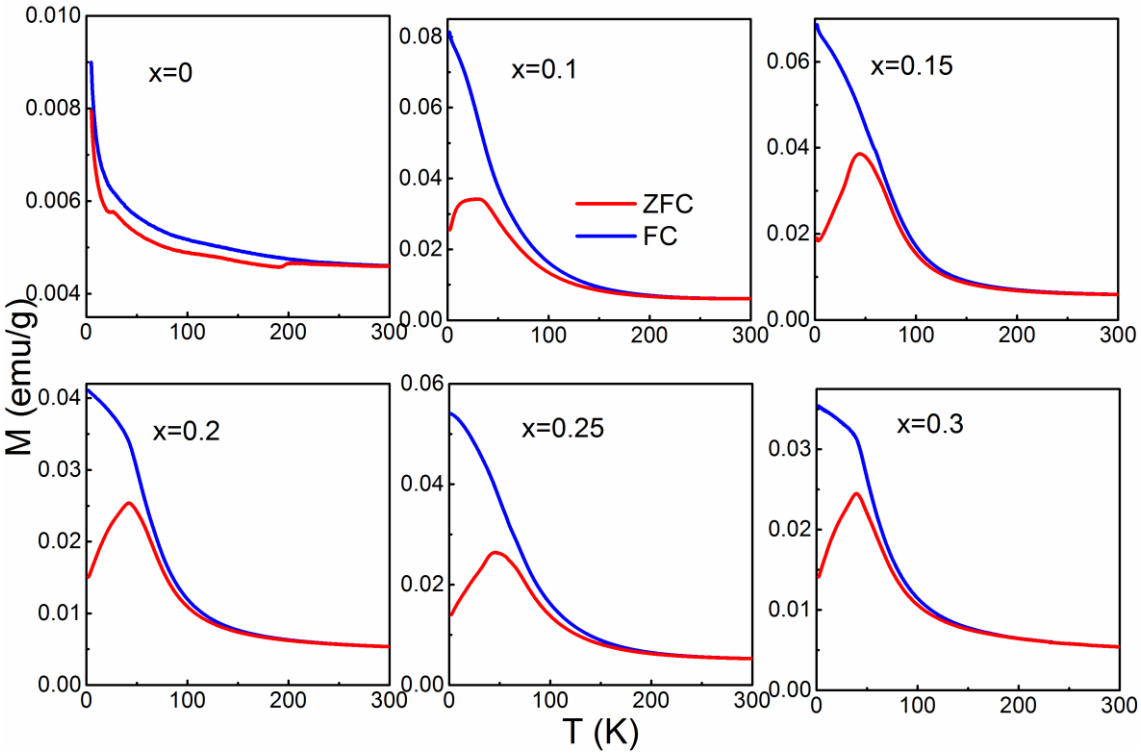

Figure 5.36. ZFC and FC magnetization curves of $Bi_{1-x}Ca_xFe_{0.9}Mn_{0.1}O_3$

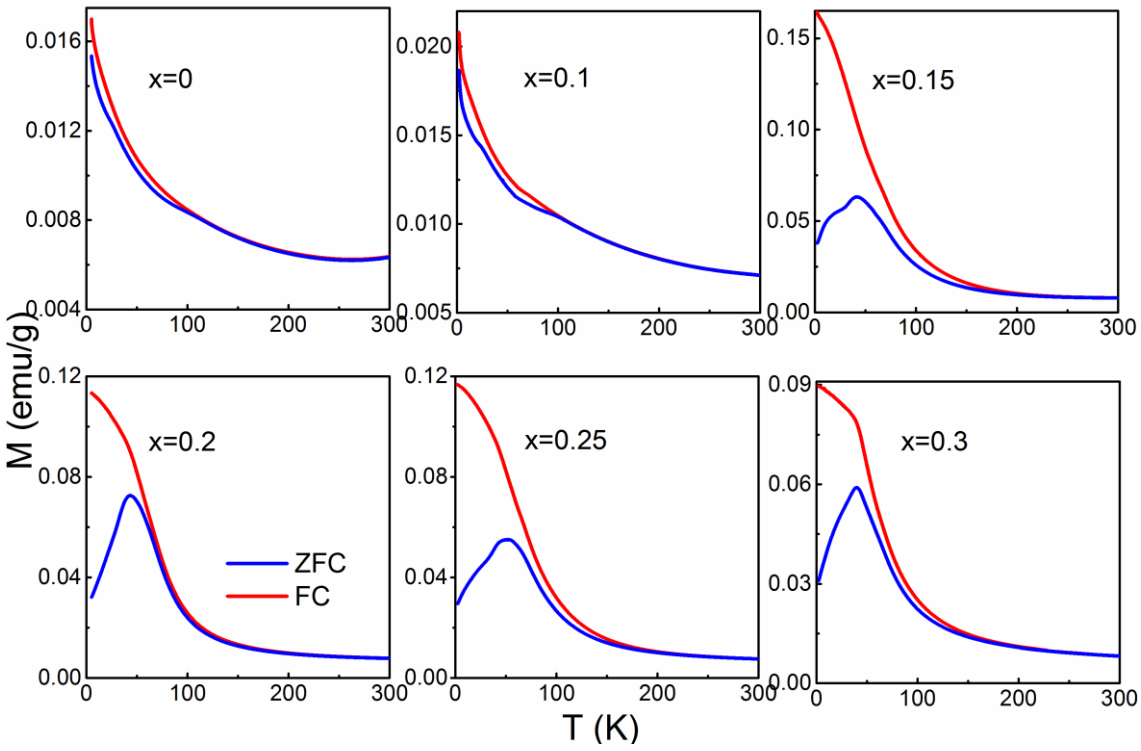

Figure 5.37. ZFC and FC magnetization curves of $Bi_{1-x}Ca_xFe_{0.8}Mn_{0.2}O_3$.

$BiFe_{0.8}Mn_{0.2}O_3$ shows a ZFC curve similar to that of $BiFe_{0.9}Mn_{0.1}O_3$, though no kinks are observed (figure 5.37). Upon Ca substitution, till x = 0.1, similar ZFC–FC behaviour is observed. The x = 0.15 composition shows a spin glass transition at T_p = 41 K. In the $Bi_{1-x}Ca_xFe_{0.8}Mn_{0.2}O_3$ series, maximum T_p (52 K) is observed for x = 0.25. In the y = 0.2 system, magnetic hysteresis loop at 5 K is observed only for $x \geq 0.15$ which exhibit a spin glass state. In $Bi_{1-x}Ca_xFe_{0.7}Mn_{0.3}O_3$, compositions with $x \geq 0.1$ show spin-glass-like behaviour. $Bi_{0.9}Ca_{0.1}Fe_{0.7}Mn_{0.3}O_3$ shows a very low T_p (4 K) as compared to the y = 0.1 and y = 0.2 systems (figure 5.38). In the y = 0.3 series, T_p is maximum (45 K) at x = 0.25. Similar to the y = 0.1 and 0.2 systems, for y = 0.3, magnetic hysteresis loop is observed only for $x \geq 0.1$ for which a spin glass state is observed.

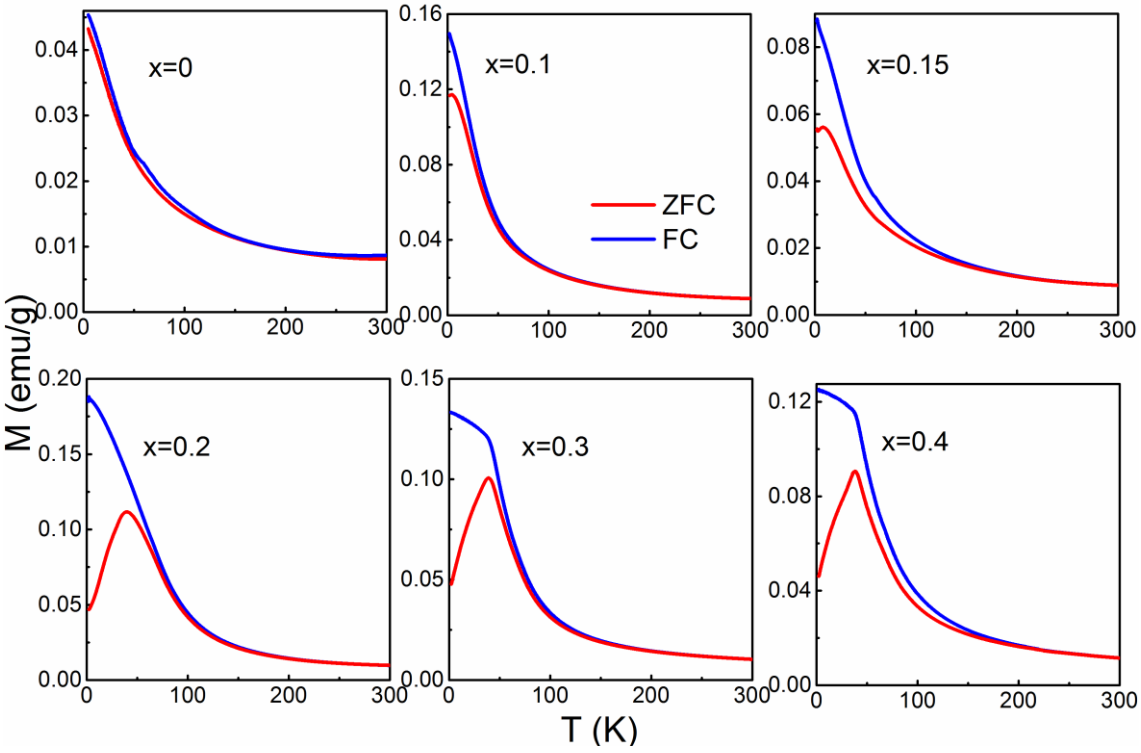

Figure 5.38. ZFC and FC magnetization curves of $Bi_{1-x}Ca_xFe_{0.7}Mn_{0.3}O_3$.

Unlike the $BiFe_{1-x}Mn_xO_3$ systems for $x \leq 0.3$, $BiFe_{0.6}Mn_{0.4}O_3$ shows a spin glass transition with T_p around 4.5 K as shown figure 5.39. Upon Ca substitution the spin glass transition temperature slowly increases and gives a maximum value of T_p = 46 K at x = 0.25. A magnetic hysteresis loop is observed for $x > 0$ in the $Bi_{1-x}Ca_xFe_{0.6}Mn_{0.4}O_3$ series (as explained

with respect to figure 5.31). The narrower loop at 5 K observed for $BiFe_{0.6}Mn_{0.4}O_3$ is due to its low T_p (4.5 K) which is close to the lowest measurement temperature. In the y = 0.5 series, $Bi_{0.95}Ca_{0.05}Fe_{0.5}Mn_{0.5}O_3$ shows a peak in the ZFC curve at T_p = 9 K (figure 5.40). Surprisingly $Bi_{0.9}Ca_{0.1}Fe_{0.5}Mn_{0.5}O_3$ exhibits two peaks in the ZFC curve, at T_{p1} and T_{p2} at 16 K and 48 K, respectively, as shown in figure 5.41. For $Bi_{0.88}Ca_{0.12}Fe_{0.5}Mn_{0.5}O_3$ the first transition gets diminished and for $Bi_{0.86}Ca_{0.14}Fe_{0.5}Mn_{0.5}O_3$ it almost disappears. For comparison, ZFC magnetization curves of different compositions in $Bi_{1-x}Ca_xFe_{0.5}Mn_{0.5}O_3$ are shown in figure 5.42. Compositions with x > 0.2 show a hump in the ZFC curves around 10 K (figure 5.42). In x = 0.2, it is possible that T_{p1} is not observed due to the higher magnetization. Though the first transition (at T_{p1}) is observed in the $x = y$ systems and some of the compositions in the $x \neq y$ series, it appears as a weak transition and observed only as a hump/shoulder and variation of T_{p1} with substitution is not observed. On the other hand, in $B_{i1-x}Ca_xFe_{0.5}M_{n0.5}O_3$, T_{p1} shows a clear variation with increasing Ca content as shown in the inset of figure 5.41. T_{p2} varies with Ca substitution showing a maximum at x = 0.3. Maximum T_p = 60 K is shown by $Bi_{0.7}Ca_{0.3}Fe_{0.5}Mn_{0.5}O_3$ among the different compositions in the five series. As all the compositions in $Bi_{1-x}Ca_xFe_{0.5}Mn_{0.5}O_3$ show spin-glass-like behaviour, correspondingly all compositions show magnetic hysteresis loops at 5 K as shown in figure 5.32.

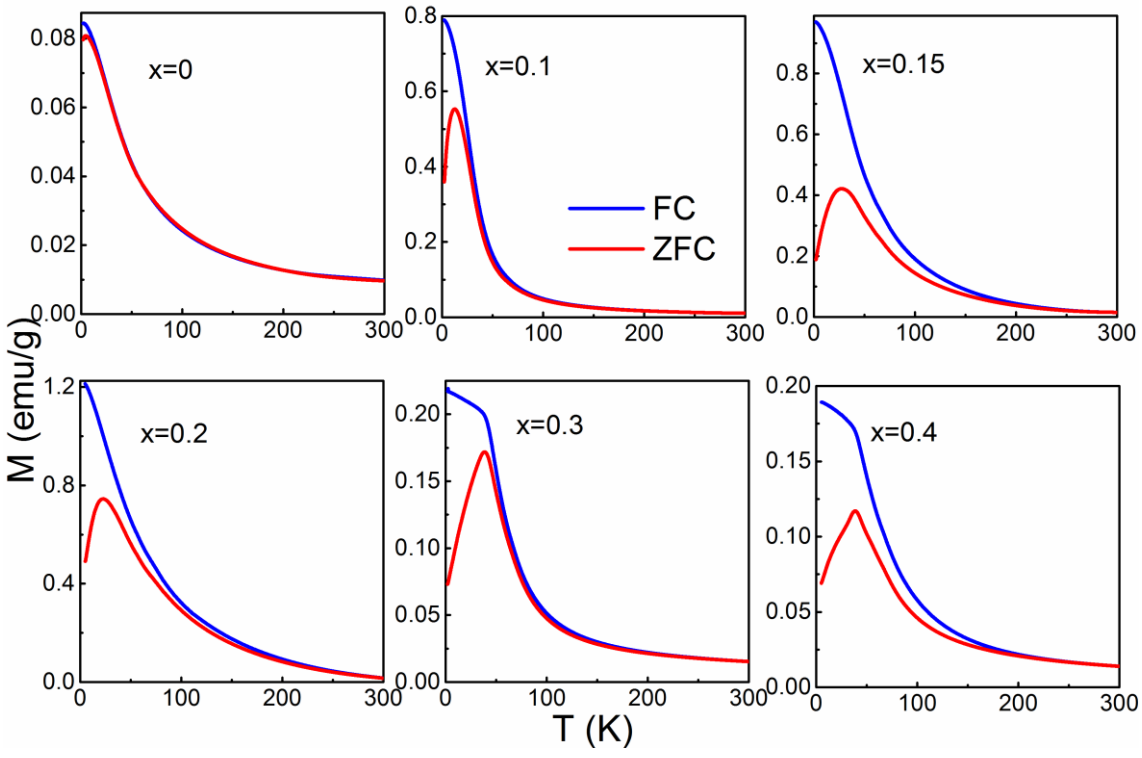

Figure 5.39. ZFC and FC magnetization curves of $Bi_{1-x}Ca_xFe_{0.6}Mn_{0.4}O_3$.

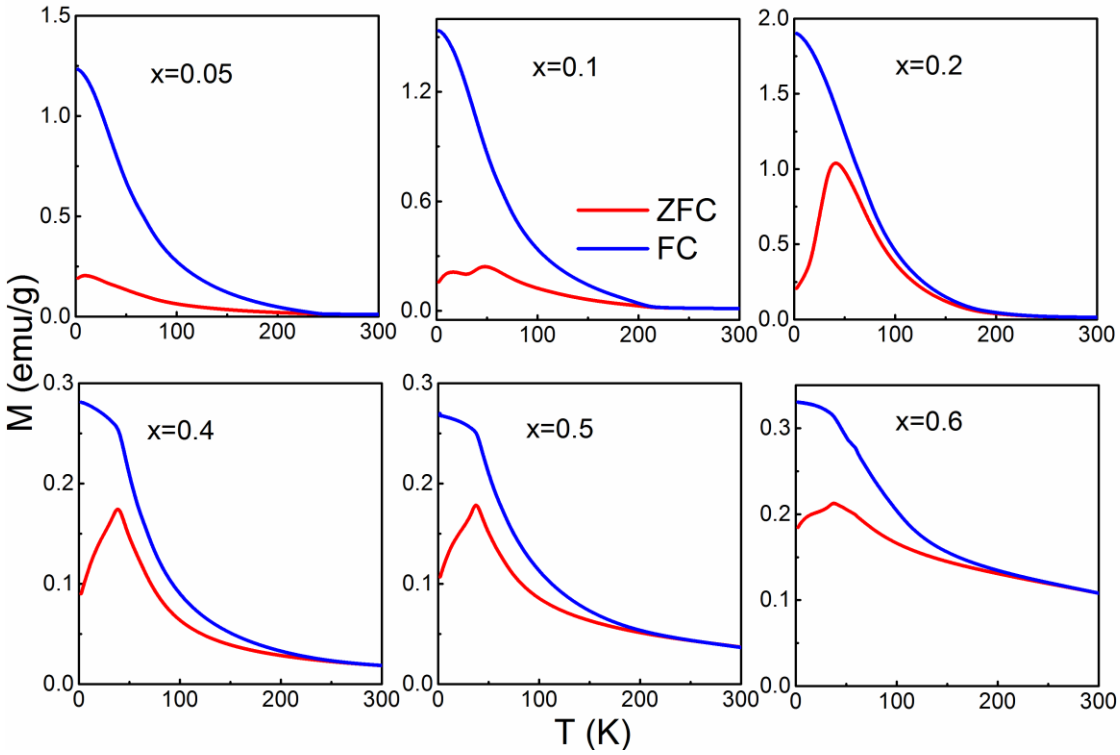

Figure 5.40. ZFC and FC magnetization curves of $Bi_{1-x}Ca_xFe_{0.5}Mn_{0.5}O_3$.

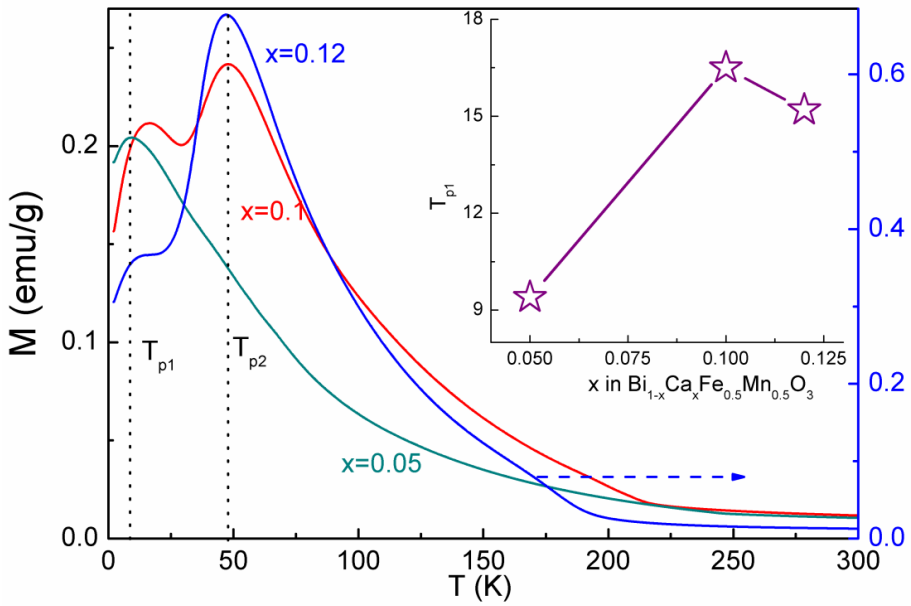

Figure 5.41. ZFC magnetization curves of $Bi_{0.95}Ca_{0.05}Fe_{0.5}Mn_{0.5}O_3$, $Bi_{0.9}Ca_{0.1}Fe_{0.5}Mn_{0.5}O_3$ and $Bi_{0.92}Ca_{0.12}Fe_{0.5}Mn_{0.5}O_3$ showing the two transitions observed. Inset shows the variation of T_{p1} vs. x in $Bi_{1-x}Ca_xFe_{0.5}Mn_{0.5}O_3$.

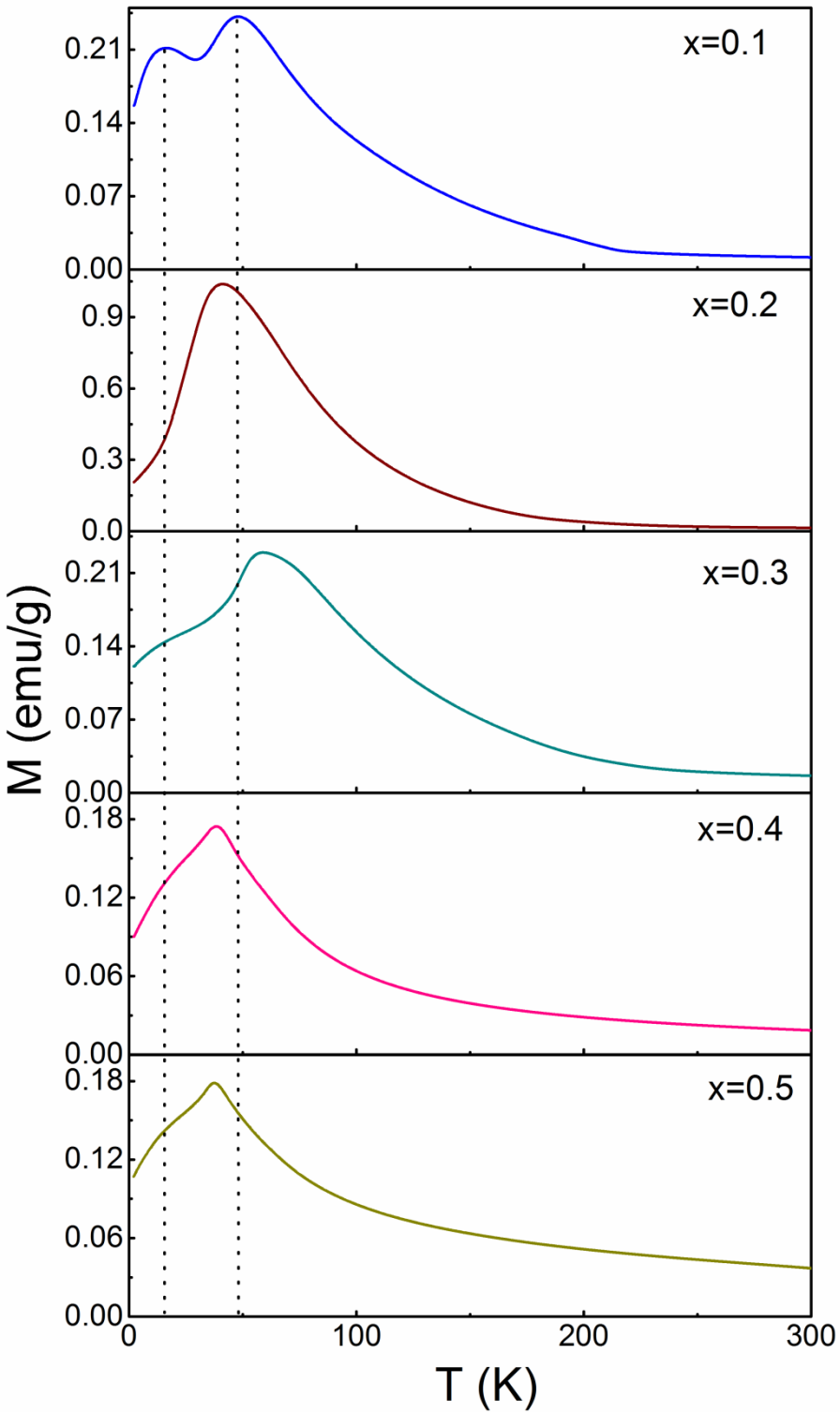

Figure 5.42. Comparison of the ZFC magnetization curves of different $Bi_{1-x}Ca_xFe_{0.5}Mn_{0.5}O_3$ compositions.

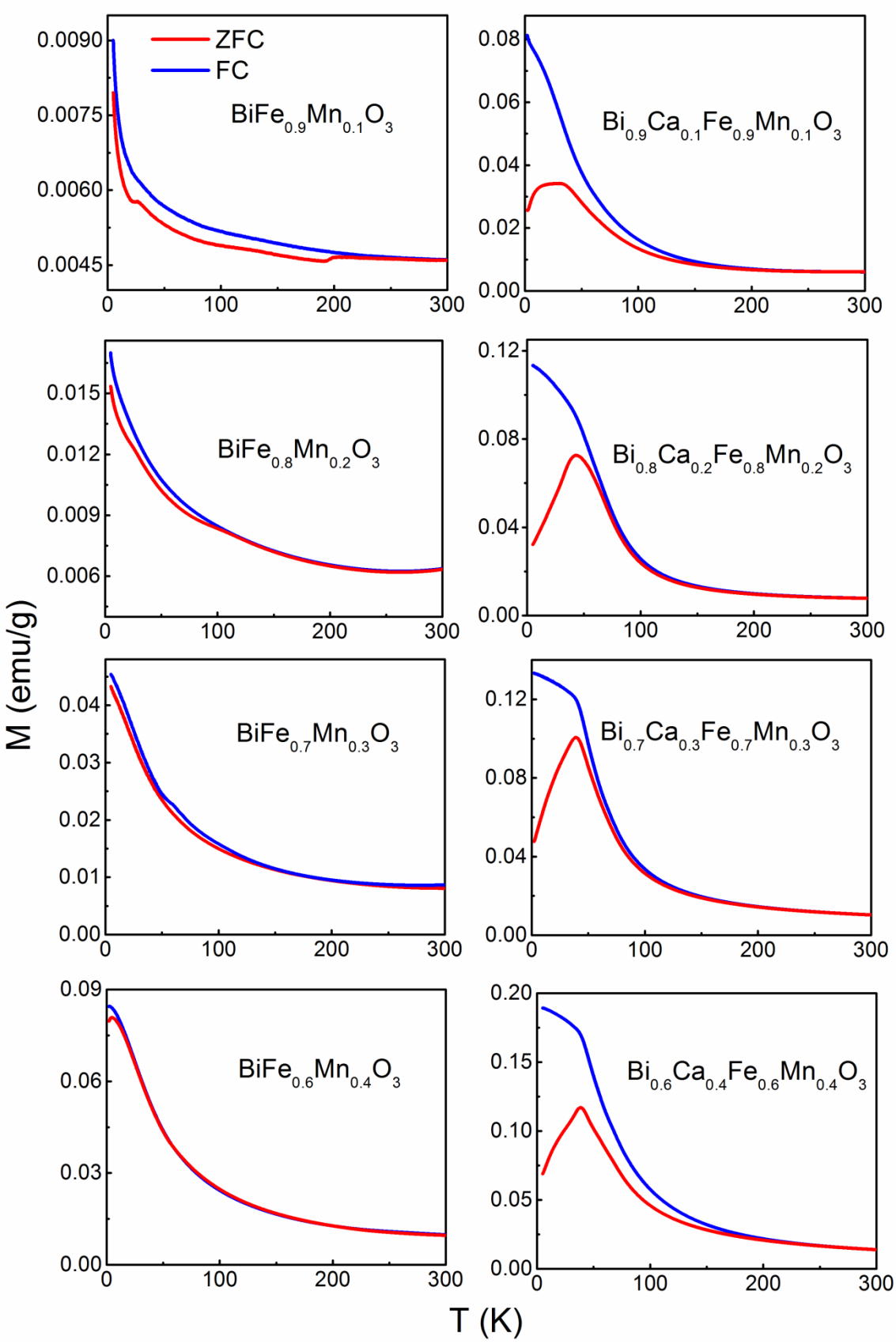

Figure 5.43. Comparison of the ZFC/FC magnetization curves of different compositions in $Bi_{1-x}Ca_xFe_{1-y}Mn_yO_3$ for $x = 0$ and $x = y$.

The FC/ZFC magnetization curves of different compositions in $Bi_{1-x}Ca_xFe_{1-y}Mn_yO_3$ for $x = 0$ ($BiFe_{1-y}Mn_yO_3$) and $x = y$ ($Bi_{1-x}Ca_xFe_xMn_xO_3$) are compared in figure 5.43. All the compositions in $BiFe_{1-y}Mn_yO_3$ show a decrease in the magnetization with increasing temperature. $BiFe_{0.4}Mn_{0.6}O_3$ shows a spin glass transition at a very low temperature (4.5 K). On the other hand, the Ca-substituted compositions for $x = y$ show a spin glass transition around 40 K. Ca substitution in $BiFe_{1-y}Mn_yO_3$ probably induces frustrated/spin glass phase possibly due to the creation of competing exchange interactions involving Mn^{3+} and Mn^{4+}.

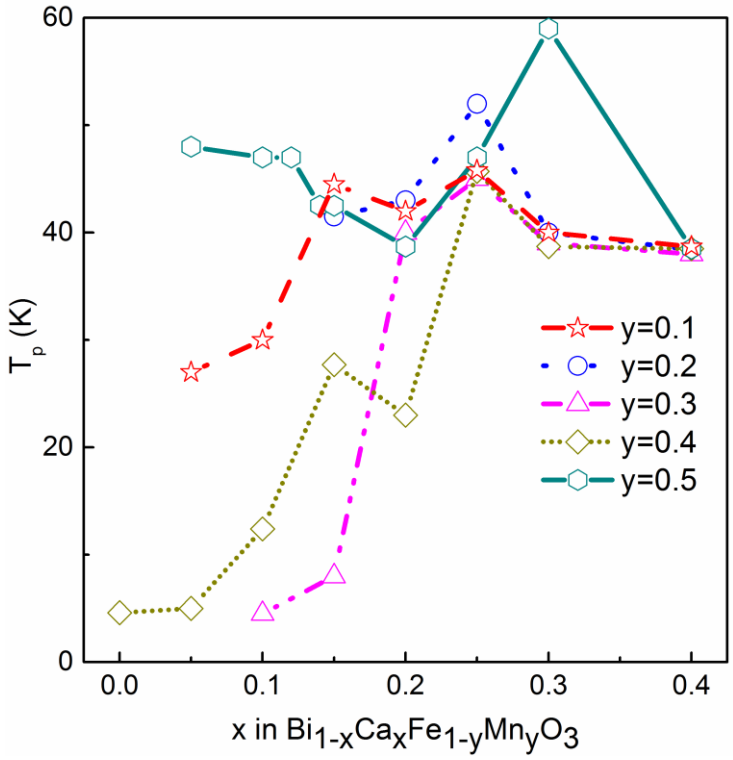

Figure 5.44. Spin glass transition temperature, T_p, vs. x of $Bi_{1-x}Ca_xFe_{1-y}Mn_yO_3$.

Figure 5.44 shows the spin glass transition temperature observed for the different series of compositions plotted against the calcium substitution content. Except for $y = 0.5$, maximum T_p is observed at $x = 0.25$ in the $Bi_{1-x}Ca_xFe_{1-y}Mn_yO_3$ series. The $y = 0.5$ series show maximum T_p at $x = 0.3$. All the series show almost similar $T_p \approx 40$ K at $x = 0.4$. Furthermore, only the compositions which exhibit spin glass transition (above 5 K) show magnetic hysteresis loop at 5 K which confirms that the magnetic loop observed at 5 K is

associated with the spin glass state and not from any other impurities. There is no particular trend observed in the magnitude of T_p with respect to the Mn content and the $Bi_{1-x}Ca_xFe_{0.5}Mn_{0.5}O_3$ compositions exhibit relatively higher T_p. It is possible that this is due to the difference in the Mn^{3+}/Mn^{4+} content in different compositions which determines the strength of the different competing ferro- and antiferromagnetic exchange interactions leading to spin glass behaviour.

5.6. Dielectric properties

The dielectric constant measured for the different compositions in $Bi_{1-x}Ca_xFe_{1-y}Mn_yO_3$, as a function of frequency in the range of 1 kHz to 1 MHz, is shown in figures 5.45–5.49. The pellets of $Bi_{0.95}Ca_{0.05}Fe_{0.7}Mn_{0.3}O_3$, $Bi_{0.95}Ca_{0.05}Fe_{0.6}Mn_{0.4}O_3$ and $Bi_{0.9}Ca_{0.1}Fe_{0.6}Mn_{0.4}O_3$ melted and cracked when sintered at 850 °C, and hence dielectric measurements could not be carried out on these compositions. The dielectric constant decreases with increasing frequency and becomes almost constant at higher frequencies as in the the $x = y$ co-substituted system, discussed in chapter 4. The dielectric constant at 10 kHz is plotted against Ca content in figure 5.50. A maximum in the dielectric constant is observed at x = 0.1, 0.25, 0.2, and 0.15 for y = 0.1, 0.2, 0.3, and 0.4, respectively. In the y = 0.5 system, the dielectric constant shows a maximum around x = 0.05 with another maximum at x = 0.25. In all the five series, an anomaly in the value of the dielectric constant is observed at x = 0.25. The mixed phase nature in the MPB region and the interfacial space charge accumulation could lead to such higher values of the dielectric constant [24].

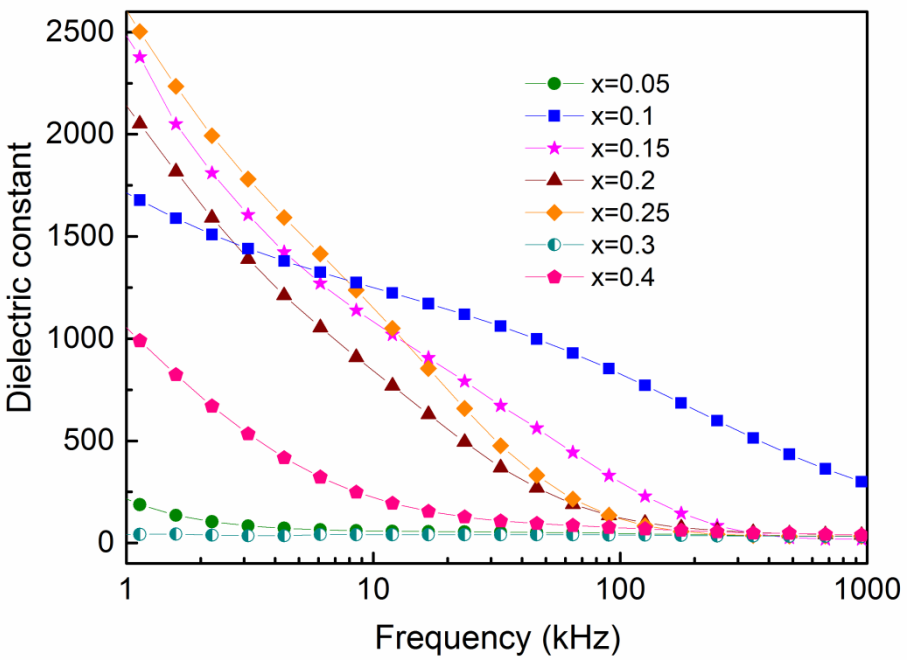

Figure 5.45. Dielectric spectra of $Bi_{1-x}Ca_xFe_{0.9}Mn_{0.1}O_3$.

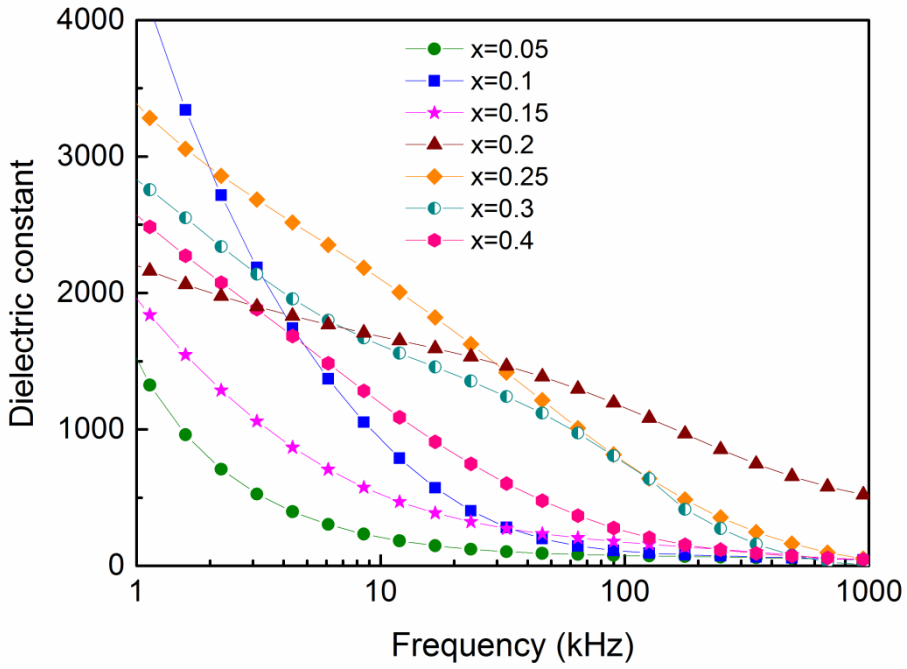

Figure 5.46. Dielectric spectra of $Bi_{1-x}Ca_xFe_{0.8}Mn_{0.2}O_3$.

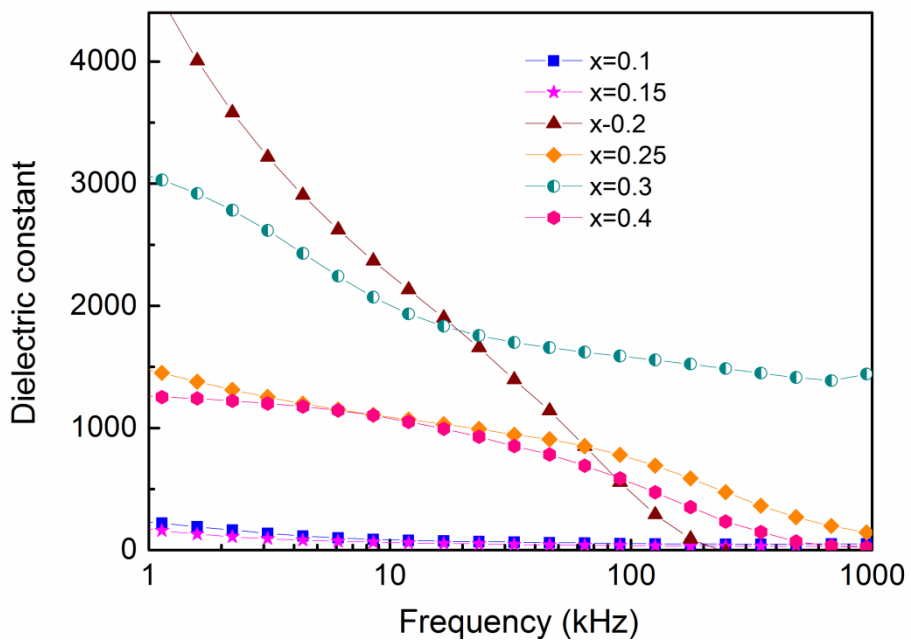

Figure 5.47. Dielectric spectra of $Bi_{1-x}Ca_xFe_{0.7}Mn_{0.3}O_3$.

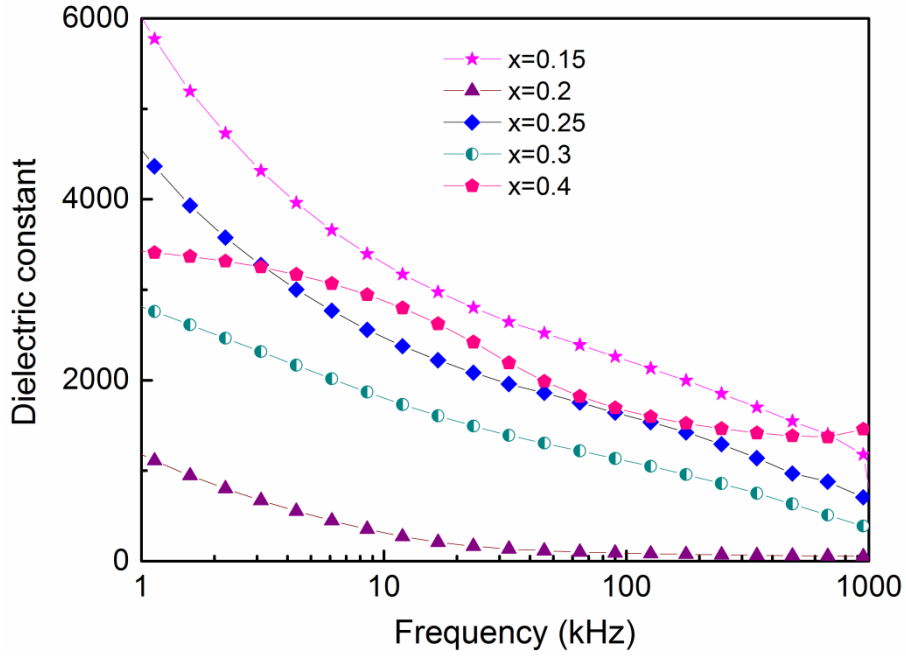

Figure 5.48. Dielectric spectra of $Bi_{1-x}Ca_xFe_{0.6}Mn_{0.4}O_3$.

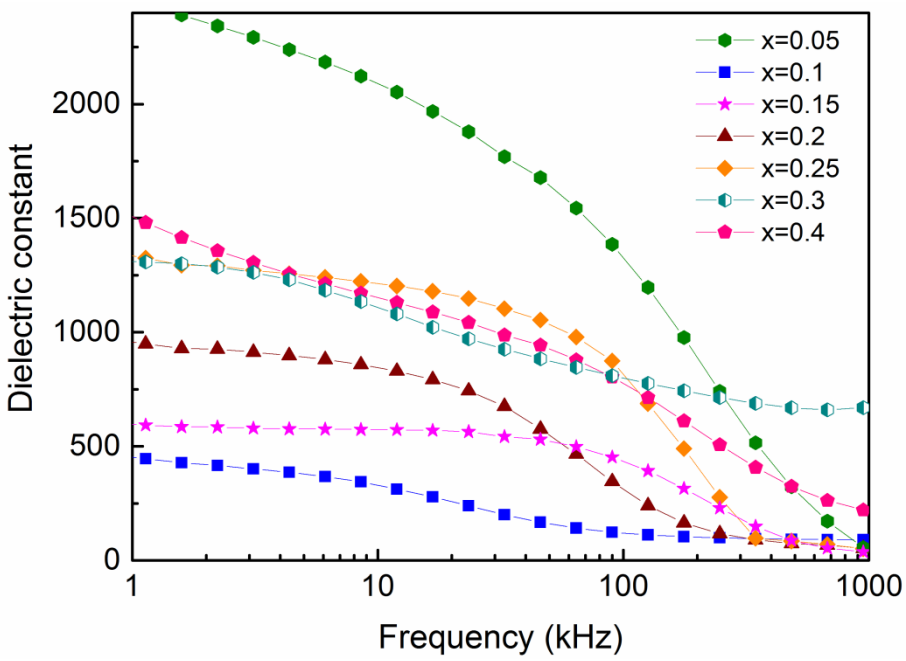

Figure 5.49. Dielectric spectra of $Bi_{1-x}Ca_xFe_{0.5}Mn_{0.5}O_3$.

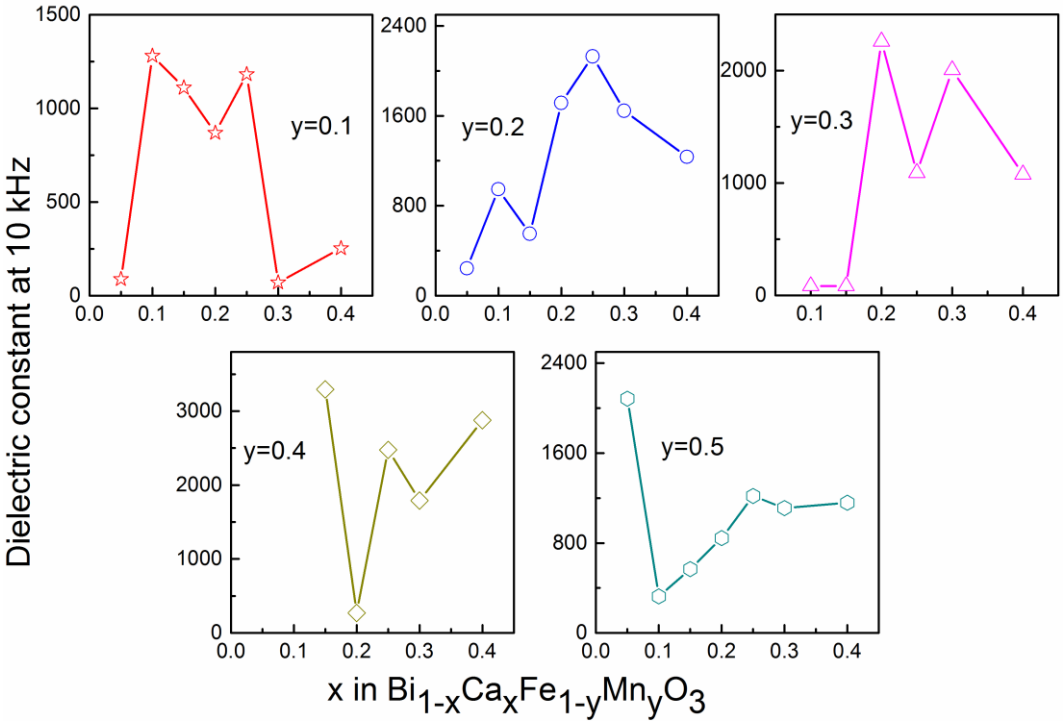

Figure 5.50. Dielectric constant at 10 kHz vs. x in $Bi_{1-x}Ca_xFe_{1-y}Mn_yO_3$.

Similar to that observed for the $x = y$ system, as discussed in chapter 3, an anomaly in the dielectric constant is observed for the $x \neq y$ system around the structural phase transition

region. Higher dielectric constant indicates the possibility of higher ferroelectric polarization of the compositions. Higher magnetic parameters and higher dielectric constant in the structural phase transition region in $Bi_{1-x}Ca_xFe_{1-y}Mn_yO_3$ possibly will enhance the magnetoelectric coupling in the $BiFeO_3$ system. Thus, it would be possible to tune the dielectric (ferroelectric) and magnetic properties of $BiFeO_3$ by varying the Ca and Mn substitution level in $Bi_{1-x}Ca_xFe_{1-y}Mn_yO_3$.

5.8. Conclusions

Structural, magnetic and dielectric properties of Ca and Mn co-substituted bismuth ferrite, $Bi_{1-x}A_xFe_{1-y}Mn_yO_3$, ($0 \leq x \leq 0.4$; $0.1 \leq y \leq 0.5$) have been studied. The rhombohedral *R3c* phase is stabilized up to the Ca substitution content $x = 0.15$. Rietveld refinement analysis of the XRD patterns revealed that all the five series show a structural change from rhombohedral *R3c* to orthorhombic *Pbnm* around $x = 0.15$ similar to the $x = y$ co-substituted series. An *R3c*-*Pbnm* mixed phase was observed in the MPB region. Raman spectra of the compositions also confirmed structural transition around this region. The decrease in the lattice parameters and unit cell volume suggested the presence of Mn^{4+} in the compositions. XPS analysis of compositions confirmed the presence of both Mn^{3+} and Mn^{4+}. Weak ferromagnetism is observed for compositions except for $y \geq 0.4$. Weak ferromagnetism of the samples can be attributed to the DMI assisted canted antiferromagnetism and the effective suppression of spin cycloid structure upon co-substitution. Coercivity and remanence showed higher values around the MPB region, whereas the magnetization at 60 kOe increases with calcium and manganese substituent. A very high room temperature coercivity around 8 kOe is observed for $Bi_{0.85}Ca_{0.15}Fe_{0.9}Mn_{0.1}O_3$ which is the highest among all the Ca and Mn co-substituted compositions studied. Most of the compositions show a spin-glass-like behaviour whose glass transition temperature varies with the substituent level. The frustrated magnetic behaviour in the system is probably due to the competing magnetic exchange interactions involving Fe^{3+}, Mn^{3+} and Mn^{4+} which could lead to the formation of ferromagnetic clusters. A large magnetic hysteresis loop with high magnetization is observed at low temperature is associated with this spin glass state observed. Dielectric constant also shows an anomaly around the structural transition region. The high magnetic parameters, along with the high dielectric constants in the MPB region are likely to lead to higher magnetoelectric coupling in specific composition.

References

[1] Tzankov D, Kovacheva D, Krezhov K, Puźniak R, Wiśniewski A, Sváb E and Mikhov M 2005 *J. Phys. Condens. Matter.* **17** 4319.

[2] Tzankov D, Kovacheva D, Krezhov K, Puźniak R, Wiśniewski A, Sváb E and Mikhov M 2008 *J. Appl. Phys.* **103** 053910.

[3] Yin L H, Sun Y P, Zhang F H, Wu W B, Luo X, Zhu X B, Yang Z R, Dai J M, Song W H and Zhang R L 2009 *J. Alloys Compd.* **488** 254

[4] Huang J-Z, Shen Y, Li M and Nan C-W 2011 *J. Appl. Phys.* **110** 094106

[5] Khomchenko V A, Pereira L C and Paixão J A 2015 *J. Mater. Sci.* **50** 1740

[6] Agarwal A, Sanghi S and Ahlawat N 2012 *J. Phys. D: Appl. Phys.* **45** 165001

[7] Verma K C and Kotnala R K 2016 *RSC Adv.* **6** 57727

[8] Makhdoom A R, Akhtar M J, Rafiq M A, Siddique M, Iqbal M and Hasan M M 2014 *AIP Adv.* **4** 037113

[9] Yang C H, Koo T Y and Jeong Y H 2005 *Solid State Commun*. **134** 299

[10] Azuma M, Kanda H, Belik A A, Shimakawa Y and Takano M 2007 *J. Magn. Magn. Mater*. **310** 1177

[11] Ianculescu A, Gheorghiu F P, Postolache P, Oprea O and Mitoseriu L 2010 *J. Alloys Compd*. **504** 420

[12] Chauhan S, Kumar M, Chhoker S, Katyal S C, Singh H, Jewariya M, Yadav K L 2012 *Solid State Commun.* **152** 525

[13] Catalan G, Sardar K, Church N S, Scott J F, Harrison R J and Redfern S A 2009 *Phys. Rev.* B **79** 212415.

[14] Troyanchuk I O, Chobot A N, Mantytskaya O S and Tereshko N V 2010 Inorg. Mater. **46** 424

[15] Zheng X, Xu Q, Wen Z, Lang X, Wu D, Qiu T and Xu M X 2010 *J. Alloys Compd*. **499** 108

[16] Ederer C and Spaldin N A 2005 *Phys. Rev.* B **71** 060401

[17] Kumar M and Yadav K L 2006 *J. Appl. Phys.* **100** 74111

[18] Yuan G L, Or S W and Chan H L 2007 *J. Phys.* D*: Appl. Phys*. **40** 1196

[19] Troyanchuk I O, Karpinsky D V, Bushinsky M V, Khomchenko V A, Kakazei G N, Araujo J P, Tovar M, Sikolenko V, Efimov V and Kholkin A L 2011 *Phys. Rev.* B **83** 054109

[20] Karpinsky D V, Troyanchuk I O, Zheludkevich A L, Ignatenko O V, Silibin M V and Sikolenko V V 2016 *Phys. Solid State* **58** 1590

[21] Arya G S and Negi N S 2013 *J. Phys.* D **46** 095004

[22] Wen Z, Shen X, Wu D, Xu Q and Wang J, Li A 2010 *Solid State Commun.***150** 2081

[23] Xing Z, Zhu X, Zhu J, Liu Z and Al-Kassab T 2014 *J. Am. Ceram. Soc.* **97** 2323

[24] Yan F, Zhu T J, Lai M O and Lu L 2010 *Scripta Mater.* **63** 780

Chapter 6

Conclusions and Future Perspectives

6.1. Conclusions

Magnetoelectrics or multiferroics, due to their combined order parameters, have potential applications in the fields of data storage, sensors, actuators, etc. There are very few known room temperature multiferroics and perovskite based multiferroics are of great interest as it is easy to alter its properties. Though composite multiferroics can exhibit magnetoelectricity, the coupling shown by them is very low and thus it is important to find single phase multiferroics having higher magnetic/ferroelectric transition temperatures with large magnetoelectric coupling. Bismuth ferrite, $BiFeO_3$ (BFO) is one of the well-known and well-studied single phase room-temperature multiferroic materials, due to its higher ferroelectric Curie temperature and antiferromagnetic transition temperature, both above room temperature. Large polarization values had been reported for BFO, but due to its antiferromagnetic nature and spin cycloidal structure, it shows very weak magnetization and coercivity, resulting in a very low magnetoelectric coefficient. Different approaches have been made to enhance the magnetic properties of BFO by destructing the spin periodicity, such as fabrication of nanoparticles and thin films, where particles with size below the spin cycloidal wavelength (64 nm) can show weak ferromagnetism.

The easiest way to alter the properties of $BiFeO_3$ is the substitution at the Bi- or Fe- site with suitable ions, where, due to structural distortions, the spin cycloidal structure collapses resulting in weak ferromagnetism and thus enhancing the magnetoelectric properties. In the case of Fe-site substitution, besides the structural distortions, magnetic exchange interactions between the Fe and the substituted ions can also lead to better magnetic properties. In the last five years, there have been many reports on the co-substitution in $BiFeO_3$, which is the simultaneous substitution at the Bi and Fe sites, where both the magnetic and ferroelectric properties can be altered simultaneously. Many co-substituted systems are known to show higher ferroelectric and magnetic properties with enhanced magnetoelectric coupling. However, on co-substitution, the system becomes too complex to understand due to the many exchange interactions pathways. To completely understand the properties of such a system, bulk or single crystalline samples are needed since nanoparticle and thin film systems could exhibit anomalous properties due to size effect.

In most of the substituted BFO systems, only room temperature magnetic properties are explored, and not much is known about the low-temperature magnetic properties. To fully understand the magnetic nature of the Bi/Fe-site substituted or co-substituted systems, studies

at low temperatures are required. In this context, we have attempted to study divalent ion and manganese co-substituted bulk polycrystalline $BiFeO_3$, where Mn^{4+} and/or oxygen vacancies will be created in order to compensate the charge and this will largely effect on the magnetic and electrical properties. Detailed studies are made on the magnetic characteristics below room temperature on different compositions in the co-substituted systems. All the compositions are prepared by the solid state method of synthesis.

To understand the role of the size of the Bi-site substituted ion on the magnetic properties, studies are made on bulk polycrystalline samples of $Bi_{1-x}A_xFe_{1-x}Mn_xO_3$ (A = Ca, Sr, Ba) for $0 \leq x \leq 0.3$. Ca^{2+} has almost comparable ionic radii to that of Bi^{3+} whereas Sr^{2+} and Ba^{2+} are comparatively larger ions. All the systems studied showed a structural transition at higher levels of substitution, with mixed phase behaviour in intermediate compositional regions. A decrease in the lattice parameters and unit cell volume are observed in all cases, irrespective of the size of the substituted divalent ion which indicated the presence of Mn^{4+} in all the three co-substituted systems. Among the three co-substituted systems, higher magnetic parameters and dielectric constant were observed for the Ca-Mn co-substituted samples. Similarly, in all the three cases, higher magnetic parameters were observed around $x = 0.15$, in the MPB region. Higher magnetic parameters observed around $x = 0.15$ could be due to the decreased rhombohedral distortion, presence of more than one phase, changes in the Fe-O-Fe bond angle and Fe-O bond lengths upon co-substitution.

Since the higher magnetic parameters at room temperature were observed for the Ca-Mn co-substituted system, detailed structural and magnetic studies have been carried out on close compositions in the $Bi_{1-x}Ca_xFe_{1-y}Mn_yO_3$ (both $x = y$ and $x \neq y$) systems, to identify the structural transition and MPB regions. Rietveld refinement of the XRD patterns and Raman spectra analysis indicated that in $Bi_{1-x}Ca_xFe_{1-x}Mn_xO_3$ ($x = y$) rhombohedral (*R3c*) to orthorhombic (*Pbnm*) structural transition occurs around $x = 0.15$ with a mixed phase of *R3c* and *Pbnm* existing in the $x = 0.12–0.175$ region. The existence of Mn^{3+} and Mn^{4+} as evident from XPS and titration analysis can lead to double exchange magnetic interaction which again contributes to the enhanced magnetic properties observed. A wide magnetic hysteresis loop was observed in the MPB region with very high coercivity and relatively larger remanence. Room temperature magnetization increased with the degree of co-substitution. Large hysteresis loop was observed at 5K, with anomalous magnetic parameters around the MPB region. Weak ferromagnetism observed is due to the canted antiferromagnetism and the efficient suppression of the spin cycloid by the structural distortion caused by co-substitution.

The anomaly in the parameters around the structural transition region can be explained from the anomaly in the structural parameters such as the rhombohedral angle, Fe-O-Fe bond angle, Fe-O bond length, Helen-Megaw parameters, etc., apart from the larger amounts of Mn^{3+} and oxygen vacancies around x = 0.15. The magnetic transition observed in the high-temperature magnetization studies confirmed the formation of the single phase compositions and excludes the possibility of any impurities or phase separation. Low-temperature ZFC-FC magnetization curves indicated a composition dependent spin-glass-like transition showing a maximum spin glass transition temperature in the MPB region. $Bi_{1-x}Ca_xFe_{1-x}Mn_xO_3$ system showed higher dielectric constant at x = 0.15 which again falls within the MPB region. Higher dielectric properties could be due to the existence of MPB as in the case of known ferroelectric systems or due to the dense microstructure existing around the MPB region as evidenced from the SEM images. Magnetodielectric (MD) measurements revealed a positive MD value for the rhombohedral phase and negative MD for the orthorhombic phase with a maximum at x = 0.1. This composition-dependent magnetodielectric property is quite interesting and further analysis is required. A very high remanence and coercivity were observed for $Bi_{0.825}Ca_{0.175}Fe_{0.825}Mn_{0.175}O_3$, at room temperature, which is comparatively much larger than for many of the reported BFO systems, and hence could possibly perform as a very good candidate for device applications.

To understand more about the Ca and Mn co-substituted $BiFeO_3$ system, we have varied the Ca concentration by fixing the Mn substitution level with the general formula $Bi_{1-x}Ca_xFe_{1-y}Mn_yO_3$ ($0.05 \leq x \leq 0.4$ and $0 \leq y \leq 0.5$). The aim was to study the effect of Ca substitution on the structural and magnetic properties of $BiFe_{1-y}Mn_yO_3$. In all five different series analyzed, rhombohedral to orthorhombic structural transition around x = 0.15, similar to that in the $Bi_{1-x}Ca_xFe_{1-x}Mn_xO_3$ system, was observed. The decrease in lattice parameters was observed with increasing Ca content (with constant amount of Mn) or increase in the Mn (with constant amount of Ca) content suggesting the presence of Mn^{4+} in all compositions. Structural analysis by XRD and Raman spectroscopy also revealed that Ca and Mn substitution helps to stabilize the rhombohedral phase of $BiFeO_3$ till a particular degree of substitution (for Ca, $x \approx 0.15$, for Mn, $y \approx 0.3$) and a higher degree of substitution leads to a transition to orthorhombic structure. For $y \geq 0.4$, Ca substitution helps stabilizing the rhombohedral phase till x = 0.1, above which a structural transition occurs. It is important to note that, in BFO systems, only the rhombohedral *R3c* phase is ferroelectric and in the orthorhombic *Pbnm* phase, ferroelectricity is forbidden by the symmetry considerations.

Thus, it is possible to tune the ferroelectric and magnetic properties of BFO with the proper amount of Ca and Mn substitutions. in the $x \neq y$ system, magnetization increases with increase in the Ca or Mn content. Similar to the $x = y$ system, higher magnetic and dielectric properties are observed around the structural transition region. ZFC-FC magnetization studies confirmed that the magnetic hysteresis loop observed at 5 K is associated with a spin glass state. XPS analysis revealed the presence of both Mn^{3+} and Mn^{4+} species along with oxygen vacancies in the $x \neq y$ system similar to the $x = y$ system which again brings the ferromagnetic double exchange interaction into picture. Spin-glass-like phase originates due to the competing magnetic exchange interactions involving Fe^{3+}, Mn^{3+}, Mn^{4+}, and possibly Fe^{2+} and Mn^{2+} (due to oxygen vacancies) which leads to formation of magnetic clusters. The $Bi_{1-x}Ca_xFe_{0.9}Mn_{0.1}O_3$ system exhibits almost similar trend in the magnetic and dielectric properties as that of $Bi_{1-x}Ca_xFe_{1-x}Mn_xO_3$. Similarly, $Bi_{0.85}Ca_{0.15}Fe_{0.9}Mn_{0.1}O_3$ show higher coercivity (≈ 8 kOe) than that for $Bi_{0.825}Ca_{0.175}Fe_{0.825}Mn_{0.175}O_3$.

Thus, from the studies on the different compositions in the Ca and Mn co-substituted $BiFeO_3$, it is found that many of the compositions with equal or unequal amounts of Ca and Mn exhibit better magnetic and dielectric properties. Interesting but complex magnetic characteristics are exhibited by different compositions at low temperatures, due to the formation of magnetic clusters involving competing magnetic exchange interactions. The cluster-glass-like nature is likely to be responsible for the anomalous magnetic characteristics at low temperature. Among the various compositions studied, enhanced properties were observed for the $Bi_{1-x}Ca_xFe_{1-x}Mn_xO_3$ and $Bi_{1-x}Ca_xFe_{0.9}Mn_{0.1}O_3$ series. The magnetic transition temperatures is not much affected on substitution, which suggests that the Ca/Mn co-substituted $BiFeO_3$ can be considered as one of the ideal systems for magnetoelectric device applications within a large temperature window.

6.2. Future perspectives

The work reported in this thesis is only a preliminary investigation of a complex magnetic system. Although improved magnetic, dielectric and magnetodielectric properties are observed in the Ca and Mn co-substituted $BiFeO_3$, when compared to only Ca substitution at the Bi-site or Mn substitution at the Fe-site, which are essential for better magnetoelectric coupling, we have not performed any ferroelectric polarization and direct magnetoelectric measurements. Higher dielectric constant shown around the structural transition region could be due to dense microstructure and not due to higher ferroelectric polarization. Even the

oxygen vacancies and the mixed valency of Mn can contribute to the higher dielectric constant observed. Ferroelectricity in BFO based system are many times compromised due to the low electrical resistance from the secondary phases, defects and oxygen vacancies. In the studied systems, it is possible that the mixed valency of Fe and Mn as well as oxygen vacancies could deteriorate the ferroelectric properties. Thus detailed analysis of the ferroelectric and magnetoelectric characteristics of the studied compositions is required to come to any conclusions on the applicability of the materials as multiferroics.

The bond angle and bond distances along with the Megaw parameters in each composition should be calculated to know the effect of structural distortion on the magnetic and ferroelectric properties. Further, temperature dependent Raman and XRD analysis can give more information on the structural changes and spin-phonon coupling in the system. Due to the different oxidation states and the competing magnetic exchange interactions involving Mn^{3+}-Mn^{3+}, Mn^{3+}-Mn^{4+}, Fe^{3+}-Fe^{3+}, Fe^{3+}-Mn^{3+} and Fe^{3+}-Mn^{4+}, etc., the co-substituted systems become very complex and it is not easy to completely understand the magnetic properties of the system with the current work done. Neutron diffraction analysis can give more details about the magnetic structure of the system. The spin-glass-like characteristics observed could be from spin glass or cluster glass nature or even from domain pinning effects. To confirm this, ac susceptibility measurement has to be performed. Frequency-dependent ac susceptibility measurements can differentiate spin glass and cluster glass systems, but it would be difficult to differentiate domain pinning effect even from this experiments. Also one has to know the exact composition of the system, i.e., oxygen stoichiometry and oxidation states of the ions, precisely to make any conclusion.

As the physics of the $Bi_{1-x}Ca_xFe_{1-x}Mn_xO_3$ system is very interesting, single crystals of some compositions should be grown without any defects or secondary phase. Structural and magnetic analysis of $Bi_{1-x}Ca_xFe_{1-x}Mn_xO_3$ single crystals can give more information about the system. Thus, more detailed studies are required to understand the system fully, in order to propose some of the best compositions showing enhanced properties for magnetoelectric applications.

Appendix

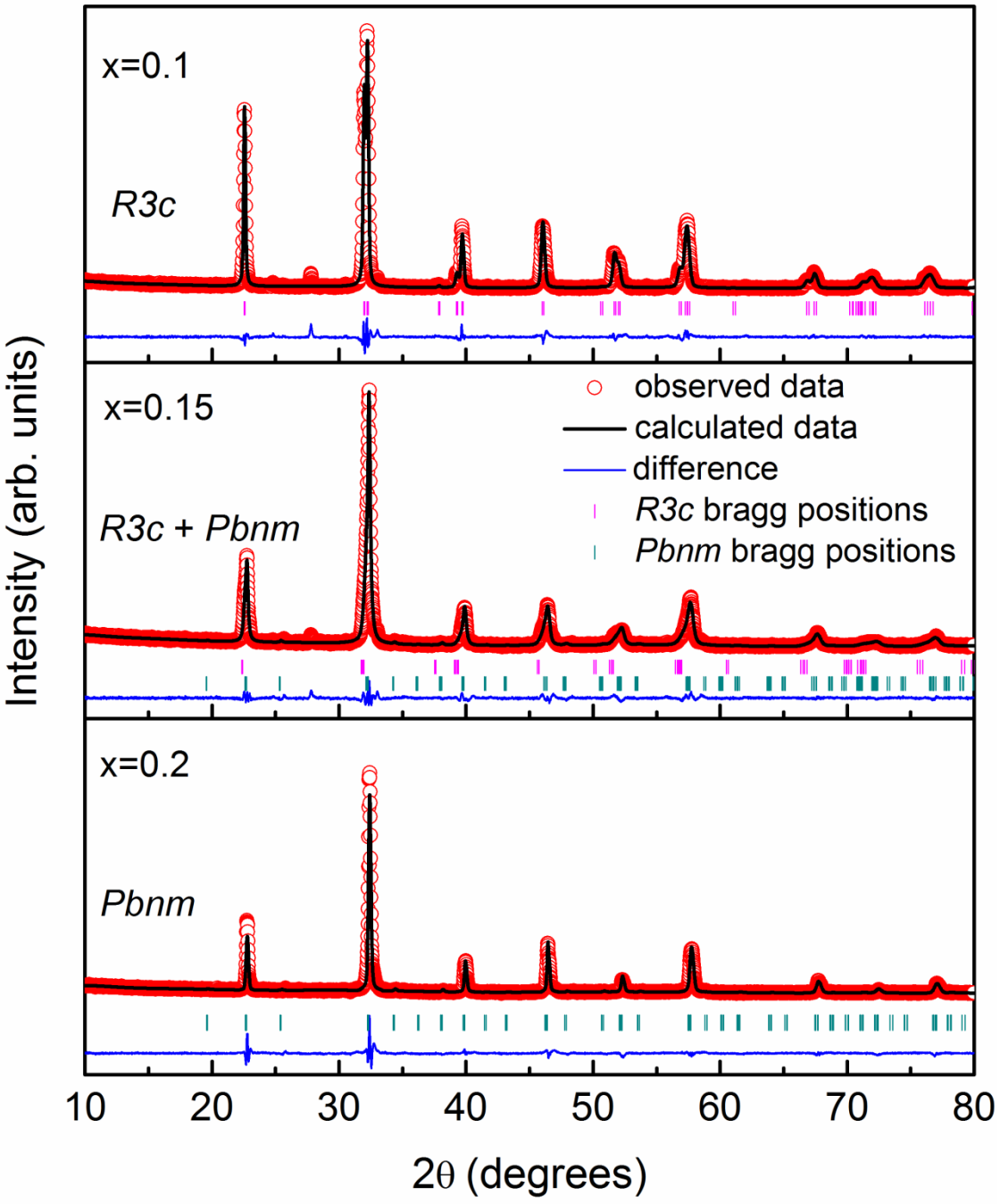

Figure A.1. Results of the Rietveld refinement of selected compositions in $Bi_{1-x}Ca_xFe_{0.9}Mn_{0.1}O_3$.

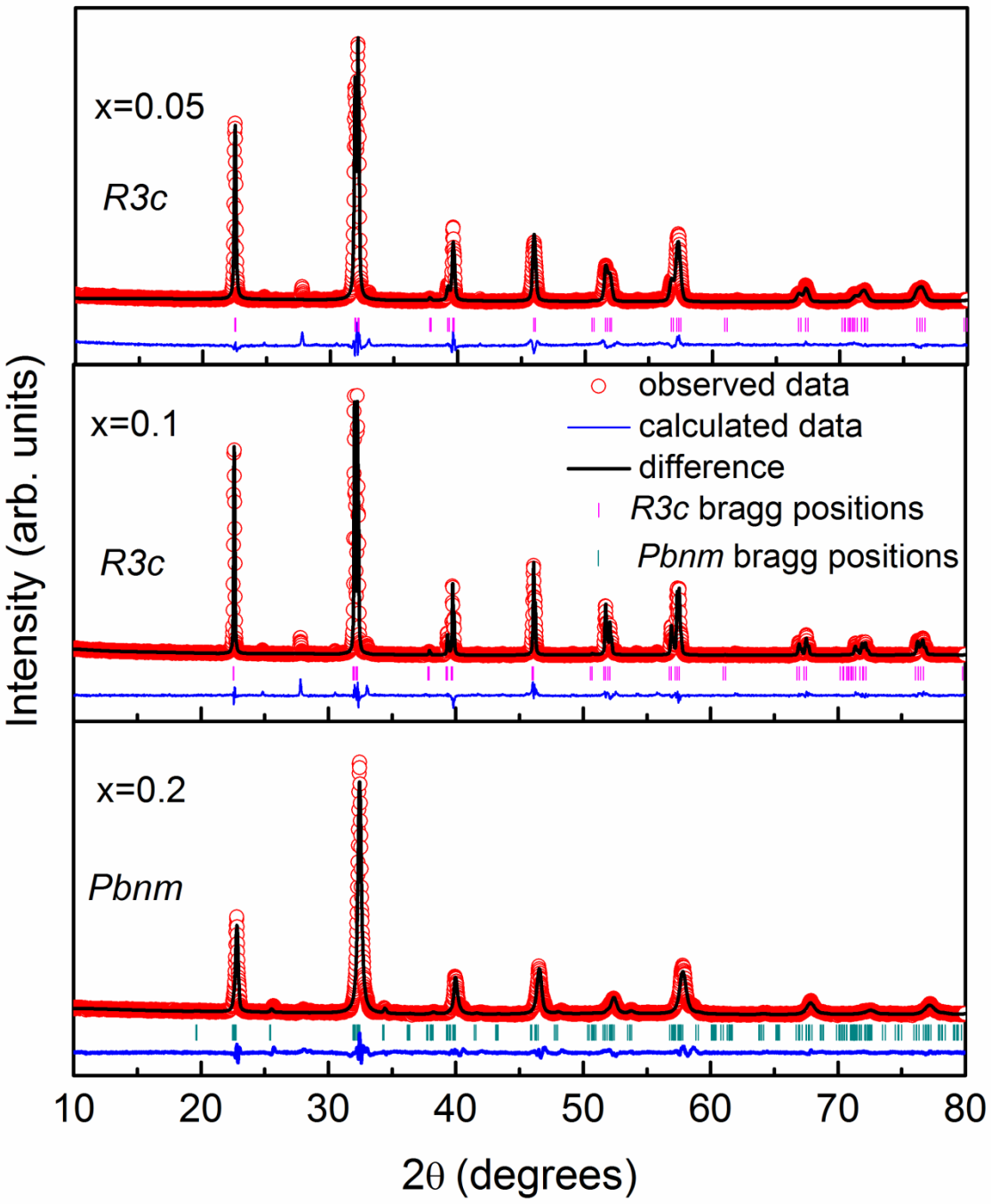

Figure A.2. Results of the Rietveld refinement of selected compositions in $Bi_{1-x}Ca_xFe_{0.8}Mn_{0.2}O_3$.

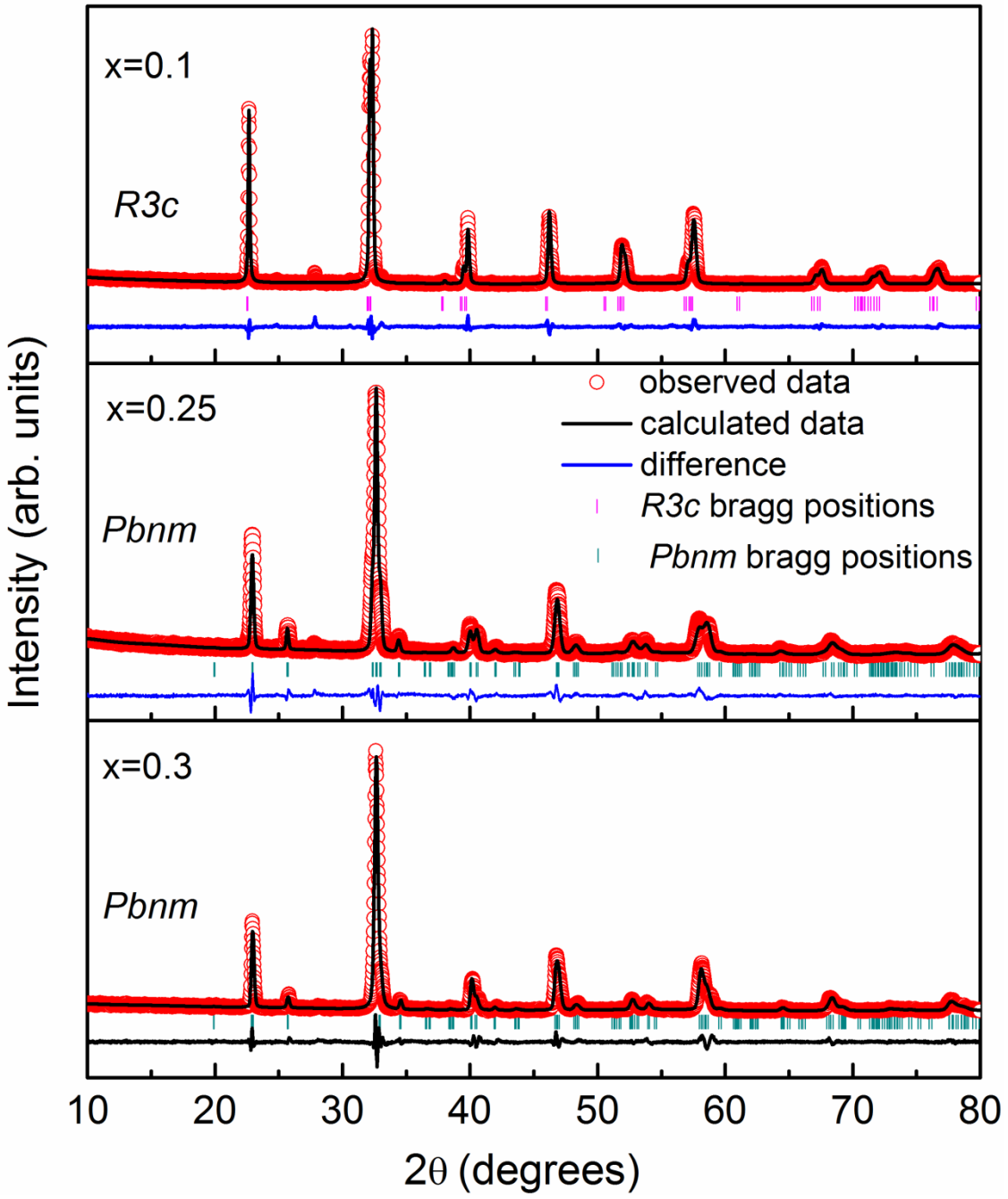

Figure A.3. Results of the Rietveld refinement of selected compositions in $Bi_{1-x}Ca_xFe_{0.7}Mn_{0.3}O_3$.

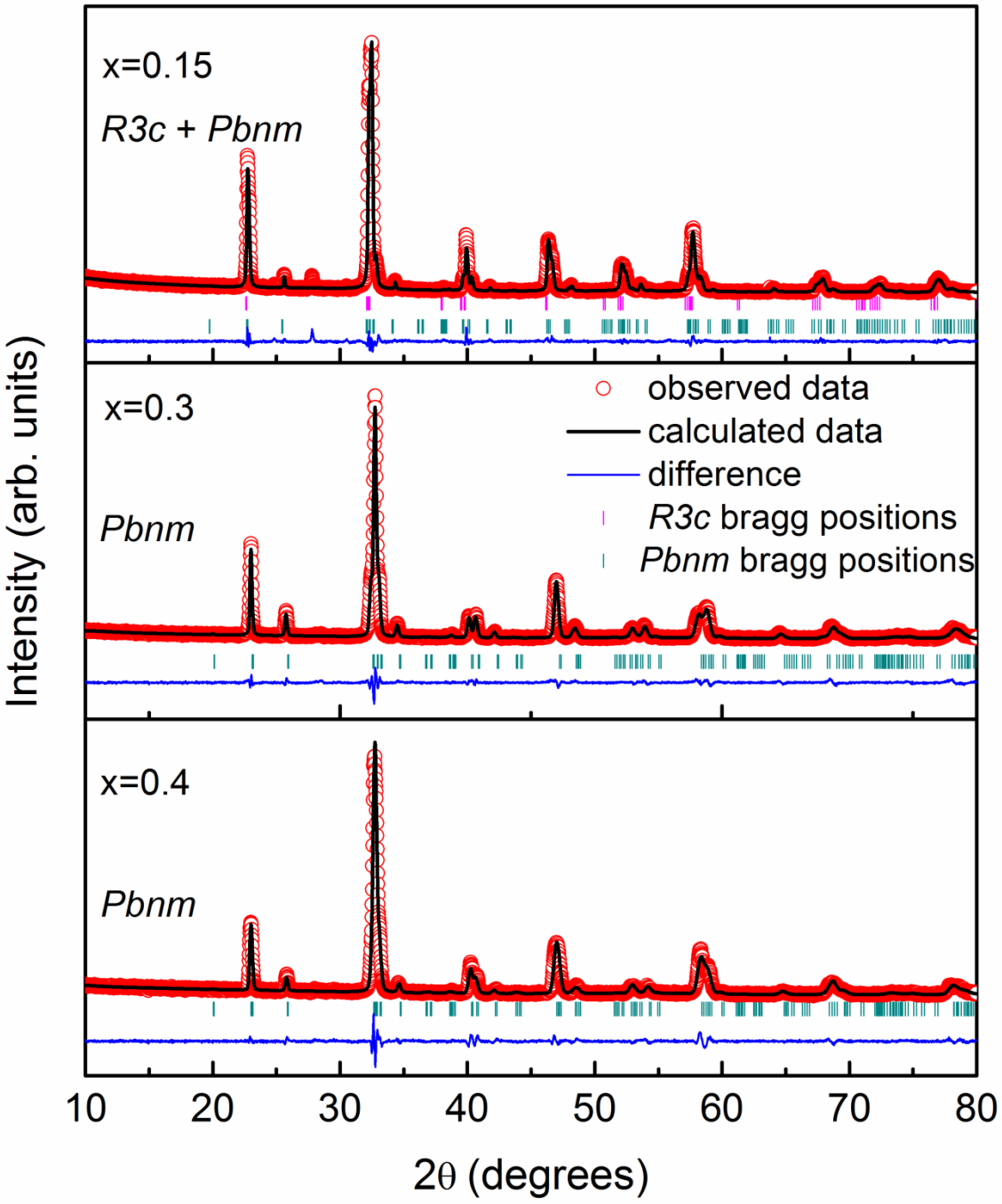

Figure A.4. Results of the Rietveld refinement of selected compositions in $Bi_{1-x}Ca_xFe_{0.6}Mn_{0.4}O_3$.

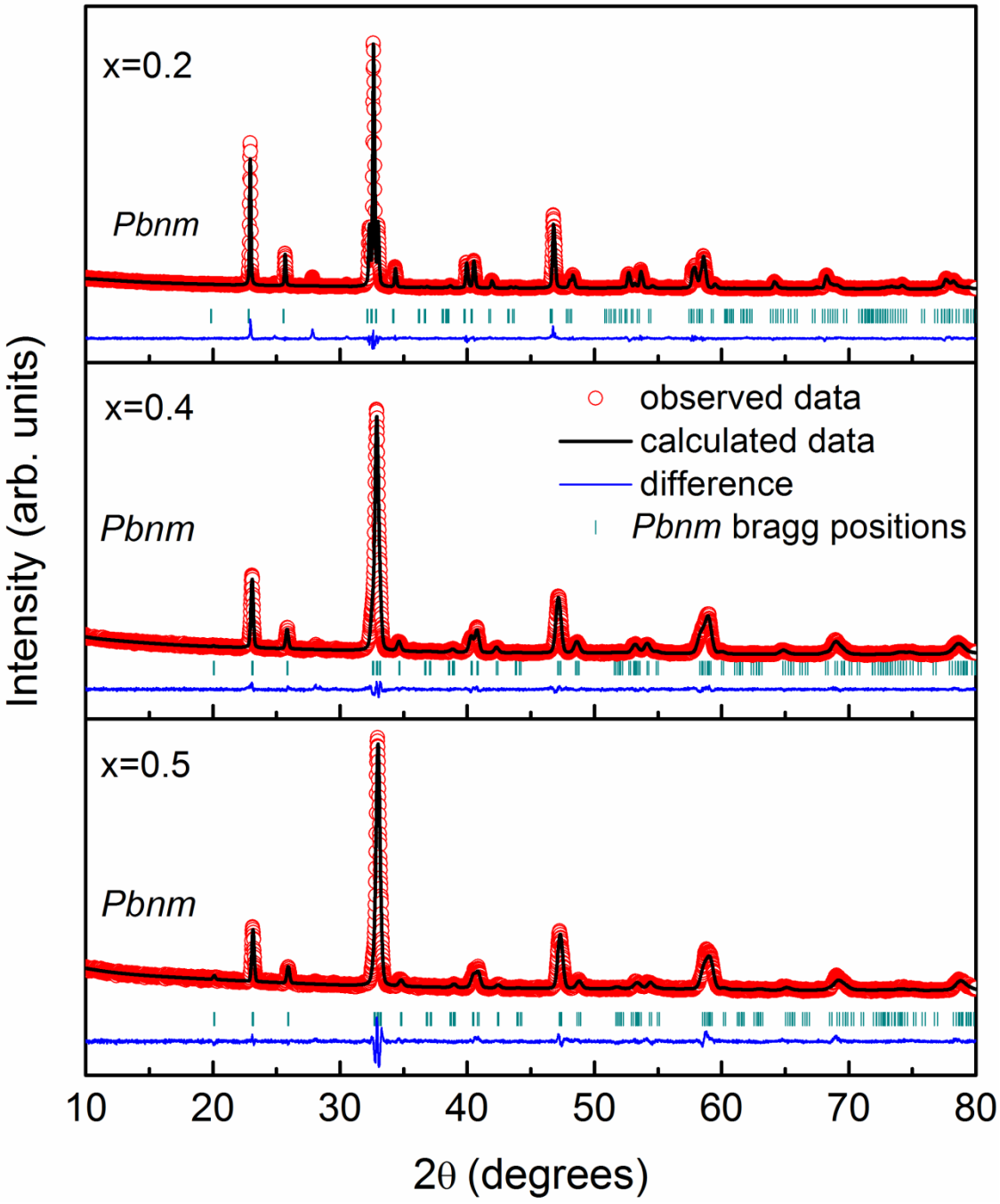

Figure A.5. Results of the Rietveld refinement of selected compositions in $Bi_{1-x}Ca_xFe_{0.5}Mn_{0.5}O_3$.

List of Publications

1. Manjunath B, Thakuria P and Joy P A, “Structural, magnetic, dielectric and magnetodielectric properties of $Bi_{1-x}Ca_xFe_{1-x}Mn_xO_3$ in the morphotropic phase boundary region.” Materials Research Express. 2017, 4(1), 016104.
2. Low temperature magnetic properties of $Bi_{1-x}Ca_xFe_{1-x}Mn_xO_3$, Manjunath B and Joy P A (Manuscript under preparation)
3. Structural and Magnetic properties of $B_{i1-x}A_xFe_{1-x}Mn_{xO3}$ (A = Ca, Sr, Ba), Manjunath B and Joy P A (Manuscript under preparation)
4. Effect of Ca substitution on the structural and Magnetic properties of $BiFe_{1-y}Mn_{yO3}$, Manjunath B and Joy P A (Manuscript under preparation)